Biomimetic Microsystems to Study Cell Migration Mechanoreciprocity in Health and Disease

by

William Y. Wang

A dissertation submitted in partial fulfillment
of the requirements for the degree of
Doctor of Philosophy
(Biomedical Engineering)
in the University of Michigan
2021

Doctoral Committee:

Assistant Professor Brendon M. Baker, Chair
Assistant Professor Matthew L. Kutys
Professor Andrew J. Putnam
Associate Professor Ariella Shikanov

William Y. Wang

wangwy@umich.edu

ORCID iD: 0000-0001-9669-4841

Dedication

To Hannah Rhee, who has been an endless source of caring love and support.

To my friends, old and new, near and far, who have reminded me to celebrate victories of all sizes and picked me up in tough times.

To my family, who have supported me unconditionally and sacrificed untold amounts for my well-being and gifting me the freedom to pursue my dreams.

Acknowledgements

The contents of this thesis would not be possible without the tremendous support I have been fortunate enough to receive from my advisor, lab mates, collaborators, and thesis committee members. First and foremost, I would like to thank my PhD advisor, Brendon. Having just moved to Boston as a postdoc, Brendon first took me on (in desperate times I believe) as an undergraduate research trainee. I can still recall my first interview with Brendon, where I stumbled through my minimal scientific vocabulary in an effort to express my interest in biomedical research. Looking past the subtitles, I think what Brendon sensed in me was a student eager to learn with an innate curiosity for science in and of itself. Next, Brendon joined the University of Michigan as a new Assistant Professor and (again in desperate need of a trainee) took me on as his first graduate student. Over the past 8 years, both as an undergraduate and graduate student, Brendon has tirelessly molded, trained, and developed me into a self-sufficient, critically thinking research scientist. Brendon, I will be forever grateful for the undying support and bountiful opportunities you have provided me with. … However, outside of the lab, whether it be at the poker table, ping pong, or volleyball court, Brendon *The Advisor* has often morphed into one of my fiercest rivals aka *The Builder* or especially in poker, *The Imploder*. Brendon, I am honored to have had the privilege of learning from you and consider you as one of my closest friends.

This thesis contains several key contributions from other members of the Baker Lab and close collaborators. Christopher and Dan: as the original trio of Baker Lab graduate students, I feel so fortunate to have shared my PhD experience with you two every step of the way. Daphne and Evan: thank you for placing your trust in me as your research mentor and for diligently carrying

out challenging experiments that I have placed on you. Harrison, Sam, and Bobby: As the new wave of Baker Lab students, I have often turned towards your counsels as your fresh energy and excitement for research always reinvigorates my own enjoyment for science. Bill and Matt: Thank you for expanding my research horizons and providing me with your expertise in fluid mechanics and molecular biology, which have each added new dimensions to my thesis work.

Table of Contents

List of Tables

List of Figures

List of Movies

Abstract

Mechanoreciprocity in cell migration is an emerging concept describing the dynamic, bi-directional interactions between migrating cells and the surrounding extracellular matrix (ECM) they negotiate. Migrating cells not only sense and adapt to biochemical and biophysical ECM cues, but also, exert forces, deposit matrix, and secrete chemokines, matrix metalloproteinases, and matrix crosslinking enzymes that dynamically alter the same ECM properties known to regulate cell migration. Due to limitations in standard cell migration assays, how matrix properties influence cell migration and in turn, how cells influence matrix properties, has previously been studied as separate processes. However, observations from development, wound healing, and a variety of disease processes highlight the interdependency and iterative relationship between cell migration and ECM. An improved understanding of the underlying mechanisms that orchestrate the coevolution of migrating cells and ECM will aid in tissue engineering and regenerative medicine efforts to guide repair fibroblasts to regenerate wound beds, direct collective endothelial cell migration to vascularize ischemic or engineered tissue grafts and confine otherwise metastatic cancer cells to the primary tumor. Thus, the focus of this dissertation is to design biomimetic microsystems that afford investigation of cell migration mechanoreciprocity with a focus on fibroblasts, endothelial cells, and cancer cells.

First, this thesis investigated how single mesenchymal cells (fibroblasts and cancer cells) migrate in fibrous stromal tissue settings, such as in trans-stromal cancer cell migration during metastasis. To model fibrous stromal tissue, 3D fiber networks were electrospun over

microfabricated wells to define ECM mechanics. Independently tuning alignment and stiffness of these matrices resulted in two phenotypically distinct cell migration modes. In contrast to stiff matrices where cells migrated continuously in a traditional mesenchymal fashion, cells in deformable matrices stretched matrix fibers to store elastic energy; subsequent adhesion failure triggered sudden matrix recoil and rapid cell translocation (termed slingshot migration). Across a variety of cell types, traction force measurements revealed a relationship between cell contractility and the matrix stiffness where slingshot migration mode occurred optimally.

Next, this thesis describes how microenvironmental cues influence collective endothelial cell migration during sprouting angiogenesis towards the design of pro-angiogenic biomaterials. This work employed a multiplexed angiogenesis-on-a-chip platform to assess the chemokine-directed 3D invasion of endothelial cells from a lumenized parent vessel into user-defined ECM. By tuning soluble and physical cues of the ECM, this work identified how 1) functional angiogenesis requires microenvironmental cues that balance cell invasion speed and proliferation; 2) dynamic interactions between sprout stalk cells and ECM regulates neovessel lumenization; and 3) imbuing microporosity within synthetic hydrogels can enhance endothelial cell invasion and angiogenic sprout lumenization.

Lastly, this thesis investigated how fibrous matrix cues activate quiescent vessel-lining endothelial cells into invasive tip cells in the context of fibrosis. Composite hydrogels (electrospun fiber segments suspended within 3D ECM) were integrated with the angiogenesis-on-a-chip platform. These studies establish that heightened matrix fiber density destabilizes cell-cell adherens junctions, reduces endothelium barrier function, and promotes the invasion of endothelial tip cells. Performing transcriptomic and secretomic analyses on fiber-induced tip endothelial cells revealed that fibrous ECM cues promote a fibrosis propagating phenotype.

Overall, the work presented in this dissertation integrates tunable biomaterials with microfabricated devices to investigate cell migration mechanoreciprocity of single mesenchymal cell migration, the collective migration of endothelial cells during angiogenesis, and endothelial-mesenchymal transition of quiescent endothelial cells into a fibrosis propagating cell phenotype.

Chapter 1: Introduction

The overarching goal of this thesis is to design biomimetic microsystems that afford careful investigation into the bi-directional interactions between migrating cells and their surrounding extracellular matrix (ECM). To do so, the following work employs a variety of matrix mimetics to model various properties of fibrous ECM, utilizes cell and ECM labelling techniques to dynamically assess cell and matrix states over time, and elucidates mechanisms of cell migration mechanoreciprocity by perturbing mediators of cell-matrix interactions.

Chapter 2 provides broad background information on the history and progression of studying cell migration beginning with *in vivo* observations to early mechanistic studies on 2D substrates to tunable 3D hydrogel-based biomaterials. Additionally, the diverse and dynamically changing structure and composition of ECM during adult homeostasis, wound healing and fibrotic progression is described in detail to provide key matrix properties that cell migration models should strive to recapitulate, namely material platforms that recapitulate the 3D, fibrous and microporous structure of native tissues. Lastly, Chapter 2 provides currently known understanding of how cells sense, respond, and alter ECM properties during migration. To advance our knowledge, the remaining chapters focus on incorporating fibrous or microporous ECM within cell migration assays.

Chapters 3 and 4 first focus on single, mesenchymal cell migration of fibroblasts and cancer cells in response to the fibrillar component of stromal tissues. Chapter 3 details a high content ECM screening array that affords the investigation of serial combinations of ECM line width,

density, and alignment on cell migration. This work identified that matrix alignment is the most critical parameter (of those tested) and promotes uniaxial cell migration by organizing focal adhesions, RAC1 activity, and cell protrusions. Building off Chapter 3's findings that matrix alignment is a critical factor, Chapter 4 details cell migration in more complex 3D fibrillar matrices that afford independent control over alignment and stiffness. Through this work, a novel cell migration mode, termed slingshot migration, was identified whereby cells apply actomyosin driven contractile forces to stretch and store strain energy in matrix fibrils. When strain energy overcomes the forces focal adhesions can bear, a physical failure at rear adhesion sites resulted in matrix recoil and rapid cell translocation.

Chapter 5 shifts in focus onto the migration of endothelial cells as single cells vs multicellular strands. This work establishes a multiplexed angiogenesis-on-a-chip platform that affords improved experimental throughput of studying how combinations of microenvironmental cues regulate the chemokine-directed, 3D invasion of endothelial cells from a lumenized parent vessel. This work identified that functional angiogenesis, endothelial cell invasion as multicellular, lumenized sprouts that are fluidically connected, requires microenvironmental cues that balance invasion speed and proliferation. In settings where invasion speed is not commensurately matched with proliferation, endothelial cell invasion occurs predominantly as single cells, and generates blunt ended neovessels with poor barrier function reminiscent of rapid tumor angiogenesis. Overall, this chapter provides a framework to tune microenvironmental cues to study angiogenesis in therapeutic or disease contexts.

Chapters 6-7 focus on the therapeutic aspect of multicellular endothelial cell migration towards designing vascularized biomaterial implants. Chapter 6 investigates how microenvironmental cues control the lateral expansion of endothelial cell sprouts that precede

lumenization. This work identified that sprout stalk cells utilize a combination of cytoskeletal forces and proteolysis to physically compact and degrade the surrounding matrix, thus generating sufficient space to lumenize. Chapter 7 builds off Chapters 5-6's findings by designing synthetic hydrogels imbued with microporosity that improves functional angiogenesis *in vitro* and through *in vivo* implantation to the murine fat pad.

Chapter 8 focuses on endothelial cell migration in fibrotic disease contexts, specifically investigating how physical ECM properties activate quiescent vessel lining endothelial cells into invasive tip cells through mesenchymal transition pathways. To model fibrotic ECM, this work integrated a composite materials approach by combining synthetic fiber segments and 3D hydrogels within a tip cell formation assay. This chapter identified that increasing fiber density (recapitulating the excessive deposition of fibrillar proteins with fibrotic progression), led to the destabilization of adherens junctions, decrease in endothelium barrier function, and promoted the invasion of endothelial cells. With transcriptional and secretome analyses, these fiber-induced tip endothelial cells were observed to take on a fibrosis propagating phenotype, specifically secreting elevated levels of TGFβ2. Lastly, this chapter investigated how endothelium in fibrous vs control ECM respond to excessive TGFβ2 and identified a VE-cadherin dependent TGFβ2-induced apoptosis pathway that may underlie the common observation of microvasculature rarefaction in late-stage fibrosis.

Finally, Chapter 9 provides a summary of the major findings from this thesis work and future directions to designing biomimetic microsystems. The integration of recently established technologies that afford careful assessment of cell and matrix states will improve our understanding of cell migration mechanoreciprocity for applications in health and disease.

Chapter 2: Background

2.1 Cell migration diversity in health and disease

2.1.1 Coevolution of migrating cells and extracellular matrix

The migration of cells to their target destinations plays a fundamental role during development, wound healing, and disease processes. Microenvironmental cues, both biochemical and biophysical characteristics of the surrounding extracellular matrix (ECM), influence the mechanisms by which cells migrate (Lauffenburger and Horwitz, 1996). Additionally, these microenvironmental cues dynamically change over various time scales (Helvert et al., 2018). During developmental processes, cells migrate within a highly cellular and pliable ECM microenvironment that undergoes structural changes over hours to days (Loganathan et al., 2016). For example, observations of heart tube formation in quail embryo have revealed that endocardial precursor cells migrate as a collective sheet with simultaneous deformation and folding of a fibronectin and fibrillin-1 rich matrix (Aleksandrova et al., 2012, 2015). In wound healing processes, a variety of cell types (fibroblasts, endothelial, epithelial, and immune cells) migrate towards the wound bed to mediate tissue regeneration. Simultaneously, the wound microenvironment undergoes incremental changes in ECM composition over days to weeks from a fibronectin/fibrin rich provisional matrix towards a more mature collagen-rich matrix . In disease contexts, such as cancer, the surrounding tumor stroma is well-documented to progressively increase in stiffness, collagen fiber density and alignment occurring over months to years (Conklin et al., 2011; Levental et al., 2009; Paszek et al., 2005; Provenzano et al., 2006). Indeed, these

changes in matrix properties correspond to various cancer cell migration mechanisms as collective strands or single cells and are indicative of patient outcomes (Hiraki et al., 2021; Ilina et al., 2018; Khalil et al., 2017; Padmanaban et al., 2019). Specifically, the more fatal invasive lobular carcinomas are primarily composed of aligned collagen fibrils with single cancer cell metastases compared to less fatal invasive ductal carcinomas that are primarily composed of more irregular collagen organization and multicellular strand like metastases with (Ilina et al., 2020).

Across these broad and distinct biological processes, an improved understanding of how dynamically changing matrix properties regulate cell migration will lead to major breakthroughs in designing cell migration-based therapies such as promoting fibroblasts to accelerate tissue regeneration at the wound bed, confining otherwise metastatic cancer cells to the primary tumor, or guiding the collective invasion of endothelial cells via angiogenesis to vascularize ischemic or engineered tissue grafts (Kim et al., 2021; Nourian Dehkordi et al., 2019; Novosel et al., 2011; Rosel et al., 2019). Towards the design of cell migration-based therapies first requires an appreciation of the diversity of migration modes cells employ and how they can be directed.

2.1.2 Mesenchymal, epithelial, and amoeboid migration modes

Cells select from a diverse repertoire of migration modes to overcome the physical barriers presented by the ECM to reach their target destination (Charras and Sahai, 2014; Yamada and Sixt, 2019). At the highest level, cell migration modes are broadly categorized by their migration phenotype as multicellular structures (epithelial) or as single cells (mesenchymal and amoeboid) and whether they employ proteolysis (epithelial and mesenchymal) or non-proteolytic cell squeezing (amoeboid) (Sabeh et al., 2009; Yamada and Sixt, 2019). Importantly, these are broad classifications with several exceptions in addition to newly identified migration mode subtypes

within epithelial, mesenchymal, and amoeboid cell migration **(Figure 2.1)**.

Within epithelial cell migration, cells migrate as a collective unit composed of individual cells that are rich in cell-cell adherens junctions (e.g. E-cadherin or VE-cadherin) (Friedl and Gilmour, 2009). Two subtypes of epithelial migration include migration as a collective sheet or collective strand. For example, endothelial cells (a specialized epithelial cell type that lines blood vessels) migrate as a collective sheet in large diameter blood vessels or to endothelialize an implanted stent (Kiosses et al., 1997; Rochon et al., 2016; Wei et al., 2013). Additionally, endothelial cells can undergo collective strand-like migration during angiogenesis to extend microvasculature from pre-existing blood vessels (Carmeliet, 2005; Michaelis, 2014). In contrast to collective epithelial cell migration, mesenchymal cell migration is characterized by the migration of single cells (low cell-cell adherens junctions) with high levels of cell-matrix adhesions, actomyosin contractility and proteolytic activity. However, mesenchymal cells can also migrate in non-proteolytic mechanisms depending on the matrix architecture (Wolf and Friedl, 2011; Wolf et al., 2007). Fibroblasts for example can physically engage and deform the surrounding matrix to create sufficient space to push its cell body forward (Doyle et al., 2021; Wisdom et al., 2018) . Immune cells typically migrate using amoeboid migration characterized as single cells with low adherens junctions and matrix adhesions, and primarily migrate using non-proteolytic means by squeezing through matrix pores (Lämmermann and Sixt, 2009; Liu et al., 2015).

Furthermore, cells can transition between these broad classifications of amoeboid, epithelial, and mesenchymal cell migration modes **(Figure 2.1)** (Friedl and Wolf, 2010). In the context of epithelial cancers such as invasive lobular carcinoma, breast cancer cells undergo epithelial-mesenchymal transition to migrate more efficiently through dense fibrillar tumor stroma

as single mesenchymal cells that are more proteolytically active (Kalluri and Weinberg, 2009). After intra- and extravasation, these metastatic cancer cells are hypothesized to undergo mesenchymal-epithelial transition to return to an epithelial cell phenotype and populate secondary metastatic tumor sites in distant organs from the primary tumor.

Overall, migrating cells utilize a variety of cell migration strategies and can dynamically adopt or interconvert between cell migration modes based off the surrounding microenvironmental properties (Friedl and Wolf, 2010) **(Figure 2.1)**. While these initial insights have been observed to occur in *in vivo* contexts, the inability to finely control and tune migration modes, in addition to the matrix properties that regulate migration diversity, limits mechanistic studies. Thus, many groups have turned towards developing *in vitro* models of cell migration to elucidate the underlying molecular machinery that orchestrate cell migration diversity. Towards designing physiologically representative *in vitro* models, we must first understand the diverse structures and compositions of native ECM that *in vitro* models strive to recapitulate.

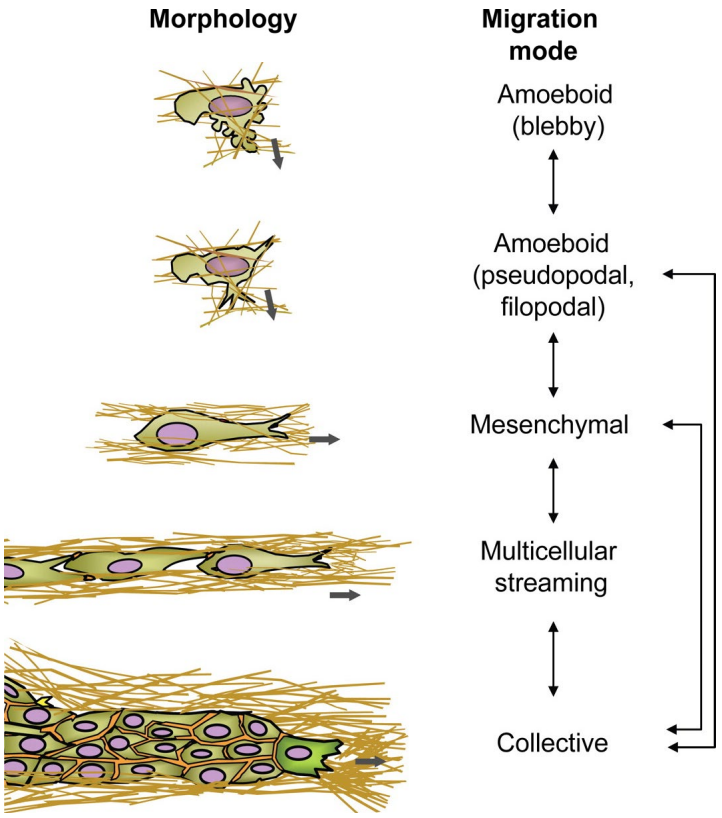

Figure 2.1: Cells can employ a variety of cell migration modes that are broadly categorized by their migration morphology and can dynamically interconvert between each mode. Image reproduced from (Friedl and Wolf, 2010).

2.2 Extracellular matrix structure and composition

2.2.1 Stromal extracellular matrix during adult homeostasis

The ECM is the non-cellular component of all tissues and provides both biophysical structure and biochemical signaling cues to resident cells. During adult tissue homeostasis, the majority of cell migration occurs within stromal tissue settings. Stromal ECM is composed of two main components: 1) networks of fibrillar proteins, primarily type I collagen fibrils, and 2) an amorphous, highly hydrated ground substance enriched with glycosaminoglycans (e.g. heparan sulfate and proteoglycan) **(Figure 2.2)**. The organization of stromal tissues varies considerably across organ and tissue systems, due in part to support each tissue's unique functions (Park et al., 2019). Stromal ECM of skeletal muscle and cardiac tissue are dense and aligned which support

directional muscle contractions (Gillies and Lieber, 2011). In contrast, adipose tissue ECM contains more loose and irregularly organized collagen fibrils (Divoux and Clément, 2011; Weigelin et al., 2012). In tendon, collagen fibrils display an aligned and crimped morphology to aid in structural stability upon force loading (Pang et al., 2017). In the lung, stromal ECM contains a higher elastin content, to better support the more elastic expansion/contraction the tissue experiences with breathing (Burgstaller et al., 2017). On top of the vast diversity of ECM structure across tissues at homeostasis, upon tissue injury or disease, several matrix properties are dynamically altered over time and may lead to dysregulated tissue function.

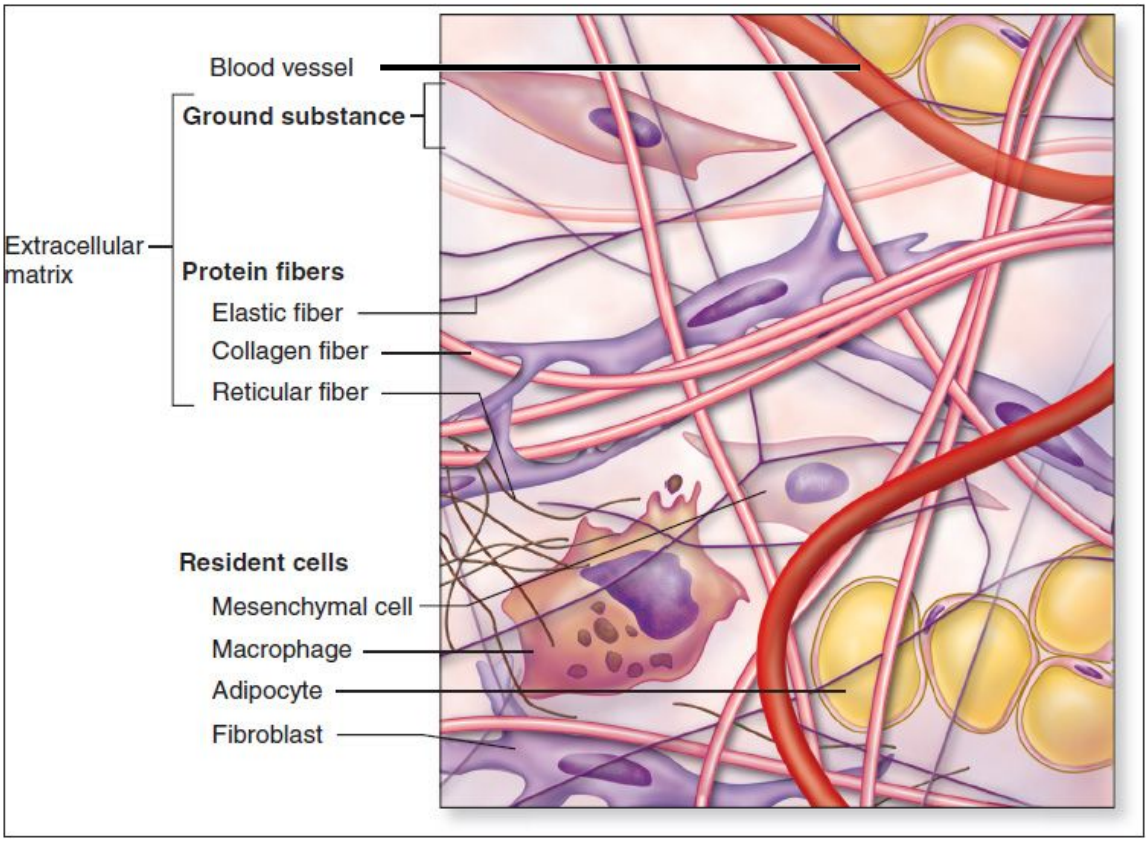

Figure 2.2: Cells reside within 3D extracellular matrix composed of protein fibers and space filling ground substance. Image reproduced from (Mescher, 2013).

2.2.2 Wound healing extracellular matrix

During the wound healing process, the wound bed matrix undergoes considerable remodeling to repair the injury site (Schultz et al., 2011). After initial injury, the blood clotting cascade generates a fibrin rich plug at the site of injury. Inflammatory cytokines are secreted by resident cells of the wound bed to recruit the migration of surrounding fibroblasts. Additionally, the endothelium responds to inflammatory cytokines by increasing the expression of immune cell adhesion receptors on the luminal surface and decrease adherens junctions between endothelial cells to both bind circulating immune cells and promote diapedesis (Koh and DiPietro, 2011). Together with immune cells, fibroblasts begin to remodel the wound bed ECM by digesting damaged tissue and provisional matrix (Hinz, 2007). During this process, fibroblasts are activated into myofibroblasts via soluble and matrix bound TGFβ (i.e. latent TGFβ complexes that require cell forces to release from the matrix) and iteratively transition the provisional matrix towards granulation tissue – a fibronectin/collagen rich matrix (Hinz, 2016; Wipff et al., 2007). In parallel, myofibroblasts and immune cells within the wound bed secrete pro-angiogenic factors that promote the collective migration of endothelial cells from nearby microvasculature to revascularize the wound matrix (Tonnesen et al., 2000). After granulation tissue is formed, the myofibroblast population undergoes programmed cell death, and the matrix transitions towards collagen-rich scar tissue with regression of microvasculature (Greenhalgh, 1998). Overall, the wound healing program involves a variety of migrating cell types to coordinate the regeneration of damaged tissues. However, when the wound healing program becomes dysregulated, or is subjected to chronic injury, wound resolution is never achieved resulting in a self-propagating myofibroblast population that can ultimately lead to fibrosis and organ failure (Diegelmann and Evans, 2004).

2.2.3 Extracellular matrix during fibrotic progression

Fibrotic diseases are often considered as wounds that never heal. These chronic injuries hijack the wound healing program and prolong wound resolution resulting in a dysregulated myofibroblast population that are highly contractile and excessively deposit ECM (Hinz and Lagares, 2020). The combination of excessive matrix deposition and condensation leads to an increase of matrix density and stiffness over time, ultimately resulting in organ failure (Pakshir and Hinz, 2018). For example, in idiopathic pulmonary fibrosis, the elastin rich matrix that affords cyclic expansion/contraction of alveoli is replaced with mechanically incompliant, collagen rich fibrotic matrix that reduces alveoli function (Fernandez and Eickelberg, 2012). In liver cirrhosis, matrix is deposited as aligned collagen tracts that connect vessel structures, a pathology known as bridging fibrosis (Desai et al., 2016). Overtime, the fibrotic matrix leads to reduced diffusion rates and failure to efficiently process/filter toxins within blood.

Although it is well accepted that the myofibroblast is the principal cell type that drives fibrosis, therapeutic targeting of myofibroblasts has been met with several challenges (Yazdani et al., 2017). As myofibroblasts also serve a critical role in normal wound healing program, global targeting of myofibroblast markers may reduce the capacity of physiologic tissue homeostasis and maintenance of stromal tissues (Chandler et al., 2019). Furthermore, single cell sequencing of myofibroblasts have demonstrated that they are transcriptomically heterogeneous (Adams et al., 2020; Habermann et al., 2020; Valenzi et al., 2019). Due in part to this heterogeneity may be that there have been several reports that other cell types, besides fibroblasts, that can differentiate into a myofibroblasts and differ with each organ system **(Figure 2.3)** (Hinz et al., 2007). For example, in cardiac, lung, kidney, and liver fibrosis, lineage tracing studies, among other measures, have demonstrated endothelial cells can undergo endothelial-mesenchymal transition (akin to epithelial-

mesenchymal transition) and contribute as much as 20% of the myofibroblast population in a mouse model of cardiac fibrosis (Aguiar et al., 2020; Hashimoto et al., 2010; Li et al., 2019; Zeisberg et al., 2007).

Overall, native tissues are primarily composed of fibrillar collagen proteins intermingled within a highly hydrated ground substance. The organization and mechanics of these components varies considerably across tissue systems and are documented to undergo dynamic structural changes.

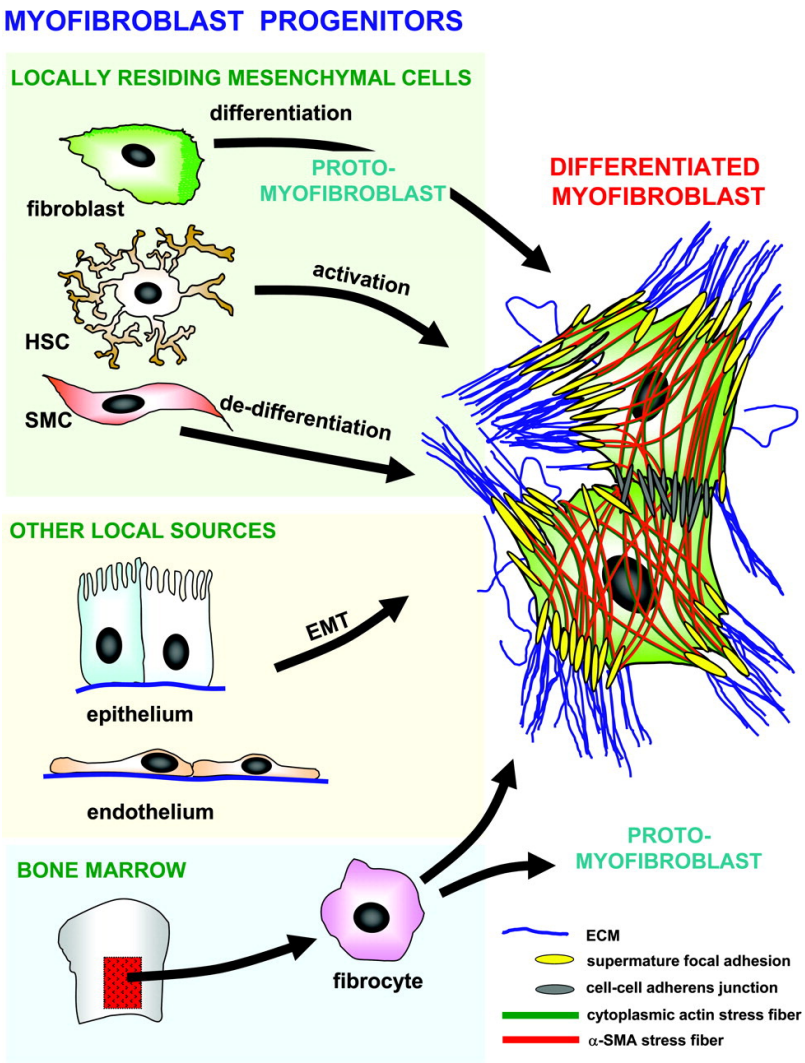

Figure 2.3: In addition to fibroblasts, there are many other cellular sources that have been identified to differentiate into myofibroblasts. Image reproduced from (Hinz et al., 2007).

2.3 Engineered models of cell migration

2.3.1 Traditional cell migration cycle

Despite our understanding of the complex structure and composition of native tissues, early *in vitro* cell migration models utilized reductionist approaches in favor of improved control and assessment of the molecular signaling networks that underlie cell migration. At the simplest level, with the highest level of molecular control and analysis, early assays involved plating single fibroblasts onto glass coverslips or tissue culture plastic coated with isolated matrix proteins (e.g. fibronectin). These initial studies have provided foundational understanding of the mesenchymal cell migration cycle and regulation from the family of Rho GTPases (Ridley, 2001). Fibroblasts in these settings migrate in an iterative process cycling through the following steps: 1) protrusion/extension of the leading edge, 2) adhesion of the leading edge to the substrate, 3) contraction of the cell body towards the leading edge, 4) retraction/release of the trailing edge **(Figure 2.4)** (Hanna and El-Sibai, 2013).

Among the large family of Rho GTPases, the Rho, Rac, and Cdc42 subfamilies are the most well characterized regulators of cell migration (Kutys and Yamada, 2014; Ridley, 2015). The polarization of cells is maintained by the position of the microtubule organizing center which directs directional growth of microtubules to define leading and trailing edges of the cell (Luxton and Gundersen, 2011). Protrusions of the leading edge are extended by active actin polymerization through the actin nucleating activity of actin-related protein (Arp) 2/3 complexes (Schaks et al., 2019). Additionally, Cdc42 and Rac are preferentially activated (GTP-bound) at the leading edge to help mediate Arp 2/3 actin polymerization and their inhibition results in decreased leading edge extension and subsequent migration. Interestingly, the levels of Rac activity have been identified to control cell migration directionality in 2D settings (Pankov et al., 2005; Petrie et al., 2009).

While Rac inhibition reduces cell migration, highly activated Rac also reduces cell migration by generating several protrusions, each providing a conflicting directional migration cue resulting in less persistent migration. Intermediate levels of Rac activity promote select, defined protrusions that optimally guide directional (persistent) cell migration.

Actomyosin-driven cell contractility provides the intercellular forces necessary to contract the cell body forward during migration and is regulated by Rho (Provenzano et al., 2008). Rho acts on ROCK (a Rho-kinase) to influence myosin light chain (MLC) phosphorylation by both inhibiting MLC phosphatase and promoting MLC phosphorylation thus, regulating actomyosin-dependent cell contractility (Amano, 1997; Amano et al., 1996). Lastly, the release of the trailing edge is considered as the rate-limiting step of cell migration in these settings and is regulated by the rate of calpain-mediated proteases to disassemble focal adhesions (Cortesio et al., 2011; Huttenlocher et al., 1997). Interestingly, efficient cell migration in these settings is achieved when focal adhesion size and contractility are in balance (Bangasser et al., 2017; Chan and Odde, 2008; Peyton and Putnam, 2005). If focal adhesions are large, migration is limited by the disassembly of more stable trailing edge adhesions, however, when focal adhesions are small, this leads to reduced cell contractility to move the cell body forward.

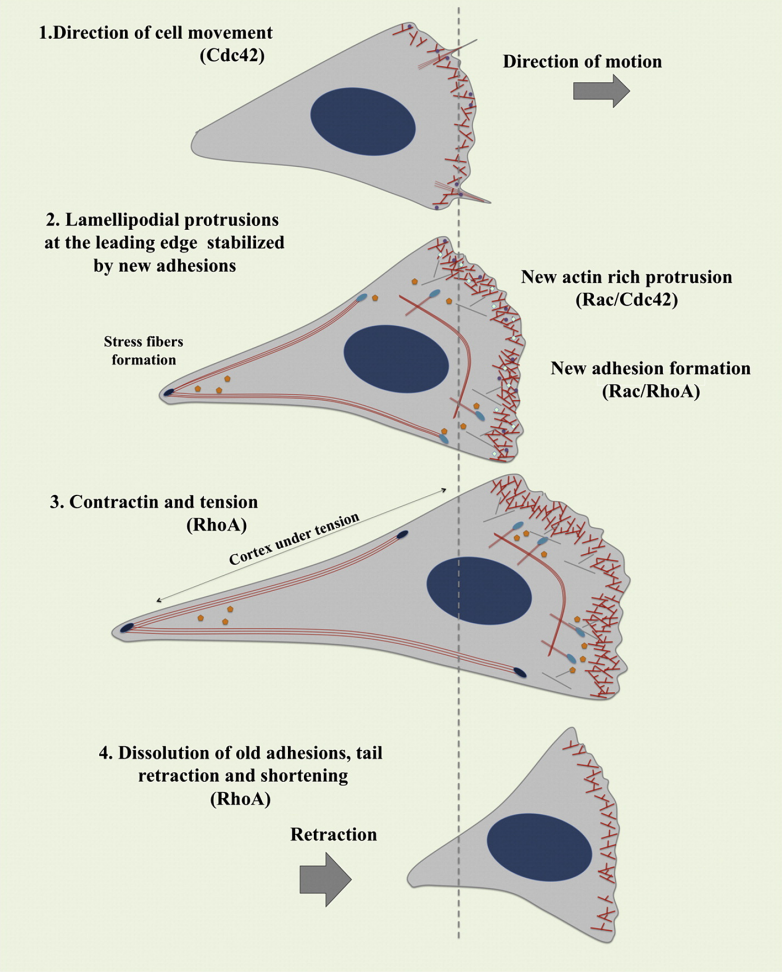

Figure 2.4: Mesenchymal cell migration in 2D settings is regulated by Rho GTPases. Image reproduced from (Hanna and El-Sibai, 2013).

2.3.2 Methods to direct cell migration

While cell migration on 2D settings provided foundational insights to the molecular machinery that regulate cell migration, the native cellular microenvironment provides a plethora of biochemical and biophysical cues that direct cell migration (Rodriguez and Schneider, 2013). To recapitulate these guidance cues, the field has turned towards engineered models of cell migration.

Gradients of chemokines or growth factors can direct cell migration towards (chemoattractant) or away (chemorepellent) from a chemotactic source. To generate defined

chemokine gradients, the field has primarily turned towards microfluidic devices with a chemokine source channel and a cell loading region (Wu et al., 2013). Chemokines bind to their respective cell receptors, polarize, and define the cell's leading edge to drive directional migration.

Led by Yu Li Wang's group, polyacrylamide gels of varying stiffness have been shown to direct cell migration, a process known as durotaxis (Lo et al., 2000; Pelham and Wang, 1997). Cellular focal adhesions are larger and more stable with increasing substrate stiffness. Thus, when presented with a gradient of stiffness, cells preferentially migrate towards stiffer regions as the kinetics of focal adhesion turnover favor the direction of more stable, longer-lasting adhesions. Following a similar principal, haptotaxis defines the preferential migration of cells towards increasing ligand density where high ligand density promotes larger, more stable focal adhesions (Engler et al., 2004). Towards modeling the fibrous topography of native tissues, several groups have engineered substrates with surface topography and have demonstrates aligned topography can polarize cells and promote migration in the direction of alignment known as contact guidance (Ray et al., 2017a).

Although engineered substrates, such as the examples provided above, improve our understanding of how biochemical and biophysical ECM cues direct migration, however many of these engineered models lack key aspects of cell migration in native tissue settings. Importantly, these engineered substrates do not afford cell-mediated matrix remodeling nor migration in 3D settings (Baker and Chen, 2012; Friedl et al., 2012; Helvert et al., 2018). 3D cell migration often requires proteolysis or cell-mediated reorganization of the surrounding matrix structure to generate sufficient space for the cell to migrate. Indeed, work utilizing 3D matrix settings have highlighted deviations from the traditional cell migration described on 2D settings to include the requirement of proteolysis (Friedl and Wolf, 2009).

2.4. Extracellular matrix determinants of 3D cell migration

2.4.1 Natural-derived hydrogels

To study cell migration with increasingly more physiologic settings, groups have turned towards encapsulating cells within 3D hydrogel-based biomaterials. These biomaterials can be largely categorized as natural (produced and/or isolated from cellular sources) or synthetic (synthesized polymers) (Tibbitt and Anseth, 2009). Commonly employed natural-derived biomaterials are collagen, fibrin, and matrigel. Collagen type I, most often purified from rat tail, is employed to model stromal ECM settings that are rich in collagen type I fibrils (Wolf et al., 2009). Fibrin hydrogels are formed from fibrinogen and thrombin purified from either bovine or human blood, and most closely mimics provisional wound healing ECM settings (Ghajar et al., 2008). Matrigel, isolated from Engelbrath-Holm-Swarm mouse sarcoma cells, is commonly used to model basement membrane matrix (Kleinman and Martin, 2005). Using these systems, groups have altered matrix properties to model the changes in ECM properties observed in native tissues to identify ECM determinants of cell migration.

These hydrogel systems can be processed to compare 2D migration (cells seeded on top of a hydrogel) with 3D migration (cells encapsulated within the hydrogel) (Baker and Chen, 2012; Fraley et al., 2010). Hakkinen et al. performed such studies directly comparing commonly used natural-derived biomaterials and identified several critical differences between 2D and 3D cell migration (Hakkinen et al., 2011). Fibroblast embedded in 3D were more polarized with less Rac activity, possessed smaller focal adhesions, and migrated more persistently than 2D settings. To tune matrix properties, a common perturbation is varying the protein concentration of these biomaterials. However, increasing matrix density results in a concurrent increase in matrix stiffness, ligand density, and decrease in porosity **(Figure 2.5)** (Vining and Mooney, 2017).

Overall, as matrix density increases, cell migration is observed to be reduced. Because these perturbations are not orthogonally tunable, it is challenging to pinpoint how specific matrix properties mediate the cell migration response. Thus, many groups have turned towards designing synthetic hydrogels with sets of orthogonally tunable properties to elucidate ECM determinants of 3D cell migration.

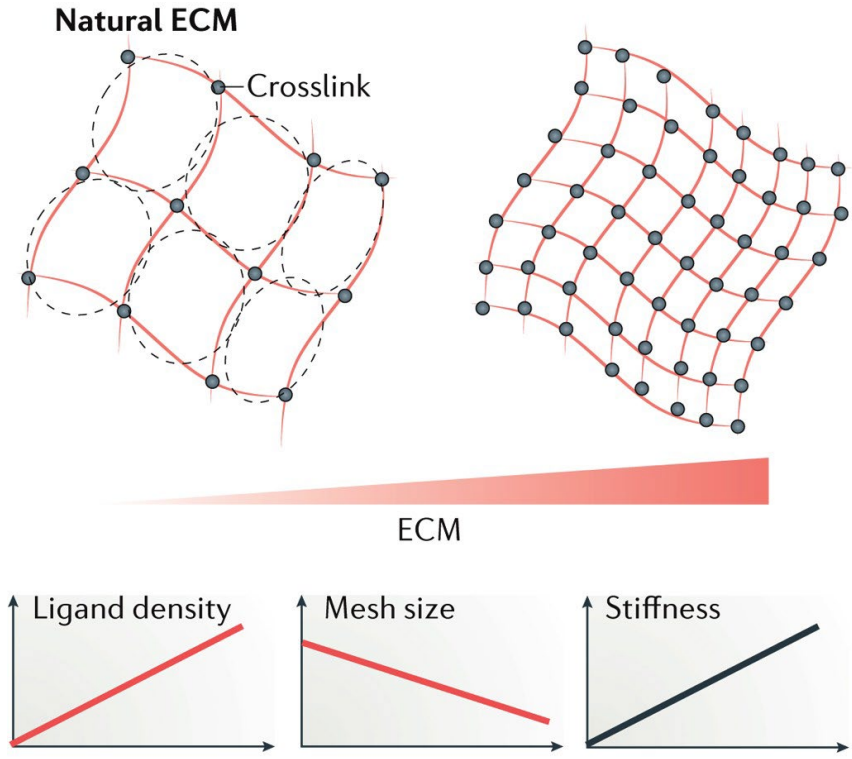

Figure 2.5: Increasing matrix density of natural-derived hydrogels results in a simultaneous decrease in porosity and increase in ligand density and stiffness. Image reproduced from (Vining and Mooney, 2017).

2.4.2 Tunable synthetic hydrogels

As many ECM properties simultaneously change with perturbations to natural-derived hydrogels, crosslinking of synthetic polymers has provided a separate avenue to test for sets of orthogonally tunable properties on 3D cell migration (Li et al., 2017a). Commonly employed synthetic polymers include modified polyethylene glycol, hyaluronic acid, and dextran among

others. In general, these hydrogels utilize a comparatively higher weight percent of material (2-5 wt%) compared to natural-derived hydrogels (0.1-2 wt%), are typically covalently crosslinked with cell degradable crosslinkers and further functionalized with cell adhesive peptides (e.g. RGD). Through this modular design, synthetic hydrogels can provide orthogonal control over crosslink density (stiffness), crosslinker susceptibility (degradability) and ligand density or identity (Beamish et al., 2019; Ehrbar et al., 2011; Gobin and West, 2002; Li et al., 2017b; Sokic and Papavasiliou, 2012; Trappmann et al., 2017). Additionally, recent advances in biomaterial crosslinking strategies have designed mechanisms to control the viscoelasticity of hydrogels by introducing non-covalent crosslinks to afford stress-relaxation properties (Chaudhuri et al., 2020; Loebel, C, Mauck, RL, Burdick, 2019; Wisdom et al., 2018). Using such material schemes, groups have identified how these various properties influence 3D cell migration **(Figure 2.6)** (Yamada and Sixt, 2019).

While synthetic hydrogels are more tunable and afford mechanistic control compared to natural-derived materials, synthetic hydrogels are nanoporous and amorphous in structure (Chiu et al., 2011). Specifically, synthetic hydrogels lack the heterogeneously shaped microporosity and fibrillar architecture of native tissues (Weigelin et al., 2012). Thus, a major focus of this thesis work is to design tunable, synthetic materials imbued with microporosity or fibrous architecture to better understand how ECM determinants of more physiologic ECM environments influence cell migration. Furthermore, the inclusion of fibrillar ECM plays a critical role in how cells sense, polarize, exert forces and mechanically communicate to the matrix and to neighboring cells, and thus mediates the dynamic interactions between cell and matrix during cell migration (Baker et al., 2015; Cao et al., 2017a; Gjorevski et al., 2015; Hall et al., 2016; Harris et al., 1981; Wang et al., 2015).

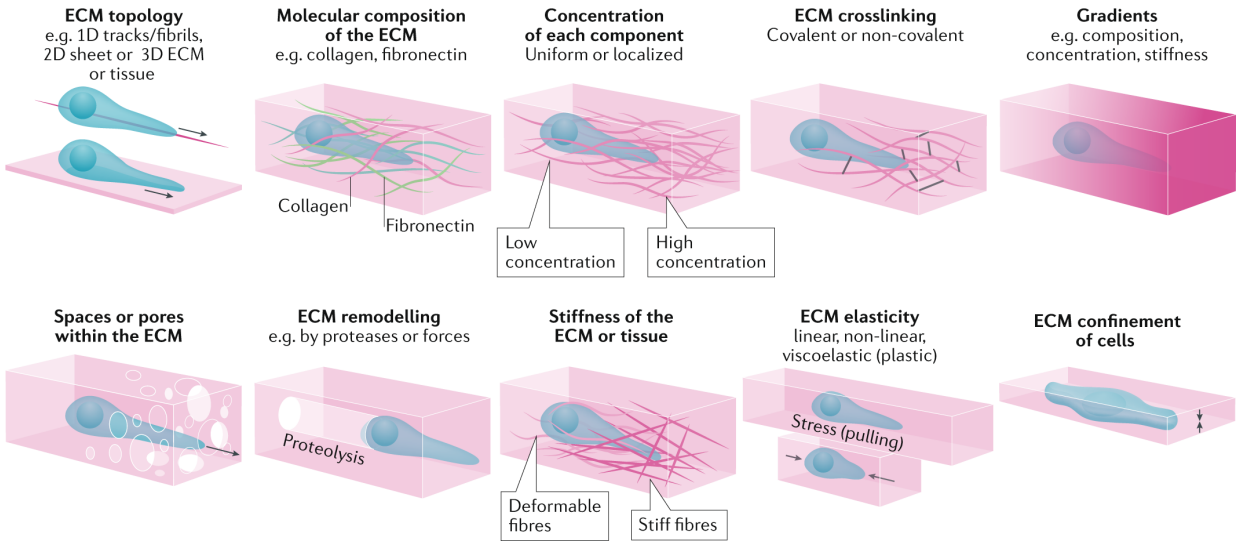

Figure 2.6: Natural and synthetic hydrogels have identified a variety of ECM properties that modulate mechanisms of cell migration. Image reproduced from (Yamada and Sixt, 2019).

2.5 Cell migration mechanoreciprocity

While several ECM properties influence cell migration, migrating cells can in turn remodel or physically reorganize ECM properties (Ford and Rajagopalan, 2018). With sufficient adhesion to the matrix, actomyosin-driven contractile forces can generate strain in the matrix, producing local fiber alignment and matrix condensation (Baker et al., 2015; Hall et al., 2016). If porosity is insufficient to allow the nucleus to bypass (a rate-limiting factor of 3D cell migration), cells can apply proteolytic activity and enzymatically degrade space in the matrix (McGregor et al., 2016; Wolf and Friedl, 2011). In combination, cells can also apply physical forces to push open spaces of proteolytically weakened ECM. Additionally, migrating cells can deposit cell-derived matrix and secrete matrix crosslinking enzymes (e.g. lysl oxidase) thereby altering the matrix composition and stiffness as evident in myofibroblasts during wound healing and fibrosis (Kutys and Yamada, 2014; Levental et al., 2009).

Theorized nearly 4 decades ago, Mina Bissell coined the concept of 'Dynamic Reciprocity', a process that defines the dynamic, and reciprocal interactions between cells and matrix (Bissell et al., 1982). Since that time, the inception and growth of the mechanobiology field has come to identify several key cellular regulators and mechanisms responsible for how cells sense matrix properties (mechanosensing), convert physical stimuli into transcriptional changes (mechanotransduction) and remodel matrix properties (mechanoresponse) **(Figure 2.7)** (Kanchanawong et al., 2010; Vogel and Sheetz, 2006). Indeed the extracellular matrix is physically linked to the cell nucleus from matrix to focal adhesions to cytoskeleton to LINC (linker of nucleoskeleton to cytoskeleton) and nuclear lamin proteins such that deformations from the matrix-adhesion interface can be applied directly onto the nucleus to induce morphologic and transcriptional changes **(Figure 2.7)** (Elosegui-Artola et al., 2017; Kirby and Lammerding, 2018; Swift et al., 2013).

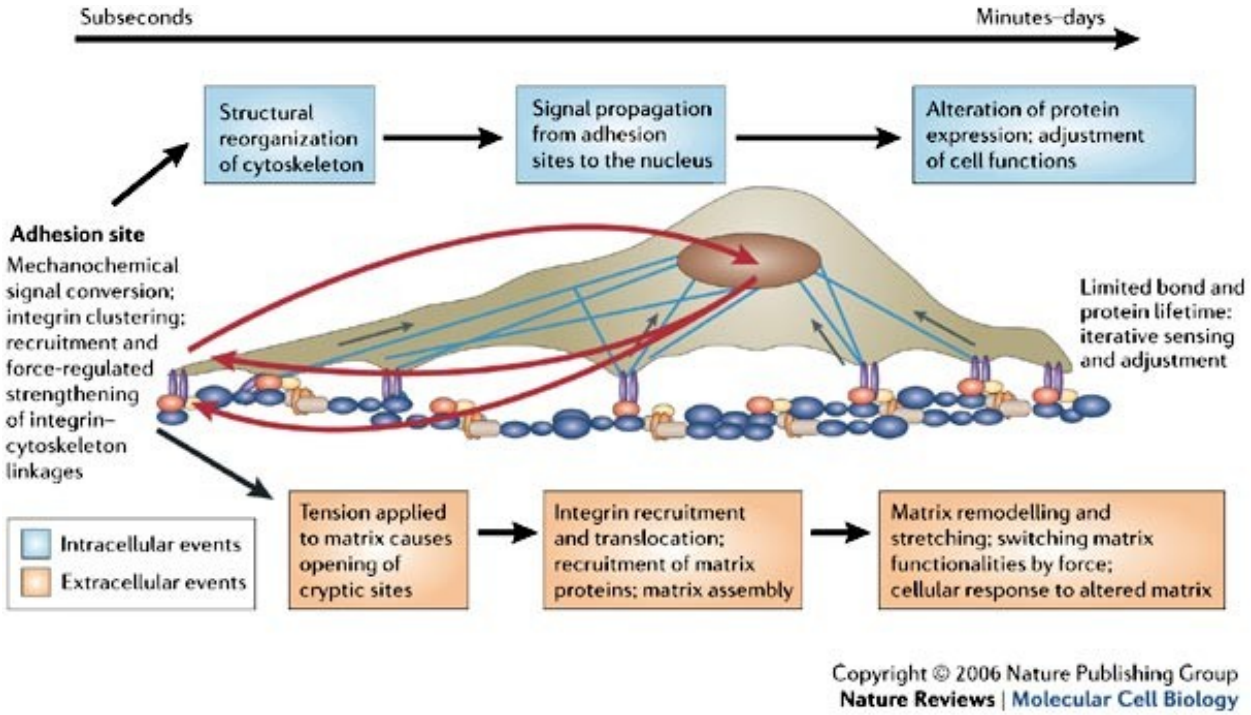

Figure 2.7: Cellular focal adhesions interface between extracellular matrix and intracellular signaling. Cells dynamically sense and respond to physical cues presented by the matrix. Image reproduced from (Vogel and Sheetz, 2006).

More recently, the cell migration field has come to appreciate the concept of dynamic reciprocity between migrating cells and the physical ECM (cell mechanoreciprocity) (Helvert et al., 2018). Over the iterative cell migration cycle, both the cell and tissue states coevolve with mediators that act on each other. In order to study such dynamic phenomena requires engineering well-defined microenvironments to establish initial cell and tissue states. Then with live -cell and -matrix labelling, track and assess the coevolution of the two. Utilizing perturbations of mediators between cells and matrix will afford a mechanistic understanding of how cell-mediated changes to the matrix subsequently influence cell migration. The following thesis chapters focus on designing improved biomimetic microsystems that integrate tunable biomaterials with engineered substrates to elucidate how cell migration mechanoreciprocity influences single mesenchymal cell migration over short timescales (Chapters 3 and 4), collective endothelial cell migration via angiogenesis

over intermediate timescales (Chapters 5-7) and endothelial-mesenchymal transition during tip cell formation in the context of fibrosis occurring over long timescales (Chapter 8). Lastly, Chapter 9 will provide a summary of the main findings from this thesis and future directions of studying cell migration mechanoreciprocity to improve cell migration-based strategies for regenerative and therapeutic applications.

Chapter 3: Extracellular Matrix Alignment Dictates the Organization of Focal Adhesions and Directs Uniaxial Cell Migration

3.1 Authors

William Y. Wang, Alexander T. Pearson, Matthew L. Kutys, Colin K. Choi, Michele A. Wozniak, Brendon M. Baker*, and Christopher S. Chen*

*Co-corresponding author

3.2 Abstract

Physical features of the extracellular matrix (ECM) heavily influence cell migration strategies and efficiency. Migration in and on fibrous ECMs is of significant physiologic importance, but limitations in the ability to experimentally define the diameter, density, and alignment of native ECMs *in vitro* have hampered our understanding of how these properties affect this basic cell function. Here, we designed a high-throughput *in vitro* platform that models fibrous ECM as collections of lines of cell-adhesive fibronectin on a flat surface to eliminate effects of dimensionality and topography. Using a microcontact printing approach to orthogonally vary line alignment, density, and size, we determined each factor's individual influence on NIH3T3 fibroblast migration. High content imaging and statistical analyses revealed that ECM alignment is the most critical parameter in influencing cell morphology, polarization, and migratory behavior.

Specifically, increasing ECM alignment led cells to adopt an elongated uniaxial morphology and migrate with enhanced speed and persistence. Intriguingly, migration speeds were tightly correlated with the organization of focal adhesions, where cells with the most aligned adhesions migrated fastest. Highly organized focal adhesions and associated actin stress fibers appeared to define the number and location of protrusive fronts, suggesting that ECM alignment influences active Rac1 localization. Utilizing a novel microcontact-printing approach that lacks confounding influences of substrate dimensionality, mechanics, or differences in the adhesive area, this work highlights the effect of ECM alignment on orchestrating the cytoskeletal machinery that governs directed uniaxial cell migration.

3.3 Introduction

Directed cell migration plays a fundamental role in numerous physiologic and pathologic processes, where biochemical and physical cues from the extracellular matrix (ECM) guide cells to their target destinations (Moissoglu and Schwartz, 2006; Petrie et al., 2009; Rodriguez and Schneider, 2013). In wound healing, gradients of chemokines recruit macrophages to wound sites to initiate the tissue repair process (Gillitzer and Goebeler, 2001). Similarly, during the progression of most solid cancers, gradients of growth factors produced by the tumor mass direct the invasion of endothelial cells required for angiogenesis and subsequent tumor growth (Carmeliet and Jain, 2000). While soluble cues clearly are important in mediating directed cell migration, physical features of the microenvironment have more recently been implicated in this process. For example, early work demonstrated that contact guidance produced by the orientation and spatial restriction of fibronectin fibrils during amphibian gastrulation direct mesodermal cell migration from the blastopore to the animal pole (Nakatsuji and Johnson, 1984). In the context of breast cancer,

Provenzano *et al.* described how the collagenous stroma undergoes marked reorganization, resulting in radially aligned collagen tracts emanating from the tumor. This organization in turn appears to facilitate cancer cell escape from the primary tumor (Provenzano et al., 2006, 2008). In both of these rather diverse processes, directional cues influencing cell migration arise from the fibrous ECM that cells negotiate during migration.

Given its ubiquity throughout the body, type I collagen gels have been widely used as a physiologically representative ECM model for *in vitro* cell migration studies (Dickinson et al., 1994; Doyle et al., 2015; Hadjipanayi et al., 2009; Kutys and Yamada, 2014; Riching et al., 2015; Xie et al., 2017). These studies further implicate physical attributes of the ECM such as alignment, density, diameter, and stiffness as integral factors in directing cell migration. However, identifying the individual contribution of these factors proves to be quite challenging in natural materials such as collagen gels. For example, increasing the concentration of a collagen gel concurrently increases fibril density, matrix stiffness, and cell-adhesive ligand density while decreasing the pore size. Thus, bioengineered *in vitro* models that simplify the complexity of natural ECM and can decouple confounding factors have helped deepen our understanding of how the physical properties of the ECM regulate cell migration (Charras and Sahai, 2014; Kramer et al., 2013; Pathak and Kumar, 2011; Paul et al., 2016a; Polacheck et al., 2013).

In particular, cell migration on micropatterned lines of adhesive ECM proteins has been suggested to recapitulate migration observed within *in vivo* 3D microenvironments composed of highly aligned fibers (Doyle et al., 2009; Ramirez-San Juan et al., 2017; Sharma et al., 2012). NIH3T3 fibroblasts migrating on single lines of patterned adhesive ECM proteins, termed "1D migration," exhibit a uniaxial cell morphology and undergo directed migration with similar speed as in 3D cell-derived matrices, whereas cells undergoing unconstrained migration on

unpatterned 2D surfaces do not (Doyle et al., 2009). Similarly, 1D micropatterned substrates have also been used to reconstitute macrophage-tumor cell interactions, validating intravital observations in highly metastatic patient-derived orthotopic mammary tumors (Sharma et al., 2012). These and other studies (Guetta-Terrier et al., 2015) implicate the dimensionality of the ECM substratum in dictating the cell migration phenotype and suggest that 1D lines of ECM recapitulate key aspects of cell migration observed in 3D fibrillar tissue settings; however, orthogonal control over the adhesive area proved to be difficult in these studies. Furthermore, in addition to dimensionality, there may be other aspects of the ECM which are important in regulating the migration phenotype. Given that many mesenchymal tissues contain adhesive fibers of ECM proteins such as fibronectin and collagen, we wondered how restricting cell adhesion to linear tracks of ECM influences migration, and furthermore, if the geometry and organization of these patterns, independent of substrate dimensionality and mechanics, could dictate the cell migration mode.

To answer these questions, we designed a microcontact printing-based ECM parameter screening tool where we modeled fibrous ECM as arrays of cell-adhesive micron-scale linear elements. We then varied over graded steps three pertinent features reflecting the distribution of adhesive ligands in fibrillary microenvironments (line alignment, density, and width) and examined changes in the morphology, cytoskeletal architecture, and migratory behavior. Using these 2D micropatterned substrates to exclude the influence of substrate dimensionality and mechanics, we found that the alignment of ECM had a dominant effect on cell morphology and migration over other geometric factors, where high alignment induced a uniaxial phenotype and rapid cell migration in a directed fashion. Underlying directed cell migration is the matrix alignment correlated with highly organized focal adhesions (FAs) and actin stress fibers. Members

of the Rho family of small GTPases have emerged as prominent players in cell motility, working to spatiotemporally modulate the signaling processes involved in cell adhesion and cytoskeletal dynamics (Ridley and Hall, 1992). In particular, Rac1 is necessary for lamellipodium extension preceding the formation of new adhesions to ECM and has been implicated in directed cell migration, where experimentally decreasing Rac1 activity switches cells from random to directionally persistent migration (Pankov et al., 2005). Given the observed influence of matrix alignment on directed cell migration, we further used two distinct molecular approaches to examine Rac1 localization and found that matrix alignment additionally influences the number and location of protrusive edges initiated by active Rac1.

3.4 Results and Discussion

3.4.1 Multiparameter ECM screening arrays for high content imaging

Given the ubiquity of micrometer-scale diameter fibrous proteins throughout mammalian extracellular matrices (ECM), we sought to develop a model that captured key aspects of adhesive ligand patterning in fibrous ECMs without confounding factors stemming from substrate dimensionality and mechanics (Baker and Chen, 2012; Charras and Sahai, 2014; Pathak and Kumar, 2011). To do so, we simplified fibrous ECMs into two-dimensional (2D) patterns of microcontact-printed fibronectin lines where the angular dispersion (alignment), number (density), and size (width) of these cell-adhesive line elements could be orthogonally varied **(Figure 3.1a)**. Building upon previous work (Doyle et al., 2009), this microcontact printing-based approach allowed us to explore how the organization of adhesive ECM proteins influenced cell migration, while sidestepping confounding factors such as steric hindrance (Liu et al., 2015; McGregor et al., 2016; Pathak and Kumar, 2012; Paul et al., 2016b; Stroka et al., 2014), the requirement for

proteolytic activity (Ehrbar et al., 2011; Friedl and Wolf, 2009; Wolf and Friedl, 2011; Zaman et al., 2006), and the influence of substrate mechanics (Baker et al., 2015; Ehrbar et al., 2011; Hadden et al., 2017; Kraning-Rush and Reinhart-King, 2012; Meehan and Nain, 2015; Pelham and Wang, 1997). Using custom MATLAB scripts, a prescribed number of initiation points were randomly selected in 2D space, and lines were extended in a direction selected randomly within prescribed bounds. To achieve submicron features, we employed a stepper with 5× optical reduction resulting in silicon masters with SU8 photoresist line features ranging between 0.5 μm and 2 μm in width. In total, 252 unique ECM patterns were generated within a single 1.2×1.2 cm^2 stamp, enabling high-throughput screening over a wide range of adhesive microenvironment parameters using high content tile-scan imaging **(Figure 3.1c)**.

The desired production of micron-scale features ranging widely in spacing across a single stamp prevented us from using standard "forward" microcontact printing, where the featured stamp is protein inked prior to transfer. Indeed, when conventional "forward" stamping was employed, only patterns with greater than 400 lines/pattern could be successfully generated; at lower line densities, stamp collapse led to protein transfer from non-feature background areas. Thus, we employed an inverse microcontact printing or "stamp off" technique (Desai et al., 2011), whereby a flat PDMS stamp is uniformly inked with adhesive protein and the activated inverse-featured stamp is first applied to remove background areas of protein before transferring the remaining protein pattern to the culture substrate **(Figure 3.1b)**. This method enabled the production of nearly all patterns over a range of line alignments (±5°, 15°, 30°, 45°, 60°, and 90°), densities (50, 100, 200, and 400 lines/pattern), and widths (0.5, 0.7, 1.0, and 2.0 μm) **(Figure 3.1d)**; arrays with 800 line/pattern at line widths of 1 and 2 μm possessed a larger line area than the total pattern area, resulting in a uniform region of fibronectin. Silicon masters were generated with 0.5 and 2.0 μm

thickness photoresist, with 2.0 μm thick features generally leading to more consistent and faithful pattern reproduction. Although linear adhesive patterns below 0.5 μm have been produced previously by other means and may impact focal adhesion growth and dynamics (Sequeira et al., 2012), the 0.5 μm wide lines achieved here match the limit previously reported for microcontact printing proteins using PDMS (Bernard et al., 2000). In summary, we successfully created multi-parametered micropatterned ECM screening arrays to model and study cell migration in fibrous microenvironments.

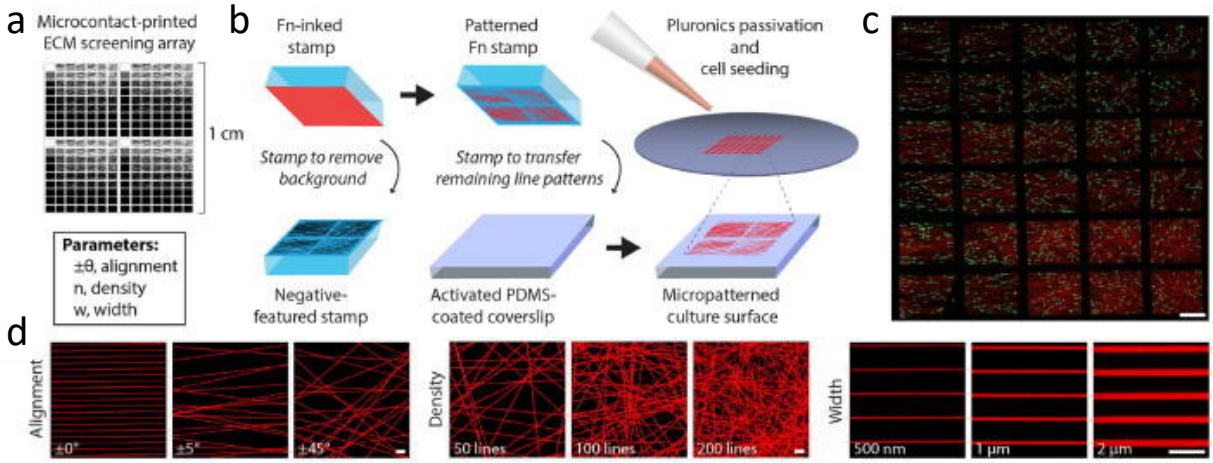

Figure 3.1: Microcontact-printed ECM screening arrays.
a) Photomask containing 252 individual ECM conditions, each containing a unique randomly generated array of line elements with varying alignments (angular dispersion), line densities, and line widths. **b)** Overview of the negative microcontact-printing procedure. Briefly, AlexaFluor555-conjugated fibronectin (Fn555, red) was uniformly coated on flat PDMS stamps and a UV-ozone activated stamp containing the negative of the intended patterns was applied to remove background areas before transferring the remaining areas to the eventual cell culture substrate. **c)** Tile-scan fluorescence image of a subsection of the Fn-printed ECM screening array seeded with phalloidin-AlexaFluor488 stained 3T3s (green) (scale bar: 1 mm). **d)** Fn555 microcontact-printed patterns demonstrating control over line alignment (left), line density (middle), and line width (right) (scale bars: 10 μm).

3.4.2 Array-wide parameter screen reveals that matrix alignment robustly dictates cell morphology and orientation

We next performed an extensive screen across the full array (with the exception of 800 lines/pattern arrays) to examine the effect of varying line alignment, density, and width on cell morphology **(Figure 3.2a, Supplemental Figure 3.1)**. For these and all subsequent studies, we chose NIH3T3s as a model cell type used widely to study how microenvironmental cues influence mesenchymal cell migration (Hakkinen et al., 2011; Tamura et al., 1998). High content tile-scan fluorescence imaging was performed on cells stained for their nucleus and actin cytoskeleton **(Figure 3.2a)**, with subsequent semi-automated image analysis to extract an assortment of morphometric features. Of the features examined, we immediately identified two factors—cell aspect ratio and orientation—which varied markedly across the array **(Figure 3.2b)**. In particular, when analyzing the entire dataset considering each parameter independently, we observed that decreasing line widths, decreasing line densities, and increasing alignment all led to an increase in the cell aspect ratio **(Figure 3.2c-d)**. A high aspect ratio corresponds to a uniaxial cell shape and has been heavily implicated in directed cell migration, where the direction of the cell's long axis (or orientation) defines the direction of migration (Petrie et al., 2009).

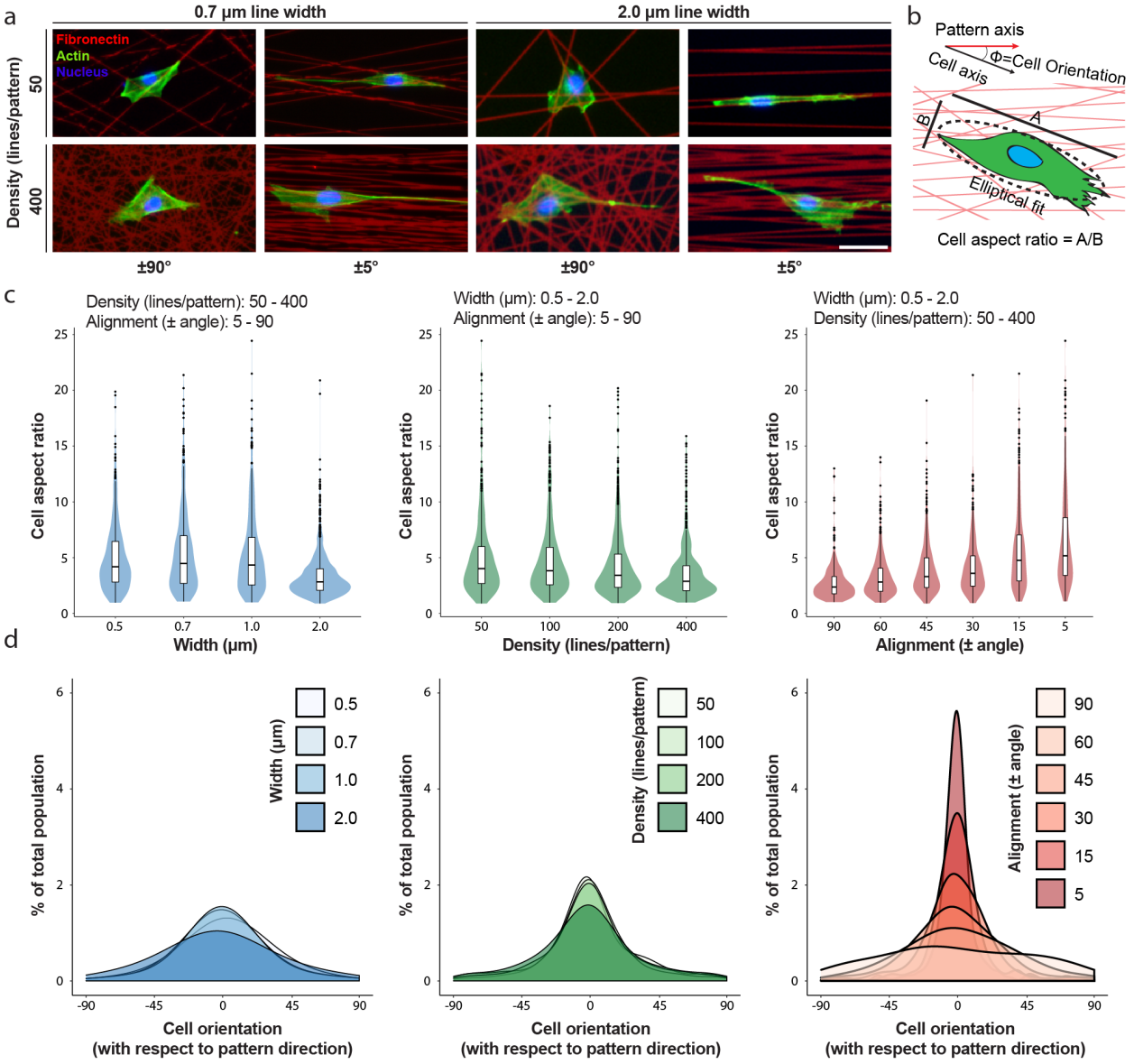

Figure 3.2: Multiparameter screening of ECM attributes reveals that fiber alignment strongly dictates the cell's aspect ratio and orientation.

a) Representative 3T3 fibroblasts seeded on selected Fn-patterns (red) stained for F-actin (green) and nuclei (blue) with phalloidin-AlexaFluor488 and Hoechst33342, respectively (scale bar: 50 μm). **b)** Schematic indicating how the cell aspect ratio and orientation were quantified. **c)** Cell aspect ratio as a function of line width (left), line density (middle), and line angular dispersion (right). Data are presented as violin plots demonstrating distribution with overlaid box plots. **d)** Histograms of cell major axis orientation with respect to the pattern axis as a function of line width (left), line density (middle), and line angular dispersion (right) ($n \geq 400$ cells per condition, total of 2938 cells analyzed).

Further statistical analyses were performed to determine the relative strength of the effect of line alignment, density, and width on the cell aspect ratio and variation in cell orientation. When the degree of linear correlation between cell aspect ratio vs. alignment, density, and width was determined, we found that the aspect ratio had the highest correlation with alignment ($r^2 = 0.156$, $p < 0.0001$). The aspect ratio was also independently correlated with density ($r^2 = 0.029$, $p < 0.0001$) and width ($r^2 = 0.089$, $p < 0.0001$). To understand the relationships among alignment, density, and width in explaining the variations in both the aspect ratio and the orientation, we performed multinomial multivariate linear regression model building using a dual-direction selection algorithm from a full interaction model, optimizing for the Akaike information criterion. The model selection proceeded for two rounds and eliminated two interaction terms from the model, without adding back either term. In our final model, alignment, density, width as well as the width by alignment and alignment by density terms were each significant for the multivariate outcome pair of cell orientation and aspect ratio **(Table 3.1)**. The interaction term between alignment and density, for example, implies that at higher alignments, density more potently increases the aspect ratio. We also determined that the variation within cell orientation was significantly associated with alignment ($p < 0.0001$), but not with density or width. Taken together, the combination of high-throughput screening of matrix conditions and statistical analyses indicates that while line width and the density significantly altered the cell aspect ratio, only the alignment of adhesive ECM tracks strongly influenced cell shape towards a uniaxial phenotype and simultaneously exerted a pronounced effect in orienting cells towards the underlying central axis of pattern alignment. Given the effect of matrix alignment in these and numerous previous studies, our subsequent studies focused on the effect of matrix alignment, maintaining the line width constant at 1 μm.

Variable	Orientation: response coefficient	Aspect ratio: response coefficient	Multinomial approximate F-statistics	Multinomial approximate p-value
Intercept	0.2780	0.1064	4425.2	<0.001
Width	-5.413×10^{-4}	-2.551×10^{-3}	196.4	<0.001
Alignment	0.1374	-8.828×10^{-2}	293.0	<0.001
Density	-2.662×10^{-3}	-6.200×10^{-3}	96.9	<0.001
Width: alignment	-6.455×10^{-5}	2.754×10^{-5}	48.8	<0.001
Alignment: density	-1.604×10^{-4}	5.648×10^{-5}	15.6	<0.001

Table 3.1: Statistical outcomes from multinomial multivariate linear regression analysis.

3.4.3 ECM alignment polarizes cells and induces directed cell migration

The multiple regression parameter screen identified matrix alignment as the strongest factor in dictating cell morphology and orientation. Isolating alignment's individual effect on cell morphology, we held the line density and width constant and examined the cell aspect ratio and orientation **(Supplementary Figure 3.1)**. Confirming our initial findings, increasing matrix alignment resulted in an increased cell aspect ratio, causing cells to adopt an elongated morphology and orient preferentially towards the underlying pattern's direction of alignment **(Figure 3.3a-d)**. This trend was found to be consistent across all line density conditions examined (data not shown). Gross cell morphology alone, however, does not necessarily indicate cell polarity. Indeed, elongated cells on aligned ECM were occasionally observed to extend bidirectionally without

evidence of a dominant leading edge. To better understand the influence of matrix alignment on cell polarization, we performed immunofluorescence staining for pericentrin to identify the microtubule organizing center (MTOC), as previous work suggests that the MTOC's location indicates cell polarity **(Figure 3.3e)** (Doyle et al., 2009; Gomes et al., 2005). We first examined the orientation of the MTOC with respect to the pattern axis **(Figure 3.3f)** and observed that increasing matrix alignment induced a higher percentage of cells to position their MTOC along the pattern axis within ±45° of the pattern axis **(Figure 3.3g)**. Several reports highlight the importance of nuclear positioning during cell migration (Gomes et al., 2005; Gundersen and Worman, 2013; Luxton and Gundersen, 2011; Luxton et al., 2010; McGregor et al., 2016), and so, we next examined the position of the MTOC relative to the nucleus and leading edge of the cell **(Figure 3.3f)**. Interestingly, we found that with increasing alignment, the MTOC preferentially positioned to the rear of the nucleus with respect to the leading edge in polarized and elongated cells **(Figure 3.3h-i)**. The position of the MTOC and its role in directed cell migration have been widely debated. The MTOC positions to the front of the nucleus with respect to the leading edge in classical studies performed with scratch wound assays—typically involving a flat 2D substrate with uniform ECM coating (Etienne-Manneville and Hall, 2001; Gomes et al., 2005; Kupfer et al., 1982; Palazzo et al., 2001). In contrast, the MTOC has been observed to favor the rear of the cell in certain cell types, in soft matrices, and in substrates that constrain the cell to 1D micropatterned lines or 3D cell-derived matrices with high matrix alignment (Doyle et al., 2009; Pouthas et al., 2008; Raab et al., 2016; Schütze et al., 1991). Our studies support two possible forms of MTOC positioning and cell polarity as a function of matrix alignment: (1) an aligned uniaxial phenotype previously observed on parallel lines and microgrooves/micropatterned lines occurring on anisotropic ECMs where the MTOC is positioned to the rear of the nucleus and direction of

migration and (2) a polarized, but non-uniaxial phenotype that occurs on isotropic ECM (e.g., on non-patterned ECM or on scratch-wound assays) where the MTOC is positioned ahead of the nucleus (Gomes et al., 2005). Although an understanding of how ECM properties influence cell polarity remains incomplete, our study clearly demonstrates that the anisotropy of adhesive ECM patterning influences cell shape, intracellular organization, and polarity.

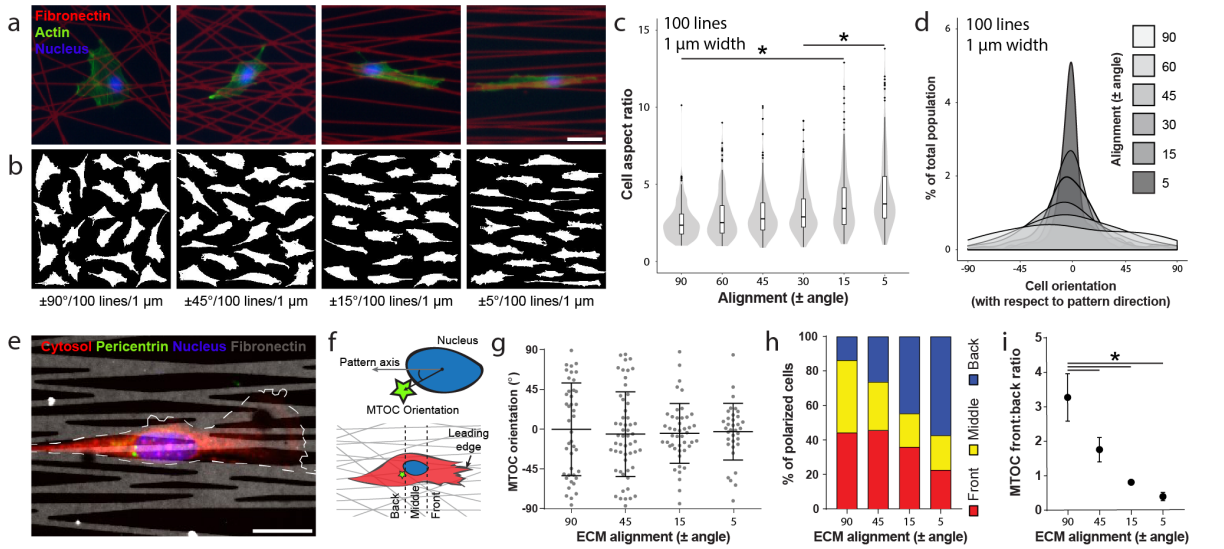

Figure 3.3: Increasing ECM alignment promotes an elongated uniaxial cell morphology and polarizes the cell.

a) Representative 3T3 fibroblasts seeded on Fn-patterns (red) of varying alignment with fixed line density and width (100 lines per pattern, 1 μm width), stained for F-actin (green) and nuclei (blue) with phalloidin-AlexaFluor488 and Hoechst33342, respectively (scale bar: 50 μm). **b)** Cell outlines of 20 representative cells. **c-d)** Aspect ratio (c) and cell orientation (d) (angle between the long axis of the cell and the fiber alignment direction) of 3T3 fibroblasts as a function of ECM alignment, keeping line density constant at 100 lines per pattern and line width at 1 μm width ($n \geq 50$ cells per condition, total of 515 cells analyzed). **e)** Representative confocal image of a 3T3 fibroblast immunostained for pericentrin to localize the microtubule organizing center (MTOC) (red: cytosol, green: pericentrin, blue: nucleus, and grey: Fn555; scale bar: 25 μm). **f)** Schematic indicating how MTOC orientation (angle between MTOC and the pattern axis using the centroid of the cell nucleus as a reference point) and position (front, middle, or back relative to the nucleus and leading edge of the cell) were determined. **g)** MTOC orientation as a function of ECM alignment ($n \geq 35$ cells per condition, total of 177 cells analyzed). **h)** Percentage of all polarized cells with MTOC located in front, in the middle, or rearwards of the nucleus ($n \geq 60$ cells per condition, total of 468 cells analyzed). **i)** Ratio between cells with MTOC located in front of the nucleus to cells with MTOC located rearwards of the nucleus (* indicates a significant difference with $p < 0.05$).

Previous work has linked an elongated, uniaxial cell shape with increased migration efficiency (Doyle et al., 2009), and so, we next examined the functional consequence of ECM organization on migration speed and persistence using our two extremes of alignment: aligned (±5°) and non-aligned (±90°) patterns **(Supplemental Figure 3.1)**. We performed live time-lapse imaging over 6 h, utilizing Hoechst-labelled nuclei to track cell movement with an automated image analysis algorithm. Representative temporal overlays of the cell shape on non-aligned patterns reveal a dynamic cell shape, while cells on aligned patterns maintained an elongated morphology throughout their migration track **(Figure 3.4a)**. Aligned patterns also produced more directionally persistent migration and faster speeds compared to cells migrating on non-aligned patterns, and furthermore, this effect remained consistently true over the full range of line densities examined **(Figure 3.4b-d)**. Tracking HT1080 fibrosarcoma cell migration, we similarly found that aligned patterns produced faster speeds and more directionally persistent migration compared to non-aligned patterns across the full range of line densities examined **(Supplemental Figure 3.2)**. These results parallel reports of increased cell migration efficiency on aligned collagen gels (Ray et al., 2017b; Riching et al., 2015) and topographically patterned substrates (Liu et al., 2009; Ramirez-San Juan et al., 2017; Ray et al., 2017a), supporting the conclusion that a high degree of ECM anisotropy critically defines a uniaxial phenotype and directed cell migration. While many studies examining migration on aligned ECM report enhanced persistence and directionality, net migration speed has not consistently been observed to increase with directed migration. Our finding of increased speeds may stem from the comparison of non-aligned vs. aligned substrates with comparable underlying adhesive areas or the fact that proteolytic activity is dispensable for migration in this setting.

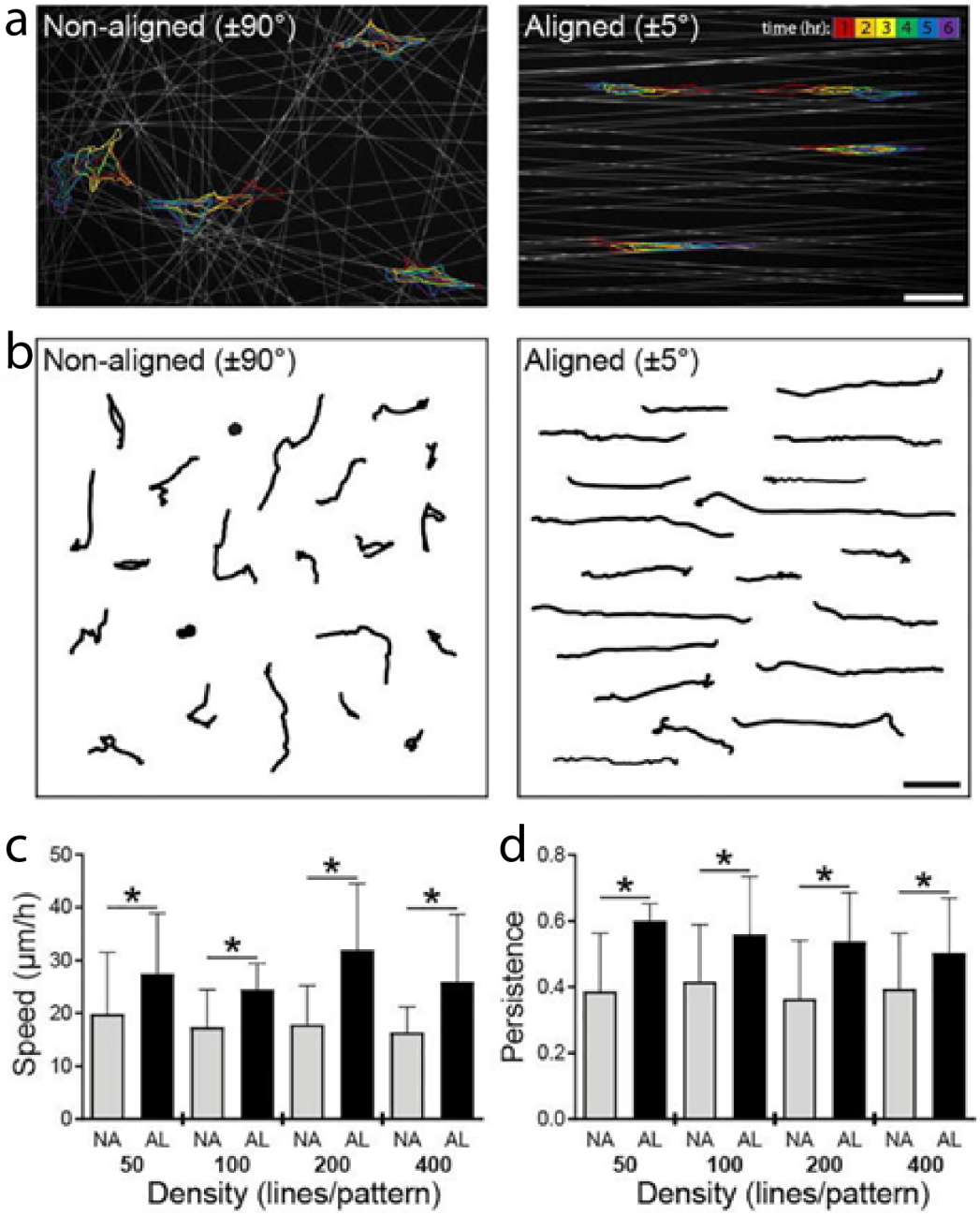

Figure 3.4: ECM alignment influences migration speed independent of ECM density.
a) Overlaid outlines of representative cells at the end of each hour (as denoted by color bar) over 6 h time-lapse imaging on non-aligned (NA, ±90°) and aligned (AL, ±5°) Fn-patterns (grey) containing 100 lines with a width of 1 μm. **b)** 20 representative cell migration tracks measured over 6 h duration of time-lapse imaging on NA and AL patterns containing 100 lines with a width of 1 μm. **c-d)** Average migration speeds (c) and persistence (d) on NA and AL patterns containing 50, 100, 200, or 400 lines ($n \geq 10$ cells per condition, ≥160 cells analyzed total, * indicates a significant difference with $p < 0.05$ vs. NA group at the same line density). Scale bars: 100 μm.

3.4.4 ECM alignment polarizes focal adhesions and localizes Rac activity to stabilize active protrusions

During mesenchymal migration, cells form adhesions to the underlying ECM to exert the necessary traction forces required to advance the cell body forward (Geiger et al., 2001, 2009; Lauffenburger and Horwitz, 1996; Petrie and Yamada, 2012; Schmidt and Friedl, 2010; Webb et al., 2002). Looking for differences in morphometric features of focal adhesions (FAs) that could explain the observed differences in migration speed as a function of ECM alignment, we performed immunofluorescence staining against vinculin (a well-accepted marker of force bearing FAs) (Bershadsky et al., 2003; Grashoff et al., 2010; Hinz and Gabbiani, 2003), high resolution confocal imaging, and image analysis to quantify characteristics of FAs on aligned (±5°) and non-aligned (±90°) patterns over a range of ECM densities **(Figure 3.5a and Supplemental Figure 3.1)**. Examining the average adhesion size and the number of adhesions per cell, we found no consistent differences as a function of alignment **(Figure 3.5b-c)**. However, when we examined the angular dispersion of adhesions with respect to the major axis of the cell, a significant discrepancy in adhesion organization existed between aligned and non-aligned ECM at each level of density examined **(Figure 3.5d)**. Non-aligned ECM resulted in a population of adhesions with high angular dispersion with respect to each other; in contrast, aligned ECM promoted the organization of FAs along the cell's long axis **(Figure 3.5a)**. This difference in adhesion angular deviation mirrored differences in migration speed across multiple ECM densities and proved to be significantly linearly correlated with an R^2 value of 0.916 **(Figure 3.5g)**. Correlations between the other adhesion metrics quantified and migration speed proved to be non-significant **(Figure 3.5e-f)**. These findings were additionally confirmed with HT1080 fibrosarcoma cells **(Supplementary Figure 3.3)**. The observation that the global orientation of adhesions uniquely predicts migration

speed is in contrast to recent reports highlighting FA size as a critical predictor. However, in contrast to the work at hand, these studies were performed on flat unpatterned substrates of varying stiffness, highlighting again a clear distinction between aligned uniaxial cell migration and unconstrained 2D migration (Kim and Wirtz, 2013).

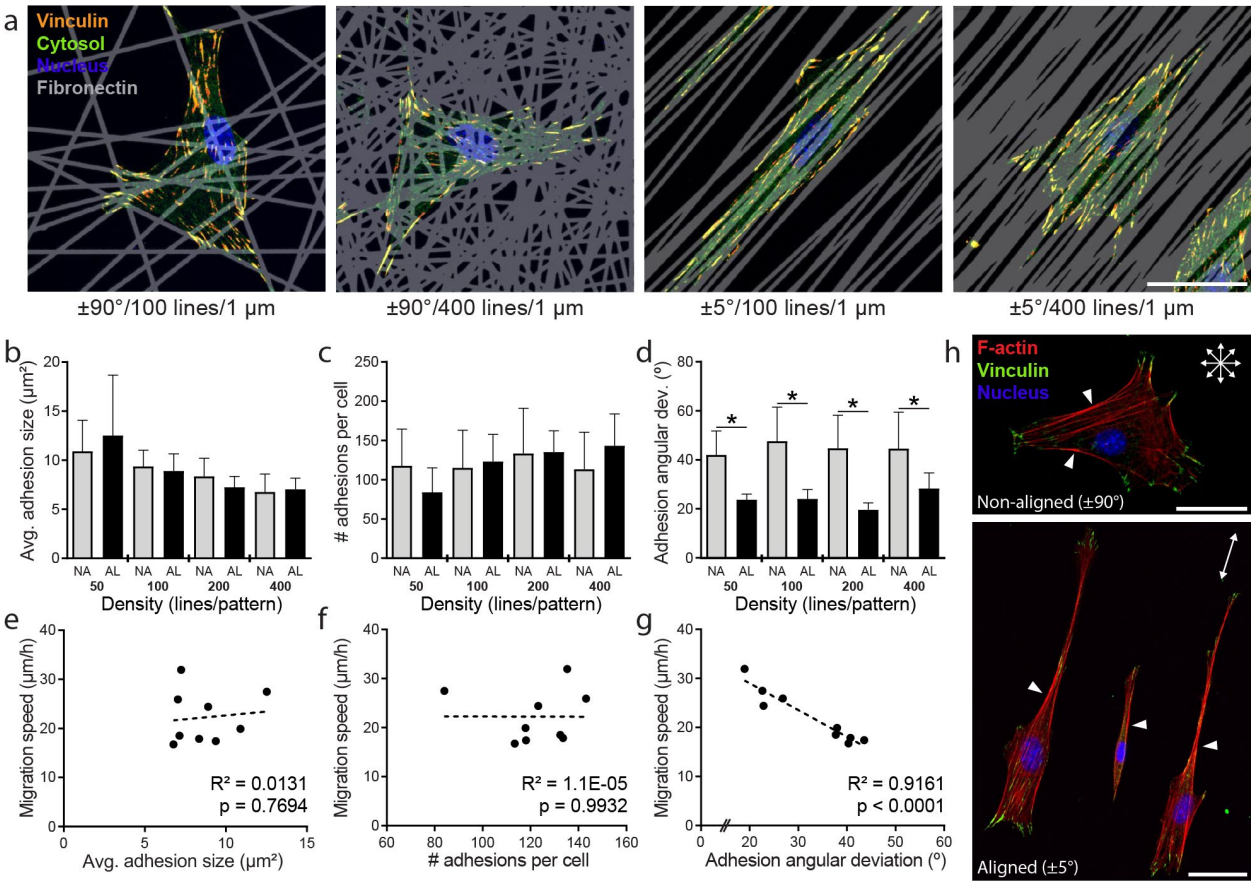

Figure 3.5: Focal adhesion organization parallels the alignment of ECM patterns.
a) Representative confocal images of 3T3 fibroblasts on non-aligned (±90°) and aligned (±5°) patterns with 100 or 400 line elements stained for vinculin to localize focal adhesions (yellow: anti-vinculin, green: cytosol, blue: nucleus, and grey: Fn555; scale bar: 50 μm). **b-d)** Average individual focal adhesion size (b), total number of adhesions per cell (c), and angular deviation of adhesion orientation within a given cell (d) for cells on non-aligned (NA, ±90°) and aligned (AL, ±5°) patterns containing 50, 100, 200, or 400 lines ($n \geq 9$ cells analyzed per condition, total of 101 cells analyzed, * indicates a significant difference with $p < 0.05$ comparing AL vs. NA group at the same line density). **e-g)** Correlations of average migration speed vs. average adhesion size (e), total number of adhesions per cell (f), and the angular deviation of FA orientation (g). Each data point represents the population average taken from a different pattern. Dashed lines indicate the linear regression lines, with R^2 and p-values indicated within each plot. **h)** Representative confocal

images of fibroblasts on NA and AL patterns with 200 line elements stained for vinculin and F-actin (green: anti-vinculin, red: F-actin, and blue: nucleus; scale bars: 50 μm).

F-actin organization reflected the organization of FAs, where cells on non-aligned ECM with randomly oriented adhesions also had disorganized F-actin stress fibers **(Figure 3.5h, top)**. In contrast, uniaxial cells on aligned ECM possessed highly aligned stress fibers running predominantly in the direction of the long axis of the elongated cell body, mirroring the co-alignment of FAs **(Figure 3.5h, bottom)**. Alignment of FAs and F-actin bundles supports observations that FA sites facilitate actin stress fiber assembly (Endlich et al., 2007; Hotulainen and Lappalainen, 2006) and intracellular force transmission to the ECM occurs via actin engagement with FA proteins (Burridge and Guilluy, 2016; Geiger et al., 2009; Livne and Geiger, 2016). For cells on aligned ECMs, we observed intense F-actin staining at the cell walls running along the direction of matrix alignment and the putative direction of migration **(Figure 3.5h, arrows)**. Cells on non-aligned ECM also possessed intense F-actin bundles along straight edges of the cell's periphery. Regardless of cell shape and orientation, FAs and active lamellipodial protrusions were seldom observed at such locations possessing robust stress fibers, echoing previous observations employing cell-sized geometric micropatterns (Brock et al., 2003; Parker et al., 2002). Given that the formation of F-actin stress fibers has been associated with augmented RhoA activity (Amano, 1997; Nobes and Hall, 1995; Ridley and Hall, 1992; Wozniak et al., 2004), previous studies suggest a mutual exclusion between RhoA and Rac1 localization (Arthur and Burridge, 2001; Machacek et al., 2009; Nimnual et al., 2003; Ohta et al., 2006; Rottner et al., 1999; Sander et al., 1999), and Rac1 activity is heavily implicated in protrusion activity (Petrie et al., 2009; Ridley, 2015; Ridley and Hall, 1992; Waterman-Storer et al., 1995), we hypothesized that highly elongated cells on aligned ECM would preferentially form protrusions at the distal ends

of the cell in the direction of ECM alignment. Furthermore, we predicted that the stability of these protrusions would be enhanced compared to cells on disorganized (non-aligned) ECM.

By identifying ruffling edges in high resolution spatiotemporal time-lapse image series, we were able to determine the location and number of active protrusions on aligned (±5°) and non-aligned (±90°) patterns with 100 lines/pattern **(Figure 3.6a and Supplemental Figure 3.1)**. Indeed, ECM alignment resulted in a lower number of active protrusions per cell (1.56 ± 0.73 vs. 3.13 ± 0.81 on aligned vs. non-aligned, $p < 0.0001$), with the direction of 92% of all protrusions falling within ±45° of the direction of ECM alignment **(Figure 3.6b)**. Furthermore, kymographs acquired at the location of ruffling protrusions highlighted a distinction in the stability of protrusions as a function of ECM organization **(Figure 3.6c-d)**. On non-aligned ECM, different protrusions within the same cell were often observed to extend **(Figure 3.6d, i)**, pause for a period of time **(Figure 3.6d, ii)**, or retract **(Figure 3.6d, iii)** concurrently. In contrast, aligned ECM promoted a steady extension of the cell's leading edge in the direction of ECM alignment **(Figure 3.6d, iv)**. These observations along with the increase in migration speed on aligned ECM **(Figure 3.4c)** support the notion that the maintenance of a single location of protrusive activity underlies efficient migration (Doyle et al., 2009; Pankov et al., 2005) and clearly demonstrate that ECM organization dictates protrusive activity.

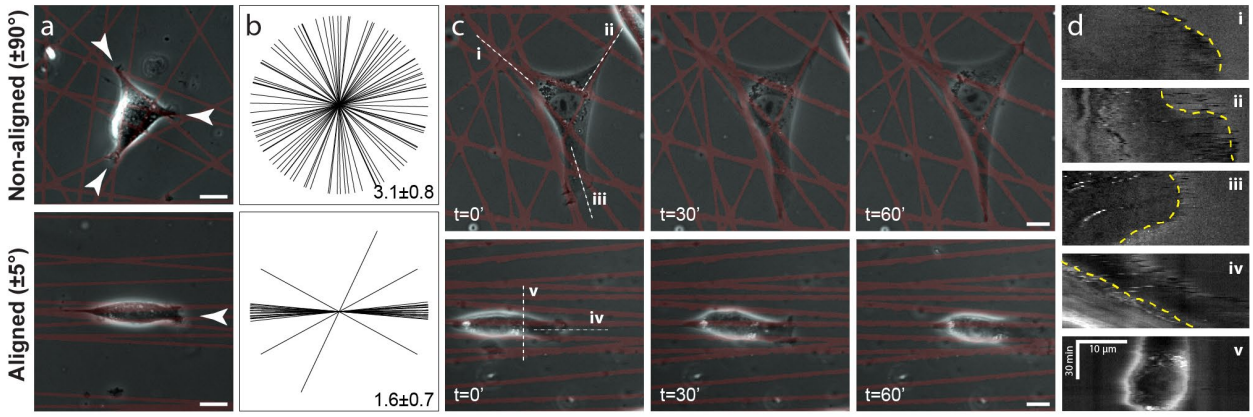

Figure 3.6: ECM alignment dictates the number and stability of active protrusions.
a) Representative phase images of 3T3s on aligned and non-aligned patterns containing 100 line elements. White arrows show locations of active protrusions (identified by ruffling activity via time-lapse imaging). **b)** Starburst plots indicating the angle of active protrusions (n = 16 cells for each condition) and average number of protrusions per cell (mean ± standard deviation). **c)** Phase images from time-lapse series at 0, 30, and 60 min. **d)** Kymographs produced from locations indicated with white dashed lines in left-most images of C over 60 minute intervals. Leading or retracting edge indicated with yellow dashed lines (scale bars: 10 μm).

Given these striking distinctions in the location of active protrusions and Rac1's known role in driving lamellipodial protrusion (Etienne-Manneville and Hall, 2002; Pankov et al., 2005), we next examined whether ECM alignment also altered the localization of active Rac1 signaling. Glutathione-S-Transferase (GST)-tagged protein binding domain (PBD) and immunofluorescence staining were used to identify intracellular locations of enriched active Rac1 on aligned (±5°) and non-aligned (±90°) patterns with 100 lines/pattern **(Figure 3.7a and Supplemental Figure 3.1)**. Cross-correlating fluorescence intensities from Rac1 and F-actin images allowed us to identify locations of high co-localization of these two proteins, both critical to protrusion activity **(Figure 3.7b)**. Qualitatively, we observed that cells on non-aligned ECM possessed multiple protrusions with co-localization of these two signals. Conversely, cells on aligned ECM possess fewer protrusions with hot spots, and these protrusions were additionally in the direction of ECM alignment and putative migration. These observations suggest that ECM

alignment influences the number and location of active protrusions, contributing to the stable and directional protrusions underlying uniaxial directional migration. To further support these observations, we employed a Förster resonance energy transfer (FRET)-based approach to image Rac1 activity modified from a previously reported construct. Within this single chain bioactivity reporter, FRET between molecules occurs upon binding of PBD to Rac1. Live imaging using this reporter revealed similar localization of Rac1 activity as a function of ECM alignment, with preferential Rac1 activation in directions corresponding to the underlying pattern alignment **(Figure 3.7c-d)**.

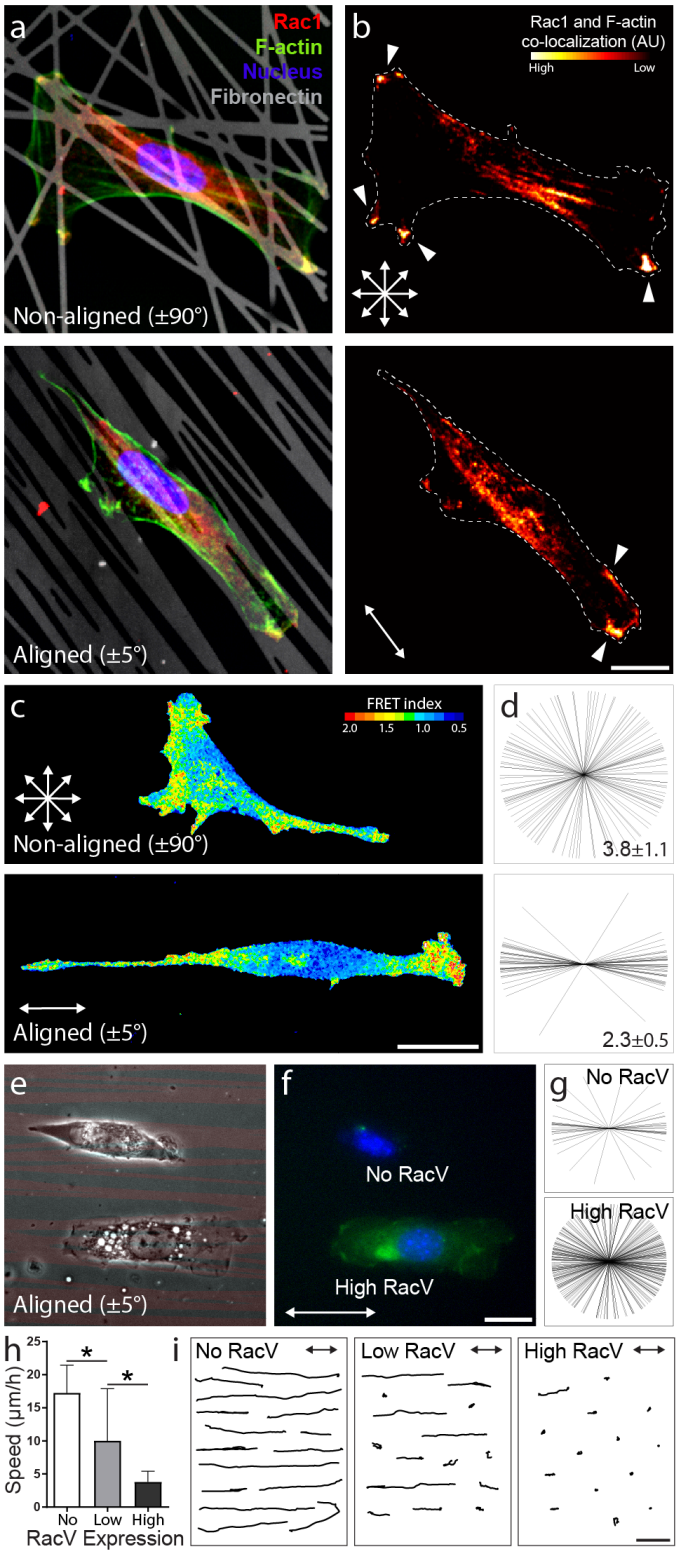

Figure 3.7: ECM alignment dictates the localization of Rac1-enriched extensions.
a-b) Representative confocal images (a) and corresponding heatmaps (b) of 3T3s stained for active Rac on NA (top) and AL (bottom) patterns containing 100 lines with a width of 1 μm [red: active Rac (PBD-GST, anti-GST antibody), green: F-actin, blue: nucleus, and grey: Fn555; scale bar:

25 μm]. Heat maps indicate co-localization of Rac activity and F-actin. White arrows indicate the direction of pattern alignment (scale bar: 25 μm). **c)** Maximum projections of confocal stacks of live-3T3 migration expressing a Rac1-PBD FRET biosensor. Pseudocolored intensity scales indicating that FRET activity was maintained for each condition; scale bars, 25 μm. **d)** Starburst plots indicating the angle of Rac1-enriched protrusions on NA (top) and AL (bottom) patterns ($n \geq 15$ cells for each condition) and the average number of active Rac1 protrusions per cell (mean ± standard deviation). **e-f)** Corresponding phase (e) and fluorescence (f) micrograph of representative transfected 3T3s that highly expressed ("High RacV," green, bottom) and failed to express ("No RacV," no fluorescence, top) the RacV12-GFP construct (red: Fn555, green: GFP, scale bar: 25 μm). **g)** Starburst plots indicating the angle of active protrusions for non- and high expressers of the RacV construct ($n \geq 16$ for each condition). **h)** Migration speed as a function of RacV expression levels; cells were grouped into three expression levels: no, low, and high ($n \geq 15$ for each condition, * indicates a significant difference with $p < 0.05$). **i)** 15 representative cell migration tracks of 3T3s with no, low, and high RacV expression measured over 6 h duration on aligned patterns containing 100 lines (scale bar: 100 μm).

We next transiently transfected 3T3s with a green fluorescent protein (GFP)-tagged constitutively active mutant copy of Rac1 (RacV12-GFP, abbreviated RacV) and plated cells onto aligned ECM (±5°, 200 lines/pattern, 1 μm width). As expression of the plasmid was heterogeneous, we segregated transfected cells into three distinct populations based on GFP intensity: no, low, and high expression **(Figure 3.7e-f)**. High RacV expression resulted in an increased frequency of active protrusions off-axis to the direction of ECM alignment relative to non-expressing cells (25% vs. 8%) **(Figure 3.7g)**. Strikingly, the loss of protrusion directionality with increasing RacV expression paralleled decreases in migration speed where the highest expression of RacV resulted in active protrusions along the entire cell periphery and virtually no cell movement **(Figure 3.7h-i)**. These findings build on previous work by Pankov *et al.* showing how graded levels of Rac1 activity switch cells between directed and random migration on unpatterned 2D substrates (Pankov et al., 2005). In addition to total levels, it is now clear that localization of active Rho GTPase are critical to cell polarity and subsequent movement (Machacek et al., 2009; Petrie et al., 2012). Our findings suggest that ECM alignment and therefore

anisotropy of the local adhesive microenvironment can modulate cell shape and cytoskeletal architecture to spatially define the location of such signals.

3.5 Summary and Outlook

Many engineered models such as 1D patterned lines, nanopatterned ridges and grooves, and electrospun fibers have been utilized to understand how contact guidance cues provided by fibrous ECM influence cell migration (Doyle et al., 2009; Guetta-Terrier et al., 2015; Natale et al., 2014; Ray et al., 2017a). Previous studies primarily compared aligned, adhesion-restrictive substrates versus uniformly coated ECM substrates, resulting in differences in ECM anisotropy as well as total adhesive area. In contrast, this work provides a microcontact printing-based platform modeling the ECM as collections of fibronectin lines with graded variations of alignment, density, and width to identify how combinations of these parameters influenced cell migration. With high content imaging and statistical analyses, we identified matrix alignment as a critical parameter in influencing cell morphology, polarization, and migratory behavior. Interestingly, we find that cells on highly aligned ECM possess organized FAs. This alignment of FAs correlates strongly with directional, high speed migration in stark contrast to other morphometric features of FAs. Highly aligned FAs and associated F-actin stress fibers result in the formation and stabilization of cell protrusions in the direction of ECM alignment, and our data suggest that this control occurs through the localization of active Rac1. This work clearly indicated that anisotropy of the adhesive ECM, independent of substrate dimensionality, dictates the cytoskeletal architecture required for directed cell migration. Furthermore, these micropatterns could provide a high-throughput screen of ECM parameters on other cell functions and may aid in identifying novel therapeutics that selectively inhibit directionally invasive tumor cells.

3.6 Materials and Methods

3.6.1 Cell culture and biological reagents

NIH3T3 fibroblasts were cultured in high glucose Dulbecco's Modified Eagle Medium containing 1% penicillin/streptomycin, L-glutamine (ThermoFisher Scientific, Waltham, MA), and 10% bovine serum (Atlanta Biologicals, Flowery Branch, GA). Cells were passaged upon achieving confluency at a ratio of 1:4 and used for studies until passage 20. For all studies, cells were trypsinized, counted, and seeded onto substrates at a density of 2000 cells/cm^2. For overexpression studies, EGFP-RacV12, a constitutively active mutant (valine substitution at amino acid residue 12) of Rac1 fused to enhanced green fluorescent protein (gift from M. Philips, NY University Medical Center, New York, NY), was transiently transfected using Lipofectamine 2000 (Life Technologies) a day before seeding onto microcontact-printed substrates.

3.6.2 Photolithography and microcontact printing

To produce microcontact-printed ECM screening substrates that model the spatial patterning of adhesive ligands in the fibrous extracellular matrix, a Matlab (Mathworks, Cambridge, MA) script was written to generate patterns consisting of lines of with varying line widths (2.5, 3.5, 5, and 10 μm), densities (50, 100, 200, 400, and 800 lines per field), and angular dispersions [±5° (most aligned), ±15°, ±30°, ±45°, ±60°, and ±90° (non-aligned or random)]. These angles reflect bounds between which each line angle was selected from a uniform distribution. Individual fields were exported in vector format, assembled *en mass* in Autocad (Autodesk, Mill Valley, CA) into arrays, and printed in chrome on a quartz reticle (Advance Reproductions, North Andover, MA). Using a Nikon G4 stepper enabling 5× optical reduction in line widths (0.5, 0.7, 1.0, and 2.0 μm) (Penn Regional Nanotechnology Facility, Philadelphia, PA),

patterns were transferred to a 5 in. silicon wafer spuncoat with 500 nm thickness Microposit S1813 photoresist (MicroChem, Westborough, MA). Following development, polydimethylsiloxane (PDMS) (Sylgard 184, Dow Corning, Midland, MI) was cast onto wafers and cured at 60 °C to generate micropatterned stamps.

To enable pattern visualization, fibronectin from human plasma (Fn, Corning, Corning, NY) was fluorescently tagged with AlexaFluor555 succidinyl ester following the manufacturer's protocol (Invitrogen, Carlsbad, CA). Briefly, a 1 mg/ml solution of fibronectin in 1 M sodium bicarbonate reacted with AlexaFluor555 succidinyl ester at a 9-fold molar excess for 2 h at RT with continual agitation. Unconjugated fluorophores were removed by overnight dialysis (6.5 kDa cutoff), and the concentration of conjugated fibronectin (Fn555) was determined by absorbance at 280 and 555 nm using a spectrophotometer. For microcontact printing, Fn555 was diluted to 50 μg/ml in phosphate buffered saline (PBS) and adsorbed uniformly onto a 1.5 cm by 1.5 cm piece of flat PDMS cast from a cleaned silicon wafer. Patterned stamps containing the negative of the intended final features were activated via UV ozone and applied to the Fn-inked stamp to selectively remove background (non-feature) areas of Fn. The remaining patterned Fn was transferred to the final cell culture substrate by applying the inking stamp a UV ozone activated, PDMS coated coverslip (via spin coater, 5000 RPM). Following storage overnight to allow for recovery of hydrophobicity, substrates were incubated in Pluronics F-127 (0.2% w/v in deionized water, Sigma-Aldrich, St. Louis, MO) for 30 min at 25 °C to prevent non-intended protein adsorption and undesired cell adhesion to non-printed regions.

3.6.3 Immunofluorescence

To examine cell morphology and the organization of the actin cytoskeleton, cells were fixed in 4% phosphate-buffered paraformaldehyde for 10 min and then permeabilized with 0.03% Triton X-100 for 10 min. Filamentous actin was stained with phalloidin-AlexaFluor488 (Life Technologies), and cell nuclei were stained with Hoechst33342, (1 μg/ml, Sigma-Aldrich) blocked in 2% bovine serum albumin. For immunofluorescence staining, fixation and permeabilization were performed as above (unless specified otherwise) followed by incubation in blocking solution (10% fetal bovine serum in PBS) for 1 h, primary antibody (below) dilution in blocking solution for 1 h, three PBS washes for 5 min each, a 1:1000 dilution of AlexaFluor conjugated IgG antibody (Life Technologies) in blocking solution for 1 h, and two PBS washes for 5 min each. To stain the microtubule organizing center (MTOC), a 1:500 dilution of rabbit anti-pericentrin was employed as the primary antibody (PRB-432C, Covance). To stain focal adhesions, samples were permeabilized and fixed simultaneously and a 1:500 dilution of monoclonal mouse anti-vinculin antibody was employed as the primary antibody (V9264, Sigma-Aldrich). To stain for Rac activity, samples were incubated with glutathione-eluted protein binding domain (PBD)-GST overnight at 4 °C (Cytoskeleton), rinsed with PBS, and incubated with goat anti-GST antibody (27-4577-01, GE Healthcare). Imaging was performed on a Nikon Eclipse Ti (10×) or on a Zeiss 710 laser scanning microscope (40×), and images are presented as maximum intensity projections.

3.6.4 Rac1 FRET imaging

To examine Rac1 activity, we modified a previously designed RaichuEV-Rac1 FRET biosensor (Komatsu et al., 2011) by replacing the mTurquoise/YPet fluorophore pair with Clover/mRuby2 (RaichuEV-Rac1-CR) to reduce fluorophore bleed-through, improve the FRET

dynamic range, and enable incorporation into lentiviral vectors. NIH3T3s were transiently transfected with the RaichuEV-Rac1-CR biosensor using Lipofectamine LTX with Plus Reagent (ThermoFisher Scientific) 24 h before seeding onto microcontact-printed substrates. Cells expressing RaichuEV-Rac1-CR were imaged 12 h after seeding. The binding of active Rac1 was detected by imaging the FRET-dependent, intramolecular emission fluorophore (mRuby2) from RaichuEV-Rac1-CR as previously described (Kutys and Yamada, 2014). Briefly, optimal FRET acquisition settings were determined for the Zeiss LSM 800 confocal microscope and strictly maintained during all subsequent FRET imaging; intensity levels of biosensor expression were similarly carefully controlled and maintained between selected cells. Images of mClover and mRuby2 were obtained for each z-plane under 488 nm and 567 nm illumination. Summed projections of confocal z-stacks were generated using ImageJ software. Images were first background subtracted, and a binary mask was applied by thresholding to the Acceptor (mRuby2) channel to isolate the cellular signal. Pixel-by-pixel FRET to Donor (Clover) ratio images were generated in ImageJ. All the resulting FRET ratio images were processed with a 3 × 3 median filter to remove any hot pixels and presented in a scaled 16 color lookup table (ImageJ).

3.6.5 Microscopy and image analysis

For migration studies, sample media were supplemented with 1 μg/ml Hoechst33342 and samples were incubated for 30 min to label cell nuclei. Coverslips were then transferred to Attofluor chambers (ThermoFisher Scientific) and media were refreshed. Samples were imaged every 10 min for a duration of 6 h on a Nikon Eclipse Ti epifluorescence microscope equipped with a custom-built environmental chamber (37 °C, 5% CO_2). Following raw image export, nuclear tracking was performed with a custom Matlab script predicated on the IDL Particle

Tracking code (Crocker and Grier, 1996). Briefly, parameters to threshold and locate the centroids of cell nuclei were identified and applied uniformly across the entire dataset. Centroids of nuclei in serial images were linked using IDL to define migration tracks. Migration speed was calculated as the total tracked distance over the total tracking duration. Persistence was defined as the distance between initial and final positions normalized to the total tracked distance. Cells that underwent proliferation or were non-migratory over the tracked duration were not analyzed, except in Rac1 perturbation studies. Kymographs were generated in ImageJ.

Additional Matlab scripts were created to analyze cell morphology and focal adhesion characteristics. For cell morphometric data, images were acquired from 4′,6-diamidino-2-phenylindole/phalloidin-stained samples. For focal adhesion analysis, images were acquired from samples immunostained for vinculin. In both cases, images were imported, background filtered, and manually thresholded, with identical threshold values applied across entire image sets. Outlines of individual features were extracted, and shape characteristics (via regionprops) including the area, aspect ratio, and orientation were exported.

3.6.6 Statistics

Significance was determined by one-way analysis of variance (ANOVA) with Bonferroni post hoc tests and generally established with $p < 0.05$, unless specified otherwise. For cell and adhesion orientation data, angular means were determined using circular statistics in Matlab (circstat). Correlation between variables was tested using Pearson's product-moment correlation and the correspondent test (Best, D.J.; Roberts, 1975; Pearson, 1895). Multinomial multivariate linear regression model building was performed using a full linear regression model, and backward selection was performed using F-test p-values. Comparisons between models of different sizes

were performed using the Aikake Information Criteria (Akaike and A, 1974). Differences within variability between groups were tested using Levene's test. Analysis was performed using GraphPad Prism 6 or program R (v3.1.0).

3.7 Supplementary figures

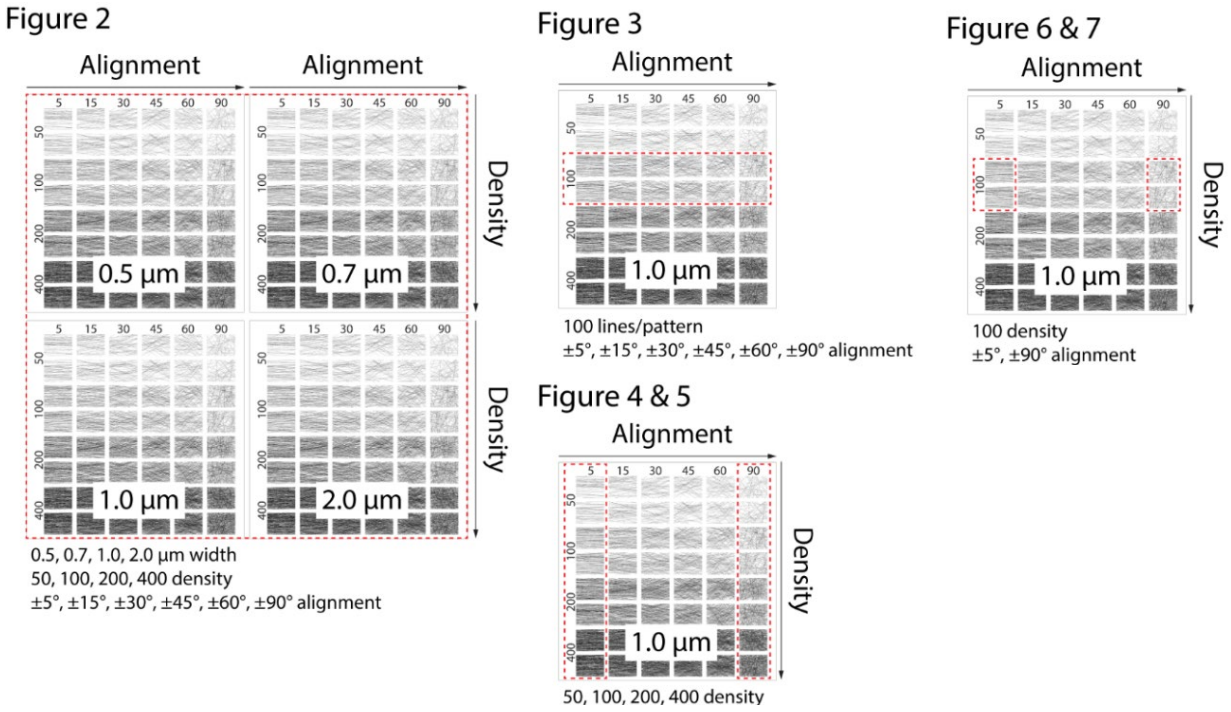

Supplementary Figure 3.1: Patterns selected for analysis (dotted red boxes) corresponding to the studies included in each of the main text Figures.

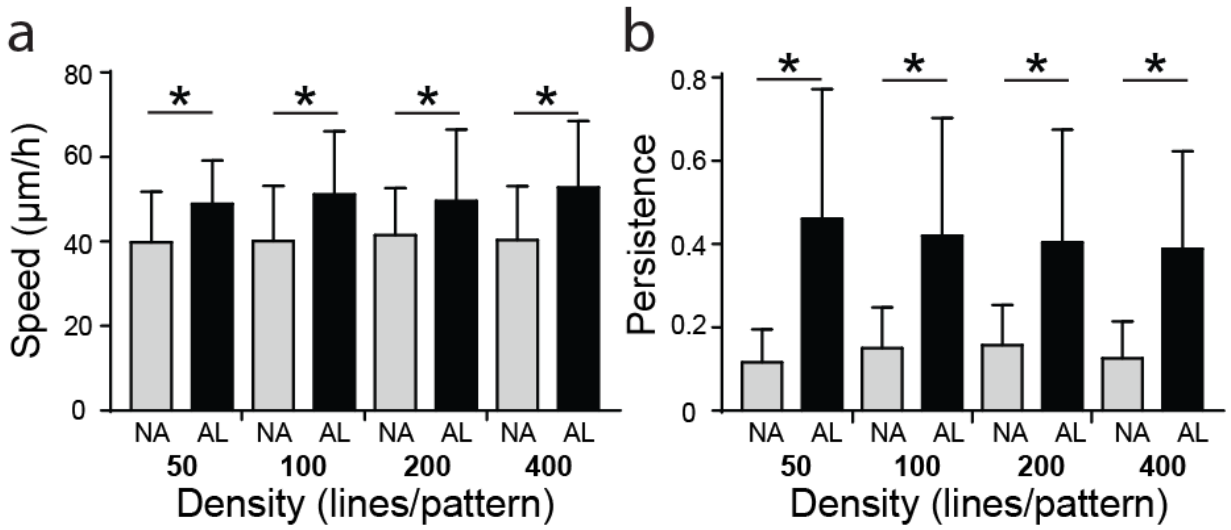

Supplementary Figure 3.2: ECM alignment influences HT1080 migration speed and persistence.

a-b) Average HT1080 migration speeds (a) and persistence (b) on NA and AL patterns containing 50, 100, 200, or 400 lines ($n \geq 35$ cells per condition, total of 500 cells analyzed, * indicates a significant difference with $p<0.05$ vs. NA group at the same line density).

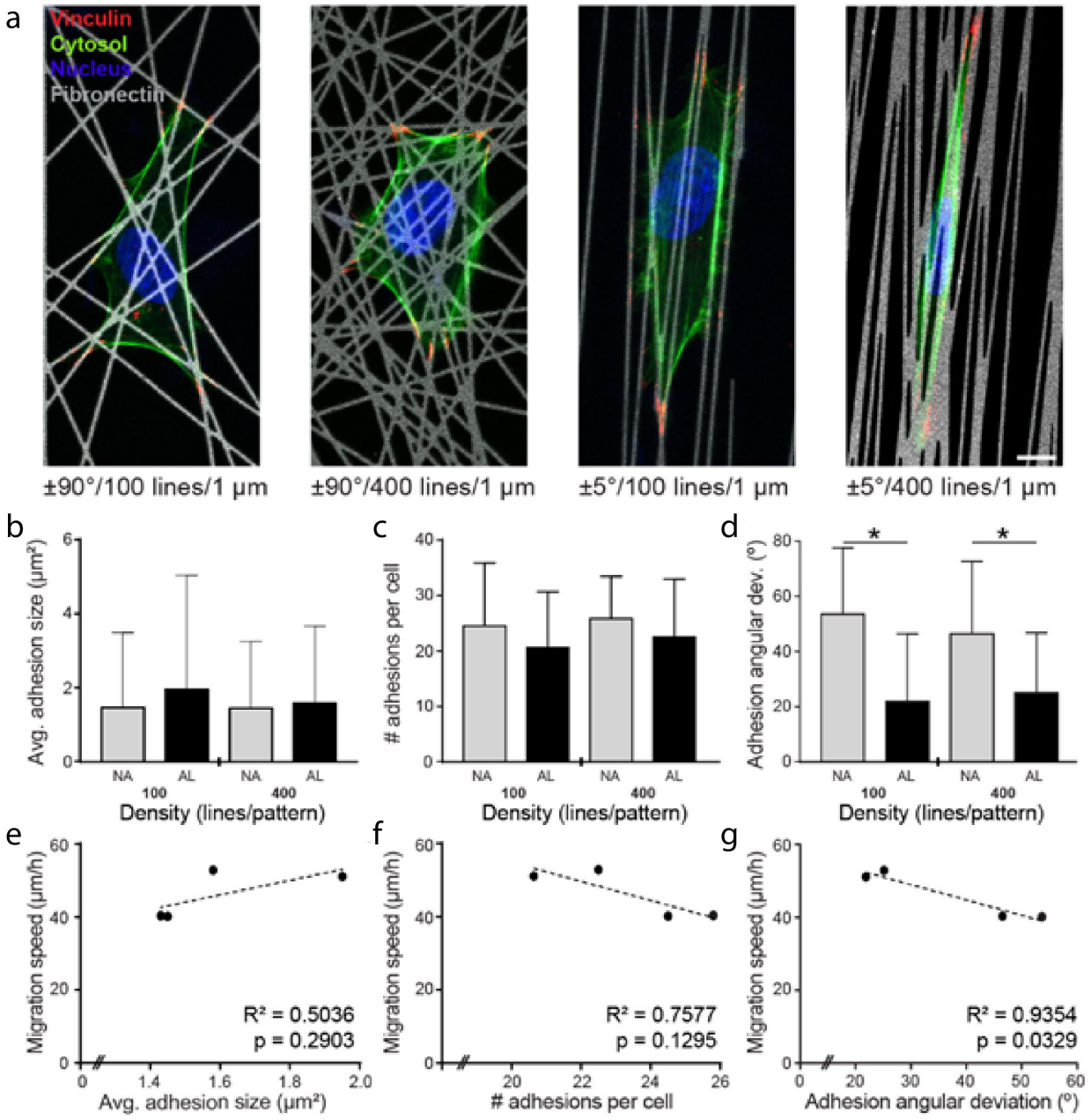

Supplementary Figure 3.3: HT1080 focal adhesion organization parallels the alignment of ECM patterns.

a) Representative confocal images of HT1080s on non-aligned (±90º) and aligned (±5º) patterns with 100 or 400 line elements stained for vinculin to localize focal adhesions (red: anti-vinculin, green: F-actin, blue: nucleus, grey: Fn555, scale bar: 10 µm). **b-d)** Average individual focal adhesion size (b), total number of adhesions per cell (c), and angular deviation of adhesion orientation within a given cell (d) for cells on non-aligned (NA, ±90°) and aligned (AL, ±5°) patterns containing 100, or 400 lines ($n \geq 6$ cells analyzed per condition, total of 34 cells analyzed, * indicates a significant difference with $p<0.05$ comparing AL vs. NA group at the same line density). **e-g)** Correlations of average migration speed vs. average adhesion size (e), total number

of adhesions per cell (f), and the angular deviation of FA orientation (g). Each data point represents the population average taken from a different pattern. Dashed lines indicate linear regression lines, with R^2 and p-values indicated within each plot.

Chapter 4: Actomyosin Contractility-Dependent Matrix Stretch and Recoil Induces Rapid Cell Migration

4.1 Authors

William Y. Wang, Christopher D. Davidson, Daphne Lin, Brendon M. Baker

4.2 Abstract

Cells select from a diverse repertoire of migration strategies. Recent developments in tunable biomaterials have helped identify how extracellular matrix properties influence migration, however, many settings lack the fibrous architecture characteristic of native tissues. To investigate migration in fibrous contexts, we independently varied the alignment and stiffness of synthetic 3D fiber matrices and identified two phenotypically distinct migration modes. In contrast to stiff matrices where cells migrated continuously in a traditional mesenchymal fashion, cells in deformable matrices stretched matrix fibers to store elastic energy; subsequent adhesion failure triggered sudden matrix recoil and rapid cell translocation. Across a variety of cell types, traction force measurements revealed a relationship between cell contractility and the matrix stiffness where this migration mode occurred optimally. Given the prevalence of fibrous tissues, an understanding of how matrix structure and mechanics influences migration could improve strategies to recruit repair cells to wound sites or inhibit cancer metastasis.

4.3 Introduction

Cell migration, a fundamental biological process in embryogenesis, tissue homeostasis, and cancer metastasis, involves dynamic interactions between cells and their local microenvironment (Charras and Sahai, 2014; Helvert et al., 2018). Biochemical and biophysical characteristics of the surrounding extracellular matrix (ECM) influences cell migration through variations in growth factors or chemokines (chemotaxis), stiffness (durotaxis), ligand density (haptotaxis), and topographical organization (contact guidance) to direct cells to target destinations (Rodriguez and Schneider, 2013). Recent advances in intravital imaging have revealed that cells can adopt a diverse set of migration strategies involving migration as single cells or collective strands, transitions between mesenchymal, epithelial, and amoeboid migration modes, deformation of the cell body and nucleus to squeeze through matrix pores, and remodeling of matrix structure to bypass the physical barriers presented by the ECM (Condeelis and Segall, 2003; Isermann and Lammerding, 2017; Weigelin et al., 2012). However, poor control over biochemical and mechanical properties of native tissues has hampered mechanistic understanding of how cells interpret and convert these external cues into the coordinated molecular signals that orchestrate cell migration. Thus, in vitro models of cell migration have proven indispensable in complementing in vivo studies to elucidate how specific ECM properties impact cell migration.

In particular, advances in tunable biomaterials and microfabricated in vitro models have helped elucidate how cells select from a repertoire of migration strategies (Charras and Sahai, 2014; Friedl and Alexander, 2011; Li et al., 2017a). In proteolysis-dependent migration, where cells are capable of biochemically remodeling the surrounding microenvironment to generate

space to move, the degree of ECM degradability influences whether cells migrate as collective multicellular strands or escape as single cells (Friedl and Wolf, 2009; Trappmann et al., 2017). Initial leader cells have been shown to use proteolytic machinery to generate microchannels within the ECM, enabling proteolysis-independent migration of follower cells (Kraning-Rush et al., 2013; Labernadie et al., 2017). Alternatively, cells are capable of employing a water permeation-based migration mode within microchannels (Stroka et al., 2014). In purely non-proteolytic migration, cells alter their morphology to squeeze through small ECM pores, leading to nuclear rupture and ESCRT III-mediated repair (Denais et al., 2016) or can transition between mesenchymal and amoeboid migration modes via alterations in matrix adhesivity and confinement (Liu et al., 2015). These studies reducing the complex physical properties of native tissues to sets of orthogonally tunable parameters have not only increased our mechanistic understanding of cell migration but also identified diverse non-proteolytic migration strategies, which may in part explain the failure of therapeutics solely targeting proteolytic activity toward confining metastatic cells to the primary tumor (Cathcart et al., 2015).

Within microenvironments in which cells can neither modify their morphology nor proteolytically degrade the ECM to effectively migrate, cell force-mediated reorganization of physical structures of the surrounding ECM may facilitate cell movement. Fibrils in collagen and fibrin gels deform as cells apply traction forces during migration (Kniazeva et al., 2012; Koch et al., 2012), however, poor control over mechanical properties and the inability to remove proteolysis-mediated remodeling of naturally derived ECM proteins has hampered our understanding of how physical reorganization of ECM fibrils influences migration (Li et al., 2017a; Wolf et al., 2009). Modeling the ECM with synthetic hydrogels composed of non-proteolytically cleavable crosslinks has elucidated how cells deform the ECM during migration in

soft three-dimensional (3D) polyethylene glycol (PEG) hydrogels (Ehrbar et al., 2011), however, these materials lack the fibrous architecture inherent to many native tissues (Qu et al., 2018). For example, the fibrous matrix of the surrounding tumor stroma of breast and pancreatic cancers undergoes marked remodeling, with increases in fibril alignment and tissue stiffness as the cancer becomes progressively more metastatic (Drifka et al., 2015; Provenzano et al., 2006). The importance of these physical changes is underscored by their clinical use as individual prognosticators of cancer patient survival rates (Conklin et al., 2011).

Toward understanding how aspects of the ECM influence dynamic interactions between cells and their physical microenvironment, here we implement a recently established synthetic material system that models fibrous ECMs and enables independent control over alignment and stiffness (Baker et al., 2015). Examining the migration of single mesenchymal cells, we find that fiber alignment enhances migration speed and directionality, while stiffness elicits a biphasic response with a maximum migration speed occurring at an intermediate matrix stiffness. Interestingly, cells within deformable matrices adopt a unique migration phenotype where cell contractility-generated matrix stretch and subsequent recoil result in rapid migratory events with effective speeds >5× than previously reported. We term this mode slingshot migration (SSM) given the requirement for matrix stretch and recoil, and further demonstrate that SSM events occur most frequently at an intermediate matrix stiffness, in part contributing to the biphasic response of migration speed to matrix stiffness. Lastly, we find that a variety of mesenchymal cell types employ this migration mode and baseline cell contractility determined by traction force microscopy (TFM) correlates with the optimal matrix stiffness where this migration mode optimally occurs.

4.4 Results

4.4.1 Synthetic matrices with tunable fiber alignment and stiffness

To better understand how matrix alignment and stiffness of fibrous ECM influence cell migration, we designed and characterized a synthetic ECM mimetic composed of electrospun dextran methacrylate (DexMA) fibers with orthogonal control over fiber alignment and bulk stiffness (Baker et al., 2015). Cell-perceived ECM mechanics were controlled by electrospinning fibrous matrices over an array of microfabricated poly(dimethylsiloxane) (PDMS) wells **(Figure 4.1a)**, such that cells seeded in well regions are not influenced by a mechanically rigid underlying support layer. To modulate fiber alignment, we altered the shape of the electric field at the collecting surface during electrospinning by controlling the separation distance between two parallel collecting electrodes (Li et al., 2003), where increasing this distance increased fiber alignment **(Figure 4.1b-c)**. We tuned photo-initiated DexMA crosslinking via ultraviolet (UV) exposure to modulate stiffness at the single fiber (measured by three-point bending with atomic force microscopy (AFM)) and bulk substrate level (measured in tension by indentation of suspended matrices with a 1 mm cylindrical indenter) **(Figure 4.1d and Supplementary Figure 4.1a)**, selecting a range of crosslinking to capture a full spectrum from maximal to undetectable matrix deformations resulting from cell-generated forces **(Figure 4.1e)**. These values for single fiber Young's modulus are within range of reported values for fibrin fibers, elastin fibers, and fibronectin fibrils (depending on their stretch state) (Guthold et al., 2007). The range for bulk stiffness values (1–30 kPa) reflects measurements taken for a variety of tissues (Engler et al., 2006), as well as the transition from normal to cancerous mammary tissue (Levental et al., 2009).

We held ligand density, fiber diameter, and scaffold thickness constant by maintaining a fixed concentration of cRGD, polymer weight percentage, and fiber collection duration, respectively **(Supplementary Figure 4.1b-e)**. Controlling these matrix properties within naturally derived ECM proteins such as collagen and fibrin hydrogels proves challenging, as these properties are inherently linked to protein concentration and gelation conditions (Li et al., 2017a; Riching et al., 2015; Wolf et al., 2009). By creating matrices with free-radical polymerized DexMA fibers, which generates proteolytically uncleavable methacrylate-methacrylate crosslinks, we sidestepped the influence of cell-mediated matrix degradation on matrix properties over time (Lutolf et al., 2003; Trappmann et al., 2017; West and Hubbell, 1999) and focused here on non-proteolytic mechanisms of 3D cell migration (Wolf and Friedl, 2011).

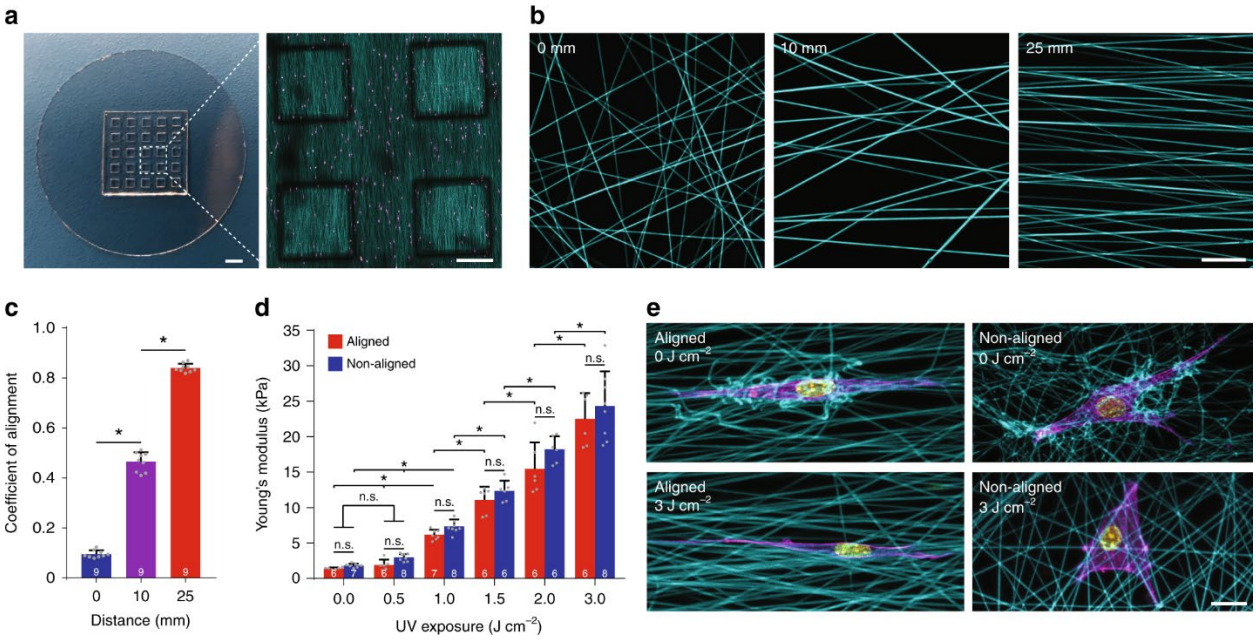

Figure 4.1: Synthetic fibrous extracellular matrix with orthogonal control over fibril alignment and stiffness.
a) Microfabricated poly(dimethylsiloxane) multiwell substrate possessing a 5 × 5 array of DexMA fiber matrices, each suspended over a well to isolate the matrix from mechanical effects of a rigid underlying support (scale bar: 2 mm). Inset: tilescan of four DexMA-cRGD matrices (cyan) seeded with NIH3T3 fibroblasts (magenta) (scale bar: 500 µm). **b)** Confocal projections of matrices (cyan) fabricated with varying spacing between collecting electrodes to modulate fiber alignment (scale bar: 20 µm). **c)** Quantification of fiber alignment as a function of electrode separation distance ($n = 9$ matrices per group). **d)** Young's modulus of aligned (electrode separation of 0 mm) and non-aligned (electrode separation of 25 mm) matrices as a function of ultraviolet (UV)-initiated crosslinking of matrix fibers. n = number of matrices per group as indicated within each bar. **e)** Composite confocal fluorescence images of representative NIH3T3 fibroblasts in soft (top row, 0 J cm^{-2}) and stiff (bottom row, 3 J cm^{-2}) matrices; rhodamine-labeled matrix fibers (cyan), F-actin (magenta), and nuclei (yellow) (scale bar: 20 µm). All data presented as mean ± s.d.; * indicates a statistically significant comparison with $p < 0.05$; n.s. indicates a non-significant comparison (one-way analysis of variance).

Utilizing NIH3T3 fibroblasts, commonly employed in studying how microenvironmental cues govern mesenchymal cell migration (Tamura et al., 1998; Wang et al., 2018), we first investigated the effect of fiber alignment at three distinct stiffness conditions (for simplicity, referred to throughout the text as low (1.42 kPa), intermediate (6.17 kPa), and high (22.5 kPa) stiffness corresponding to 0, 1, and 3 J cm^{-2} of UV exposure, respectively). Cells were cultured for 6 h prior to the start of time-lapse imaging, resulting in the majority of cells infiltrating and

embedding themselves within the matrix **(Supplementary Figure 4.1f)** . At each level of stiffness, aligned matrices resulted in higher migration speeds and more directional migration tracks **(Figure 4.2a-d and Supplementary Movie 4.1)**. The effect of alignment on migration directionality (determined by the deviation of a cell's position away from a linear fit to its overall migration track) proved consistent over all stiffnesses, suggesting the influence of contact guidance (Ray et al., 2017a; Wang et al., 2018) on directionality is stiffness-independent in this setting. This finding is consistent with previous studies utilizing 3D collagen hydrogels (Riching et al., 2015).

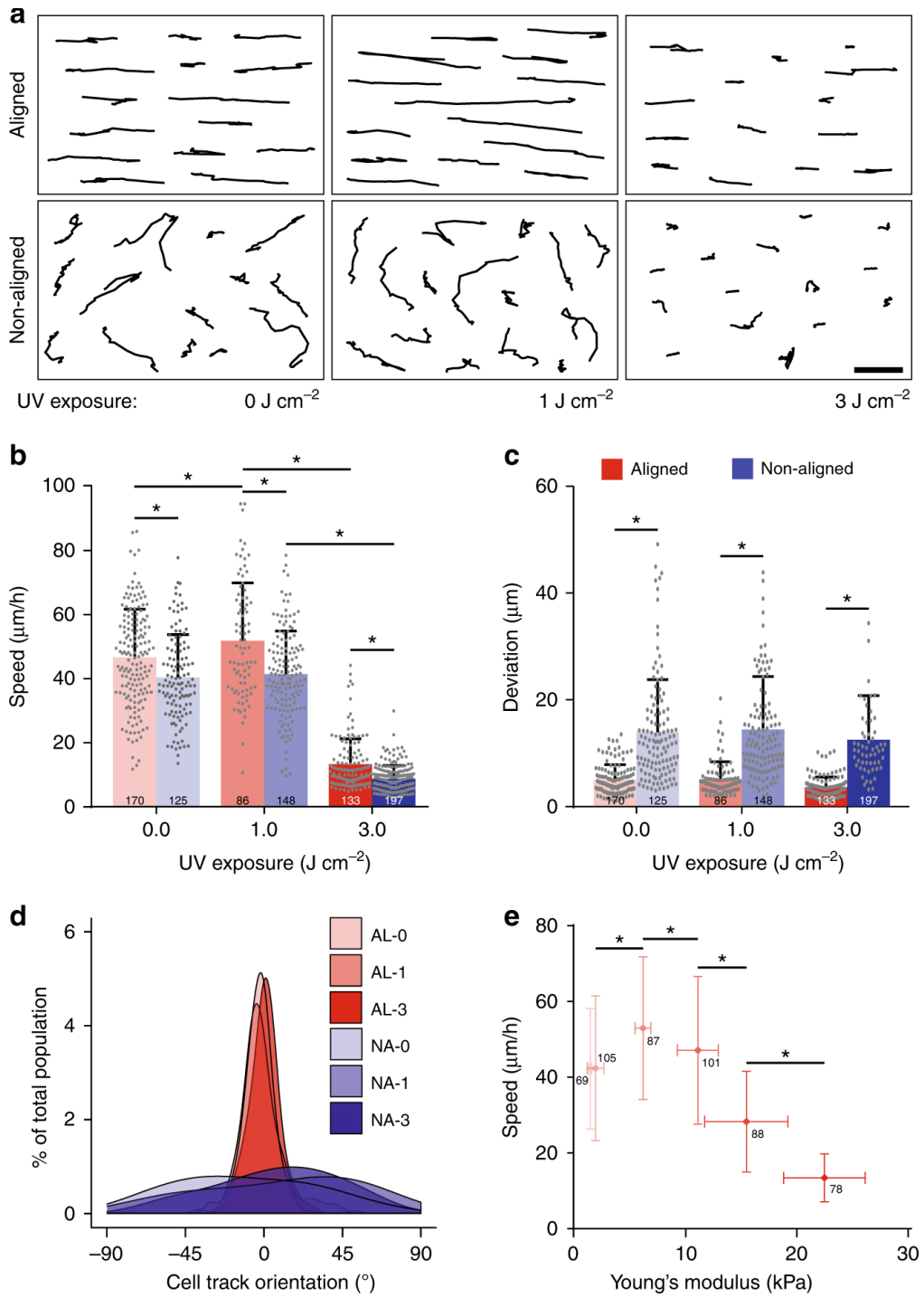

Figure 4.2: Matrix alignment and stiffness influence cell migration speed and directionality. **a)** Representative NIH3T3 migration tracks over a 6 h time course on aligned and non-aligned matrices at low (0 J cm^{-2}), intermediate (1.0 J cm^{-2}), and high (3.0 J cm^{-2}) ultraviolet (UV) exposure; scale bar: 100 µm. **b–d)** NIH3T3 net migration speed, deviation, and orientation as a function of matrix alignment and UV exposure. *n* = number of cells per group as indicated within each bar. **e)** Migration speed as a function of Young's modulus in aligned matrices. *n* = number of cells per group as indicated beside each data point. All data presented as mean ± s.d.; * indicates a statistically significant comparison with $p < 0.05$ (two-way analysis of variance)

Within aligned matrices, these initial studies indicated migration speeds were highest at an intermediate stiffness **(Figure 4.2b)**. We next modulated matrix stiffness over more graded steps, confirming a biphasic relationship between migration speed and bulk matrix stiffness for NIH3T3s **(Figure 4.2e and Supplementary Figure 4.2a-b)**. Demonstrating this response is not unique to NIH3T3s, we tracked human foreskin fibroblast migration within aligned matrices of varying stiffness and similarly found a biphasic response between migration speed and bulk matrix stiffness **(Supplementary Figure 4.2c)**. Such a biphasic relationship between migration speed and stiffness has been previously predicted by mathematical models and supported with experimental work on two-dimensional (2D) hydrogels (Bangasser et al., 2017; DiMilla et al., 1991; Elosegui-Artola et al., 2014, 2016; Klank et al., 2017; Oria et al., 2017; Zaman et al., 2006). These studies indicate matrix properties that optimize integrin engagement and traction generation feed progression of the cell migration cycle, resulting in optimal migration speeds. In particular, high matrix stiffness or ligand density leads to stable focal adhesions preventing detachment of the cell rear, and low matrix stiffness or ligand density can inhibit cell contractility and cell-generated traction forces required to contract the cell body forward. However, previous studies did not examine the effect of cell-scale local matrix deformations, which potentially could exert a pronounced influence on cell motion in soft fibrous settings (Baker et al., 2015).

4.4.2 SSM contributes to biphasic migration speed

Toward understanding one possible contribution to the biphasic response between migration speed and stiffness within aligned matrices, we imaged at higher spatiotemporal resolution to observe dynamic cell-matrix interactions during migration. Cells were observed to adopt two distinct migration modes as a function of matrix stiffness. Across all stiffnesses

examined, cells appeared to migrate using the well-described mesenchymal cell migration cycle consisting of iterative rounds of elongation, adhesion, contraction, and retraction (Ridley, 2003) (henceforth termed continuous migration) **(Figure 4.3a, c-e)**. However, in deformable matrices, cells were also observed to undergo a prolonged extension/contraction phase, during which the cell's position remained largely stagnant while active cell protrusions reorganized the adjacent matrix by recruiting fibers toward the cell body. Following this phase of matrix deformation, an apparent failure in adhesions at the cell's trailing edge led to a sudden recoil of the matrix, simultaneous with translation of the cell body forward along the axis of fiber alignment **(Figure 4.3b, f and Supplementary Movie 4.2)**. Given the phenotypic departure from traditional continuous migration, we termed this mode SSM, as the cell appears to harness matrix stretch and recoil to slingshot forward. At an intermediate stiffness, we found the percentage of the total cell population that employed SSM (SSM population, 71.2%) and the percentage of tracked time cells underwent SSM (SSM duration, 31.6%) were highest **(Figure 4.3h, i)**, as high stiffness matrices appeared insufficiently deformable to afford appreciable matrix stretch while low stiffness matrices, although significantly stretched, appeared too compliant to consistently induce a recoil event **(Supplementary Movie 4.2)**.

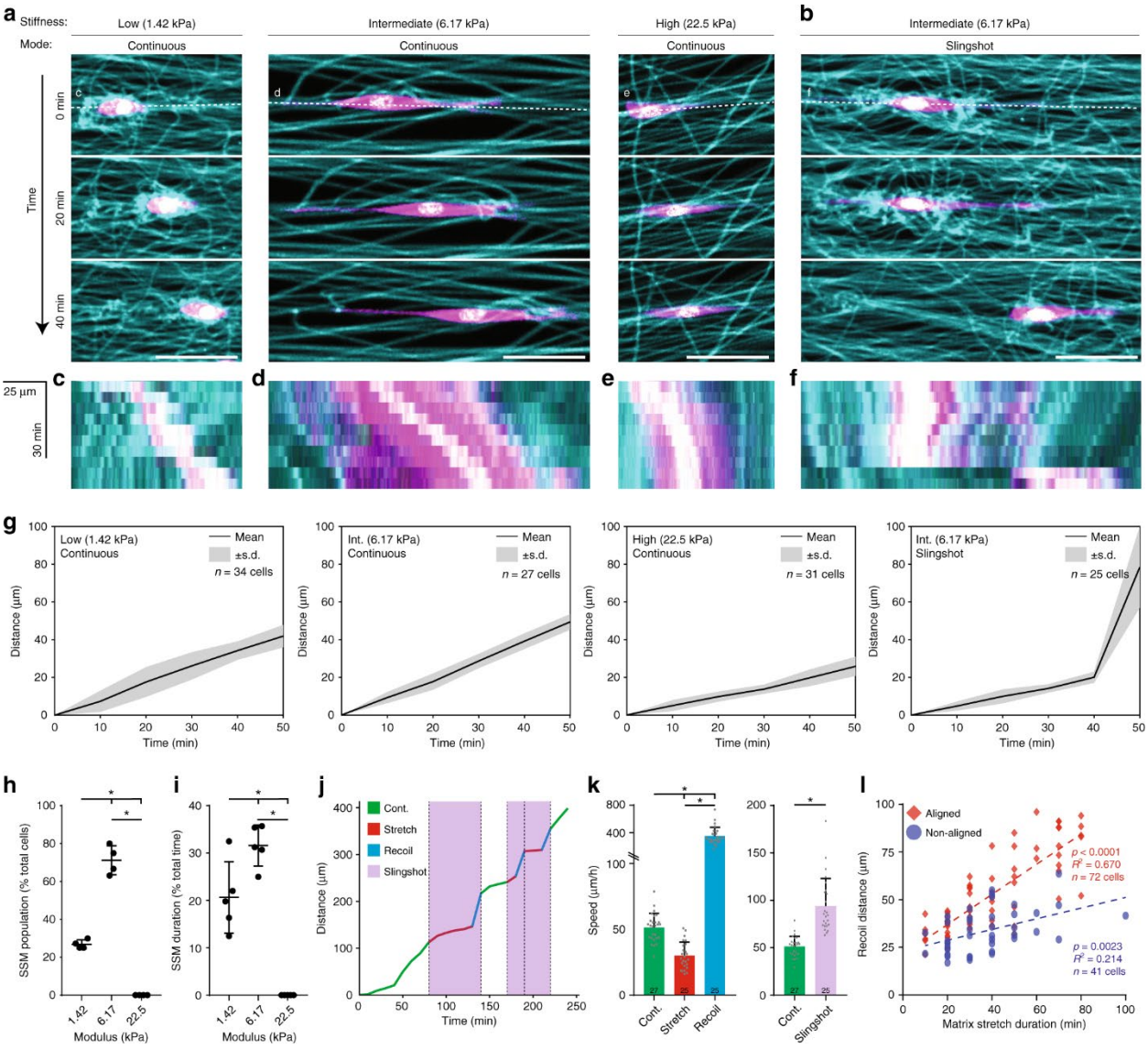

Figure 4.3: Aligned deformable matrices undergo marked deformation and promote rapid migratory events.

a-b) Representative time-lapse images of NIH3T3s within matrices of low, intermediate, and high stiffness utilizing continuous or slingshot migration (SSM) modes (matrix fibers (cyan), cytoplasm (magenta), and nuclei (white); scale bars: 50 µm). **c**–**f)** Corresponding kymographs taken along the dotted lines indicated in (a) and (b). **g)** Migration distance over time for cells undergoing continuous migration and SSM. *n* = number of cells per group as indicated within each plot; shaded region indicates standard deviation. **h)** Percentage of cells observed to employ SSM out of all cells tracked over a 6 h time course (*n* = 4 fields of view; field of view = 10 cells). **i)** Percentage of time cells employed SSM as a function of matrix stiffness (*n* = 5 fields of view; field of view = 10 cells). **j)** Representative migration track of an NIH3T3 on aligned matrix of intermediate stiffness, demonstrating interconversion between continuous migration and SSM modes over its tracked lifetime. **k)** Effective migration speeds of parsed phases of continuous, stretch, and recoil (left) and periods of continuous migration and SSM (combined stretch and recoil phases) (right). Continuous migration speeds were calculated from periods of continuous migration in cells that undergo SSM over its tracked duration. *n* = number of cells per group as indicated within each

bar. **l)** Recoil distance (net translocation of cell) as a function of duration spent stretching the matrix (n = number of cells per group as indicated within the plot). Dashed lines indicate linear correlations with indicated R^2 and p-values. All data presented as mean ± s.d.; * indicates a statistically significant comparison with $p < 0.05$ (h, i, k: one-way analysis of variance, l: linear regression).

Comparing migration distance over time of these two distinct modes, we observed steady migration speeds with continuous migration, whereas SSM consisted of two distinct speeds corresponding to separate phases of matrix stretch and recoil **(Figure 4.3g)**. Furthermore, cells within deformable matrices (both soft and intermediate stiffness) interconverted between continuous and SSM modes over the course of their tracked lifetimes **(Figure 4.3j)**. Of cells that underwent SSM within intermediate stiffness matrices, individual cell trajectories parsed into periods of continuous migration and SSM (possessing distinct phases of stretch followed by recoil) revealed that the large recoil distance (58.7 ± 21.3 μm, $n = 25$ cells), despite significantly slower cell movement during phases of matrix stretch, rendered SSM overall faster compared to continuous migration **(Figure 4.3k)**. Thus, a higher frequency of high speed SSM events at the intermediate stiffness may in part contribute to the biphasic relationship observed between migration speed and stiffness within aligned matrices. To prevent phototoxicity during fluorescence imaging, 10-min intervals were utilized in these measurements; however, matrix recoil events captured under transmitted light (one frame per second) yielded a more accurate measurement of recoil speed of 45.2 ± 15.1 μm s^{-1} ($n = 25$ cells) **(Supplementary Figure 4.3a and Supplementary Movie 4.3)**. Furthermore, cells that possessed a distinct leading edge resulted in recoil events preferentially in the direction of continuous migration prior to matrix stretch while cells with bidirectional extensions resulted in recoil events in either direction **(Supplementary Figure 4.3b)**. SSM was also observed in deformable, non-aligned matrices, and in both aligned

and non-aligned matrices recoil distance positively correlated with the duration the cell spent generating matrix stretch **(Figure 4.3l)**. For a given duration of matrix stretch, recoil distances were larger within aligned matrices, which may be due to uniaxial material stretch in aligned matrices as compared to more equiaxial stretch in non-aligned matrices.

4.4.3 SSM involves coordinated matrix deformations

Previous studies tracking fiducial markers embedded within 3D collagen hydrogels suggested cancer cells with greater metastatic potential apply uniaxial traction forces and store anisotropic strain energy within matrix deformations (Koch et al., 2012). Adopting a similar approach, we next more closely examined matrix deformations during SSM and continuous migration by embedding fluorescent microspheres (beads) within matrix fibers. As expected, cell forces underlying continuous migration within non-deformable, high stiffness matrices resulted in negligible bead displacements **(Figure 4.4a and Supplementary Movie 4.4)**. In contrast, within low stiffness matrices, displacements of beads nearby continuously migrating cells increased incrementally throughout the migration track **(Figure 4.4a and Supplementary Movie 4.4)**. Cells undergoing SSM within intermediate stiffness matrices similarly induced incremental bead displacements during matrix stretch. However, upon matrix recoil and simultaneous translocation of the cell body, we noted large forward and rearward bead displacements emanating from the former position of the cell's trailing edge **(Figure 4.4a and Supplementary Movie 4.4)**.

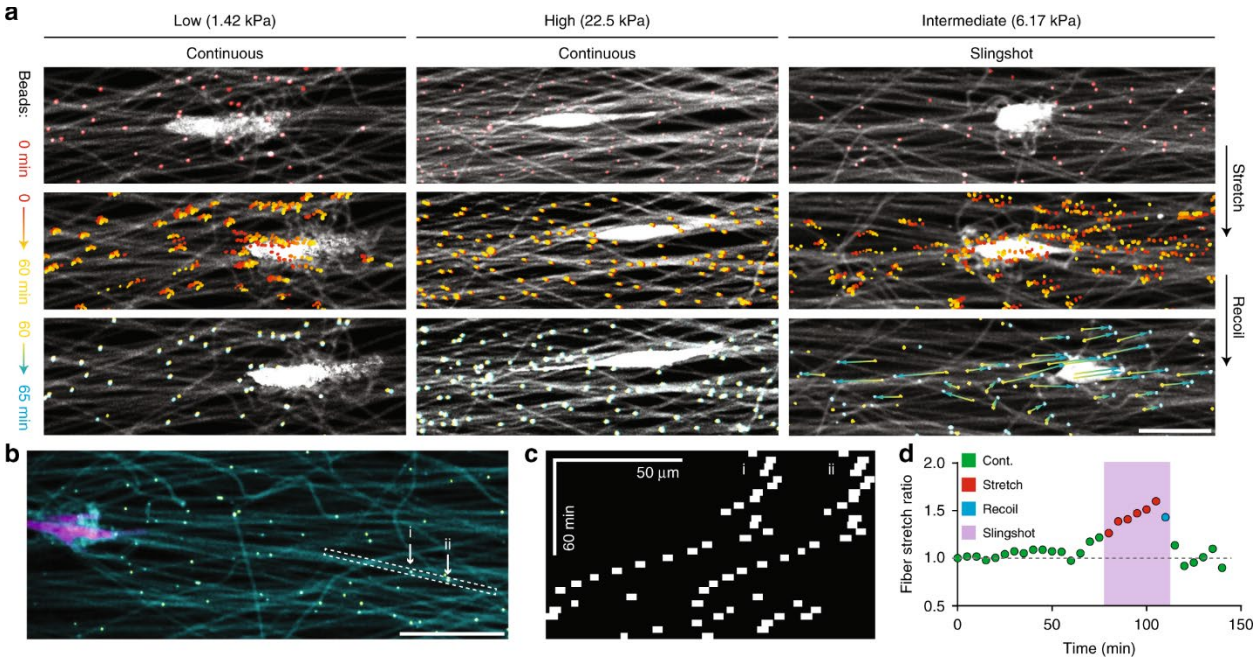

Figure 4.4: Slingshot migration involves stretch and recoil of matrix fibers.
a) Representative time-lapse images of fibers containing fluorescent microspheres, used as fiducial markers to examine matrix deformations underlying continuous and slingshot migration (scale bar: 50 µm). **b)** Composite confocal fluorescence image of an NIH3T3 within an intermediate stiffness matrix (matrix fibers (cyan), cytoplasm (magenta), and fiber-embedded beads (yellow); scale bar: 50 µm). **c-d)** Kymograph of a pair of microspheres embedded within the same fiber, as indicated in (b**)** used to determine fiber stretch ratio (d) (relative to initial distance between beads) as a function of time.

In previous work with mesenchymal stem cells, cell traction forces applied to deformable, non-aligned matrices induced isotropic fiber recruitment (an increase in fiber density local to the cell), which led to increased focal adhesion maturation, cell spreading, and proliferation (Baker et al., 2015). Within matrices of aligned fibers, cell morphology adopts a uniaxial phenotype likely leading to directional force generation and anisotropic fiber recruitment. However, given the implication of elastic strain energy storage and release during SSM, we also asked whether individual fibrils undergo stretch due to cell-generated traction forces. Tracking pairs of adjacent beads embedded within the same fiber revealed fibers engaged by cell adhesions undergo stretch, and release of this strain energy stored in the form of matrix stretch correlates temporally with forward motion of the cell **(Figure 4.4b-d)**. Interestingly, we noted that fiber engagement was

spatially heterogeneous, where nearby non-engaged fibers did not experience stretch **(Supplementary Figure 4.4a-c)**. Several studies in vivo and in vitro have identified mechanoreciprocity (the reciprocal mechanical interplay between cells and matrix) arising from cell contractility-generated matrix fibril stretch (Helvert et al., 2018; Leiss et al., 2008). For example, cell traction forces applied to fibronectin-rich matrices induce fibronectin fibril stretch to reveal cryptic binding sites, promote growth factor bioavailability, and in turn facilitate cell adhesion, proliferation, and migration (Klotzsch et al., 2009; Xu et al., 2001; Zhu and Clark, 2014). In our synthetic material system where such biochemical changes are absent, we show that mechanical stretch of matrix fibrils from cell traction forces can directly facilitate cell movement.

To more closely examine how matrix recoil events are initiated within SSM, we generated NIH3T3s stably expressing lifeact-green fluorescent protein (3T3-LA-GFP) or paxillin-enhanced GFP (EGFP) fusion protein and tracked their migration in aligned matrices of intermediate stiffness. Simultaneous with recoil of the matrix, we observed rupture of the cell's trailing edge resulting in residual actin- and paxillin-rich puncta tethered to the matrix rearward to the direction of cell movement **(Supplementary Figure 4.5a-b, Supplementary Movie 4.5 and Supplementary Movie 4.6)**. To confirm that these paxillin-rich plaques were indeed focal adhesions, we fixed and immunostained substrates directly on the microscope stage immediately following live imaging of 3T3-LA-GFP cell migration, demonstrating localization of vinculin within the actin-rich remnants resulting from matrix recoil and tail rupture **(Supplementary Figure 4.6a-b)**. Furthermore, we investigated whether SSM occurred in 3D type I rat tail collagen hydrogels, widely utilized to model fibrous stromal tissue. Tracking 3T3-LA-GFP cells embedded within fluorescently labeled 1.0 mg mL^{-1} collagen hydrogels revealed a phenotypically similar migration mode to SSM. Cells remained stagnant while deforming the surrounding matrix,

followed by rapid forward migration corresponding with recoil of the matrix and lifeact-GFP puncta residing in the matrix rearward to the direction of the migration **(Supplementary Figure 4.7a-b and Supplementary Movie 4.7)**. These data suggest matrix recoil events are initiated by a mechanical failure of the actomyosin cytoskeleton at the cell's trailing edge. Integrins and other transmembrane proteins have been observed to remain tethered to the ECM upon ripping from the plasma membrane or rear-release during migration in vivo and in vitro (Bard and Hay, 1975; Chen, 1981; Lauffenburger and Horwitz, 1996; Regen and Horwitz, 1992). These abrupt mechanical failure events bare resemblance to retraction-induced migration described in chick fibroblasts cultured on rigid glass substrates by Chen several decades ago (Chen, 1981), where tension in the cytoskeleton was hypothesized to cause elastic recoil of the cell body upon trailing edge detachment. In contrast, however, our studies employing deformable elastic substrates suggest tension stored additionally in matrix fibrils can induce substrate recoil and simultaneous cell translocation upon rupture at the trailing edge.

Given that contractility-generated traction forces induce matrix deformations and fibril stretch, we anticipated SSM would be adhesion- and contractility-dependent. Motivated by previous demonstrations that low ECM ligand density decreases cell contractility due to impaired integrin clustering and focal adhesion maturation (Gupton and Waterman-Storer, 2006; Maheshwari et al., 2000), we first modulated the concentration of cRGD coupled to the matrix (all previous experiments utilized 500 μM cRGD). At 50 and 100 μM cRGD, SSM events decreased along with overall migration speeds **(Figure 4.5a-b)**. Treating cells with 30 μM blebbistatin (myosin II inhibitor) or 25 μM Y27362 (ROCK inhibitor) to lower actomyosin-generated contractility completely abrogated matrix deformations and SSM events, and cells were observed to migrate continuously at decreased speeds comparable to cells within non-deformable stiff

matrices employing continuous migration **(Figure 4.5c-f and Supplementary Movie 4.8)**. Continuous cell migration requires cell contractility (Ridley, 2003), and a decrease in continuous migration speeds on high stiffness matrices was also noted. However, the relative decrease in migration speed on intermediate stiffness matrices was significantly larger, suggesting contractility is critical for SSM due to the requirement for matrix stretch and recoil **(Supplementary Figure 4.8a)**. While 30 μM blebbistatin completely abrogated SSM events, treating cells with 5 μM blebbistatin to partially inhibit cell contractility resulted in decreased migration speed, SSM population and duration, and decreased recoil distances for a given matrix stretch duration **(Supplementary Figure 4.8b-d and (Supplementary Figure 4.9)**. Finally, cells were treated with calyculin A, a relatively specific inhibitor of myosin II phosphatase, to increase overall myosin II activity (Gupton and Waterman-Storer, 2006). Calyculin A-mediated increase of actomyosin activity led to increases in the rate of matrix stretch and SSM population and duration compared to control, and corresponded to an overall increase in migration speeds **(Figure 4.5g-h and Supplementary Figure 4.9)**. In sum, these data suggest adjusting levels of intracellular force generation by modulating actomyosin contractility regulates the magnitude and frequency of rapid recoil events and resulting migration speeds.

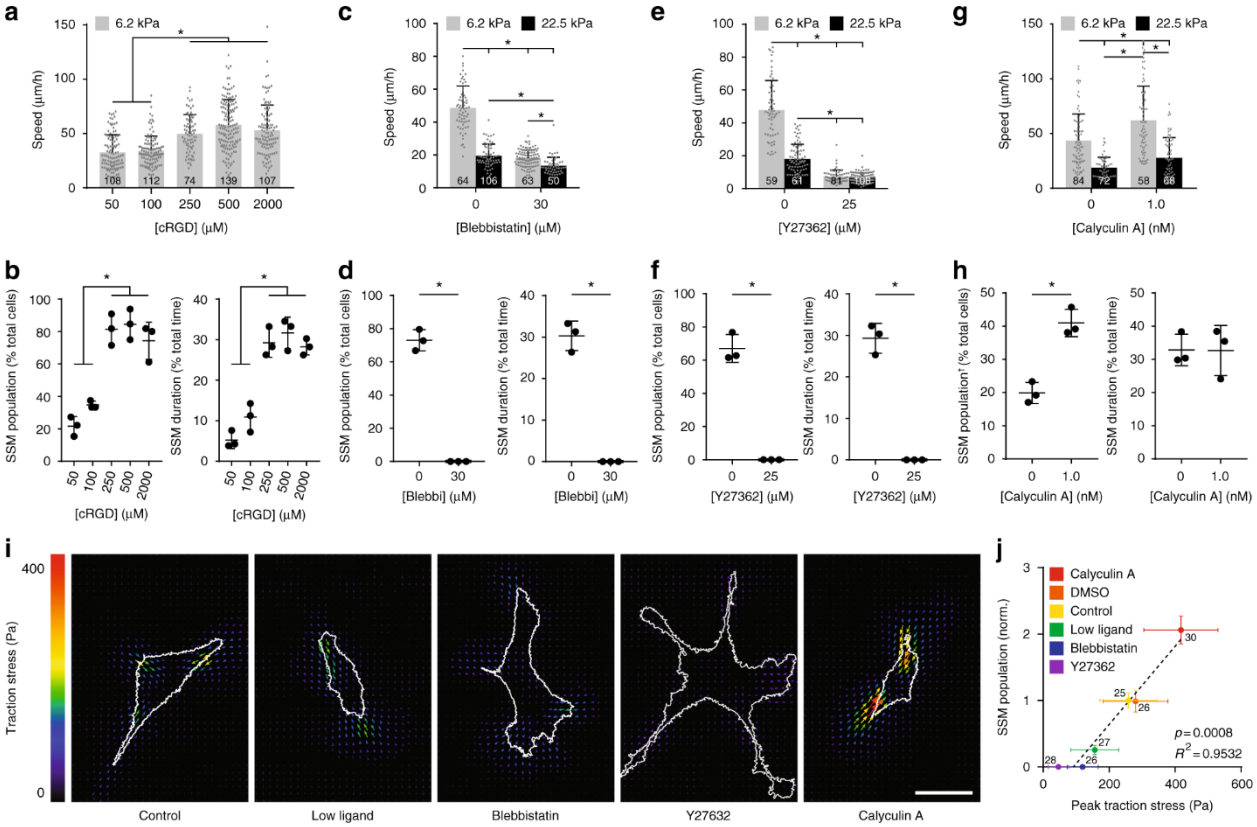

Figure 4.5: Slingshot migration (SSM) requires matrix adhesion and actomyosin contractility.

a-b) Migration speed, SSM population (% of cell population undergoing one or more SSM event), and SSM duration (% of tracked time of entire population spent in some phase of SSM) in aligned, intermediate stiffness (6.2 kPa) matrices with a range of cRGD functionalization. n = number of cells per group as indicated within each bar (a); $n = 3$ fields of view with each field of view containing 10 cells (b). **c**, **e**, **g)** Migration speed in aligned, intermediate (6.2 kPa) and high (22.5 kPa) stiffness matrices treated with blebbistatin, Y27632, or calyculin A (n = number of cells per group as indicated within each bar). **d**, **f**, **h)** SSM population and slingshot duration in aligned, intermediate stiffness (6.2 kPa) matrices treated with blebbistatin, Y27632, or calyculin A ($n = 3$ fields of view with each field of view containing 10 cells). Migration speed, SSM population, and SSM duration were quantified over a 6 h time course for cRGD, blebbistatin, and Y27 studies, and quantified over a 1 h time course for calyculin A studies (indicated with †). **i)** Representative traction stress maps of NIH3T3s on 7.9 kPa polyacrylamide hydrogels subjected to equivalent perturbations as in (a–h) (scale bar: 50 μm). **j)** Slingshot population (normalized to control) as a function of peak traction stress determined by traction force microscopy. Dashed line indicates linear correlation with indicated R^2 and p-value. n = number of cells per group as indicated beside each data point. All data presented as mean ± s.d.; * indicates a statistically significant comparison with $p < 0.05$ (a–c, e, g: one-way analysis of variance; d, f, h: two-tailed Student's t-test; **j**: linear regression).

Given the spatial heterogeneity of engaged vs. non-engaged fibers and thus non-continuum-like deformation of the matrix **(Supplementary Figure 4.4a-c)**, accurate calculation of traction forces utilizing standard TFM analysis is not currently possible in this setting. Thus, we employed 2D polyacrylamide hydrogels and the TFM method (Aratyn-Schaus et al., 2010) to measure traction forces under the above perturbations to actomyosin contractility. Plotting SSM events as a function of peak traction stress for each condition, we found that population of cells that utilized SSM significantly correlates with contractility-generated traction forces (Pearson correlation: $R^2 = 0.9532$; p-value = 0.0008; linear regression) **(Figure 4.5i, j and Supplementary Figure 4.11a)**. Taken together, these studies suggest SSM involves a dynamic force balance between actomyosin contractility and tension generated from matrix stretch. When matrix tension rises beyond the critical force level that trailing edge adhesions can bear, failure at the interface between focal adhesions and the cytoskeleton triggers a sudden imbalance of forces and rapid forward translation of the cell with matrix recoil.

4.4.4 Matrix stiffness for optimal SSM scales with traction forces

To investigate whether other cell types employ SSM, we performed similar migration studies with a variety of metastatic cancer cells, adult mesenchymal stem cells, and fibroblasts. An initial screen utilizing aligned matrices at intermediate stiffness revealed cell types that utilize adhesion-dependent mesenchymal-like migration indeed also employ SSM. However, the degree of matrix deformations generated at this stiffness, which led to maximal SSM duration for NIH3T3s, varied considerably between these cell types **(Supplementary Figure 4.10)**. Since previous work has shown optimal migration speeds between cell types shift with substrate stiffness (Bangasser et al., 2013), we hypothesized these variations may be due to intrinsic differences in

contractility-generated traction forces between cell types. Thus, we screened a range of stiffnesses for each cell type and found that the optimal SSM stiffness for metastatic breast (MDA-MB-231), squamous cell carcinoma (UM-SCC-74B), fibrosarcoma (HT1080), C2C12 myoblast, human mesenchymal stem cell, and human foreskin fibroblast significantly positively correlated with each cell type's peak traction stress (Pearson correlation $R^2 = 0.7774$; p-value = 0.0087; linear regression) **(Figure 4.6a-b and Supplementary Figure 4.11b)**. These studies suggest that the matrix stiffness that optimizes matrix stretch and subsequent recoil (and thus the frequency of SSM events) scales directly with contractility-generated traction forces.

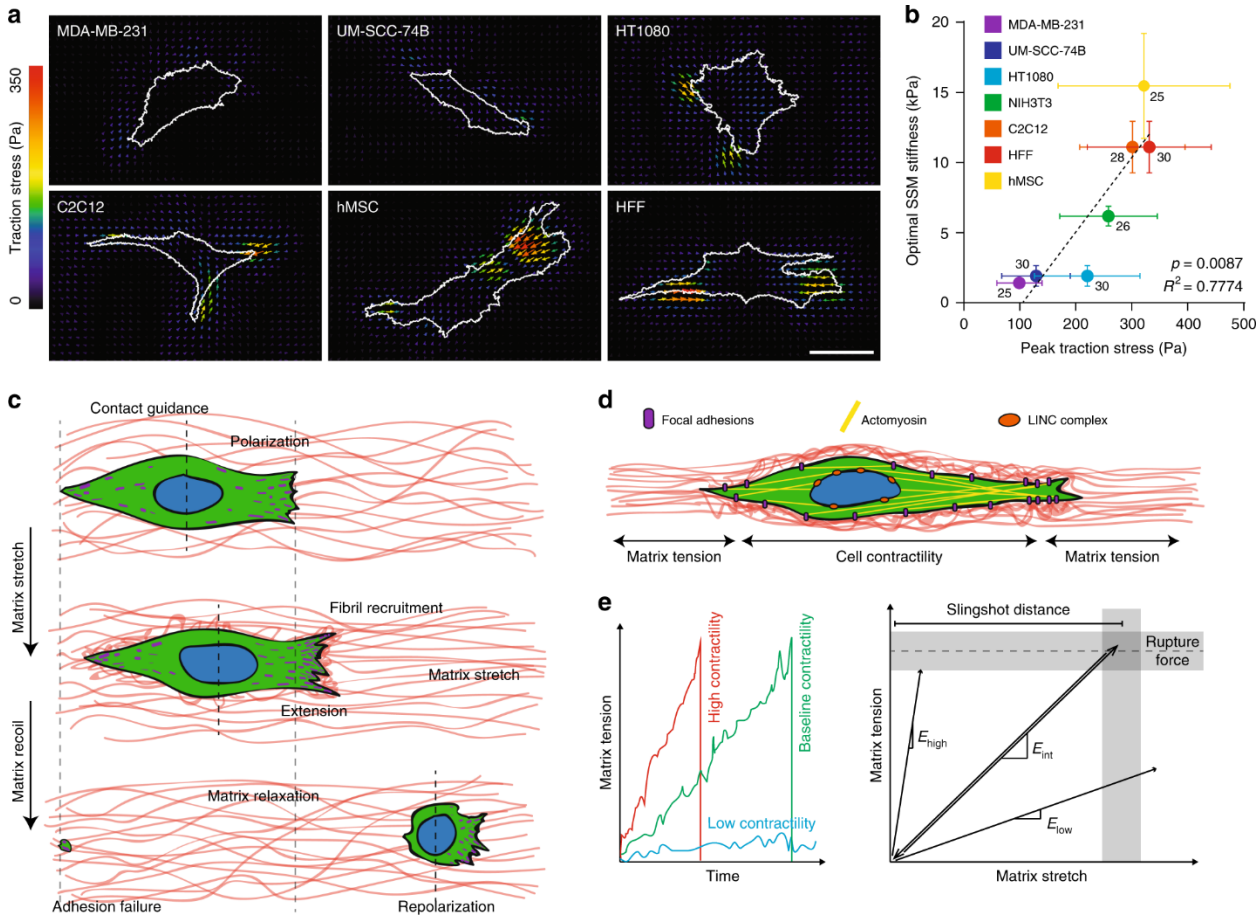

Figure 4.6: Contractile cell types employ slingshot migration in a matrix stiffness-dependent manner.

a) Representative traction stress maps of MDA-MB-231 (breast adenocarcinoma), UM-SCC-74B (head and neck squamous cell carcinoma), HT1080 (connective tissue fibrosarcoma), C2C12 (mouse myoblast cell line), hMSC (primary adult mesenchymal stem cells), and HFF (primary human foreskin fibroblasts) on 7.9 kPa polyacrylamide hydrogels (scale bar: 50 μm). **b)** Matrix stiffness leading to maximal slingshot duration for each cell type as a function of peak traction stress for each cell type, as determined by traction force microscopy. *n* = number of cells per group as indicated beside each data point. Data presented as mean ± s.d. Dashed line indicates linear correlation with indicated R^2 and *p*-value (linear regression). **c)** Top-down schematic depicting key steps underlying slingshot migration in aligned fibrous matrices, including contact guidance-mediated polarization (top), protrusion extension simultaneous with fibril recruitment and matrix stretch (middle), and adhesion failure inducing rapid recoil and cell translocation (bottom). Theorized adhesion distributions are shown in purple. **d)** Schematic highlighting force balance between cell-generated contractile forces and tension in the matrix. **e)** Proposed time evolution of matrix tension as a function of cell contractility (left) and relationship between matrix tension and stretch at different levels of matrix stiffness (right). Note: these plots are theorized, not experimental.

4.5 Discussion

This work characterizes a previously undescribed cell migration mode whereby cell contractility-mediated reorganization and stretching of matrix fibrils directly contributes to rapid cellular movement. In contrast to continuous migration, involving short iterative cycles of extension and adhesion of the leading edge followed by contraction of the cell body and detachment of the cell rear, SSM consists of two distinct phases: (1) matrix stretch and (2) matrix recoil. During matrix stretch, extension of cell protrusions and actomyosin contractility actively recruit and stretch nearby fibers to store elastic strain energy within the matrix. Once tension in the matrix surpasses maximal forces cell-ECM adhesions can withstand (potentially due to force fluctuations at adhesions (Plotnikov et al., 2012)), failure at trailing edge adhesions initiates sudden matrix recoil, the release of matrix stored strain energy, and concomitant cell translocation **(Figure 4.6c)**. This migration mode proves highly mechanosensitive and requires simultaneous production of both matrix stretch and tension: softer matrices undergo pronounced stretch but fail to generate sufficient tension to induce recoil; conversely, stiff matrices may experience high forces, but yield insignificant stretch **(Figure 4.6e)**. We find that a variety of mesenchymal cells adopt this migration mode, and furthermore, that this event occurs optimally at a matrix stiffness that scales with the cell type's baseline contractility.

Though well accepted that cell migration involves a coordination of molecular events that generates ECM tractions and contractile forces that move the cell body forward, this work extends the role of these processes to actively deforming the matrix to elicit cell translocation. The growth and decay of focal adhesions and resulting dynamics of force transmission to the ECM have previously been described using motor-clutch models, which yield a qualitatively similar biphasic response of migration speed to matrix stiffness that is likely at play in our studies (Bangasser et

al., 2017; Elosegui-Artola et al., 2016; Klank et al., 2017; Oria et al., 2017; Qu et al., 2018). Such models recently have been extended to fibrous matrices (Estabridis et al., 2018), and further adopting these models to incorporate matrix heterogeneity and cell translocation due to large-scale matrix stretch may provide additional insights into the observations described here. Besides the actomyosin cytoskeleton and focal adhesions, other cellular components that are mechanically contiguous along the matrix-cell-matrix unit **(Figure 4.6d)** may mediate force transmission and the dynamics underlying this phenomenon. For example, the nucleus is mechanically coupled to the ECM via linker of nucleoskeleton and cytoskeleton complexes, actomyosin stress fibers, and their termination at focal adhesions (Wang et al., 2009) **(Figure 4.6d)**. Although not explored here, perturbations to the nucleoskeleton or focal adhesion complexes may provide additional points of control over the force dynamics involved in SSM. Advances in single-cell isolation and RNA-sequencing techniques (Patel et al., 2014) could help identify the underlying signaling pathways responding to local ECM changes as cells actively deform the surrounding ECM during cell migration.

Cells encounter heterogeneity in ECM mechanical properties and architecture as they migrate through fibrillar interstitial tissues in vivo. How cells interpret sundry biophysical cues and adopt migration strategies to efficiently navigate through the ECM remains an ongoing effort. Recent advances in intravital imaging techniques have provided tremendous insight into visualizing cell migration in native tissue settings (Weigelin et al., 2012). However, challenges with cell and ECM labeling, image capture rates, and imaging depth may limit high spatiotemporal resolution visualization of highly dynamic cell-ECM interactions such as those described here. It has yet to be determined whether matrix deformations directly contribute to rapid motion of cells in vivo, although recent intravital studies describe buckling of collagen fibers by fibroblasts within

tumors (Perentes et al., 2009). Certainly, cell migration concurrent with deformation of fibrous ECM occurs developmentally as mesodermal cells migrate along pliable fibronectin fibrils from the blastopore to the animal pole (Nakatsuji and Johnson, 1984), in loose connective tissues, such as the stroma surrounding mammary glands during tumor cell escape (Provenzano et al., 2006), and upon early stages of wound healing as fibroblasts colonize provisional fibrin-rich ECM and exert contractile forces to close the wound gap (Davidson et al., 2008). During morphogenesis of the forming heart tube, large-scale tissue movements convect endocardial progenitors to their target destination (Aleksandrova et al., 2015; Kidokoro et al., 2018). In similar fashion, recent work patterning mesenchymal condensation demonstrated programmable movement of non-contractile epithelial and endothelial cells via fibroblastic compaction of the ECM (Hughes et al., 2017). In contrast to these observations, in our studies the same cells inducing local matrix deformations were translocated by subsequent matrix motion. Furthermore, considering heterotypic cell interactions, and given recent observations of mechanical forces underlying heterotypic cell interactions mediating tumor cell escape (Labernadie et al., 2017), it is possible that more contractile cell types could induce rapid migration of another cell type via deformations to the matrix. Future work examining mechanoreciprocal relationships between multiple cell types as well as the ECM using such biomimetic in vitro models will grow our understanding of cell migration and help inform future intravital imaging efforts.

In these studies, we modulated stiffness at the single-fiber and bulk matrix scales by tuning photocrosslinking of the polymer network within each matrix fiber. While bulk mechanical testing demonstrated orthogonal control over fiber alignment and bulk stiffness of these matrices, cells likely sense and respond to local matrix mechanics and ligand availability (Baker et al., 2015; Cao et al., 2017a), and in particular, anisotropic mechanical behavior intrinsic to matrix fibers

additionally influenced by fiber alignment at the population level. We performed TFM on 2D PAAm hydrogels to determine baseline contractility, but it is likely that cell-generated forces are highly dependent upon matrix topography and mechanics. Continued development of technologies such as magnetic bead rheology, TFM, and computational modeling will aid in our understanding of how cells reciprocally interpret the architecture and mechanics of fibrous matrices, exert traction forces, and in turn how these forces yield stresses within the ECM to engender reorganization and deformation. Such integrated approaches along with tunable biomimetic ECM models could aid in understanding and coordinating developmental migratory processes, designing biomaterials that rapidly recruit repair cells to wound sites, or identifying targeted therapeutics to arrest primary cancer cell egress through the surrounding tumor stroma.

4.6 Materials and Methods

4.6.1 Reagents

All reagents were purchased from Sigma-Aldrich and used as received, unless otherwise stated.

4.6.2 Synthesis of DexMA

Dextran (moleculat weight 86,000 Da, MP Biomedicals, Santa Ana, CA) was modified with methacrylate groups as in van Dijk-Wolthuis et al. (van Dijk-Wotthuis et al., 1995). In brief, dextran (30 g) and 4-dimethylaminopyridine (3 g) were dissolved in anhydrous dimethyl sulfoxide (DMSO; 150 mL) overnight. Next, glycidyl methacrylate (36.9 mL) was added under vigorous stirring, heated to 45 °C and allowed to react for 24 h. The solution was then cooled to 4 °C and precipitated into chilled (4 °C) 2-proponal (1 L). The crude product was recovered by centrifugation at a speed of 3000 × *g*, re-dissolved in milli-Q water and dialyzed against milli-Q

water for 3 days with two solvent exchanges daily. The solution was then lyophilized for 3 days to obtain the pure product, which was characterized by ^{1}H-nuclear magnetic resonance spectroscopy in D_2O. The degree of methacrylate functionalization was calculated as the ratio of the proton integral (6.174 and 5.713 ppm) and the anomeric proton of the glycopyranosyl ring (5.166 and 4.923 ppm). As the signal of the anomeric proton of α-1,3 linkages (5.166 ppm) partially overlaps with other protons, a pre-determined ratio of 4% α-1,3 linkages was assumed (van Dijk-Wotthuis et al., 1995) and the total anomeric proton integral was calculated solely based on the integral at 4.923 ppm. A methacrylate per dextran repeat unit ratio of 0.7 was determined.

4.6.3 DexMA fiber network fabrication

3D networks of suspended DexMA fibers were generated as in Baker et al. (Baker et al., 2015). In brief, DexMA was dissolved at 0.475 g mL^{-1} in a 1:1 mixture of milli-Q water and dimethylformamide with 0.005% Irgacure 2959 photoinitiator. This polymer solution was utilized for electrospinning within an environment-controlled glovebox held at 21 °C and 30–40% relative humidity. Electrospinning was performed at a flow rate of 0.5 mL h^{-1}, gap distance of 7 cm, and voltage of −4.3 kV, onto a collecting surface of oppositely charged (4.9 kV) parallel electrodes with varying separation distance to control alignment **(Figure 4.1b-c)**. Methacrylated rhodamine (0.5 mM; Polysciences, Inc., Warrington, PA) was incorporated into the electrospinning solution to fluorescently visualize DexMA fibers and fluorescent microspheres (stock diluted 1:20 in polymer solution; ThermoFisher Scientific, Waltham, MA) were added for matrix deformation studies. Fibers were collected on microfabricated PDMS (Sylgard 184, Dow-Corning, Midland, MI) arrays of wells to isolate cell-perceived mechanics of suspended fiber networks. In brief, silicon wafer masters possessing SU8 photoresist (Microchem, Westborough, MA) were produced

by standard photolithography and used to generate PDMS stamps. Following silanization with trichloro (1H,1H,2H,2H-perfluorooctyl)silane, stamps were used to emboss uncured PDMS onto oxygen plasma-treated coverslips. PDMS well arrays were then surface functionalized with 3-(trimethoxysilyl)propyl methacrylate (Gelest, Inc., Morrisville, PA) via vapor deposition in a vacuum oven (60 °C and 14.7 PSI) to facilitate DexMA fiber adhesion. After electrospinning over PDMS well substrates, suspended network samples were first primary crosslinked under UV light (100 mW cm^{-2}) to stabilize fibers. Samples were then hydrated in a photoinitiator solution of 1 mg mL^{-1} Irgacure 2959 in milli-Q water and exposed to a secondary crosslinking of varying durations of UV light (100 mW cm^{-2}) to control the degree of crosslinking and resulting stiffness **(Figure 4.1d)**. To promote cell adhesion, cyclo [RGDfK(C)] (cRGD, Peptides International, Louisville, KY) was coupled to methacrylates along the DexMA backbone via Michael-type addition chemistry.

4.6.4 Mechanical testing

To determine the Young's modulus of suspended fiber networks, microindentation with a rigid SU8 cylinder (1 mm diameter and 1 mm tall) was performed on a commercial Cell Scale Microsquisher (CellScale, Waterloo, Ontario). Cylinders of SU8 photoresist were microfabricated and affixed to pure tungsten filaments (0.156 mm diameter and 59.6 mm length). Fiber networks were generated over 2 mm diameter circular PDMS well substrates, crosslinked under the conditions described above, and indented to a depth of 150 μm at a strain rate of 0.05%/s to determine a Young's modulus. Young's modulus was approximated assuming an elastic membrane using the following equation:

$$F = \frac{Et\pi\delta^3(r_o^2 - r_i^2)}{2(r_o - r_i)^4(1-\nu)} \quad (1)$$

where t is the membrane thickness (determined by confocal microscopy for each sample, ranging from 20 to 40 μm), r_o is the membrane radius (1 mm), r_i is the indenter diameter (0.5 mm), and v is the Poisson ratio (0.5), F is the indentation force, δ is the indentation depth, and E is Young's modulus.

To determine Young's modulus of single fibers, three-point bending tests were performed using AFM as in (Baker et al., 2015). Single fibers were electrospun on 200 μm wide by 200 μm tall microfabricated PDMS troughs. Fibers were hydrated and crosslinked to varying degrees by UV light exposure as described above, and deformed by an AFM tip (0.06 N m^{-1}) loaded with a 25 μm diameter bead positioned centrally along the fiber's length. Young's modulus was calculated from the resulting load-displacement curves using known equations for a cylindrical rod undergoing three-point bending with fixed boundaries (Tan and Lim, 2016).

4.6.5 Cell culture and biological reagents

NIH3T3 fibroblasts (ATCC CRL-1658) were cultured in high-glucose Dulbeco's modified Eagle's medium (DMEM) containing 1% penicillin/streptomycin, L-glutamine, and 10% bovine serum (ThermoFisher Scientific, Waltham, MA). Cells were passaged upon achieving confluency at a 1:4 ratio and used for studies until passage 20. For all studies, cells were trypsinized, counted, and seeded onto substrates at a density of 1500 cells per cm^2. Human foreskin fibroblasts (a gift from Kenneth Yamada), human mesenchymal stem cells (Lonza PT-2501), C2C12 (ATCC CRL-1772), UM-SCC-74B (a gift from Thomas Carey), HT1080 (ATCC CCL-121), and MDA-MB-231 (ATCC HTB-26) cells were cultured in DMEM containing 1% penicillin/streptomycin, L-glutamine, and 10% fetal bovine serum (Atlanta Biologics, Flowery Branch, GA). Fluorescently labeled collagen hydrogels (Corning) were prepared as in Doyle et al. (Doyle et al., 2015). NIH3T3

fibroblasts were encapsulated at 250,000 cells per mL in a 1.0 mg mL^{-1} collagen hydrogel solution prepared as in Kuntz and Saltzman (Kuntz and Saltzman, 1997), and pipetted into glutaraldehyde-functionalized PDMS gaskets (6 mm diameter × 2 mm height) bonded to a 35-mm MatTek dish. Cells were imaged by confocal fluorescence time-lapse microscopy >200 μm away from glass or PDMS boundaries. For vinculin immunostaining, samples were simultaneously fixed and permeabilized in 2% paraformaldehyde in microtubule-stabilizing buffer for 15 min at room temperature to extract cytoplasmic vinculin. Samples were then blocked for 1 h in 10% fetal bovine serum, incubated for 1 h with primary mouse monoclonal anti-vinculin (1:500, Sigma-Aldrich V9264), and incubated for 1 h with secondary AlexaFluor 647 goat anti-mouse IgG (H + L) (1:1000, Life Technologies A12379) sequentially at room temperature. AlexaFluor 488 phalloidin (Life Technologies) and 4′,6-diamidino-2-phenylindole (Sigma-Aldrich D8417) were utilized to visualize F-actin and nucleus, respectively.

4.6.6 Microscopy and image analysis

Time-lapse microscopy was performed on an LSM800 laser scanning confocal microscope (Zeiss). Unless otherwise specified, migration experiments were imaged 6 h after cell seeding at 10 min frame intervals over 8 h. Immediately prior to imaging, cell nuclei were labeled with Hoechst33342 (3 μg mL^{-1}) for 10 min and rinsed once with media for 10 min. Following raw image export, cell nuclei were tracked with a custom Matlab script predicated on the IDL Particle Tracking code (Crocker and Grier, 1996). Briefly, parameters to threshold and locate the centroids of cell nuclei were identified and applied uniformly across the entire data set. Nuclei centroids in serial images were linked using IDL to define migration tracks.

Migration speed was calculated as total tracked distance over total tracked duration. Deviation was calculated as the minimum distance, for each time point, between the tracked position of a cell's nucleus and a line of best fit to the cell's overall track (determined by linear regression to model a perfectly non-deviating cell) and normalized to its total tracked duration using the following equation:

$$Deviation = \frac{\sum_1^n d_n}{n} \qquad (2)$$

where n is the number of tracked positions and d_n is the distance between a cell's tracked position and line of best fit. Cell track orientation was then calculated by the angle (−90 to +90) between the line of best fit and a reference line (direction of fiber alignment). SSM population was calculated as the percentage of all tracked cells that exhibit a slingshot event at some point during each cell's tracked migration. Values for SSM population were determined over a 6 h time course in all studies, with the one exception of the calyculin A studies (described below), which were performed over a 1 h time course. This is due to the observation that heightened contractility from dosing with 1 nM of calyculin A prevented cells from respreading following SSM events, and thus they were subsequently non-migratory for the remainder of the time-lapse. SSM duration was calculated as the percentage of time cells underwent SSM divided by the total tracked time. Recoil distances were measured from the centroid of the cell nucleus at the final frame prior to recoil, to the new position of the nuclear centroid immediately following recoil and translocation of the cell. Fluorescent microsphere tracks in deformation studies and kymographs were generated in FIJI. FibrilTool (Boudaoud et al., 2014) was utilized to quantify the coefficient of alignment of fibers within electrospun matrices.

4.6.7 Pharmacologic contractility perturbations

Blebbistatin, calyculin A, and Y27362 (Santa Cruz Biotechnology, Dallas, TX) were diluted to working stock concentrations and stored per the manufacturer protocol. Blebbistatin was utilized at 30 or 5 μM, calyculin A at 1.0 nM, and Y27362 at 25 μM; all pharmacologics were diluted in DMSO. For blebbistatin and Y27362 experiments, samples were treated with the respective dose for 1 h and imaged for 8 h at 10 min intervals. For calyculin A experiments, samples were treated for 30 min and imaged for 1 h at 10 min intervals. Beyond time points of 2 h post treatment, calyculin A induced a non-migratory, rounded cell morphology, consistent with cells plated on tissue culture plastic. Cells that exhibited a non-migratory, rounded cell morphology from calyculin A treatment were excluded from cell migration analysis.

4.6.8 Traction force microscopy

PAAm hydrogels (Young's modulus, $E = 7.9$ kPa) were prepared as in Aratyn-Schaus et al. (Aratyn-Schaus et al., 2010). Fluorescent microspheres (0.2 μm diameter; Thermofisher) were mixed into the PAAm solution at 1% v/v before polymerization. After polymerization, the PAAm surface was derivatized with sulfo-SANPAH (Proteochem, Hurricane, UT) and functionalized by 2–3 h incubation with type 1 rat tail collagen (50 μg mL^{-1}; Corning) diluted in phosphate-buffered saline (PBS). For all traction force experiments, cells were seeded at a density of 500 cells per cm^2 and allowed to adhere for 12 h before TFM was performed. Fluorescent images of 10–15 cells and embedded beads were captured at ×20 magnification. Images were taken at each cell position, and again after cells were lysed with 5% v/v sodium dodecyl sulfate in PBS. Data analysis was performed using an ImageJ plugin suite created by Tseng et al. (Tseng et al., 2012), which was adapted from Dembo and Wang (Dembo and Wang, 1999). This suite consists of stack alignment,

particle image velocimetry, and Fourier transform traction cytometry (FTTC). For FTTC, the Poisson's ratio of the PAAm gel was assumed to be 0.5 and a regularization parameter of 2×10^{-9} was used. The outputted traction force vector maps were analyzed using custom Matlab script to determine the peak traction generated by each cell. For contractility perturbation studies, blebbistatin (30 or 5 μM) and Y27362 (25 μM) were added 1 h prior to imaging, and calyculin A (1.0 nM) was added 2 h prior to imaging. For decreased ligand studies, 0.1 μg mL^{-1} collagen was utilized.

4.6.9 Lentivirus production

cDNA for pLenti CMV GFP Puro (658-5) was a gift from Eric Campeau and Paul Kaufman (Addgene plasmid #17448) (Campeau et al., 2009). Portions of paxillin-pEGFP (a gift from Rick Horwitz, Addgene plasmid # 15233) or mRuby-Paxillin-22 (a gift from Michael Davidson, Addgene plasmid #55877) were subcloned into a modified version of the pRRLSIN.cPPT.PGK-GFP.WPRE (a gift from Didier Trono, Addgene plasmid # 12252) by restriction enzyme cloning. pLenti.PGK.LifeAct-GFP.W was a gift from Rusty Lansford (Addgene plasmid # 51010). To generate lentivirus, plasmids were co-transfected with pCMV-VSVG (a gift from Bob Weinberg, Addgene plasmid #8454), pMDLg/pRRE, and pRSV-REV (gifts from Didier Trono, Addgene plasmid #12251 and #12253) (Dull et al., 1998; Stewart et al., 2003) in 293T cells using the calcium phosphate precipitation method (Kingston et al., 2004). Viral supernatants were collected after 48 h, concentrated with PEG-it™ (System Biosciences, Palo Alto, CA) following the manufacturer's protocol, filtered through a 0.45 μm filter (ThermoFisher Scientific Nalgene, Waltham, MA), and stored at −80 °C. Viral titer was determined by serial dilution and infection of NIH3T3s in the presence of 10 μg mL^{-1} polybrene (Santa Cruz Biotechnology, Dallas, TX). Titers

yielding maximal expression without cell death or detectable impact on cell proliferation or morphology were selected for studies.

4.6.10 Statistics

Statistical significance was determined by one- or two-way analysis of variance or two-sided Student's *t*-test where appropriate, with significance indicated by $p < 0.05$. Sample size is indicated within corresponding figure legends and all data are presented as mean ± s.d.

4.7 Supplementary figures

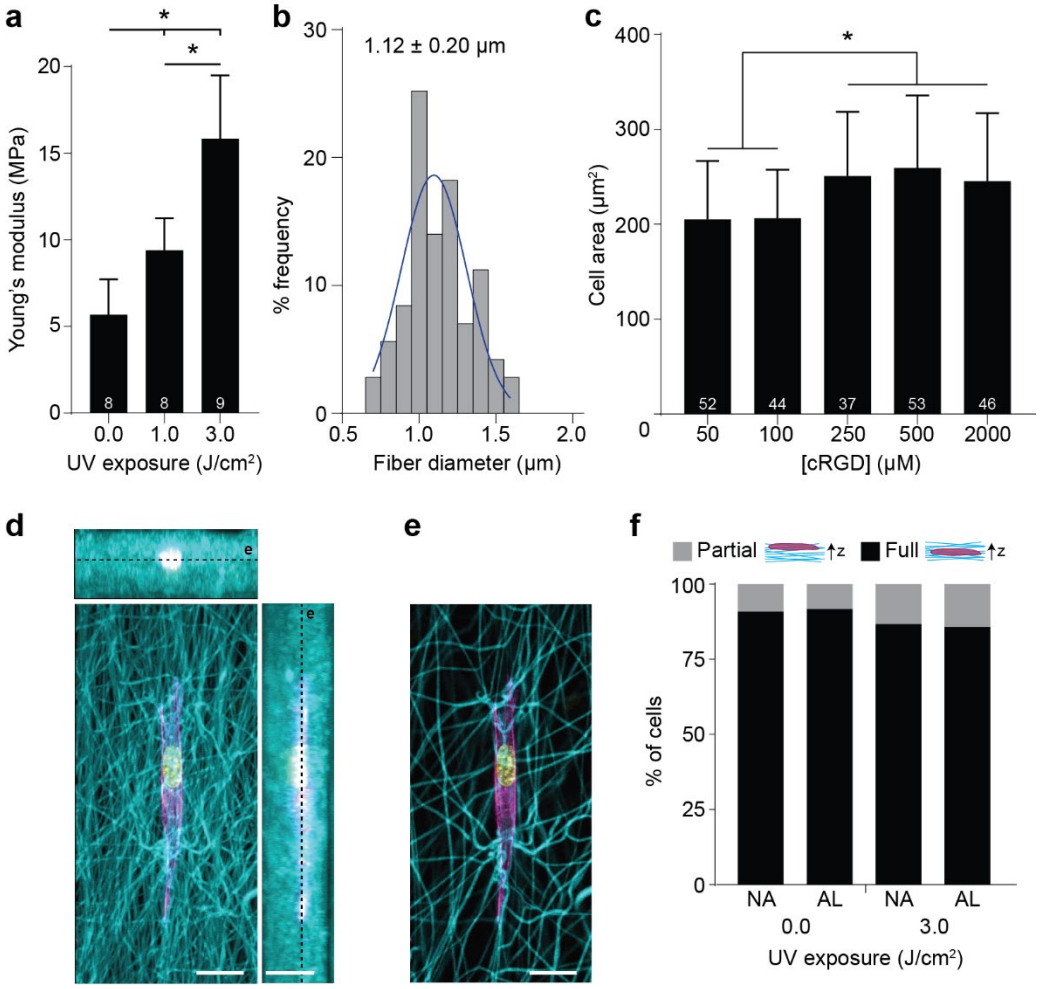

Supplementary Figure 4.1: Properties of DexMA fibrous matrices.
a) Young's modulus of individual fibers measured by AFM as a function of UV-initiated crosslinking. n=number of matrices analyzed per condition indicated within each bar. Data presented as mean ± s.d. **b)** Histogram of DexMA fiber diameter resulting from 47.5 wt% polymer solution (n=71 fibers). **c)** NIH3T3 spread area as a function of [cRGD]. 500 µM cRGD was utilized for all migration studies unless otherwise noted. n=number of cells analyzed per condition indicated within each bar. Data presented as mean ± s.d. **d-e)** Orthogonal x-y, x-z, and y-z maximum intensity projections (d) and single x-y plane (e) views of a composite confocal fluorescence image of representative NIH3T3 fibroblast within a suspended 3D fibrous matrix (rhodamine-labeled matrix fibers (cyan), F-actin (magenta), and nuclei (yellow); scale bars: 20 µm). **f)** Percentage of cells that are partially or fully embedded within suspended fiber matrices 6 hours post seeding (n=30 cells per condition). * indicates a statistically significant comparison with $p<0.05$ (one-way ANOVA).

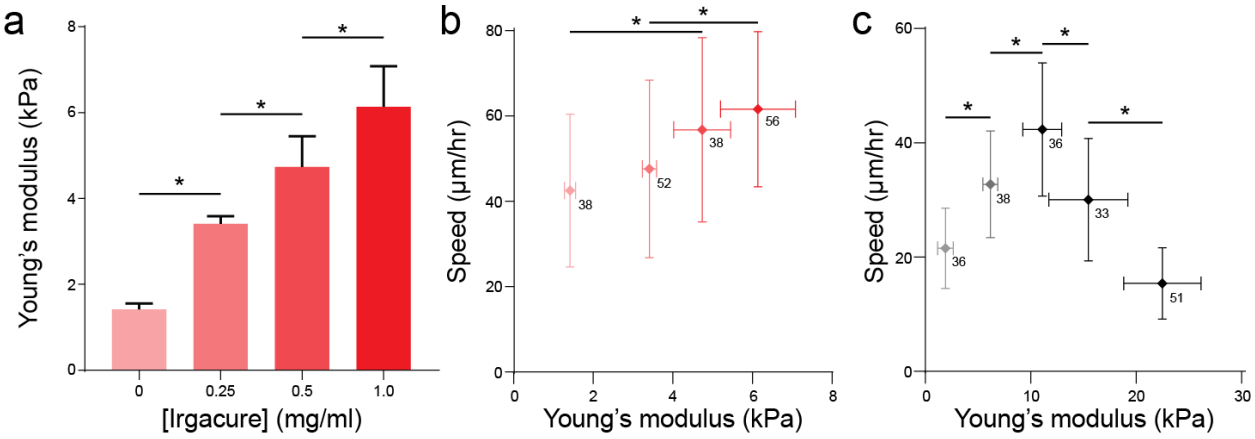

Supplementary Figure 4.2: Bulk mechanical properties influence cell migration speeds.
a) Bulk mechanical testing of aligned matrices as a function of Irgacure photoinitiator (I2959) concentration with a constant UV exposure of 1 J cm^{-2} (n=6 matrices per group). **b)** NIH3T3 fibroblast migration speed as a function of Young's modulus in aligned matrices tuned by I2959 concentrations (a). n=number of cells per group as indicated beside each data point. **c)** Human foreskin fibroblast migration speed as a function of Young's modulus in aligned matrices with a constant 1.0 mg ml^{-1} I2959, but varying durations of UV exposure (as in Figure 1d). n=number of cells per group as indicated beside each data point. All data presented as mean ± s.d. * indicates a statistically significant comparison with $p<0.05$ (one-way ANOVA).

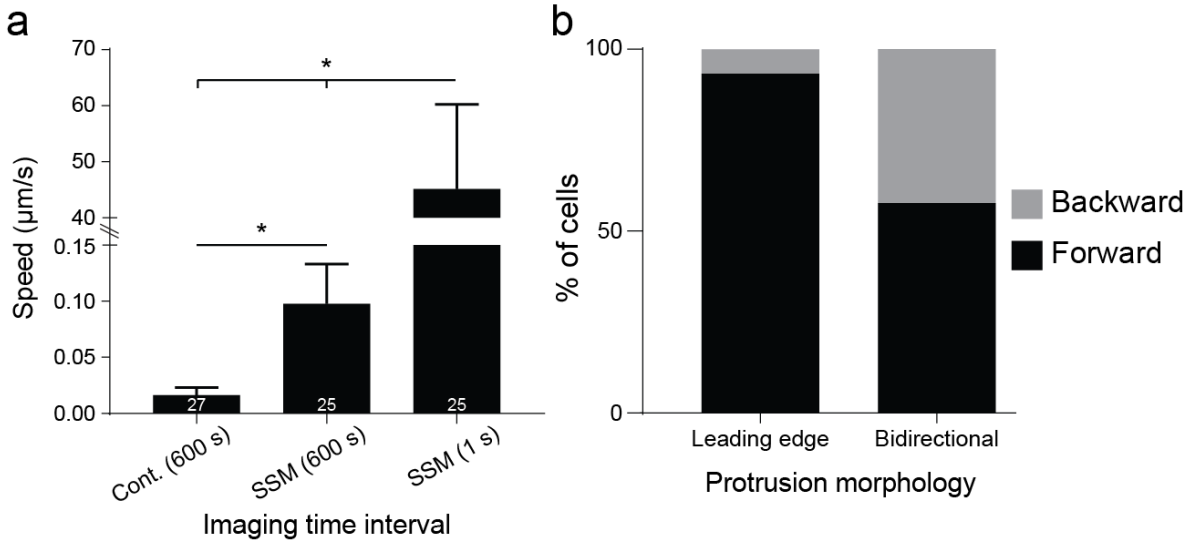

Supplementary Figure 4.3: Additional characteristics of slingshot migration.
a) Capturing matrix recoil events under transmitted light at 1 second frame intervals (SSM (1 s)) reveals more accurate matrix recoil speeds when compared to 10-minute frame intervals (SSM (600 s)). n=number of cells per group as indicated within each bar. Data presented as mean ± s.d. **b)** Percentage of cells employing SSM that recoil in the same direction (forward) or in the reverse direction (backward) with respect to its direction of continuous migration prior to SSM. Cells were parsed into two categories (leading edge and bidirectional) based on the morphology of cell protrusions during matrix stretch (n=30 cells per group). * indicates a statistically significant comparison with $p<0.05$ (one-way ANOVA).

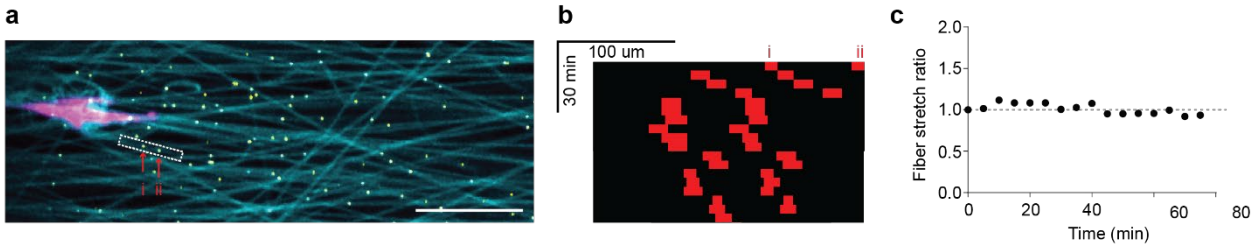

Supplementary Figure 4.4: Non-engaged fibers do not undergo stretch.
a) Composite confocal fluorescence image of an NIH3T3 in an intermediate stiffness matrix (matrix fibers (cyan), cytoplasm (magenta), and fiber-embedded beads (yellow); scale bar: 50 μm). **b)** Kymograph of a pair of microspheres embedded within the same fiber indicated by red arrows in (a) that is not directly engaged by the cell. **c)** Determination of fiber stretch ratio (relative to initial distance between fiducial markers) as a function of time.

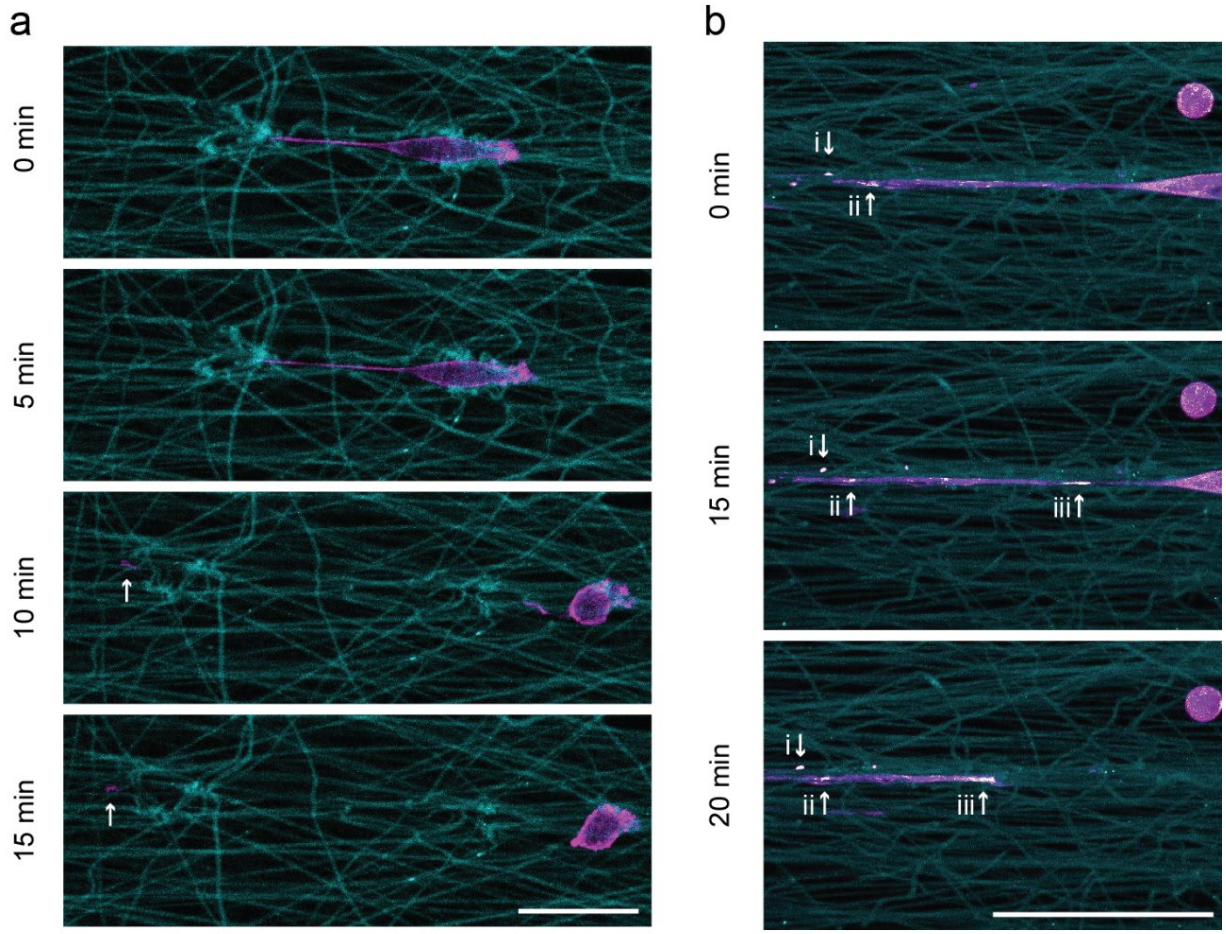

Supplementary Figure 4.5: Rupture of trailing edge concurrent with matrix recoil.
a) Select frames from confocal fluorescence time-lapse imaging shown in Supplemental Movie 5 of Lifeact-GFP expressing NIH3T3s within an aligned, intermediate stiffness matrix (matrix fibers (cyan), Lifeact-GFP (magenta); scale bar: 50 μm). Arrows indicate Lifeact-GFP puncta tethered to the matrix with matrix recoil. **b)** Select frames from confocal fluorescence time-lapse imaging

shown in Supplemental Movie 6 of Paxillin-GFP expressing NIH3T3s within an aligned, intermediate stiffness matrix (matrix fibers (cyan), cytoplasm (magenta), and paxillin (white), scale bar: 50 μm. Arrows highlight paxillin-rich puncta that remain tethered to the matrix within actin containing pieces of the cytoplasm that are separated from the cell upon matrix recoil. Roman numerals indicate paxillin-rich puncta associated across time frames.

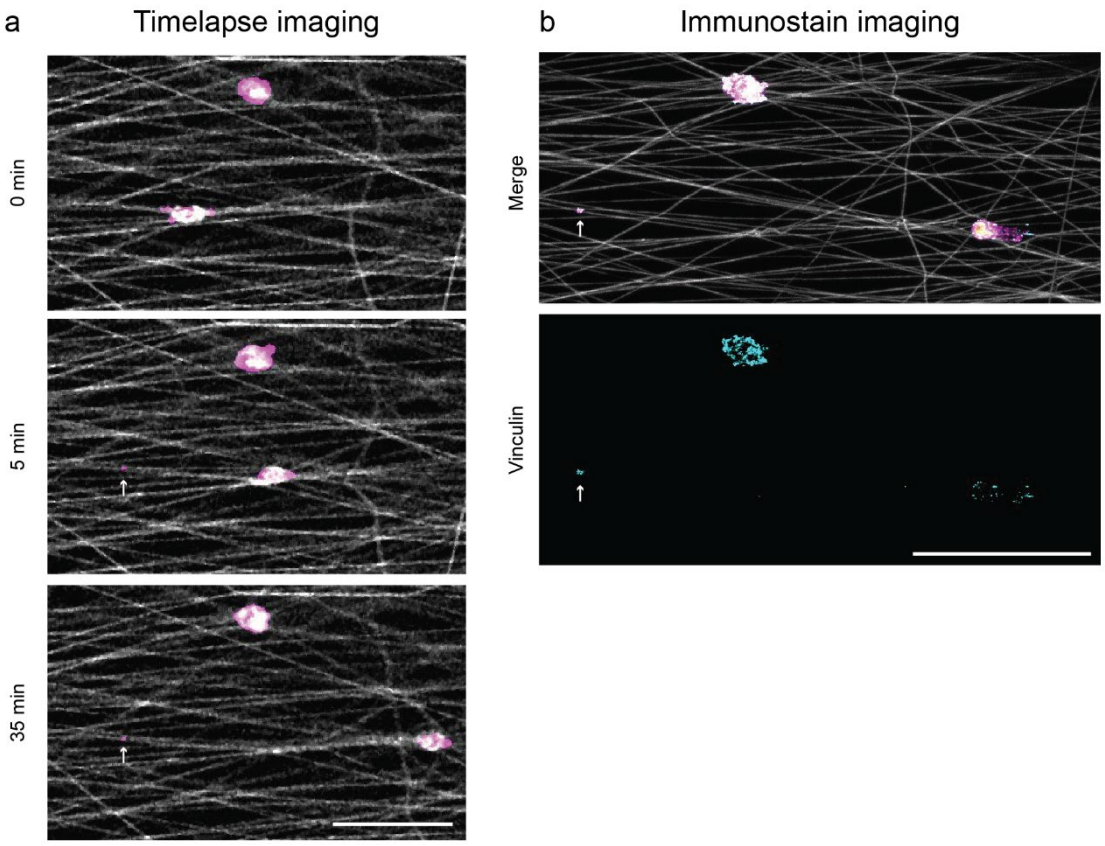

Supplementary Figure 4.6: Confirmation of vinculin within ruptured trailing edge plaques that contain paxillin.
a) Select frames from confocal fluorescence time-lapse imaging of NIH3T3-Lifeact-GFP cells within an aligned, intermediate stiffness matrix (matrix fibers (gray), Lifeact-GFP (magenta), and nuclei (yellow); scale bar: 50 μm). Matrix deformations are less visible due to low resolution imaging required for the sake of throughput. Arrow indicates Lifeact-GFP puncta tethered to matrix following matrix recoil. **b)** Confocal fluorescence images of identical location as in (a), subsequently immunostained for vinculin directly on the microscope stage (matrix fibers (gray), Lifeact-GFP (magenta), nuclei (yellow), and vinculin (cyan); scale bar: 50 μm).

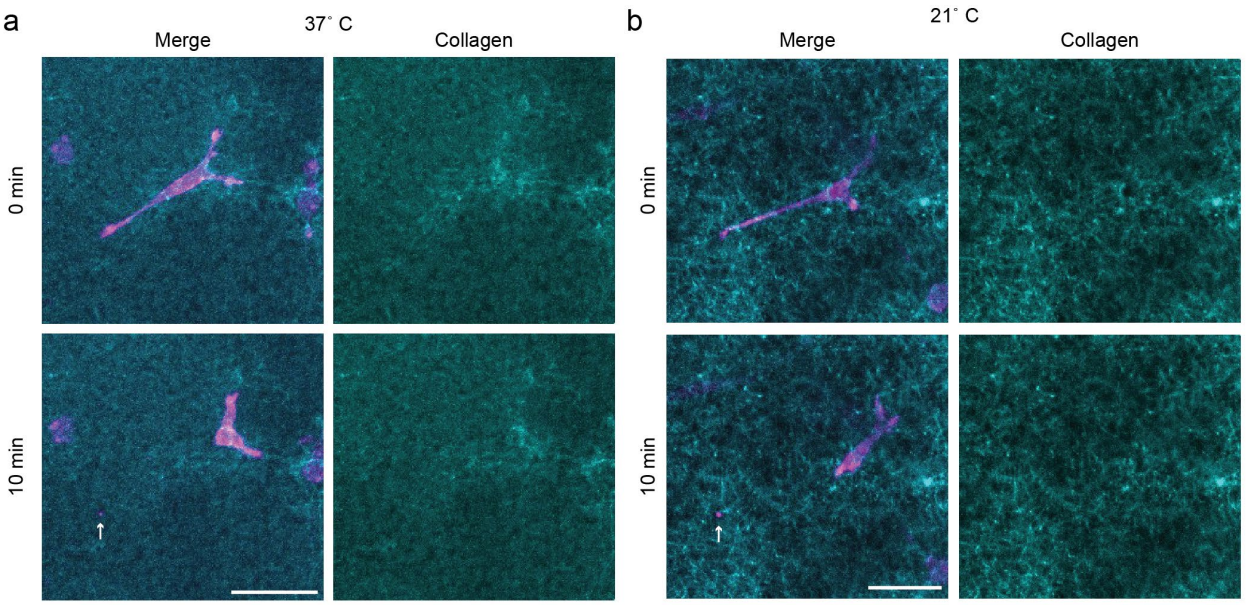

Supplementary Figure 4.7: Slingshot migration within 3D type I collagen hydrogels.
a-b) Select frames from confocal fluorescence time-lapse imaging **(Supplemental Movie 4.7)** of embedded NIH3T3-Lifeact-GFP cell migrating within Alexa555-succidinyl ester labeled 1.0 mg ml^{-1} collagen 3D hydrogels (collagen-Alexa555 (cyan), Lifeact-GFP (magenta); scale bars: 50 μm). Collagen gels were formed at 37° C (a) and 21° C (b). Arrows indicate Lifeact-GFP puncta left behind in the collagen following matrix recoil and slingshot migration.

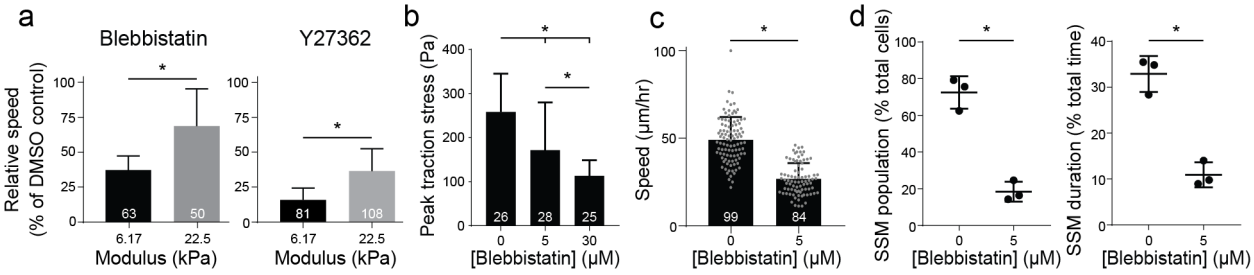

Supplementary Figure 4.8: Influence of contractility perturbations on slingshot migration.
a) Relative migration speed (normalized to DMSO control for each matrix stiffness) upon treatment with 30 μM blebbistatin or 25 μM Y27362 treatment. **b)** Peak traction stress of NIH3T3s as a function of blebbistatin concentration measured via traction force microscopy on 7.9 kPa PAAm hydrogels. **c-d)** Migration speed, SSM population (quantified over a 6-hour duration) and SSM duration of NIH3T3s treated with an intermediate blebbistatin dosage (5 μM) on aligned, intermediate stiffness matrices. n=3 fields of view; field of view=10 cells (d). All data presented as mean ± s.d. * indicates a statistically significant comparison with $p<0.05$ (a, c-d: two-sided student's t-test; b: one-way ANOVA). For (a-c), n=number of cells per group as indicated within each bar.

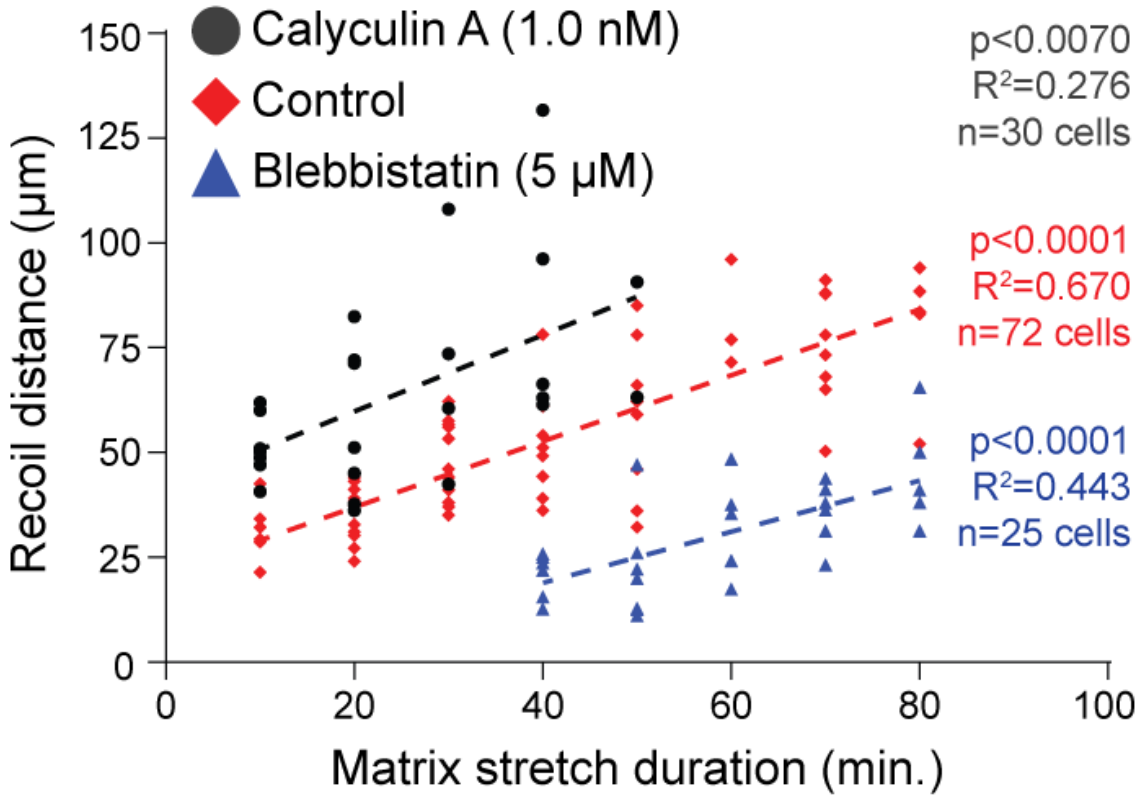

Supplementary Figure 4.9: Matrix stretch duration and recoil distance is dependent on intracellular contractility.
Recoil distance (net translocation of cell) as a function of duration spent stretching the matrix. Dashed lines indicate corresponding linear correlations with indicated R^2 and p-values (linear regression). n=number of cells per group indicated within the plot.

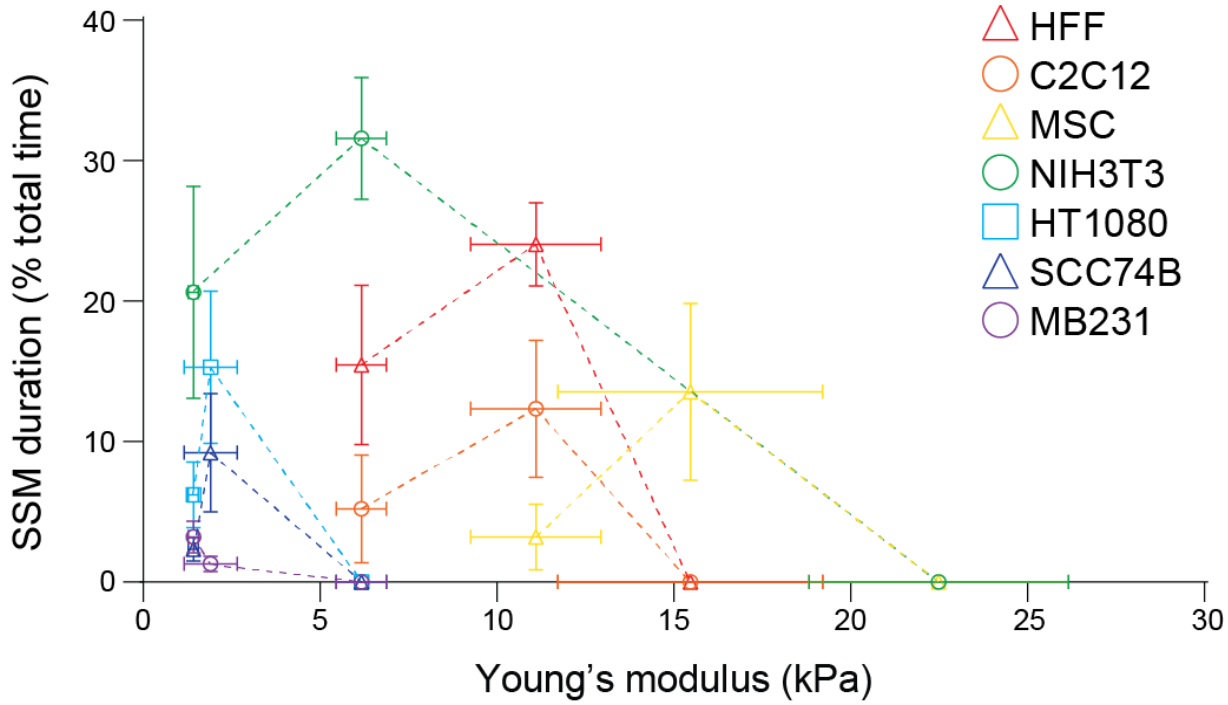

Supplementary Figure 4.10: Optimal stiffness for slingshot migration varies by cell type. Percentage of total imaging duration cells spent in some phase of matrix stretch and recoil (SSM duration) as a function of Young's modulus for a variety of cell types (n=3 fields of view per group; field of view=10 cells). Dashed lines connect data points for each cell type. Data presented as ± s.d.

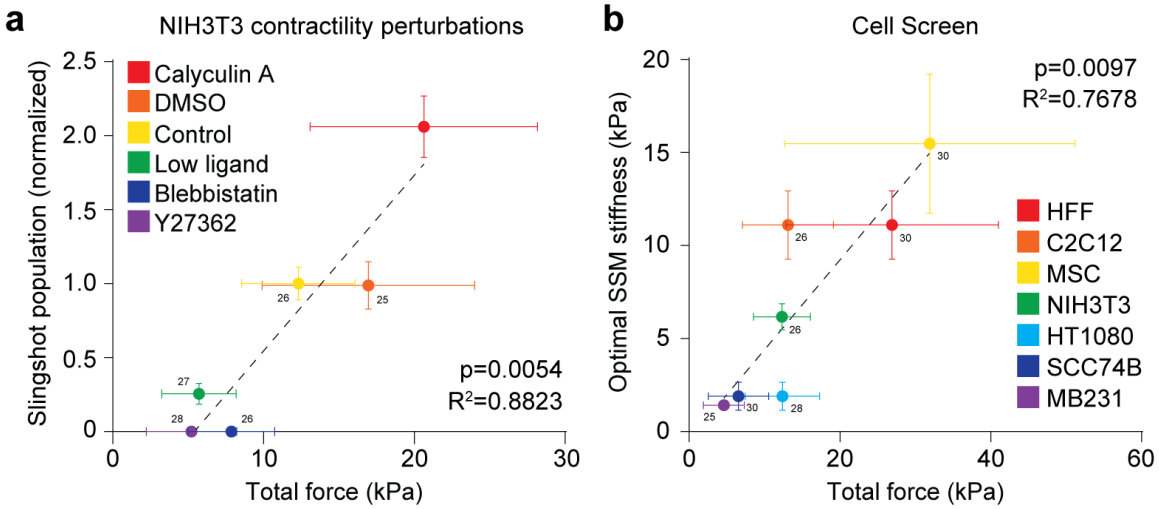

Supplementary Figure 4.11: SSM population and optimal SSM stiffness scales with total traction forces.
a) NIH3T3 slingshot population on aligned, intermediate stiffness matrices (normalized to DMSO control) positively correlates with total contractile force determined by traction force microscopy. Dashed line indicates linear correlation with indicated R^2 and p-value=0.0054 (linear regression). n=number of cells per group as indicated beside each data point. **b)** Matrix stiffness corresponding to optimal slingshot migration positively correlates with total contractile force for a variety of cell types. Dashed line indicates linear correlation with indicated R^2 and p-value=0.0097 (linear regression). n=number of cells per group as indicated beside each data point. All data presented as mean ± s.d.

Supplementary Movie 4.1: Representative confocal fluorescence time-lapse imaging (10x magnification) of NIH3T3 migration within aligned and non-aligned matrices of low, intermediate, and high stiffness (movies play successively and are labeled individually; matrix fibers (cyan), cytoplasm (magenta), nuclei (yellow); scale bar: 100 µm).
https://static-content.springer.com/esm/art%3A10.1038%2Fs41467-019-09121-0/MediaObjects/41467_2019_9121_MOESM4_ESM.avi

Supplementary Movie 4.2: Representative confocal fluorescence time-lapse imaging (32x magnification) of NIH3T3 migration within aligned matrices of low, intermediate, and high stiffness undergoing continuous migration and SSM within aligned matrices of intermediate stiffness (movies play successively and are labeled individually; matrix fibers (cyan), cytoplasm (magenta), nuclei (yellow); scale bar: 50 µm).
https://static-content.springer.com/esm/art%3A10.1038%2Fs41467-019-09121-0/MediaObjects/41467_2019_9121_MOESM5_ESM.avi

Supplementary Movie 4.3: High temporal resolution transmitted light time lapse imaging (5x magnification) of NIH3T3 migration undergoing matrix recoil within aligned matrix of intermediate stiffness (scale bar: 50 μm).
https://static-content.springer.com/esm/art%3A10.1038%2Fs41467-019-09121-0/MediaObjects/41467_2019_9121_MOESM6_ESM.avi

Supplementary Movie 4.4: Representative confocal fluorescence time-lapse imaging (32x magnification) of NIH3T3 matrix deformations during migration within aligned matrices of low, intermediate, and high stiffness matrices (movies play successively and are labeled individually; matrix fibers (cyan), cytoplasm (magenta), fiber-embedded fluorescent microspheres (yellow); scale bar: 50 μm).
https://static-content.springer.com/esm/art%3A10.1038%2Fs41467-019-09121-0/MediaObjects/41467_2019_9121_MOESM7_ESM.avi

Supplementary Movie 4.5: Representative confocal fluorescence time-lapse imaging (32x magnification) of NIH3T3- LA-GFP migration within aligned, intermediate stiffness matrices (matrix fibers (cyan) and LifeactGFP (magenta); scale bar: 50 μm). Track marked in yellow highlights Lifeact-GFP puncta separated from the cell's trailing edge that remains tethered to the recoiled matrix.
https://static-content.springer.com/esm/art%3A10.1038%2Fs41467-019-09121-0/MediaObjects/41467_2019_9121_MOESM8_ESM.avi

Supplementary Movie 4.6: Representative confocal fluorescence time-lapse imaging (32x magnification) of NIH3T3- Paxillin-GFP migration within aligned, intermediate stiffness matrices (matrix fibers (cyan), cytoplasm (magenta), and paxillin (white); scale bar: 50 μm). Marked track denotes paxillincontaining focal adhesion.
https://static-content.springer.com/esm/art%3A10.1038%2Fs41467-019-09121-0/MediaObjects/41467_2019_9121_MOESM9_ESM.avi

Supplementary Movie 4.7: Representative confocal fluorescence time-lapse imaging (10x magnification) of embedded NIH3T3-LA-GFP within fluorescently labelled 1.0 mg ml-1 type I collagen hydrogels crosslinked at 37° C and 21° C (collagen-Alexa555 (cyan), and Lifeact-GFP (magenta); scale bar: 50 μm). Arrows denote Lifeact-GFP puncta separated from cells within the collagen matrix.
https://static-content.springer.com/esm/art%3A10.1038%2Fs41467-019-09121-0/MediaObjects/41467_2019_9121_MOESM10_ESM.avi

Supplementary Movie 4.8: Representative transmitted light and fluorescence time-lapse imaging (10x magnification) of NIH3T3 migration within aligned, intermediate stiffness matrices treated with DMSO, 30μM blebbistatin, or 1.0 nM calyculin A. Note: transmitted light was utilized for blebbistatin studies to avoid photoinactivity by blue light. Scale bar: 100 μm.
https://static-content.springer.com/esm/art%3A10.1038%2Fs41467-019-09121-0/MediaObjects/41467_2019_9121_MOESM11_ESM.avi

Chapter 5: Functional Angiogenesis Requires Microenvironmental Cues Balancing Endothelial Cell Migration and Proliferation

5.1 Authors

William Y. Wang, Daphne Lin, Evan H. Jarman, William J. Polacheck, Brendon M. Baker

5.2 Abstract

Angiogenesis is a complex morphogenetic process that involves intimate interactions between multicellular endothelial structures and their extracellular milieu. *In vitro* models of angiogenesis can aid in reducing the complexity of the *in vivo* microenvironment and provide mechanistic insight into how soluble and physical extracellular matrix cues regulate this process. To investigate how microenvironmental cues regulate angiogenesis and the function of resulting microvasculature, we multiplexed an established angiogenesis-on-a-chip platform that affords higher throughput investigation of 3D endothelial cell sprouting emanating from a parent vessel through defined biochemical gradients and extracellular matrix. We found that two fundamental endothelial cell functions, migration and proliferation, dictate endothelial cell invasion as single cells *vs.* multicellular sprouts. Microenvironmental cues that elicit excessive migration speed incommensurate with proliferation resulted in microvasculature with poor barrier function and an inability to transport fluid across the microvascular bed. Restoring the balance between migration speed and proliferation rate rescued multicellular sprout invasion, providing a new framework for

the design of pro-angiogenic biomaterials that guide functional microvasculature formation for regenerative therapies.

5.3 Introduction

The microvascular network of arterioles, capillaries, and venules is a critical component of the circulatory system required for the function and maintenance of nearly every tissue in the human body. Once regarded simply as passive fluidic microstructures, it is now understood that the microvasculature (vessels <50 μm in diameter) dynamically alters its structure and function to service the changing metabolic demands of tissues (Aird, 2005; Huxley and Rumbaut, 2000). Rapid changes in microvessel diameter through vasoconstriction or vasodilation allow for temperature and blood pressure regulation (Johnson et al., 2014). In response to tissue injury, local microvasculature rapidly adjusts permeability, enabling immune cells to extravasate and fight infection; over longer timescales, the microvasculature expands to revascularize the healing tissue (Tonnesen et al., 2000). Angiogenesis, the formation of new microvasculature from an existing parent vessel, is the predominant method by which microvasculature extends and is critical to tissue healing and homeostasis (Fraisl et al., 2009). Indeed, dysregulated angiogenesis producing excessive or insufficient microvasculature is a hallmark of many diseases, and as such, microvascular morphology and function are clinical indicators of pathology (Carmeliet, 2005; Wimmer et al., 2019). During cancer progression for example, abnormal gradients of soluble pro-angiogenic factors recruit endothelial cells (ECs) from adjacent tissues to invade into the tumor stroma (Carmeliet and Jain, 2000). This rapid and excessive angiogenesis results in a high density of disorganized and highly permeable neovessels that facilitates tumor growth and provides metastatic access (Siemann, 2011). In contrast, insufficient angiogenesis impairs tissue regeneration for example in cardiac ischemia or diabetic foot ulcers (Martin et al., 2003). An

understanding of how the surrounding microenvironment appropriately guides the formation of functional microvasculature rather than excessive or insufficient angiogenesis in disease contexts would be critical to designing vascularized biomaterials for regenerative medicine and novel therapies to treat vasculopathies (Losordo and Dimmeler, 2004; Novosel et al., 2011; Wimmer et al., 2019).

Observations consistent across a wide range of *in vivo* and *in vitro* models of angiogenesis have established several key steps including (1) chemokine gradients promoting endothelial tip cell formation and directed invasion into the extracellular matrix (ECM), (2) collective migration of leading tip cells and ensuing stalk cells, (3) proliferation and lumenization of the invading strand, and (4) maturation into functional neovasculature (Francavilla et al., 2009; Potente et al., 2011). Each of these steps is regulated by both biochemical and physical microenvironmental cues presented by the surrounding ECM, the 3D fibrous, collagenous meshwork through which EC sprouts navigate (Crosby and Zoldan, 2019). As characterizing and tuning microenvironmental cues (*e.g.* profiling biochemical gradients and controlling physical ECM properties) is challenging *in vivo*, *in vitro* models have proven instrumental in providing mechanistic insight into each step of angiogenesis (Nowak-Sliwinska et al., 2018). To build our understanding of how ECs migrate collectively, 2D scratch wound assays are widely utilized. While these assays have provided detailed insight into the molecular pathways governing collective migration of EC monolayers (Hayer et al., 2016), the model fails to recapitulate the 3D nature of sprouting morphogenesis (Baker and Chen, 2012). EC outgrowth assays from spheroids or microbead carriers embedded within 3D ECM have been instrumental in studying the role of matrix proteolysis and tip *vs.* stalk cell identity and dynamics (Bordeleau et al., 2017; Gerhardt et al., 2003; Ghajar et al., 2006; Jakobsson et al., 2010; Juliar et al., 2018). However, sprouts in these

models do not originate from an accessible lumenized parent vessel, making it difficult to assess key microvascular functions such as fluidic connectivity and permeability. More recently, advances in biomicrofluidics and efforts to engineer tissues-on-chips have generated 3D human engineered microvessels (Akbari et al., 2017; Chen et al., 2017; Polacheck et al., 2017); these models have been utilized to study how chemokine gradients, ECM degradability, shear stress and support cells regulate vessel barrier function, EC sprouting and tumor and immune cell extravasation (Alimperti et al., 2017; Chen et al., 2017; Nguyen et al., 2019; Polacheck et al., 2017; Trappmann et al., 2017). While much information has been learned from these various models, how EC migration speed and proliferation – two fundamental cell processes required for angiogenesis – influence the formation and function of subsequent microvasculature remains unresolved.

In this work, we multiplexed a microfluidic device that recapitulates key aspects of sprouting morphogenesis, namely the directional, chemokine-driven invasion of ECs from the stable and quiescent endothelium of a fluid-bearing arteriole-scale parent vessel into the surrounding 3D ECM. We used this biomimetic model to investigate how soluble and physical ECM properties regulates EC invasion speed and proliferation during sprouting and how independently tuning the rate of these two basic cell functions influences the quality of formed microvasculature. We find that the formation of functional microvasculature capable of transporting fluid and performing barrier function requires a delicate balance between EC migration speed and proliferation rate. Furthermore, we demonstrate that aberrant angiogenic sprouting driven by altered physical and soluble microenvironmental cues can in fact be rescued by correcting the imbalance between these two fundamental EC functions. As the proper vascularization of large tissue engineered constructs remains an outstanding challenge for the

biomedical engineering community, the findings of this work establish a new framework for biomaterial design parameters that balance EC migration speed and proliferation to optimally generate functional microvasculature.

5.4 Results

5.4.1 Multiplexed angiogenesis-on-a-chip platform

To investigate how soluble and physical microenvironmental cues regulate angiogenic sprouting, we adapted a previously established microfluidic device that recapitulates 3D EC sprouting morphogenesis from the stable, quiescent endothelium of a parent vessel (Nguyen et al., 2013; Trappmann et al., 2017). The parent vessels modeled in this work possess a diameter that lies near the upper end of values previously described for arterioles, but lack additional support cells such as vascular smooth muscle cells and pericytes (Kinstlinger and Miller, 2016; Traore and George, 2017). We improved the fabrication throughput of these devices by reducing their assembly to a single layer design in addition to multiplexing the number of devices resulting from each fabrication such that a single chip contains a 2 × 4 array of devices **(Figure 5.1a)**. To generate parent vessels in these devices, a hydrogel precursor solution is first injected through device ports and is allowed to crosslink around two parallel needles (300 μm diameter) suspended across each device's central chamber **(Figure 5.1a-b)**. The void space created after needle extraction forms a pair of parallel hollow channels fully embedded within extracellular matrix (ECM) terminating in two media reservoirs **(Figure 5.1b)**. ECs seeded into one channel of each device attach to the inner channel surface and self-assemble into a perfused endothelialized tube serving as the parent vessel (300 μm diameter, 3 mm length) **(Figure 5.1c-e)**. Within 24 hours, the assembled EC monolayer of the engineered parent vessel localizes VE-cadherin to cell–cell junctions and maintains a

consistent diameter and cell density over a range of collagen densities **(Figure 5.1d and Supplemental Figure 5.1a-d)**.

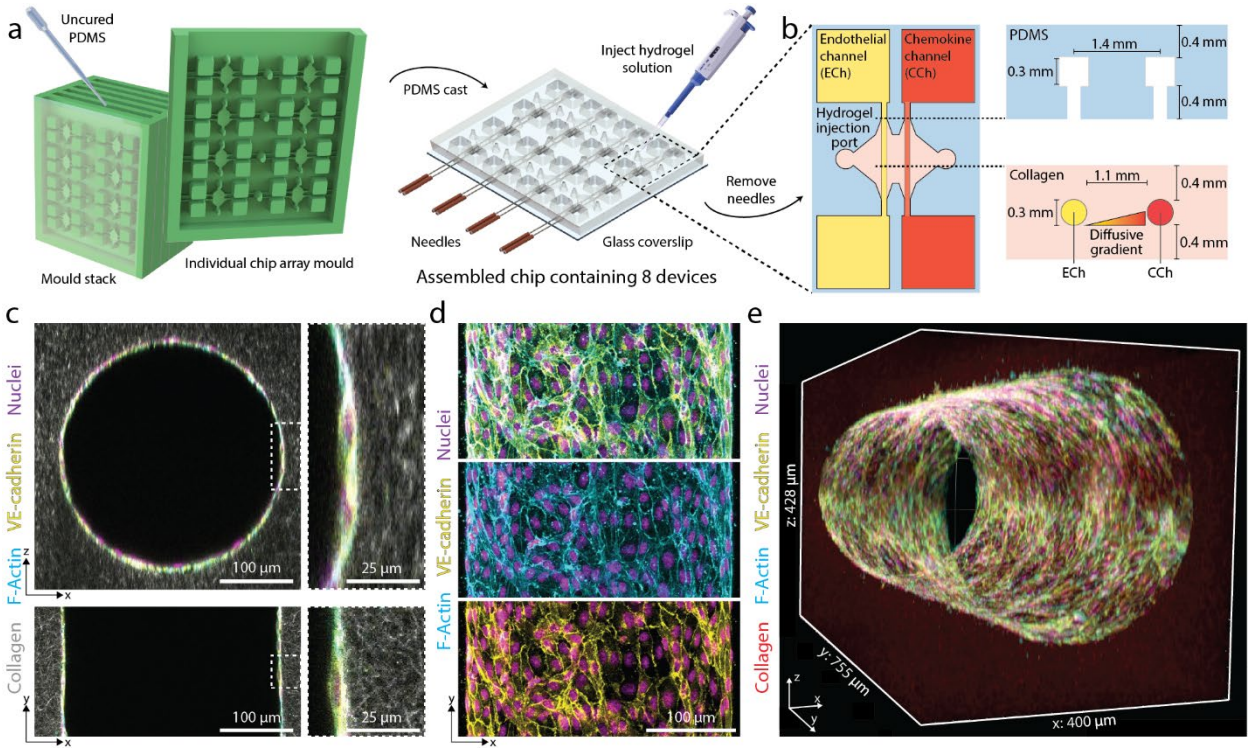

Figure 5.1: Multiplexed angiogenesis-on-a-chip platform.
a) PDMS replica casts from 3D-printed moulds are bonded to glass coverslips. Each chip is composed of a 2 × 4 array of single devices. A pair of needles are inserted into each device, and type I collagen solution is injected into each device and gelled around needles. Hollow channels are generated upon needle removal. **b)** Inserted needles are suspended above the glass coverslip bottom and below the PDMS housing to form 3D channels fully embedded within a collagen hydrogel. Each device is composed of two parallel channels. The endothelial channel (ECh) is seeded with endothelial cells to form the parent vessel. Pro-angiogenic factors are added to the chemokine channel (CCh) and form a diffusive gradient to promote 3D endothelial cell invasion across the collagen hydrogel. **c)** Representative images of *x–z* (top) and *x–y* (bottom) orthogonal views of parent vessels formed within fluorescently labeled 3 mg ml^{-1} collagen hydrogel 24 hours post-seeding. Insets indicated with dashed white lines. **d)** Representative images of *x–y* (max intensity projection) formed within a 3 mg ml^{-1} collagen hydrogel 24 hours post-seeding. Merge (top), F-actin (middle), VE-cadherin (bottom). **e)** 3D rendering of parent vessel formed within fluorescently labeled 3 mg ml^{-1} collagen hydrogel.

5.4.2 Soluble factors regulate multicellular sprouting

Utilizing 3 mg ml^{-1} collagen, parent vessels cultured in EGM2 proved stable as single ECs minimally invaded (5.5 ± 14.9 μm) into the ECM over 5 day culture under continual reciprocating flow **(Figure 5.2a, c)**. To induce EC invasion, we introduced an established EC chemoattractant, sphingosine 1-phosphate (S1P), to the adjacent chemokine channel to produce a diffusive gradient that drives directional 3D EC invasion through the ECM (Nguyen et al., 2013; Paik et al., 2001; Trappmann et al., 2017). We found EC invasion depth over 5 day culture to be dependent on [S1P], with increasing [S1P] resulting in increased invasion speed **(Figure 5.2a, c)**. To assess the morphologic quality of EC invasion, we categorized ECs as isolated single cells or multicellular sprouts and determined the ratio of sprouts to single cells as a metric of invasion multicellularity. Due to variations in invasion depth across conditions, we restricted quantification of single cells to 150 μm from the leading invasive front and defined sprouts as contiguous multicellular structures with a length greater than half the max invasion depth **(Supplementary Figure 5.2)**. Although [S1P] clearly mediated cell invasion in a dose-dependent manner, the phenotype of invading ECs was primarily as single, disconnected cells and multicellular sprouts were rarely observed **(Figure 5.2a, c, e-g)**. Due to the low levels of EC proliferation observed in these conditions **(Figure 5.2d)** and given previous evidence that EC proliferation is required for angiogenesis *in vivo* (Ausprunk and Folkman, 1977; Pontes-Quero et al., 2019), we hypothesized that enhancing proliferation rates would increase the number of ECs collectively invading as multicellular sprouts. Media supplementation with 25 ng ml^{-1} phorbol 12-myristate 13-acetate (PMA), another well-established pro-angiogenic factor and potent activator of PKC (Cross et al., 2010; Nguyen et al., 2013; Osaki et al., 2015; Trappmann et al., 2017), resulted in elevated proliferation rates as assayed by EdU incorporation **(Figure 5.2d)**. Few invading ECs were

observed at 0 nM S1P with 25 ng ml^{-1} PMA implying that the addition of PMA alone does not induce EC invasion **(Figure 5.2b-c)**. Invasion speed remained S1P dose-dependent in the presence of 25 ng ml^{-1} PMA while proliferation rates proved independent of S1P dose **(Figure 5.2b-d)**. In support of our hypothesis, PMA supplementation and elevated EC proliferation corresponded to significant increases in the number of invading multicellular sprouts at each level of [S1P] **(Figure 5.2d-g, Supplemental Figure 5.3, Supplemental Movie 5.1, Supplemental Movie 5.2, and Supplemental Movie 5.3)**. In conditions with 25 ng ml^{-1} PMA, sprout invasion depth over 5 day culture anti-correlated with the ratio of multicellular sprouts to single ECs **(Figure 5.2c, g)**; the highest level of S1P (500 nM) resulting in the fastest invasion speed, most single cells, and fewest multicellular sprouts **(Figure 5.2c, e, f)**. These data clearly indicate proliferation in this model is a requirement for multicellular sprout invasion, supporting previous observations *in vivo* (Ausprunk and Folkman, 1977; Pontes-Quero et al., 2019). Furthermore, while a chemokine gradient is an additional key requirement for angiogenesis, stronger gradients that increase invasion speed elicit a single cell migration phenotype in lieu of multicellular sprouts.

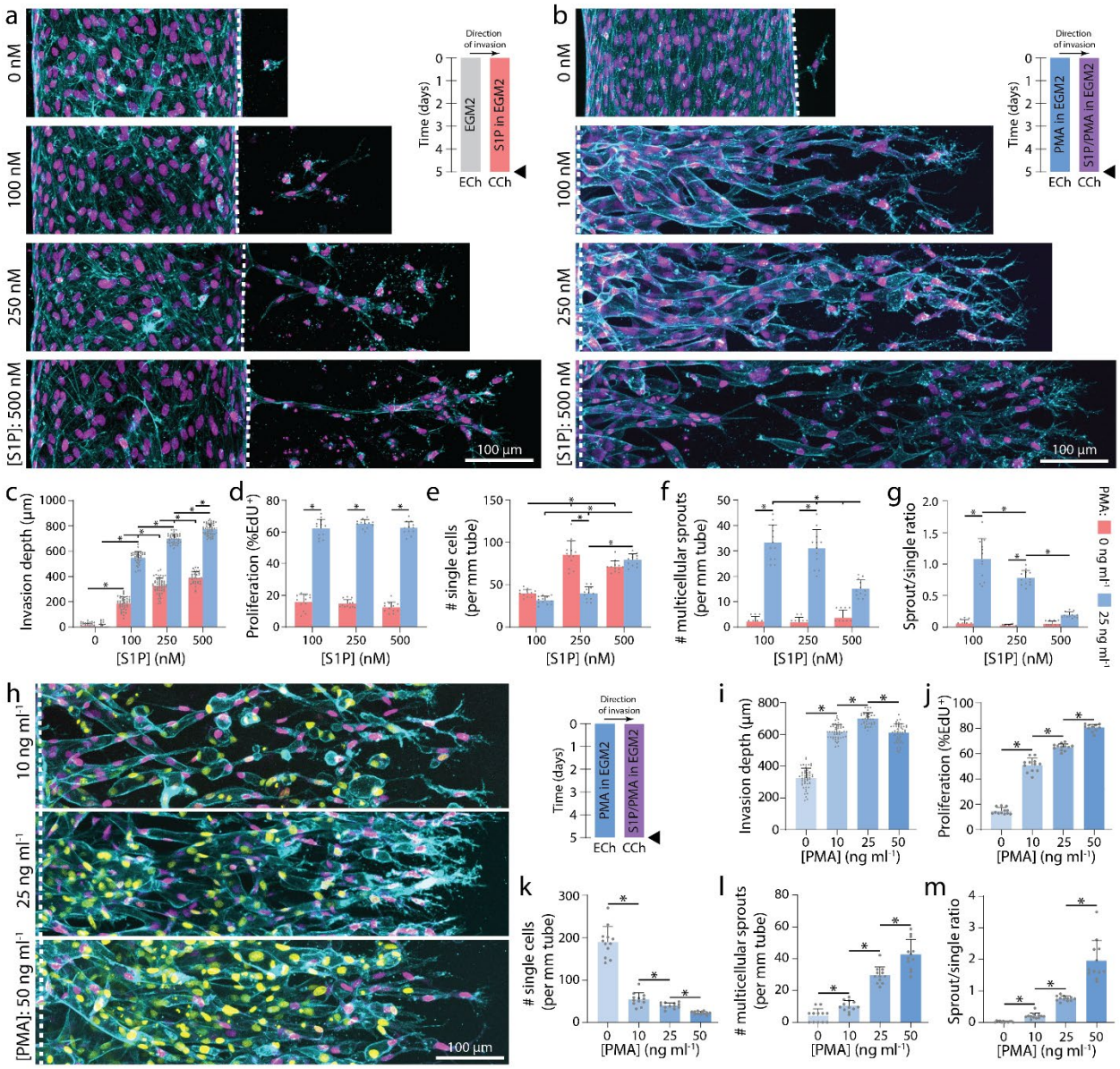

Figure 5.2: Soluble factors modulate EC invasion, proliferation, and multicellular sprouting. **a)** Representative images (max intensity projection) of invading endothelial cells in response to varying [S1P]. **b)** Representative images (max intensity projection) of invading endothelial cells in response to varying [S1P] with 25 ng ml^{-1} PMA. F-actin (cyan), nucleus (magenta), and dashed white lines indicate parent vessel edge (a and b). **c–g)** Quantifications of invasion depth, proliferation, and morphology of invading endothelial cells as single cells or multicellular sprouts. **h)** Representative images (max intensity projection) of invading endothelial cells in response to varying [PMA] with 250 nM S1P. **i–m)** Quantifications of invasion depth, proliferation, and morphology of invading endothelial cells as single cells or multicellular sprouts. UEA (cyan), nucleus (magenta), EdU (yellow). All data presented as mean ± s.d.; * indicates a statistically significant comparison with $P < 0.05$ (one-way analysis of variance). For invasion depth analysis (c and i), $n \geq 32$ vessel segments (each 100 µm length) per condition; for proliferation and migration mode analysis (d–g, j–m), $n = 12$ vessel segments (each 800 µm length) per condition

from $n = 2$ devices/condition (technical replicates) over $n \geq 4$ independent studies (biological replicates).

To investigate the effects of proliferation rates on multicellular angiogenic sprouting, we next varied [PMA] while maintaining [S1P] constant at 250 nM. Proliferation rates proved PMA dose-dependent and positively correlated with the number of multicellular sprouts **(Figure 5.2h, j-m, Supplemental Figure 5.3, Supplemental Movie 5.4 and Supplemental Movie 5.5)**. Although PMA alone did not induce EC invasion **(Figure 5.2b-c)**, increasing [PMA] in the presence of S1P resulted in a biphasic relationship with invasion depth **(Figure 5.2i)**. The influence of increasing [PMA] from 0 to 25 ng ml^{-1} on increased invasion depth may be due to a greater number of invading cells, each of which secretes matrix metalloproteinases (MMPs). Elevated MMP levels would hasten localized matrix degradation, allowing ECs to more rapidly generate open space within 3D ECM required to advance forward. Interestingly, at the highest tested concentration of PMA resulting in the most proliferation, invasion depth decreased **(Figure 5.2i)**. As cells are transiently non-migratory during mitosis, this decrease may stem from frequent proliferative events hampering efficient migration of ECs. Varying [PMA] and thus PKC activation may have multiple downstream effects, so we treated ECs with mitomycin C (a crosslinker that prevents DNA replication and inhibits mitosis) to confirm the role of proliferation as the primary effector of enhancing multicellular sprout invasion. Even in the presence of the highest level of PMA, proliferation-inhibited ECs invaded only as single cells with significantly decreased invasion depth as compared to controls **(Supplemental Figure 5.4a-f)**. These studies therefore indicate cell proliferation is not only required for multicellular sprout invasion, but additionally influences the rate at which sprouts traverse 3D ECM.

In the experiments above individually modulating migration speed and proliferation, higher migration speeds resulted in disconnected single EC invasion while increasing proliferation rates enhanced multicellular sprouting. We thus hypothesized that proliferation rate commensurate with invasion speed is essential to the collective invasion of multicellular sprouts. Indeed, proportionally increasing or decreasing both [S1P] and [PMA] simultaneously resulted in invasion depth and proliferation rate increases or decreases, respectively, but did not alter the ratio of multicellular sprouts to single ECs **(Figure 5.3a-g)**. This suggests that multicellular angiogenic sprouting requires a critical balance between EC invasion speeds and proliferation rates, which can be finely tuned by these two established soluble pro-angiogenic factors. While balanced soluble conditions maintained similar invasion multicellularity, the magnitude of these cues influenced sprout diameter, with higher levels of S1P and PMA increasing sprout diameter **(Figure 5.3a, b, h)**. Larger neovessel diameters would allow for increased fluid transport, but smaller diameter vessels would allow for increased capillary density and more efficient nutrient-waste exchange. Although this requires further exploration, including investigation of the influence of vascular smooth muscle cells and pericytes that support microvasculature *in vivo* (Grainger et al., 2013; Kosyakova et al., 2020), here we demonstrate that tuning concentrations of soluble factors regulates EC sprout diameters within the diameter range of microvasculature (<50 μm) (Aird, 2005; Kinstlinger and Miller, 2016; Traore and George, 2017).

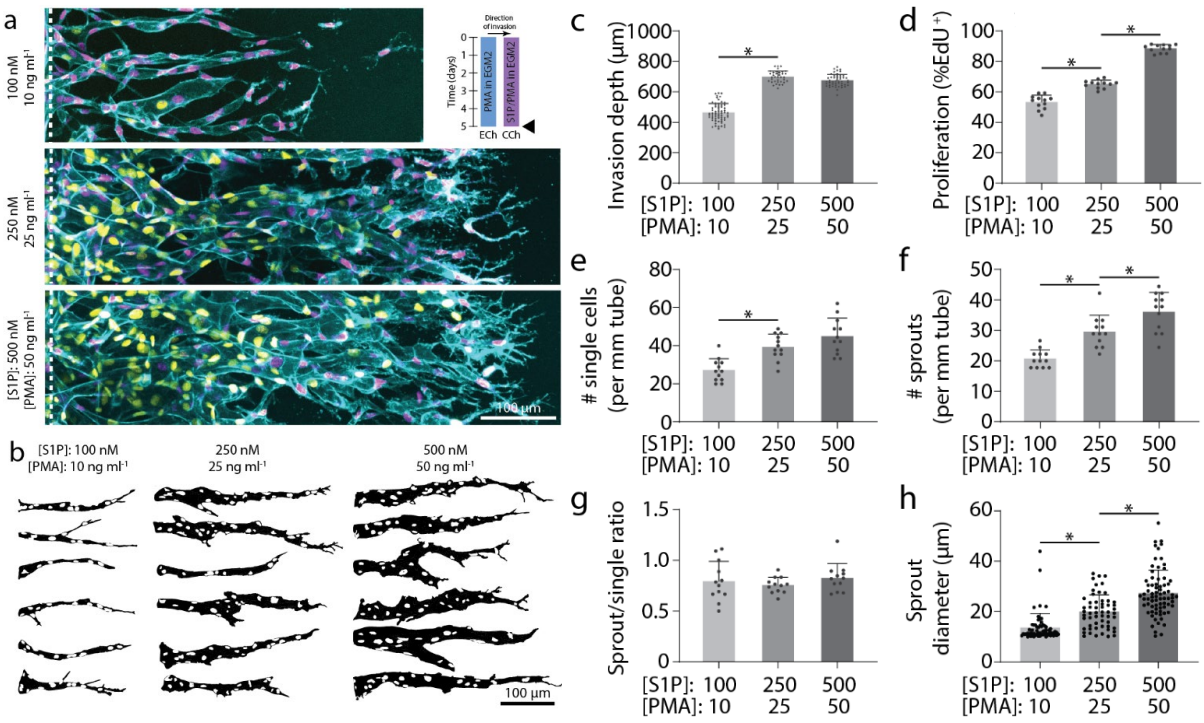

Figure 5.3: Multicellular sprouting requires balanced migration and proliferation.
a) Representative images (max intensity projection) of invading endothelial cells in response to proportional variations of [S1P] and [PMA]. UEA (cyan), nucleus (magenta), EdU (yellow). **b)** Representative sprout outlines from conditions in (a). **c–h)** Quantifications of invasion depth, proliferation, morphology of invading endothelial cells as single cells or multicellular sprouts, and sprout diameter. All data presented as mean ± s.d.; * indicates a statistically significant comparison with $P < 0.05$ (one-way analysis of variance). For invasion depth analysis (c), $n \geq 36$ vessel segments (each 100 µm length) per condition. For proliferation and migration mode analysis (d–g), $n = 12$ vessel segments (each 800 µm length) per condition from $n = 2$ devices/condition (technical replicates) over $n \geq 4$ independent studies (biological replicates). For sprout diameter analysis (h), $n \geq 56$ sprout segments.

5.4.3 Differential roles of tip and stalk endothelial cells

Previous work indicates that tip cells responsive to angiogenic chemokine gradients lead invading sprouts by degrading the ECM and guiding ensuing stalk cells (Francavilla et al., 2009; Potente et al., 2011). To investigate whether tip cells require chemokine receptors, we performed mosaic sprouting studies where untreated ECs were mixed with GFP-labeled ECs pre-treated with FTY720 (FTY720-GFP-ECs), an S1P receptor inhibitor. Preliminary studies confirmed the inhibitory effect of FTY720, as ECs pre-treated with 100 nM FTY720 prior to device seeding

demonstrated minimal invasion over 5 day culture despite appropriate soluble conditions of 250 nM S1P and 25 ng ml^{-1} PMA (S250 : P25) **(Supplemental Figure 5.5a-b)**. Furthermore, when ECs were allowed to sprout for 3 days prior to FTY720 treatment, subsequent S1P receptor inhibition halted any further advance of already established sprouts **(Supplemental Figure 5.5a-b)**. Performing mosaic studies with controlled ratios of FTY720-GFP-ECs *vs.* untreated ECs, a higher fraction of FTY720-GFP-ECs decreased invasion depth, the number of single ECs, and thereby enhanced sprout multicellularity as evident by increased sprout–single cell ratios **(Figure 5.4a, e-i)**. Furthermore, FTY720-GFP-ECs primarily remained in the parent vessel and did not assume the tip cell position of invading sprouts. FTY720-GFP-ECs were occasionally found within sprout stalks, suggesting that pushing or pulling forces from adjacent stalk cells may enable the movement of FTY-GFP-ECs lacking functional S1P receptors.

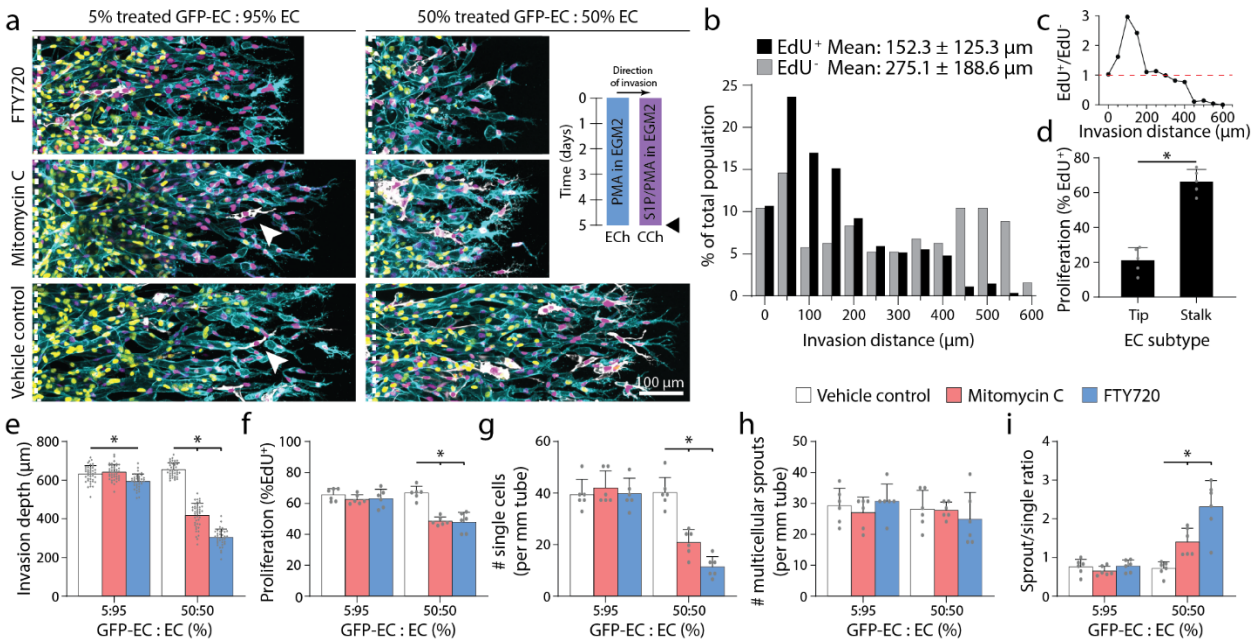

Figure 5.4: Invading tip cells require chemokine receptors but do not require proliferative capacity.

a) Representative images (max intensity projection) of invading endothelial cells with S250 : P25 and varying ratios of treated GFP-EC to untreated EC with indicated treatment. UEA (cyan), nucleus (magenta), EdU (yellow), GFP-EC (white). **b)** Histogram of EdU^+ and EdU^- invaded endothelial cells with S250–P25 after 5 day culture. **c)** Ratio of EdU^+ to EdU^- endothelial cells from (b). **d)** Percentage of EdU^+ tip or stalk cells from (b). **e–i)** Quantifications of invasion depth, proliferation, and morphology of invading endothelial cells as single cells or multicellular sprouts. All data presented as mean ± s.d.; * indicates a statistically significant comparison with $P < 0.05$ (two-tailed Student's *t*-test (d) and one-way analysis of variance (e–i)). For spatial EdU analysis (b and c), $n \geq 192$ cells. For tip *vs.* stalk proliferation analysis (d), $n = 5$ vessel segments (each 800 µm length). For invasion depth analysis (e), $n \geq 37$ vessel segments (each 100 µm length) per condition. For proliferation and migration mode analysis (f–i), $n = 6$ vessel segments (each 800 µm length) per condition from $n = 2$ devices/condition (technical replicates) over $n \geq 3$ independent studies (biological replicates).

Previous work *in vivo* has shown that the frequency of proliferation is spatially segregated by EC subtype (*i.e.* tip and stalk ECs) (Gerhardt et al., 2003; Pontes-Quero et al., 2019). Examining the localization of proliferation during sprouting angiogenesis in this model, ECs at the invasion front were indeed the least proliferative **(Figure 5.4b-c)**. Furthermore, while only a small percentage of tip ECs underwent proliferation, the majority of EdU^+ nuclei were positioned within sprout stalks closest to the parent channel **(Figure 5.4b-d)**. To test whether tip cells require

proliferative capacity, we performed additional mosaic studies seeding parent vessels with mixtures of mitomycin C pre-treated GFP-labeled ECs (MitoC-GFP-EC) and untreated ECs. At low mosaic ratios (5% MitoC-GFP-EC) where overall sprouting was not influenced by non-proliferating ECs, MitoC-GFP-ECs were observed at the tip cell position, confirming previous observations *in vivo* that tip cells do not require the capacity to proliferate **(Figure 5.4a, e-i)** (Gerhardt et al., 2003; Pontes-Quero et al., 2019). At high mosaic ratios (50% MitoC-GFP-EC), overall proliferation rates decreased as expected **(Figure 5.4f)**. While impaired proliferation should decrease multicellular sprouting based on the studies above **(Figure 5.2h-m)**, invasion speeds also decreased such that the balance between migration speed and proliferation was maintained and the number of multicellular sprouts did not differ from controls **(Figure 5.4e, f, h)**. With decreased invasion speed, fewer tip cells at the invasive front broke away as single cells resulting in enhanced ratios of sprouts to single cells **(Figure 5.4g-i)**. Taken together, tip and stalk cells perform differential roles during sprouting and possess distinct requirements for chemotaxis and proliferation. Tip cells require chemokine receptors to migrate in response to soluble gradients, but do not require proliferative capacity; in contrast, proliferation primarily occurs in ensuing stalk cells, perhaps providing a requisite cell density needed to maintain intercellular connectivity within the invading multicellular structure.

5.4.4 Functional assessment of fluidic connectivity and permeability

A critical function of microvasculature is the transport of nutrients, waste, platelets, and immune cells. To assess the patency and fluidic connectivity of neovessels, we allowed ECs to fully traverse the 1.1 mm wide collagen matrix and reach the adjacent CCh. Time-lapse confocal imaging while introducing fluorescent microspheres ($\varnothing$ = 1 μm) into ECh reservoirs enabled rapid assessment of flow across the formed vascular bed (ECs spanning ECM). In vascular beds

generated under balanced levels of invasion speed and proliferation rates (*i.e.* conditions resulting in high sprout–single ratios), beads readily flowed through the neovessel network spanning across ECh to CCh, demonstrating fluidic connectivity of functional microvasculature **(Figure 5.5a)**. In stark contrast, dysfunctional microvascular beds formed with excessively high invasion speed (S500 : P25) or deficient proliferation (S250 : P10) resulting in disconnected sprouts (*i.e.* low sprout–single ratio), fluorescent microspheres failed to flow across the ECM space and remained sequestered near the endothelialized parent channel **(Figure 5.5a)**. Indeed, max intensity projections of the full height of the 3D vascularized ECM revealed a complete absence of bead flow, confirming observations from individual *z*-slices captured during time-lapse imaging **(Figure 5.5b)**.

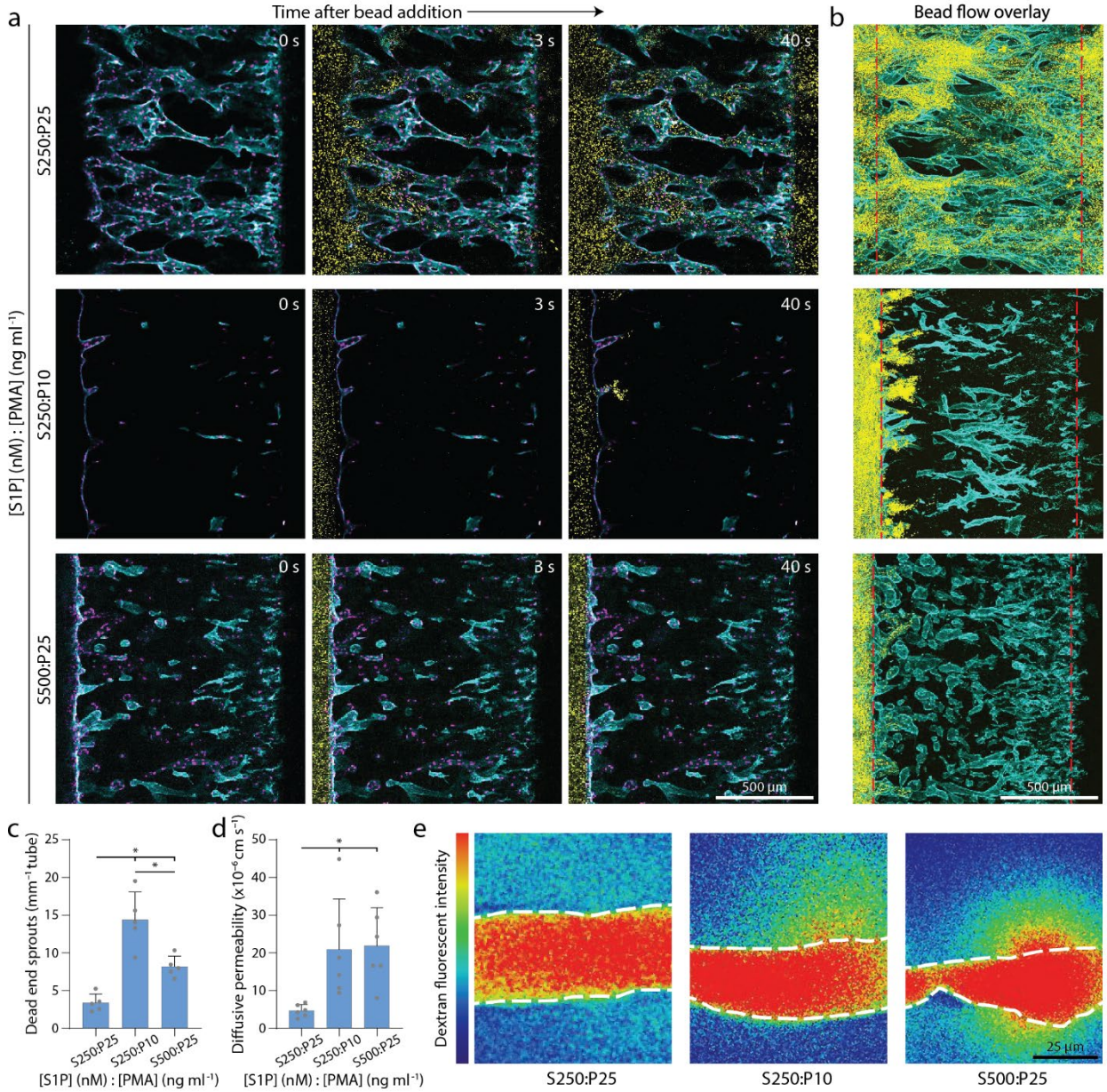

Figure 5.5: Balanced migration and proliferation optimize microvasculature fluidic connectivity and permeability.

a) Representative time course images of 1 µm bead flow across vascular beds formed with balanced cues (top), low proliferation (middle), and high migration (bottom). Nucleus (magenta), F-actin (cyan), beads (yellow). **b)** Max intensity projection at steady state from (a); red dashed lines indicate ECh and CCh edges. F-actin (cyan), beads (yellow). **c)** Quantification of sprouts incapable of fluidically transporting beads. **d)** Quantification of diffusive permeability of 70 kDa dextran. **e)** Representative heat map images of 70 kDa dextran diffusion across neovessels within vascular beds formed with balanced cues (left), low proliferation (center), and high migration (right). White dashed lines indicate vessel edge. All data presented as mean ± s.d.; * indicates a statistically significant comparison with $P < 0.05$ (one-way analysis of variance). $n = 5$ devices per condition (c), $n = 6$ neovessels per condition (d).

Barrier function and endothelial permeability regulated by cell–cell junctions are a closely related aspect of microvascular function (Polacheck et al., 2017). To assess the permeability of formed vascular beds, we introduced fluorescent 70 kDa dextran to the endothelial parent channel after ECs fully traversed the collagen matrix reaching the adjacent CCh, allowed flow across the vascular bed, and time-lapse imaged dextran diffusion across neovessel walls into the surrounding ECM. Low permeability was only achieved when vascular beds were formed under soluble cues that balanced invasion speed with proliferation rates **(Figure 5.5d-e)**, and are comparable to reported values *in vivo* of protein diffusion across capillaries (4.3×10^{-6} cm s^{-1}) (Adamson et al., 1988). Interestingly, in both bead flow and permeability assessments, imbalanced soluble conditions resulting in disconnected sprouts were composed of neovessels that were highly permeable at the tip cell position, such that 1.0 μm beads collected in the adjacent ECM **(Figure 5.5c)**. Taken together, multicellular invasion driven by soluble cues that balance invasion and proliferation yields fluidically functional microvascular beds with low permeability. Beyond these two features critical for transport, future efforts are required to assess other key functions of the microvasculature including gas exchange, regulation of permeability in response to inflammatory cytokines, and the ability to initiate the clotting cascade upon disruption of the endothelium.

5.4.5 Matrix density regulates sprouting speed and morphology

In addition to soluble cues, physical properties of the ECM are known to regulate EC morphology and function during angiogenesis (Crosby and Zoldan, 2019). We hypothesized that independent of soluble cues, physical ECM cues may also influence the balance between EC migration speed and proliferation, and therefore invasion as multicellular sprouts. For example, ECM density, stiffness, and degradability define the susceptibility of ECM to proteolytic activity required for 3D migration (Bordeleau et al., 2017; Ghajar et al., 2008; Trappmann et al., 2017). To

investigate whether physical properties of ECM influence EC invasion as multicellular sprouts we tuned ECM density by modulating collagen concentration (all previous studies were performed in 3 mg ml^{-1} collagen). Maintaining constant soluble cues of S250 : P25, increasing collagen density resulted in decreased invasion depth over 3 day culture **(Figure 5.6a, d)**. Interestingly, varying collagen density from 2–6 mg ml^{-1} did not significantly alter EC proliferation rates, perhaps due to PMA's potent enhancement of proliferation **(Figure 5.6e)**. Mimicking the response of EC invasion speed to [S1P] **(Figure 5.2c)**, decreasing matrix density increased EC invasion speeds with a parallel shift in the morphology of invading ECs from primarily multicellular sprouts towards single cells **(Figure 5.6d, f-h)**. Time-lapse imaging capturing the dynamics of EC invasion revealed that tip ECs break away from the parent vessel more frequently in matrices with low collagen density **(Figure 5.6b-c)**. Furthermore, within multicellular sprouts, tip cells were also observed to lose connectivity with trailing stalk cells **(Supplemental Figure 5.6)**.

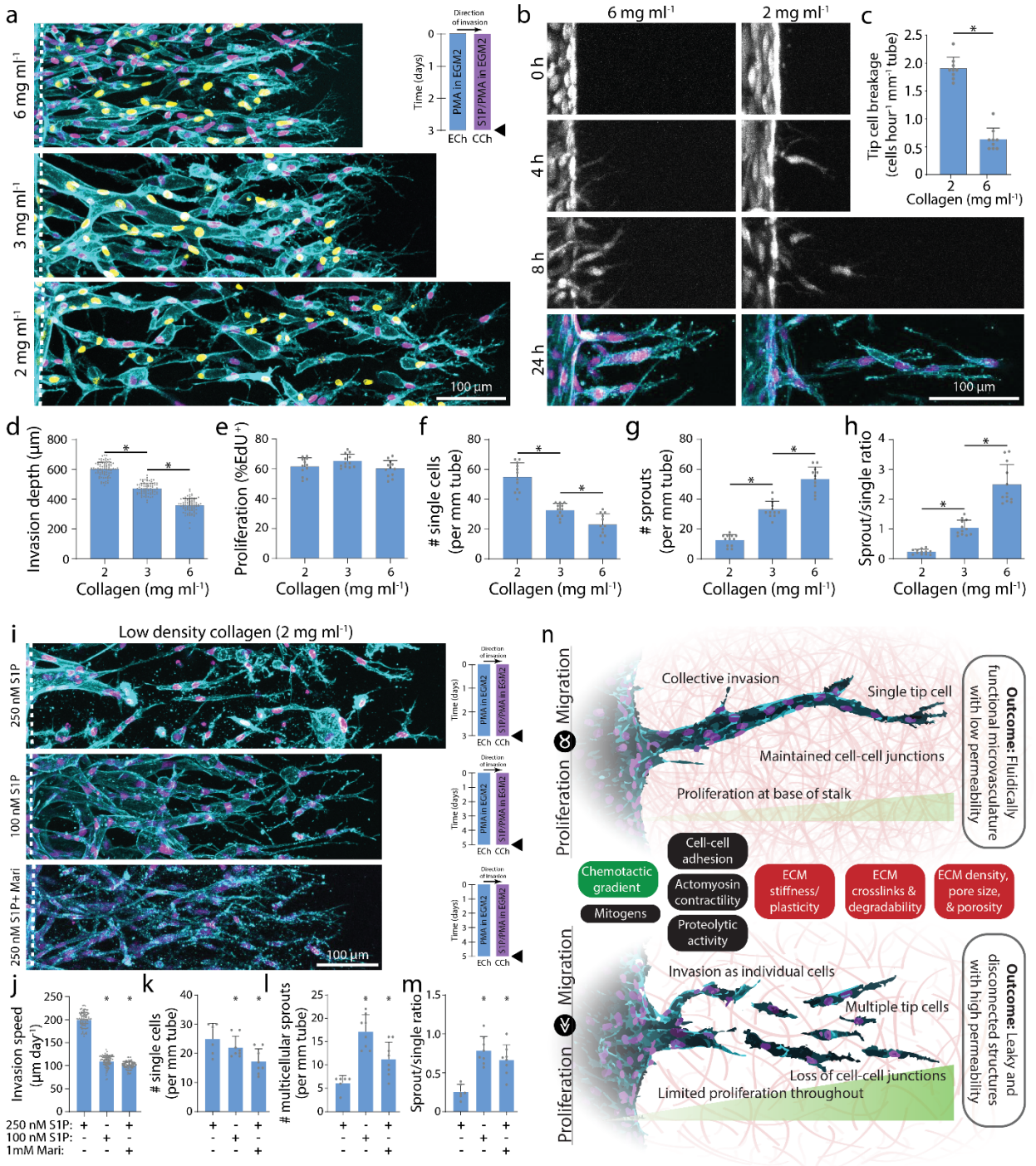

Figure 5.6: Increasing collagen density decreases invasion speed and enhances multicellular sprouting.

a) Representative images (max intensity projection) of invading endothelial cells in response to varying collagen density with S250 : P25. UEA (cyan), nucleus (magenta), EdU (yellow). **b)** Representative time course images (max intensity projection) of invading endothelial cells (labeled with cell tracker dye) in response to varying collagen density with S250 : P25. F-actin (cyan) and nucleus (magenta). **c)** Quantification of the frequency of tip cell breakage events from the parent vessel. **d–h)** Quantifications of invasion depth, proliferation, and morphology of invading

endothelial cells as single cells or multicellular sprouts from conditions in (a). **i)** Representative images (max intensity projection) of invading endothelial cells in 2 mg ml^{-1} collagen with control (S250 : P25), decreased S1P (S100 : P25), and MMP inhibition (S250 : P25). F-actin (cyan) and nucleus (magenta). **j–m)** Quantifications of invasion speed, and morphology of invading endothelial cells as single cells or multicellular sprouts. All data presented as mean ± s.d.; * indicates a statistically significant comparison with $P < 0.05$ (two-tailed Student's *t*-test (c, j–m) and one-way analysis of variance (d–h)). For tip cell breakage analysis (c), $n = 9$ vessel segments (each 400 μm length) per condition. For invasion depth analysis (d), $n \geq 80$ vessel segments (each 100 μm length) per condition. For proliferation and migration mode analysis (e–h and k–m), $n \geq 6$ vessel segments (each 800 μm length) per condition from $n = 2$ devices/condition (technical replicates) over $n \geq 3$ independent studies (biological replicates). For invasion speed analysis (j), $n \geq 81$ vessel segments (each 100 μm length) per condition. **n)** Schematic illustration highlighting the relationship between endothelial cell migration and proliferation on invasion morphology as multicellular sprouts (top; balanced migration and proliferation) *vs.* single cells (bottom; excessive migration or insufficient proliferation). Soluble (green) and physical extracellular matrix (red) cues influence this balance in addition to other potential cell functions (black) that may regulate multicellular sprouting and formation of functional microvasculature.

We thus hypothesized that reducing EC invasion speed in low density collagen would rescue multicellular sprout invasion by allowing trailing stalk cells to maintain intercellular connectivity with leading tip cells. We first decreased EC invasion speed by reducing the strength of the chemokine gradient. Decreasing [S1P] from 250 nM to 100 nM resulted in decreased invasion speed and increased EC invasion as multicellular sprouts **(Figure 5.6i-m)**. To reduce 3D migration speed without modifying the chemokine gradient, we treated ECs with low doses of marimastat (1 mM) to reduce MMP activity. In similar fashion to decreased [S1P], marimastat treatment decreased invasion speed and increased EC invasion as multicellular sprouts **(Figure 5.6i-m)**. Taken together, an interplay of soluble and physical microenvironmental cues regulate EC migration and proliferation, and a critical balance between these two basic cell functions is required for multicellular sprout invasion **(Figure 5.6n and Supplemental Table 5.1)**.

5.5 Discussion

EC migration and proliferation have been previously identified as key requirements for the formation of microvasculature in several models of angiogenesis (Ausprunk and Folkman, 1977; Pontes-Quero et al., 2019), but the relationship between these two fundamental cell functions has not been established. Furthermore, assessing the integrity of multicellular sprouts and resulting function of formed microvasculature has been challenging in previous *in vitro* model systems. In this work, we streamlined the fabrication of a multiplexed microfluidic device that recapitulates key aspects of 3D angiogenic sprouting and enables functional assessments of microvasculature fluidic connectivity and diffusive permeability. Tuning soluble and physical microenvironmental factors that affect EC migration and proliferation, we found that these two fundamental cell functions must be in balance to drive multicellular strand-like invasion of connected lumenized sprouts. Furthermore, microenvironmental conditions that balanced EC migration and proliferation yielded fluidically patent microvasculature with low diffusive permeability, two key traits of functional microvasculature. In stark contrast, imbalanced soluble or physical microenvironmental cues that elicited disproportionate migration and proliferation caused tip cells to break away from ensuing stalk cells; this resulted in disconnected ECs, blunt ended sprouts, fluidic leakiness, and high diffusive permeability.

While here we examined ECM density by tuning collagen concentration, our previous work demonstrates that ECM degradability also regulates the relationship between EC invasion speed and single *vs.* collective migration phenotypes, where highly degradable synthetic hydrogels increased EC invasion speed and invasion as single cells (Trappmann et al., 2017). Of note, these synthetic matrices elicited limited EC proliferation. Coupled with the findings presented here where proliferation rates positively correlated with the diameter of lumenized neovessels,

insufficient proliferation may in part explain why multicellular sprouts failed to lumenize in our previous studies employing synthetic matrices. We posit that pro-angiogenic materials must ensure multicellular invasion and also support subsequent lumenization, with proliferation potentially impacting both of these key steps of angiogenesis. As such, future investigations should aim to connect matrix structure and mechanics to EC proliferation, local density, and cytoskeletal organization during neovessel lumenization. Given the highly dynamic nature of both cells and surrounding matrix during angiogenic sprouting, the use of live imaging techniques and reporters for both cell and matrix state will be essential to these endeavors (Juliar et al., 2018; Kirkpatrick et al., 2007; Vaeyens et al., 2020). Other cell functions that influence 3D cell migration efficiency such as proteolytic activity, cell–cell and cell–ECM adhesions, nuclear rigidity, and cytoskeletal contractility may also feed into whether cells migrate as single cells *vs.* collective multicellular strands **(Figure 5.6n)** (Fraley et al., 2010; Krause et al., 2019; Trappmann et al., 2017; Wang et al., 2018, 2019). Cell migration mode is critical in both developmental and disease processes (Friedl and Gilmour, 2009). Cancer cells, for example, display a diversity of migratory phenotypes during metastasis including single cells or collective strands (Wang et al., 2019; Wolf et al., 2007). How microenvironmental cues regulate cell invasion mode and further, how invasion mode subsequently impacts metastatic efficiency are both important unanswered questions.

A balance of pro- and anti-angiogenic factors normally guide physiologic angiogenesis, but in many diseases an imbalance of soluble factors can dysregulate angiogenesis (Carmeliet and Jain, 2000). Prior to metastasis, primary tumors stimulate rapid angiogenesis to sustain the increasing metabolic demand of the growing tumor mass (Almog et al., 2009). The tumor vasculature, however, is disorganized and hyperpermeable with heterogeneous EC populations and acellular gaps along the vessel wall (Hashizume et al., 2000; Siemann, 2011; Di Tomaso et al.,

2005). In our model system, high [S1P] drove excessively high EC invasion speeds resulting in disconnected and highly permeable microvasculature, mimicking the rapid assembly of poor quality tumor vasculature. Indeed, elevated S1P levels have previously been observed in breast cancer murine models, where paracrine signaling from breast cancer cells secreting S1P enhances tumor angiogenesis and tumor burden (Nagahashi et al., 2012; Takabe et al., 2010). Hyperpermeable, tortuous vasculature impairs proper blood flow, which hampers traditional therapeutic delivery and oxygen transport. Hypoxic conditions further reduce the susceptibility of the tumor to radio- and chemotherapy (DeClerck and Elble, 2010). Given recent efforts to normalize vascular phenotype to better treat solid tumors, on-a-chip models integrating cancer cells with disorganized vasculature could provide a novel testbed for anti-cancer strategies focused on rescuing tumor microvasculature phenotype and function (Jain, 2005). Based on the findings of our work, localized delivery of EC-targeting therapeutics that dually modulate invasion and proliferation may prevent or slow the progression of angiogenesis-mediated diseases.

Besides excessive angiogenesis, insufficient angiogenesis also contributes to disease progression. Seemingly paradoxical, both excessive and insufficient angiogenesis occur simultaneously in distinct organs of patients suffering from diabetes mellitus(Martin et al., 2003). In the retina, the onset of EC proliferation delineates the transition between low (non-proliferative) and high (proliferative) grade diabetic retinopathy where rapid angiogenesis forms hyperpermeable microvasculature that contributes to eventual blindness (Durham and Herman, 2011). Many of these same patients also present with impaired angiogenesis in the lower extremities, which inhibits wound healing and contributes to chronic diabetic foot ulcers (Martin et al., 2003). A close examination of EC proliferation and invasion during angiogenesis through the lens of altered soluble and physical microenvironmental factors in diabetic tissues could help

inform new strategies to halt or promote angiogenesis in the retina or skin, respectively. Outside of diabetes, there are currently no available therapies to address insufficient angiogenesis in ischemic conditions such as critical limb and cardiac ischemia (Losordo and Dimmeler, 2004). Towards the design of vascularized tissue transplants to treat such conditions, this work emphasizes a need for balanced EC migration and proliferation for functional angiogenesis.

The vascularization of large bioengineered tissue constructs at organ relevant scales remains an outstanding challenge in the tissue engineering and regenerative medicine community (Novosel et al., 2011). Recent advances in 3D printing technologies enable exquisite control over arteriole and venule scale microchannels in synthetic hydrogel matrices, with such constructs subsequently endothelialized by flow-through seeding (Grigoryan et al., 2019). However, current 3D bioprinting approaches cannot achieve the 5–25 μm diameter length scale relevant to capillaries (Aird, 2005; Gong et al., 2015; Traore and George, 2017). Furthermore, given that capillaries are narrower than fluid-suspended ECs (20–30 μm), flow-through seeding would prove difficult. Therefore, an integrated approach of 3D printed arteriole/venule-scale vasculature followed by controlled angiogenesis to elaborate the smallest scale capillaries may hold the most promise for generating functional hierarchical microvascular beds with potential for surgical integration (Mirabella et al., 2017). However, a key challenge will be identifying hydrogel properties that enable high fidelity 3D printing while supporting angiogenesis, as several reports have indicated EC mechanosensitivity during migration, proliferation, and sprouting (Bordeleau et al., 2017; Crosby and Zoldan, 2019; Davidson et al., 2019; Ghajar et al., 2008; Juliar et al., 2020; Trappmann et al., 2017). Overall, continued efforts to carefully dissect how architectural and mechanical attributes of the surrounding 3D space influence angiogenesis are critical **(Figure 5.6n)**. Here, we utilized collagen hydrogels to model the collagenous stroma where angiogenesis typically occurs.

However, it is challenging to orthogonally tune material properties such as stiffness, degradability, and ligand density in natural materials such as collagen (Li et al., 2017a). Thus, the continued development of synthetic hydrogels and their integration with microfluidic devices will be critical to shedding deeper insight into how specific aspects of the ECM regulate angiogenesis. As many commonly utilized synthetic hydrogels lack the fibrous architecture of native tissues, recent developments in fiber-reinforced synthetic hydrogels may provide novel insights into how fibrous cues regulate EC sprouting morphology (Matera et al., 2019). The information gleaned from such studies would provide rich data sets to inform computational models of angiogenic sprouting and help in identifying mechanochemical design parameters that optimize implant vascularization for regenerative tissue therapies (Heck et al., 2015). A multi-disciplinary approach combining on-a-chip platforms, synthetic biomaterials, imaging of live cell molecular reporters, and computational modeling would enable prediction and control of angiogenesis across a diversity of tissue environments, essential to elucidating mechanisms of disease progression, designing therapeutics to normalize vasculature, and engineering vascularized biomaterial implants.

5.6 Materials and Methods

5.6.1 Reagents

All reagents were purchased from Sigma-Aldrich and used as received, unless otherwise stated.

5.6.2 Microfluidic device fabrication

3D printed moulds were designed in AutoCAD and printed *via* stereolithography from Protolabs (Maple Plain, MN). Polydimethylsiloxane (PDMS, 1 : 10 crosslinker : base ratio) devices were replica casted from 3D printed moulds, cleaned with isopropyl alcohol and ethanol,

and bonded to glass coverslips with a plasma etcher. Devices were treated with 0.01% (w/v) poly-L-lysine and 0.5% (w/v) L-glutaraldehyde sequentially for 1 hour each to promote ECM attachment to the PDMS housing, thus preventing hydrogel compaction from cell-generated forces. 300 μm stainless steel acupuncture needles (Lhasa OMS, Weymouth, MA) were inserted into each device and sterilized. Type I rat tail collagen (Corning, Corning, NY) was prepared as in (Doyle, 2016), injected into each device, and polymerized around each set of needles for 30 minutes at 37 °C. Collagen hydrogels were hydrated in EGM2 for 2 hours and needles were removed to form 3D hollow channels fully embedded within collagen, positioned 400 μm away from PDMS and glass boundaries.

5.6.3 Device cell seeding and culture

Human umbilical vein endothelial cells (HUVEC, Lonza, Switzerland) were cultured in endothelial growth media (EGM2, Lonza). HUVECs were passaged upon achieving confluency at a 1 : 4 ratio and used in studies from passages 4 to 9. A 20 μl solution of suspended HUVECs was added to one reservoir of the endothelial channel and inverted for 30 minutes to allow cell attachment to the top half of the channel, followed by a second seeding with the device upright for 30 minutes to allow cell attachment to the bottom half of the channel. HUVEC solution density was varied with collagen density as attachment efficiency was dependent on collagen density (1.5 M ml^{-1} for 2 mg ml^{-1}, 2 M ml^{-1} for 3 mg ml^{-1} and 5 M ml^{-1} for 6 mg ml^{-1}). HUVEC seeding densities were determined experimentally to achieve parent vessels with consistent cell densities across each collagen density **(Supplemental figure 5.1c)**. HUVECs reached confluency and self-assembled into stable parent vessels over 24 hours. Media and chemokines were refreshed every 24 hours and devices were cultured with continual reciprocating flow utilizing gravity-driven flow

on a seesaw rocker plate at 0.33 Hz. To inhibit cell proliferation, cells were treated with 40 μg ml^{-1} mitomycin C for 2 hours. To inhibit S1P receptor, cells were treated with 100 nM FTY720 for 24 hours.

5.6.4 Lentivirus production

cDNA for pLenti CMV GFP Puro (658-5) was a gift from Eric Campeau and Paul Kaufman (Addgene plasmid #17448) (Campeau et al., 2009). To generate lentivirus, plasmids were co-transfected with pCMV-VSVG (a gift from Bob Weinberg, Addgene plasmid #8454), pMDLg/pRRE, and pRSV-REC (gifts from Didier Trono, Addgene plasmid #12251 and #12253 (Dull et al., 1998; Stewart et al., 2003) in 293T cells using the calcium phosphate precipitation method. Viral supernatants were collected after 48 h, concentrated with PEG-it™ (System Biosciences, Palo Alto, CA) following the manufacturer's protocol, filtered through a 0.45 μm filter (ThermoFisher Scientific Nalgene, Waltham, MA), and stored at −80 °C. Viral titer was determined by serial dilution and infection of HUVECs in the presence of 10 μg ml^{-1} polybrene (Santa Cruz Biotechnology, Dallas, TX). Titers yielding maximal expression without cell death or detectable impact on cell proliferation or morphology were selected for studies.

5.6.5 Fluorescent staining

Samples were fixed with 4% paraformaldehyde and permeabilized with a PBS solution containing Triton X-100 (5% v/v), sucrose (10% w/v), and magnesium chloride (0.6% w/v) for 1 hour each at room temperature. Alexa Fluor 488 phalloidin (Life Technologies, Carlsbad, CA) was utilized to visualize F-actin. 4′,6-Diamidino-2-phenylindole (DAPI, 1 μg ml^{-1}) was utilized to visualize cell nuclei. For proliferation studies, EdU was supplemented in culture media for the

final 24 hours prior to fixation of each study. EdU fluorescent labelling was performed following the manufacturer's protocol (ClickIT EdU, Life Technologies). DyLight 649 labelled *Ulex europaeus* Agglutinin-1 (UEA, 1 : 200, Vector Labs, Burlingame, CA) was utilized to visualize endothelial cell morphology in samples stained with EdU due to EdU ClickIT incompatibility with phalloidin staining. To visualize VE-cadherin, samples were sequentially blocked in bovine serum albumin (0.3% w/v), incubated with primary mouse monoclonal anti-VE-cadherin (200 ng ml^{-1}, Santa Cruz Biotechnology), and incubated with secondary Alexa Fluor 647 goat anti-mouse IgG (H + L) (2 μg ml^{-1}, Life Technologies) each for 1 hour at room temperature. Fluorescently labelled collagen hydrogels were prepared as in (Doyle, 2016).

5.6.6 Microscopy and image analysis

Fluorescent images were captured on a Zeiss LSM800 confocal microscope. Parent vessel endothelial cell density and EdU proliferation was quantified by counting DAPI and EdU positive cell nuclei. Invasion depth was quantified as the distance from the parent vessel edge to the tip cell and measured in FIJI. Invasion depth measurements were performed at 100 μm intervals along the parent vessel **(Supplemental Figure 5.2)**. Leading edge single cells were quantified as the number of single cells in the leading 150 μm front of cell invasion **(Supplemental Figure 5.2)**. Sprouts were quantified as the number of connected multicellular sprouts (parent vessel edge to tip cell) with a length greater than half the maximum invasion depth per condition **(Supplemental Figure 5.2)**. Sprout diameter measurements were performed in FIJI; diameter measurements smaller than the width of a cell nuclei (10 μm) were not included in the analysis to avoid measurements of smaller, non-lumenized cellular structures such as tip cell protrusions that would skew diameter measurements to lower values.

5.6.7 Single vs. multicellular sprout analysis

Single cell and multicellular sprout analysis was performed manually in FIJI utilizing fluorescent markers of nuclei and F-actin. This analysis was performed utilizing single *z*-slices within a 300 μm *z*-stack. Leading edge single cells were quantified as the number of isolated single cells without actin connections to other cells in the leading 150 μm front of cell invasion **(Supplemental Figure 5.2)**. Sprouts were quantified as the number of connected multicellular sprouts with F-actin connections from the parent vessel edge to tip cell and a length greater than half the maximum invasion depth per condition **(Supplemental Figure 5.2)**. The parent vessel edge was clearly distinguished utilizing single *z*-slice views **(Supplemental Movies 5.1 – 5.5)**.

5.6.8 Neovessel permeability measurement

To assess fluidic connectivity and diffusive permeability, endothelial cells were first allowed to invade and reach the chemokine channel over 10–14 day culture. Diffusive permeability was quantified as in (Polacheck et al., 2019). Fluorescent dextran (70 kDa Texas Red, Thermo Fisher) was incorporated into EGM2 media at 12.5 μg ml^{-1} and dextran diffusion was imaged at 1 second intervals to measure the flux of dextran from neovessels into the ECM. The resulting diffusion profile was fitted to a dynamic mass-conservation equation as in (Adamson et al., 1994). with the diffusive-permeability coefficient (P_D) defined by $J = P_D(c_{vessel} - c_{ECM})$, where J is the mass flux of dextran, c_{vessel} is the concentration of dextran in the vessel, and c_{ECM} is the concentration of dextran in the perivascular ECM.

5.6.9 Statistics

Statistical significance was determined by one-way analysis of variance (ANOVA) or two-sided Student's *t*-test where appropriate, with significance indicated by $p < 0.05$. Sample size is indicated within corresponding figure legends and all data are presented as mean ± standard deviation.

5.7 Supplementary Material

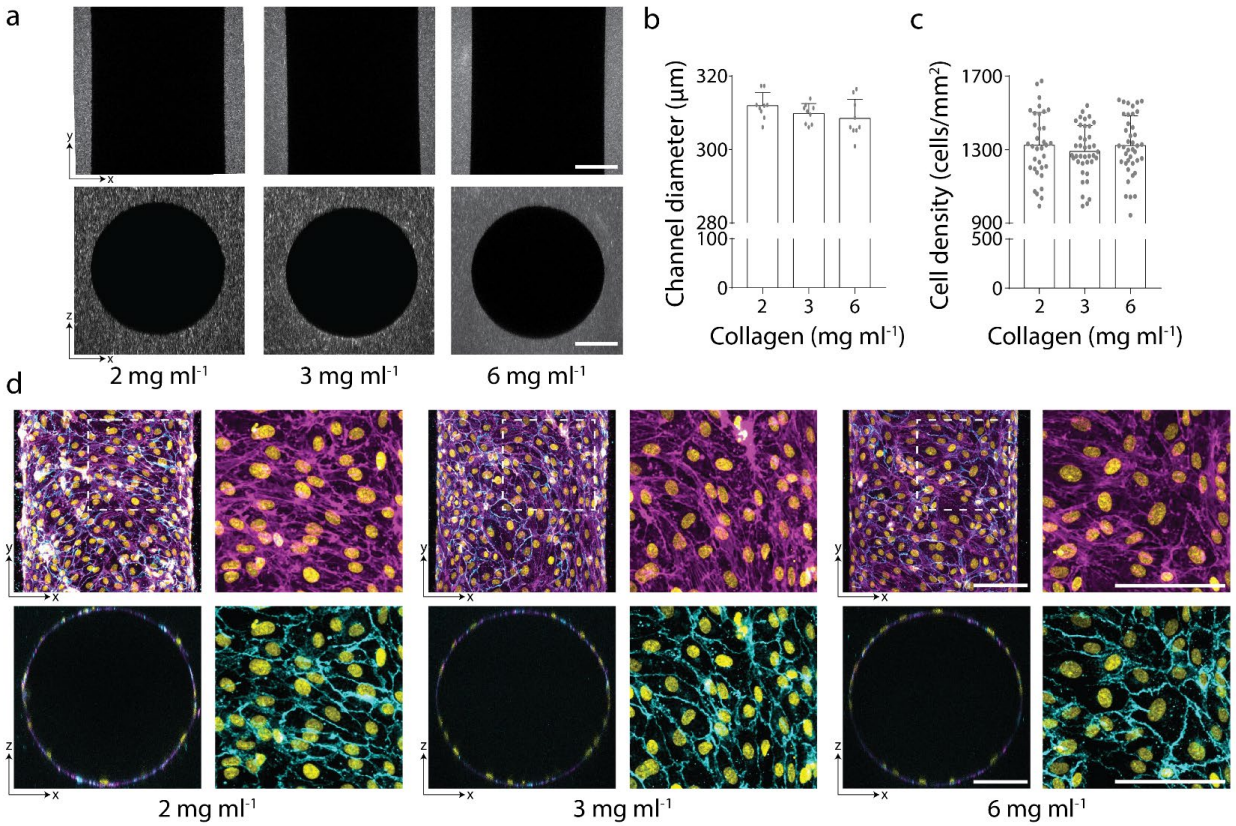

Supplementary Figure 5.1: Parent vessels with consistent diameter and cell density.
a) Representative images of x-y and x-z orthogonal views of 3D channels generated in indicated collagen density. **b-c)** Quantifications of channel diameter and parent vessel endothelial cell density with varying collagen concentration. Cell seeding density was varied as EC attachment efficiency was dependent on collagen density (1.5 M/ml for 2 mg ml^{-1}, 2 M/ml for 3 mg ml^{-1} and 5 M/ml for 6 mg ml^{-1}). All data presented as mean ± s.d.; * indicates a statically significant comparison with $P<0.05$ (one-way analysis of variance). $n \geq 8$ channels (b) and $n \geq 34$ vessel segments (each 400 µm length) (c) per condition, $n \geq 3$ biologically identical replicates. **d)** Representative images of x-y (max intensity projection) and x-z (single slice) orthogonal views of

parent vessels generated with varying collagen concentration after 24-hour culture. Insets indicated with dashed white lines. Nucleus (yellow), F-actin (magenta), and VE-cadherin (cyan).

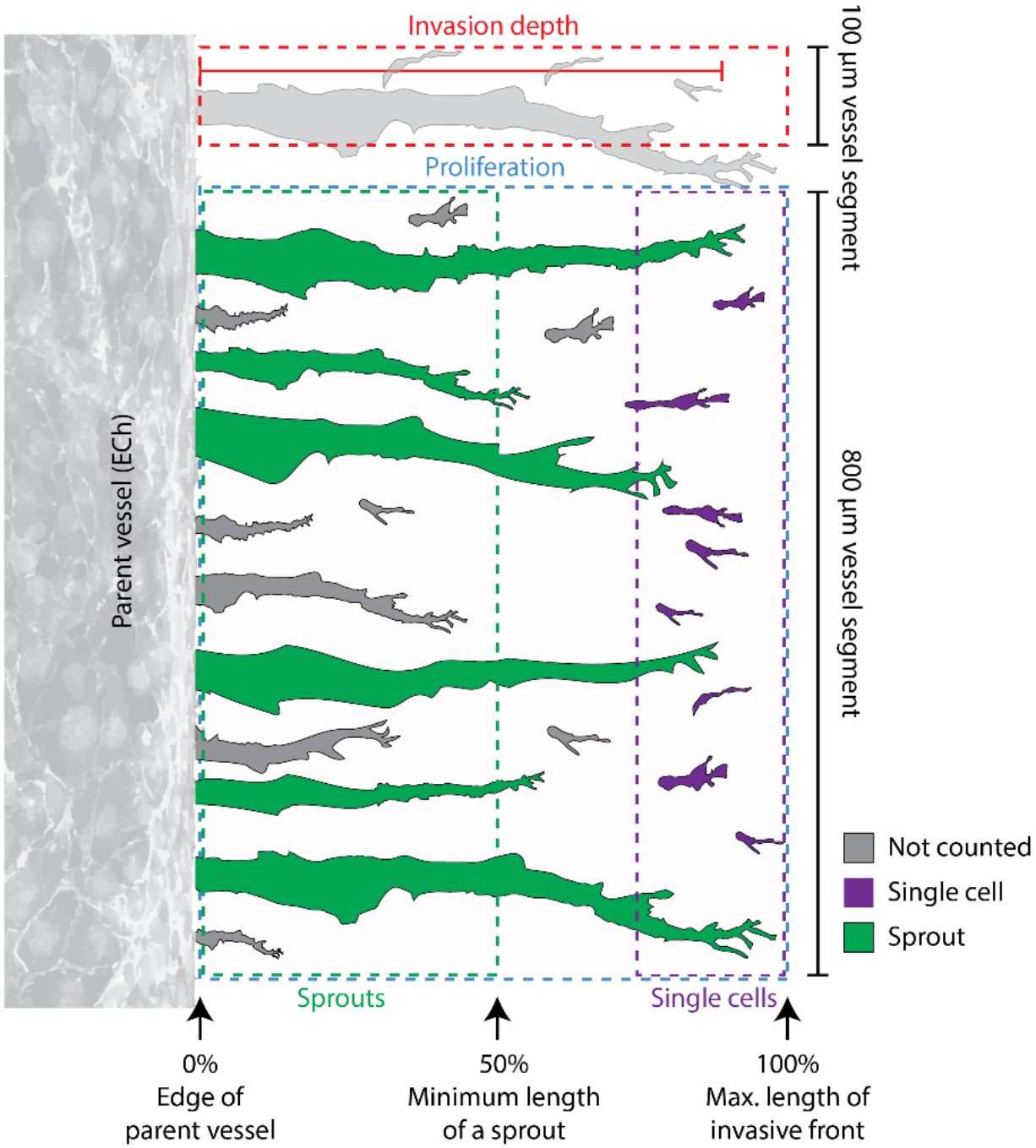

Supplementary Figure 5.2: Schematic of quantification metrics.
To quantify invasion depth (red), images were segmented into 100 µm segments along the parent vessel and measurements were taken from the ECh edge to the tip of the endothelial cell that invaded furthest within that segment. To quantify proliferation (blue), images were segmented into

800 μm segments along the parent vessel, and the percentage of EdU^+ nuclei was measured only in endothelial cells that had invaded into the extracellular matrix from the ECh edge to leading invasive front. To quantify leading edge single cells (purple), images were segmented into 800 μm segments along the parent vessel and isolated single cells were quantified within 150 μm of the leading invasive front. To quantify multicellular sprouts (green), images were segmented into 800 μm segments along the parent vessel, and quantified connected endothelial sprout structures (from ECh edge to sprout tip) with a minimum length of half the max invasion depth. Single cells and sprouts outside of these criteria were not included in the analysis (grey).

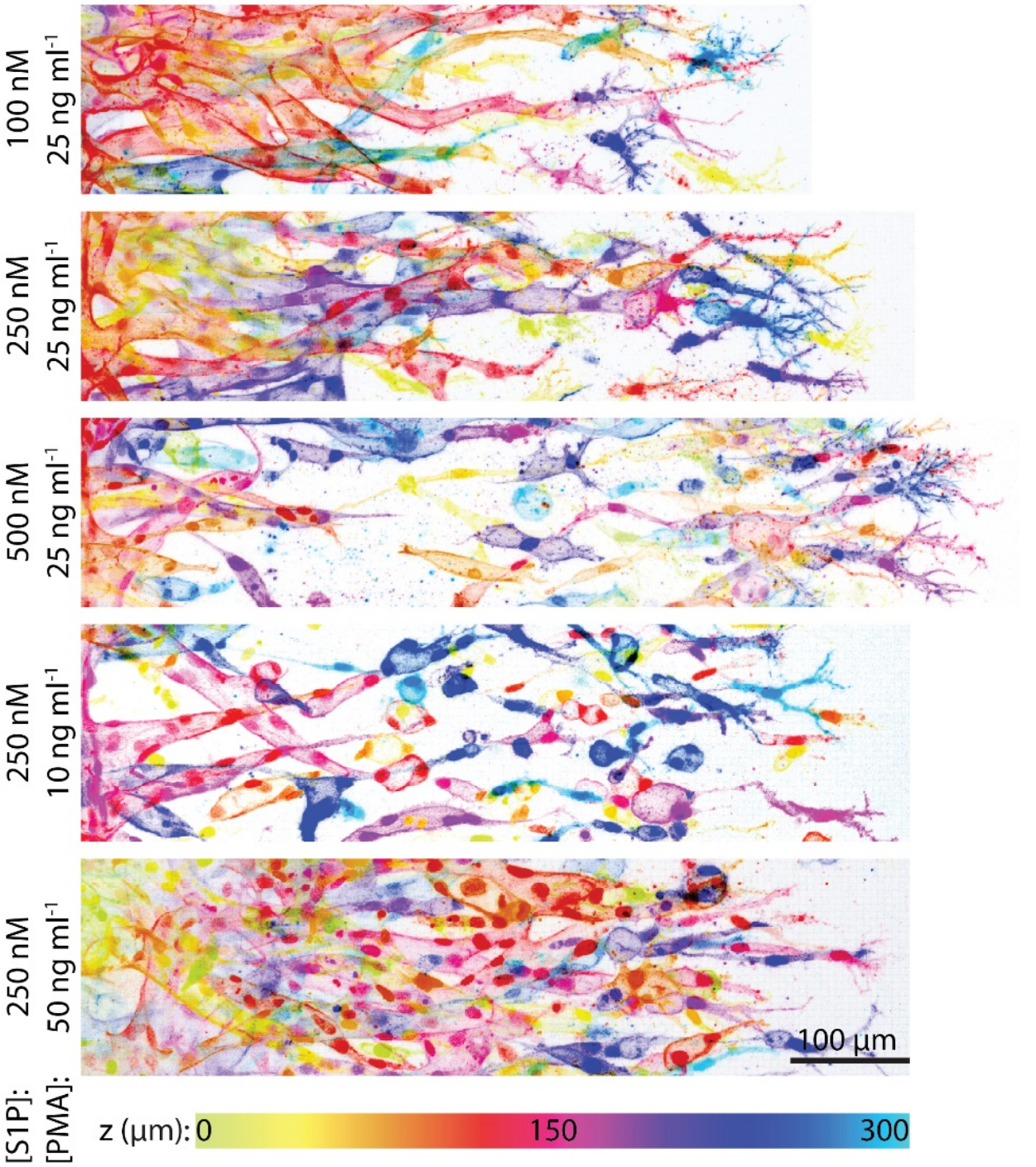

Supplementary Figure 5.3: Z-depth encoded projections.
300 µm max intensity projections from Figure 2 pseudo-colored with z-position. Z-stack image files were processed in FIJI using "Temporal-Color Code" function to assign each z-slice an individual color. "Physics" color scale was utilized and inverted.

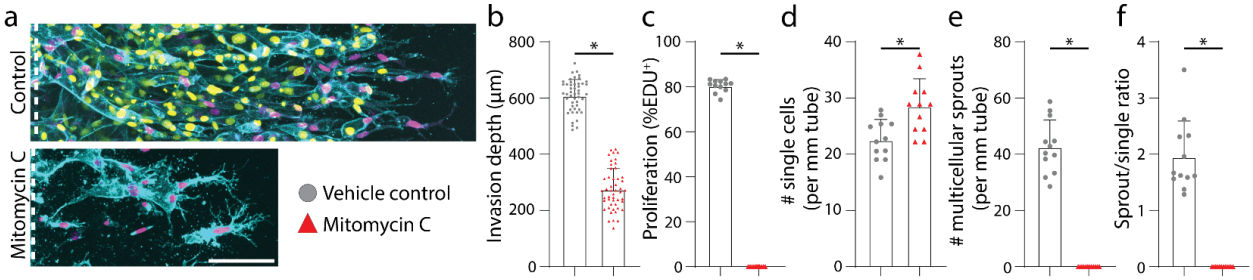

Supplementary Figure 5.4: Proliferation inhibition abrogates multicellular sprouting.
a) Representative images (max intensity projection) of endothelial cell invasion in response to mitomycin C proliferation inhibition with S250:P50 and 3mg ml^{-1} collagen. **b-f)** Quantifications of invasion depth, proliferation, and morphology of invading endothelial cells as single cells or multicellular sprouts. All data presented as mean ± s.d.; * indicates a statically significant comparison with P<0.05 (two-tailed Student's t-test). For invasion depth analysis (b), n=48 vessel segments (each 100 µm length) per condition. For proliferation and migration mode analysis (c-f) n=12 vessel segments (each 800 µm length) per condition, n≥4 biologically identical replicates.

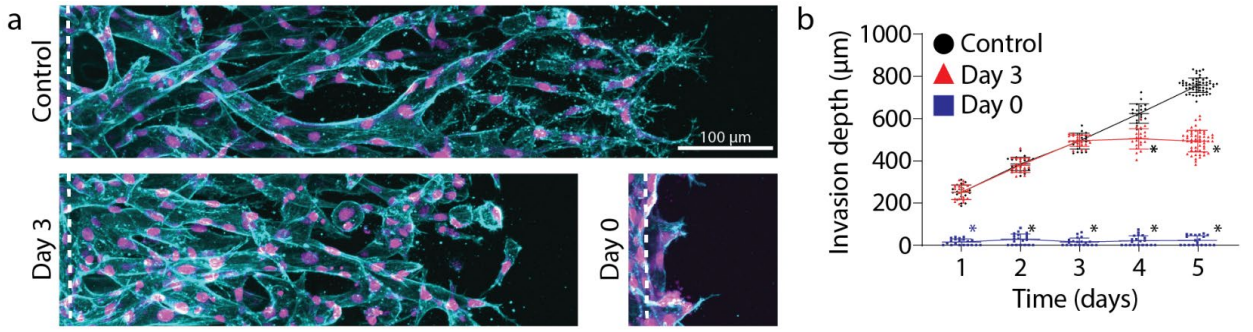

Supplementary Figure 5.5: S1P receptor inhibition abrogates S1P-driven EC invasion.
a) Representative images (max intensity projection) of invading endothelial cells in response to 100 nM FTY720 treatment with S250:P25 and 3mg ml^{-1} collagen. Day 0 conditions were composed of ECs pre-treated with FTY720. F-actin (cyan), nucleus (magenta). **b)** Endothelial cell invasion depth over time in response to 100 nM FTY720 treatment. All data presented as mean ± s.d.; * indicates a statically significant comparison with P<0.05 (one-way analysis of variance). n≥20 vessel segments (each 100 µm length) per condition, n≥3 biologically identical replicates.

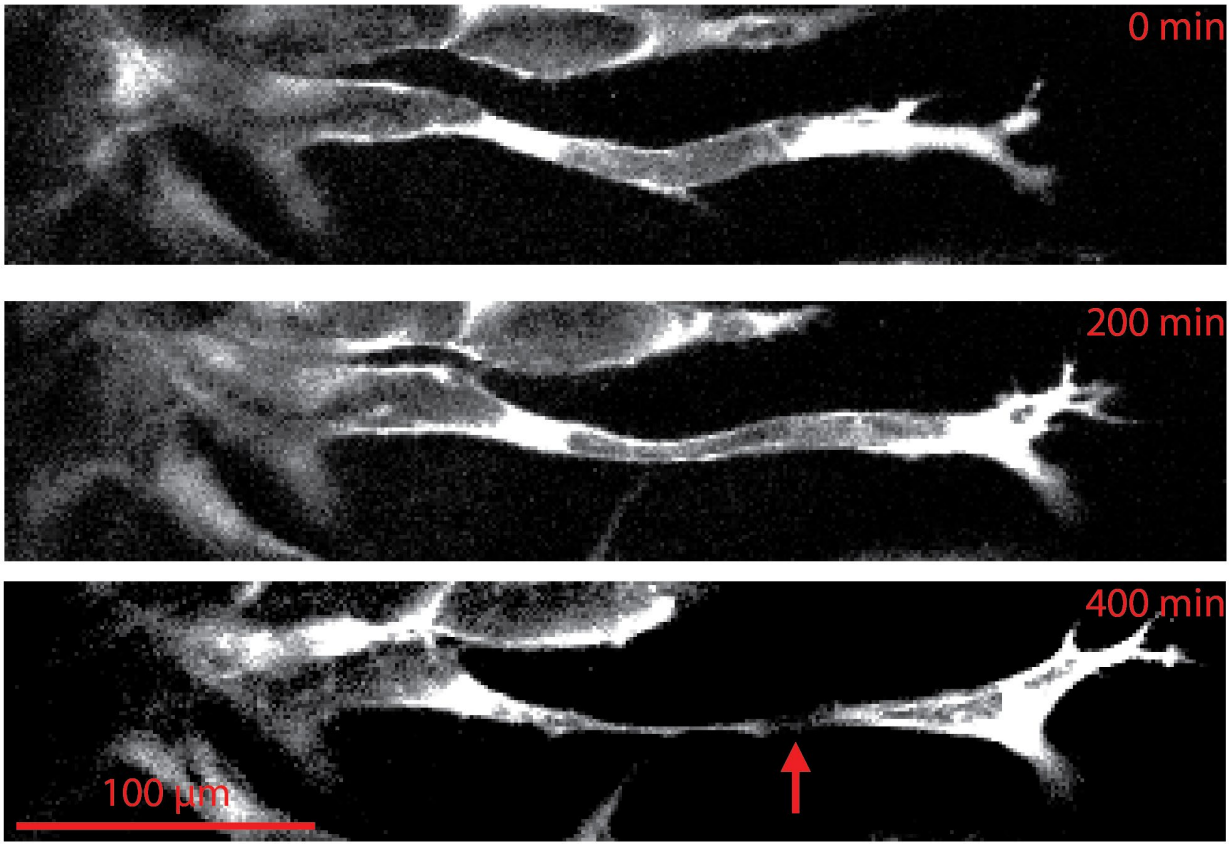

Supplementary Figure 5.6: Tip cell breakage from stalk cell.
Time-lapse series demonstrating the separation of tip and stalk cell connectivity of a sprout cultured within 3 mg ml^{-1} collagen with 250 nM S1P and 25 ng ml^{-1} PMA. Time-lapse imaging began on day 2 of sprout culture. Red arrow indicates tip and stalk cell breakage.

Figure #	[S1P] (nM)	[PMA] (ng ml^{-1})	[Collagen] (mg ml^{-1})
5.1c-e	0	0	3
5.2a	0-500	0	3
5.2b	0-500	25	3
5.2h	250	0-50	3
5.3a	100-500	10-50	3
5.4a	250	25	3
5.5	250-500	10-25	3
5.6a	250	25	2-6
5.6b	250	25	2-6
5.6i	100-250	25	2
Supp. 5.1d	0	0	2-6
Supp. 5.4	250	50	3
Supp. 5.5	250	25	3
Supp. 5.6	250	25	3

Supplemental Table 5.1: Microenvironmental cues utilized in experiments by figure.

Supplementary Movie 5.1: Endothelial sprouts cultured with 100 nM S1P and 25 ng ml^{-1} PMA in 3 mg ml^{-1} collagen over 5 days.
http://www.rsc.org/suppdata/c9/lc/c9lc01170f/c9lc01170f2.avi

Supplementary Movie 5.2: Endothelial sprouts cultured with 250 nM S1P and 25 ng ml^{-1} PMA in 3 mg ml^{-1} collagen over 5 days.
http://www.rsc.org/suppdata/c9/lc/c9lc01170f/c9lc01170f3.avi

Supplementary Movie 5.3: Endothelial sprouts cultured with 500 nM S1P and 25 ng ml^{-1} PMA in 3 mg ml^{-1} collagen over 5 days.
http://www.rsc.org/suppdata/c9/lc/c9lc01170f/c9lc01170f4.avi

Supplementary Movie 5.4: Endothelial sprouts cultured with 250 nM S1P and 10 ng ml^{-1} PMA in 3 mg ml^{-1} collagen over 5 days.
http://www.rsc.org/suppdata/c9/lc/c9lc01170f/c9lc01170f5.avi

Supplementary Movie 5.5: Endothelial sprouts cultured with 250 nM S1P and 50 ng ml^{-1} PMA in 3 mg ml^{-1} collagen over 5 days.
http://www.rsc.org/suppdata/c9/lc/c9lc01170f/c9lc01170f6.avi

Chapter 6: Dynamic Endothelial Stalk Cell-Matrix Interactions Regulate Angiogenic Sprout Diameter

6.1 Authors

William Y. Wang, Evan H. Jarman, Daphne Lin, Brendon M. Baker

6.2 Abstract

Angiogenesis is a complex, multicellular process that involves bidirectional interactions between extracellular matrix (ECM) and collectively invading endothelial cell (EC) sprouts that extend the microvasculature during development, wound healing, and disease processes. While many aspects of angiogenesis have been well studied, the relationship between endothelial sprout morphology and subsequent neovessel function remains relatively unknown. Here, we investigated how various soluble and physical matrix cues that regulate endothelial sprouting speed and proliferation correspond to changes in sprout morphology, namely, sprout stalk diameter. We found that sprout stalk cells utilize a combination of cytoskeletal forces and proteolysis to physically compact and degrade the surrounding matrix, thus creating sufficient space in three-dimensional (3D) ECM for lateral expansion. As increasing sprout diameter precedes lumenization to generate perfusable neovessels, this work highlights how dynamic endothelial stalk cell–ECM interactions promote the generation of functional neovessels during sprouting angiogenesis to provide insight into the design of vascularized, implantable biomaterials.

6.3 Introduction

Vasculature is a hierarchical network of blood vessels with a wide range of diameters spanning the micron (capillaries) to centimeter (aorta) length scales. A major focus in the fields of biomaterials and tissue engineering has been placed on engineering microvasculature (<50 μm diameter range), as without functional microvasculature, implantable cell-dense tissue constructs are limited in size (<200 μm thickness) due to insufficient gas/nutrient/waste exchange (Huxley and Rumbaut, 2000; Kinstlinger and Miller, 2016; Novosel et al., 2011). One such strategy to resolve the vascularization challenge lies in the design of biomaterials that promote host angiogenesis, the extension of microvasculature from the host's preexisting vessels into the implant, thereby ensuring circulation between implant and host. Observations consistent across a wide range of *in vivo* and *in vitro* models of angiogenesis have established several key steps including (1) chemokine gradients promoting endothelial tip cell formation and directed invasion into the extracellular matrix (ECM); (2) collective migration of leading tip cells and ensuing stalk cells; and (3) proliferation and expansion of stalk cells into lumenized, fluid-bearing neovessels (Francavilla et al., 2009; Potente et al., 2011). Each of these steps is regulated by both biochemical and physical microenvironmental cues provided by the surrounding ECM, the three-dimensional (3D) fibrous, collagenous meshwork through which endothelial sprouts navigate (Crosby and Zoldan, 2019).

While many aspects of angiogenesis have been studied, continued efforts are required to better understand the relationship between endothelial cell (EC) invasion morphology and subsequent neovessel function. Recent work by our group and others has established how cell intrinsic features (contractility and cell–cell adhesions), soluble factors (chemoattractants and mitogens), and matrix properties (matrix density, degradability, and stiffness) regulate the

multicellularity and connectivity of invading EC sprouts, which are critical factors to the ultimate function of neovessels (e.g., perfusability and permeability) (Trappmann et al., 2017; Wang et al., 2020; Yoon et al., 2019). Beyond sprout multicellularity, prior work has also established that the speed of sprout invasion impacts their resulting geometry, where sprout length has been observed to anti-correlate with diameter (Wood et al., 2012). While sprout invasion speed and resulting length are critical determinants of the thickness of an implant that can be vascularized before hypoxia takes hold, sprout diameter is equally important: insufficiently sized sprout diameters may prevent subsequent lumenization required for generating fluid-bearing neovessels (Van Hinsbergh and Koolwijk, 2008). While matrix proteolysis has been the central focus on how invading EC sprouts may create space in 3D ECM to migrate and lumenize (Chun et al., 2004; Van Hinsbergh and Koolwijk, 2008), studies from single-cell encapsulation of mesenchymal stem cells, fibroblasts, and cancer cells have elucidated other means of 3D ECM reorganization that dictate cell shape and subsequent function such as proliferation, migration, and differentiation (Baker et al., 2015; Chaudhuri et al., 2016; Yamada and Sixt, 2019). Continued investigation is required to understand structure–function relationships in multicellular contexts such as collectively invading EC sprouts during angiogenesis.

Extracellular matrix properties regulate the morphologies, migratory modes, and cellular machineries used by cells to spread and migrate in confining 3D microenvironments. Within sufficiently porous and pliable environments, cells can navigate through a confining ECM meshwork by squeezing through pores or utilizing cell forces to physically deform the 3D space to move the cell body forward (Denais et al., 2016; Ilina et al., 2020; Wang et al., 2019; Wisdom et al., 2018). Cell protrusions driven by cooperative cytoskeletal filaments, primarily coordinated microtubule cores and actin-rich tips, engage adhesive ECM binding sites and apply pushing or

pulling forces that reorganize the surrounding matrix (Baker et al., 2015; Dogterom and Koenderink, 2019; Hall et al., 2016; Rhee et al., 2007; Shakiba et al., 2020). However, in ECM with smaller pores relative to the migrating cell unit, proteolytic degradation of the matrix is required to create sufficient 3D space into which cells can migrate (Friedl and Wolf, 2009; Wolf and Friedl, 2011). While the majority of these studies have been focused on single cells, recent work has shown that endothelial tip cells apply actomyosin-driven contractile forces to deform the ECM and that tip cell forces generate local collagen fibril alignment to help guide their continued invasion *via* contact guidance (Du et al., 2016; Vaeyens et al., 2020; Yoon et al., 2019). However, how trailing stalk cells of an invading sprout apply forces and remodel the ECM to provide the required space to increase sprout diameter and enable lumenization remains unknown.

In this work, we utilized a multiplexed angiogenesis-on-a-chip platform to examine how various soluble and physical microenvironmental cues regulate endothelial sprout morphology, namely, sprout stalk diameter. We identified soluble cues that modulate sprouting speed and proliferation to be anti- and positively correlated with sprout diameter, respectively. Interestingly, modulating sprouting speed with collagen matrix density resulted in a positive correlation between speed and diameter. As EC sprouts require space in 3D ECM to increase in stalk diameter, we examined how both biochemical remodeling *via* proteolytic matrix degradation and physical pushing forces driven by actomyosin and microtubules compact the ECM surrounding sprout stalk cells to regulate sprout morphology. Overall, this work expands our understanding of how endothelial stalk cells (in addition to previously established tip cells) within angiogenic sprouts dynamically interact with the surrounding ECM to control the morphology and eventual functionality of neovessels formed *via* angiogenesis.

6.4 Results

6.4.1 Endothelial cell migration speed and proliferation influence sprout diameter

To investigate how ECM remodeling events influence angiogenic sprout morphology, we implemented a recently established multiplexed angiogenesis-on-a-chip platform that affords improved experimental throughput to explore a wide parameter space of soluble and physical cues **(Figure 6.1a)** (Wang et al., 2020). This microfluidic-based device has been shown to recapitulate 3D EC sprouting morphogenesis from the stable, quiescent endothelium of a parent vessel (Nguyen et al., 2013; Trappmann et al., 2017; Wang et al., 2020; Yoon et al., 2019). The parent vessels modeled in this work possess a diameter (300 μm) that lies near the upper end of values previously described for arterioles but lack support cells such as vascular smooth muscle cells or pericytes; although these additional cell types can be included with this approach, we focused here on how microenvironmental cues affect ECs in the absence of confounding cross talk between cocultured cell types (Alimperti et al., 2017; Kinstlinger and Miller, 2016; Traore and George, 2017). To induce EC invasion into 3D ECM, we introduced an established EC chemoattractant, sphingosine 1-phosphate (S1P), to the adjacent chemokine channel to produce a diffusive gradient that drives EC activation and directional 3D invasion (Nguyen et al., 2013; Paik et al., 2001; Wang et al., 2020). As prior work has demonstrated that sprout invasion speed is anti-correlated with sprout diameter (Wood et al., 2012), we first investigated the effect of S1P on sprout morphology, as our previous studies indicate an S1P dose-dependent increase in invasion speed (Wang et al., 2020). Indeed, increasing S1P resulted in higher sprout invasion speeds **(Figure 6.1b-c)**. As the diameter along the length of a sprout was variable, we measured sprout diameters toward the sprout stalk region (30–50 μm away from the parent vessel edge and orthogonal to the long axis of each sprout). With increasing S1P and greater invasion speeds, sprout diameters decreased, producing

a significant and strong negative correlation between invasion speed and sprout diameter **(Figure 6.1d-e)**. In sum, this result within a distinct model system supports findings from prior studies (Wood et al., 2012).

In addition to chemoattractant-mediated directional EC invasion, another key requirement of angiogenesis is sufficient cell proliferation, which occurs predominantly within stalk cells of an invading angiogenic sprout (Gerhardt et al., 2003). To investigate the relationship between proliferation and sprout morphology, we supplemented EGM2 media with varying concentrations of phorbol 12-myristate 13-acetate (PMA), a well-established pro-angiogenic factor and potent activator of protein kinase C (PKC) upstream of cell proliferation (Cross et al., 2010; Nguyen et al., 2013; Osaki et al., 2015; Wang et al., 2020). To assess EC proliferation, we utilized an EdU assay that labels proliferating cell nuclei, while all cells were labeled with DAPI and UEA. Indeed, EC proliferation proved dose-dependent with PMA, where increasing PMA resulted in stepwise increases in proliferation rates (the ratio of EdU^+ cells to all cells labeled with DAPI and UEA) **(Figure 6.2a-b)**. Sprout diameter was also found to be dose-dependent with PMA, where increasing PMA led to larger diameters, yielding a significant and strong positive correlation between EC proliferation and sprout diameter **(Figure 6.1c-d)**. Taken together, soluble factors that drive cell invasion (i.e., S1P) and proliferation (i.e., PMA) differentially regulate resulting sprout morphology (i.e., diameter). Our previous work demonstrates a critical balance between these two fundamental cellular functions in maintaining cell–cell adhesion during collective sprout invasion (Wang et al., 2020). These findings suggest that a similar balance is required for invading ECs to generate sprout diameters in the <50 μm diameter range reported for microvasculature *in vivo* (Aird, 2005; Kinstlinger and Miller, 2016; Traore and George, 2017).

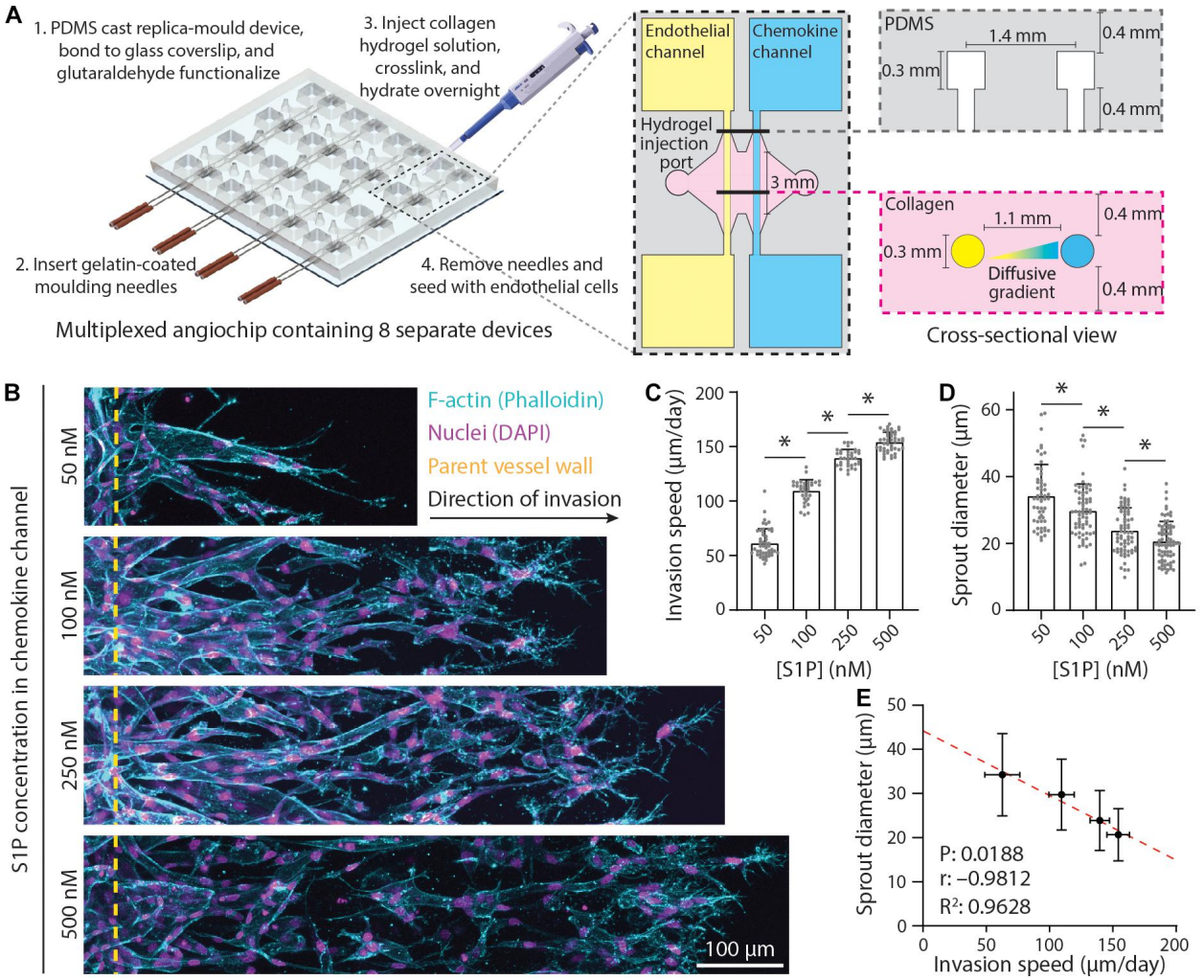

Figure 6.1: Endothelial sprout invasion speed is anti-correlated with sprout diameter.
a) Schematic overview of multiplexed angiogenesis-on-a-chip platform. Polydimethylsiloxane (PDMS) replica casts are generated from 3D printed molds and are composed of a 2 × 4 array of single devices. These PDMS molds are bonded to glass coverslips and functionalized with glutaraldehyde (Step 1). Gelatin-coated needles are then inserted into the device (Step 2). Type 1 collagen hydrogel precursor solution is injected into each device, allowed to cross-link around the needles, and hydrated overnight (Step 3). Needle removal generates 3D channels fully embedded within user-defined hydrogel (Step 4). Each device is composed of two parallel channels: (1) an endothelial channel seeded with endothelial cells (ECs) to serve as the parent vessel from which angiogenic sprouting is induced and (2) a chemokine channel to which pro-angiogenic factors [e.g., sphingosine 1-phosphate (S1P)] are added to generate diffusive gradients that promote EC activation and invasion across a user-defined 3D extracellular matrix (e.g., collagen hydrogel). **b)** Representative images (max intensity projections) of invading ECs in response to varying S1P. All conditions were cultured for 5 days with indicated S1P dose in endothelial cell growth medium 2 [EGM2; supplemented with 25 ng ml^{-1} phorbol 12-myristate 13-acetate (PMA)] added to the chemokine channel within 3 mg ml^{-1} collagen hydrogels. *F*-actin (cyan), nuclei (magenta), and yellow dashed lines indicate parent vessel edge. **c-d)** Quantifications of invasion speed and sprout diameter as a function of S1P. For invasion speed: $n \geq 36$ per condition and for sprout diameter: $n \geq 55$ per condition. **e)** Relationship between invasion speed and sprout

diameter, with red dashed line indicating a linear regression and statistical analysis performed by Pearson's correlation. Sample size for each mean was taken from panels (c-d). All data presented as mean ± SD; *indicates a statistically significant comparison with $P < 0.05$ (one-way analysis of variance).

6.4.2 Matrix density regulates sprouting speed and diameter

Beyond soluble biochemical factors, physical properties of ECM have also been shown to modulate angiogenesis (Crosby and Zoldan, 2019; Wang et al., 2020). We next investigated the influence of matrix density on sprout morphology (all previous studies were performed in 3 mg ml^{-1} collagen) under constant levels of S1P (250 nM) and PMA (25 ng ml^{-1}). With increasing collagen density, we observed no change in proliferation rates (perhaps due to PMA's potent effect on proliferation) but stepwise decreases in invasion speeds **(Figure 6.3a-c)**. Despite the reduction in invasion speeds, sprout diameter surprisingly decreased with increasing matrix density **(Figure 6.3d)**. We observed a weak positive correlation between proliferation and sprout diameter and a strong positive correlation between invasion speed and sprout diameter **(Figure 6.3e-f)**. We note that none of these correlations proved significant likely due to the low number of groups in the analysis. Thus, while diminishing the S1P chemoattractive gradient and increasing collagen density both act to slow sprout invasion, decreased invasion speeds do not consistently correlate with thicker sprouts. Modulating S1P in 3 mg ml^{-1} collagen yields a significant and strong negative correlation between speed and diameter while modulating matrix density results in a strong positive correlation.

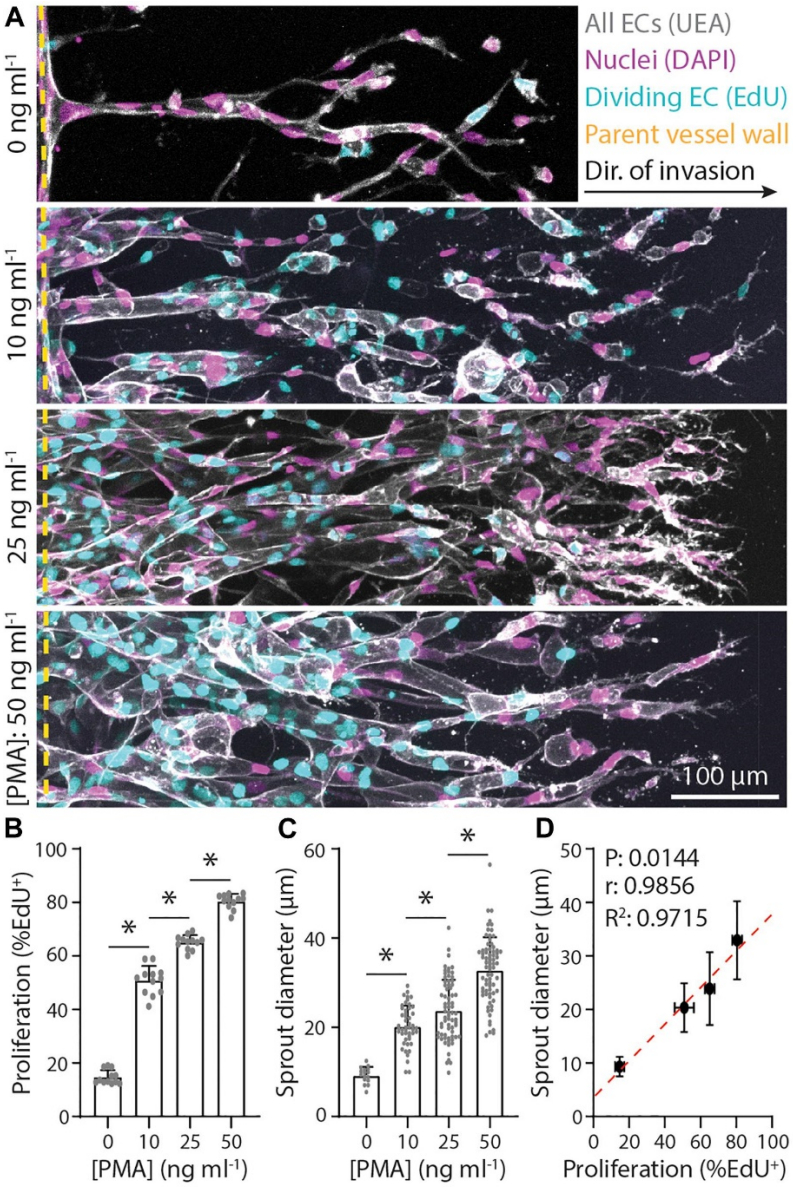

Figure 6.2: Endothelial stalk cell proliferation is positively correlated with sprout diameter. **a)** Representative images (max intensity projections) of invading endothelial cells (ECs) in response to varying phorbol 12-myristate 13-acetate (PMA). All conditions were cultured for 5 days with 250 nM sphingosine 1-phosphate (S1P) in endothelial cell growth medium 2 (EGM2; supplemented with indicated PMA) added to the chemokine channel within 3 mg ml^{-1} collagen hydrogels. Ulex Europaeus Agglutinin-1 (UEA; white), nuclei (magenta), 5-ethynyl-2′-deoxyuridine (EdU; cyan), and yellow dashed lines indicate parent vessel edge. **b-c)** Quantifications of proliferation and sprout diameter as a function of PMA. For proliferation: $n \geq 12$ per condition and for sprout diameter: $n \geq 16$ per condition. **d)** Relationship between proliferation and sprout diameter, with red dashed line indicating a linear regression and statistical analysis performed by Pearson's correlation. Sample size for each mean is identical to those of panels (b-c). All data presented as mean ± SD; *indicates a statistically significant comparison with $P < 0.05$ (one-way ANOVA).

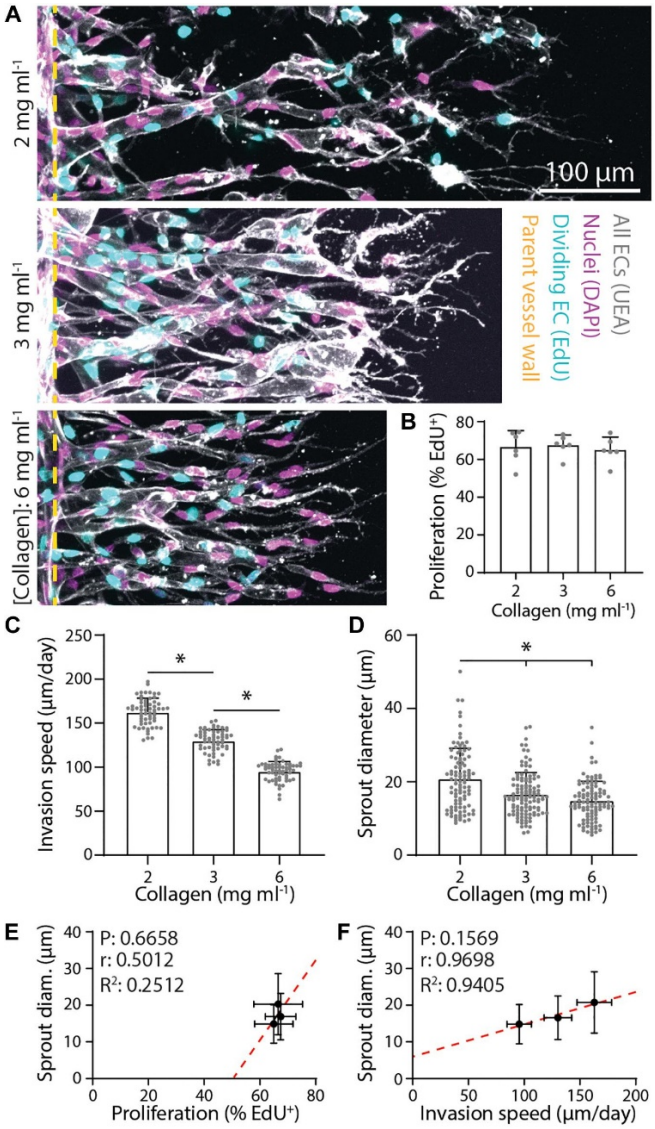

Figure 6.3: Denser matrix that slows sprout invasion leads to smaller sprout diameters.
a) Representative images (max intensity projections) of invading endothelial cells (ECs) in response to varying collagen density. All conditions were cultured for 3 days with 250 nM sphingosine 1-phosphate (S1P) in endothelial cell growth medium 2 [EGM2; supplemented with 25 ng ml^{-1} phorbol 12-myristate 13-acetate (PMA)] added to the chemokine channel within collagen hydrogels of the indicated density. Nuclei (magenta), 5-ethynyl-2′-deoxyuridine (EdU; cyan), Ulex Europaeus Agglutinin-1 (UEA; white), and yellow dashed lines indicate parent vessel edge. **b-d)** Quantifications of proliferation, invasion speed, and sprout diameter as a function of collagen hydrogel density. For proliferation: $n \geq 6$ per condition, for invasion speed: $n \geq 60$ per condition, and for sprout diameter: $n \geq 100$ per condition. **e-f)** Relationships between proliferation and sprout diameter (e) and invasion speed and sprout diameter (f), with red dashed lines indicating a linear regression and statistical analyses performed by Pearson's correlation. Sample size for each mean is identical to those of panels (b–d). All data presented as mean ± SD; *indicates a statistically significant comparison with $P < 0.05$ (one-way ANOVA).

6.4.3 Dynamic sprout-extracellular matrix interactions regulate sprout diameter

To further investigate these seemingly contradictory invasion speed vs. sprout diameter relationships, we employed live time-lapse imaging with fluorescently labeled collagen to capture dynamic cell–ECM interactions over the course of EC sprouting through 3D ECM. As angiogenic sprouting occurs over several days, we first performed live cell imaging over 24 h imaging intervals to examine long-term changes **(Figure 6.4a)**. Imaging the same region over 5 days, we observed the invasion of an endothelial tip cell at day 1 with no appreciable changes to the surrounding ECM structure or density. By day 2, tip cells continued invading and led ensuing stalk cells, with localized collagen degradation evident at the location of the sprout stalk. Over days 3–5, sprouts continued to elongate as well as expand laterally, increasing in diameter. Interestingly, the area devoid of collagen continued to grow with expansion of the sprout, with marked increases of collagen fluorescence intensity at the sprout periphery. This observation suggests collagen is not only proteolytically degraded but also physically compacted by stalk cells to accommodate the expanding sprout. We next employed time-lapse imaging at shorter frame intervals (every 20 min over 8 h) on day 2 of culture to capture more transient cell–ECM interactions **(Figure 6.4b-c and Supplemental Movie 6.1)**. The dynamics of sprout morphology (fluctuations in sprout diameter) mirrored that of the surrounding collagen matrix, with the compacted peripheral zone of collagen moving in tandem with the expanding diameter of the sprout (best viewed in **Supplemental Movie 6.1**). Live cell imaging over these two different timescales suggests that over shorter durations (<1 day), invading sprouts appear to dynamically displace the surrounding collagen through active cellular shape changes and resulting forces. Over longer timescales (>1 day), sprouts can degradatively remodel the collagen to create space for the growing sprout.

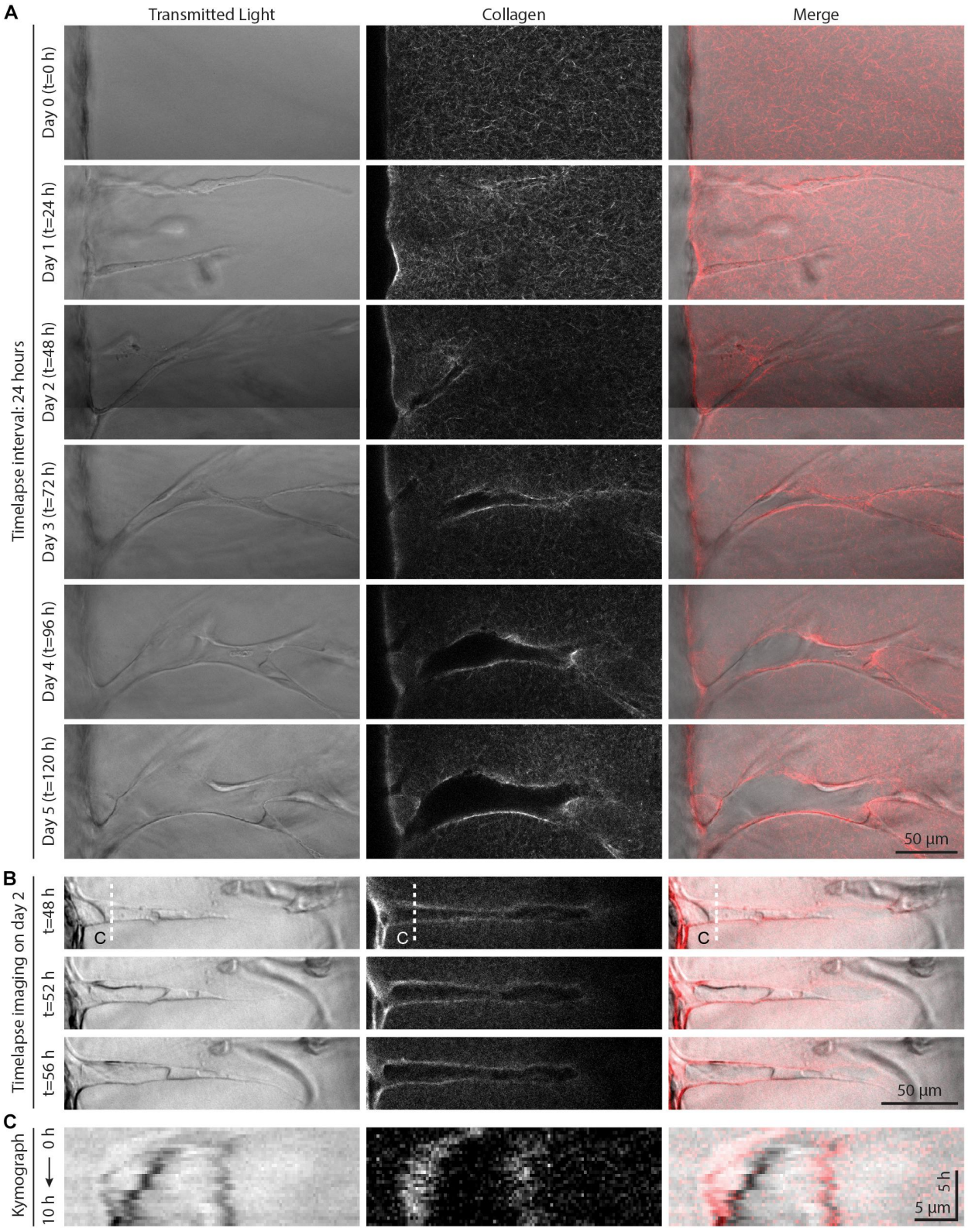
A
Transmitted Light
Collagen
Merge
Timelapse interval: 24 hours
Day 0 (t=0 h)
Day 1 (t=24 h)
Day 2 (t=48 h)
Day 3 (t=72 h)
Day 4 (t=96 h)
Day 5 (t=120 h)
50 µm
B
Timelapse imaging on day 2
t=48 h
t=52 h
t=56 h
C
50 µm
C
Kymograph
0 h
10 h
5 h
5 µm

Figure 6.4: Live time-lapse imaging reveals dynamic sprout and extracellular matrix (ECM) interactions.
a) Representative time course images (individual z-slices) of an invading sprout over 5 days with a frame interval of 24 h. Sprouts were cultured in 250 nM sphingosine 1-phosphate (S1P) and 50 ng ml^{-1} phorbol 12-myristate 13-acetate (PMA) within 3 mg ml^{-1} collagen hydrogel. **b)** Representative time course images (individual z-slices) of an invading sprout over 8 h with a frame interval of 20 min (for full time-lapse series, see **Supplemental Movie 6.1**). Sprouts were cultured in 250 nM S1P and 50 ng ml^{-1} PMA within 3 mg ml^{-1} collagen hydrogel, and imaging was initiated after 2 days in culture. **c)** Kymographs taken along white dashed line indicated in panel (b).

Given that both physical compaction and degradative remodeling would be significantly influenced by matrix density, we next examined sprout stalk-driven collagen compaction as a function of collagen density. To measure a relative degree of collagen compaction, sprouts were allowed to invade in fluorescent collagen and line intensity profiles orthogonal to the long axis of each sprout 30–50 μm away from the parent vessel edge were acquired by confocal imaging (shaded lines in **Figure 6.5a**). An intensity fold change was determined by normalizing fluorescence intensity to a baseline collagen intensity from surrounding acellular regions **(Figure 6.5b)**. Collagen compaction diminished with increasing collagen density, suggesting that with higher collagen density, expansive stalk cell forces are no longer sufficient to compact the surrounding matrix, thereby restricting lateral expansion of growing sprouts **(Figure 6.5c)**. Supporting this, we noted a significant and strong positive correlation between the degree of collagen compaction and sprout diameter **(Figure 6.5d)**. Additionally, GA treatment of collagen hydrogels, which introduces non-cell-degradable cross-links and increases collagen gel stiffness, also reduced the degree of collagen compaction and sprout diameter **(Figure 6.5a-d)**. As cytoskeletal proteins are responsible for cellular shape changes associated with forces applied to the ECM, we co-stained sprouts for *F*-actin and α-tubulin. *F*-actin and α-tubulin were both enriched and co-localized along the periphery of sprout stalks where collagen compaction was also

most pronounced, suggesting that actomyosin and microtubules provide the driving forces behind matrix compaction **(Figure 6.5e)**. Taken together, sprout stalk cells dynamically engage and deform the surrounding ECM and over longer timescales, can permanently remodel the structure to create sufficient space for the growing sprout.

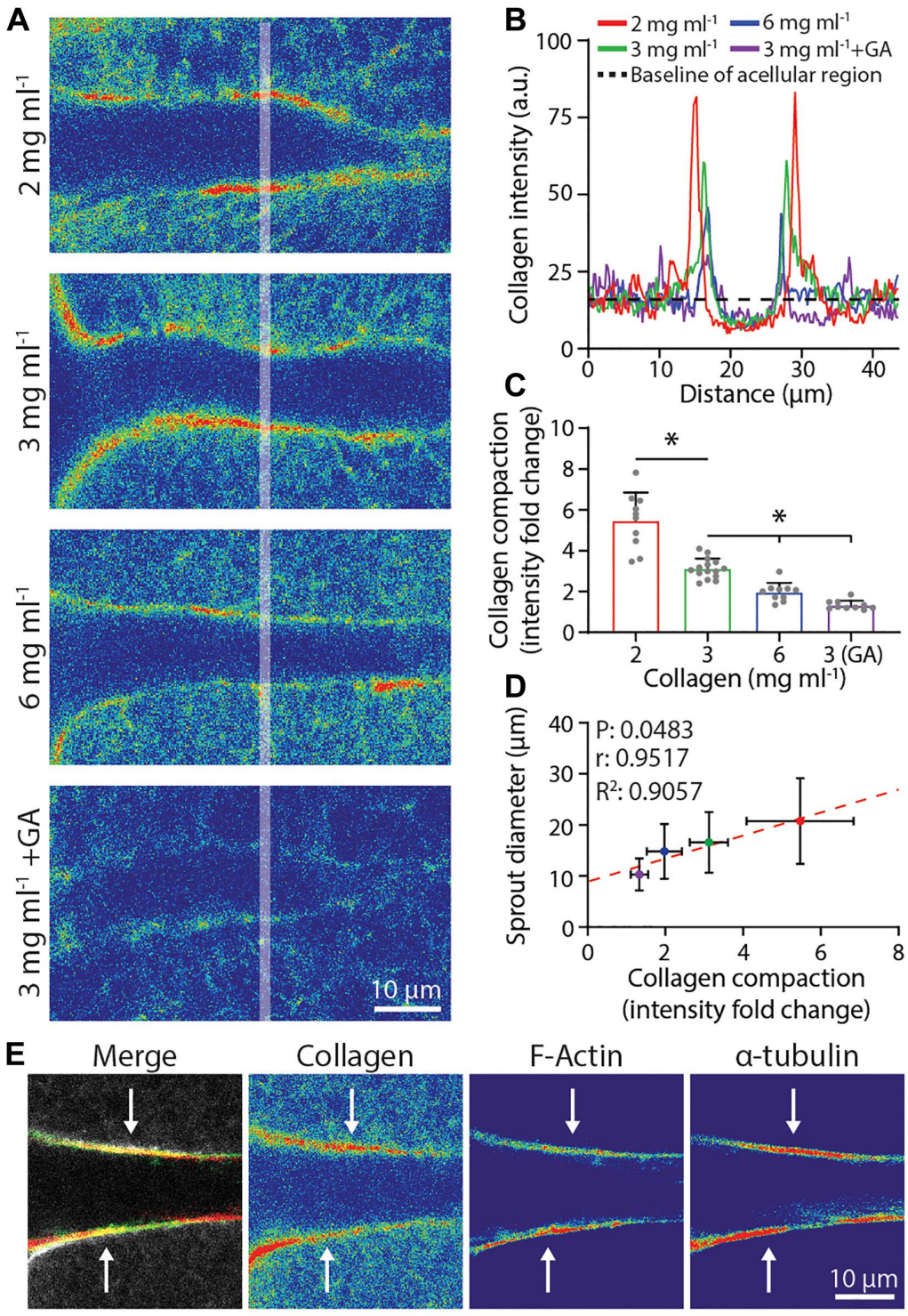

Figure 6.5: Degree of collagen compaction adjacent to sprout stalk cells positively correlates with sprout diameter.

a) Representative images (individual z-slices) of fluorescently labeled collagen (shown as intensity heat map) surrounding sprout stalk cells in collagen matrices of varying density and stiffness. Sprouts were cultured for 3 days in 250 nM sphingosine 1-phosphate (S1P) and 50 ng ml^{-1} phorbol 12-myristate 13-acetate (PMA) within collagen matrices of indicated density or with

glutaraldehyde (GA) cross-linking. **b)** Representative fluorescent collagen intensity profiles acquired along shaded white line indicated in panel (a). 2 mg ml^{-1} (red line), 3 mg ml^{-1} (green line), 6 mg ml^{-1} (blue line), and 3 mg ml^{-1} with GA cross-linking (purple line) and average intensity of non-compacted, acellular areas (dashed black line). Intensity values of the non-compacted, acellular collagen regions were normalized to each other in panels (a-b) to compare collagen intensity fold change of compacted regions. **c-d)** Quantification of collagen compaction and relationship between collagen compaction and sprout diameter, with red dashed line indicating a linear regression and statistical analysis performed by Pearson's correlation. For collagen compaction: $n \geq 10$ per condition. For each mean in panel (d), $n \geq 10$ for collagen compaction and $n \geq 70$ for sprout diameter. **e)** Representative images (individual *z*-slices) of sprout stalk region stained for *F*-actin (green) and α-tubulin (red) within fluorescently labeled collagen (gray). Individual channels visualized as intensity heat maps. All data presented as mean ± SD; *indicates a statistically significant comparison with $P < 0.05$ (one-way ANOVA).

6.4.4 Actomyosin, microtubules, and proteolysis regulate sprout diameter and extracellular matrix compaction

As F-actin and α-tubulin appeared to be enriched at areas of collagen compaction at the sprout stalk periphery and are known drivers of cell shape and cell-mediated matrix deformations, we used pharmacologic inhibitors of actomyosin activity and microtubule assembly to test whether they cooperatively regulate sprout diameter and ECM compaction. The addition of 25 μM blebbistatin, a myosin II inhibitor, resulted in decreased sprout diameters with corresponding decreases in collagen compaction **(Figure 6.6a-d)**. Reducing microtubule assembly with the addition of 50 ng ml^{-1} nocodazole also resulted in decreased collagen compaction but without commensurate decreases in sprout diameter **(Figure 6.6a-d)**. Live imaging revealed nocodazole-treated stalk cells lose connectivity to tip cells and retract collectively toward the parent vessel **(Supplemental movie 6.2)**. In retracting and reducing their length, stalk cells condensed, and expanded laterally. Lacking the ability to re-extend, nocodazole-treated sprouts were shorter in length (i.e., invasion depth) and sprout diameters were not significantly different compared to

controls. Sprouts treated with podophyllotoxin, which fully prevents microtubule assembly, resulted in disassembly of multicellular sprouts into individual cells **(Supplemental Movie 6.3)**.

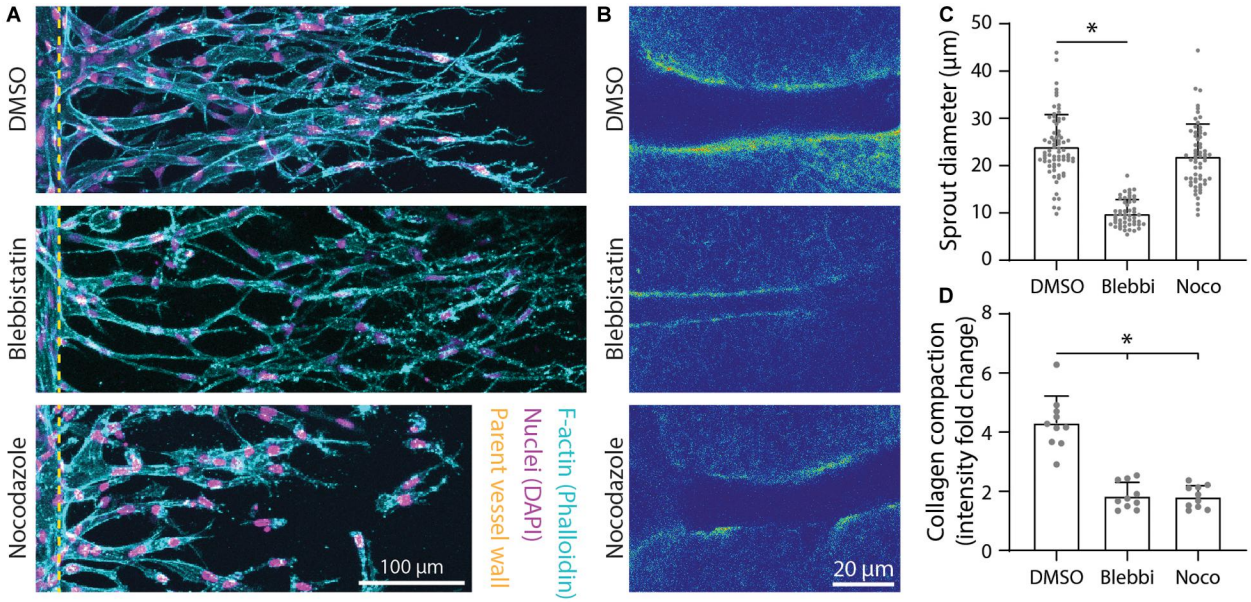

Figure 6.6: Inhibition of actomyosin activity and microtubule polymerization reduces collagen compaction.
a) Representative images (max intensity projections) of dimethylsulfoxide (DMSO) control, 25 µM blebbistatin-, and 50 ng ml^{-1} nocodazole-treated sprouts cultured over 5 days with 250 nM sphingosine 1-phosphate (S1P) and 25 ng ml^{-1} phorbol 12-myristate 13-acetate (PMA) within 3 mg ml^{-1} collagen. **b)** Representative images (individual z-slices) of fluorescently labeled collagen (intensity heat map) of conditions from panel (a). **c-d)** Quantifications of sprout diameter and collagen compaction from conditions in panels (a-b). For sprout diameter: $n \geq 52$ per condition and for collagen compaction: $n \geq 10$ per condition. All data presented as mean ± SD; *indicates a statistically significant comparison to DMSO control with $P < 0.05$ (two-tailed Student's *t*-test).

In addition to physical reorganization of ECM, EC sprouts also enzymatically degrade the ECM by using matrix metalloproteinases (MMPs) to create space in 3D. Utilizing a collagen hybridization peptide (CHP), which binds to degraded collagen (individual collagen peptides cleaved from tropo-collagen), we found CHP to be enhanced along the periphery of sprout stalks relative to acellular ECM regions **(Figure 6.7a)**. The addition of 1 µM marimastat, a broad-spectrum MMP inhibitor, over 5 days of culture resulted in decreased sprout diameter but without

changes to the degree of collagen compaction **(Figure 6.7b-e)**. To assess whether sprout diameter impacts subsequent lumenization and perfusability, we perfused 1 μm-diameter fluorescent microspheres through the endothelial channel. We found that all sprouts with a diameter < 6 μm were incapable of supporting microsphere perfusion within the multicellular sprout, while all sprouts with a diameter ≥ 11 μm were lumenized, as evident by the presence of microspheres within sprouts **(Figure 6.7f-g)**. Sprouts with diameters between 6 and 11 μm displayed a stepwise increase in the percentage of sprouts that were perfused with microspheres with increasing sprout diameter **(Figure 6.7g)**. Taken together, EC sprouts create space in 3D ECM with a combination of biochemical and physical means to afford increases in sprout diameter and lumenization. Inhibition of actomyosin and microtubules reduced collagen compaction around sprout stalk cells and are critical regulators of maintaining EC invasion morphology as collective, multicellular strands **(Figure 6.6)**. Reduction of matrix proteolysis decreases sprout diameter; however, persistent actomyosin and microtubule-driven expansive forces were sufficient to physically reorganize ECM and enable the invasion of thin multicellular strands **(Figure 6.7)**.

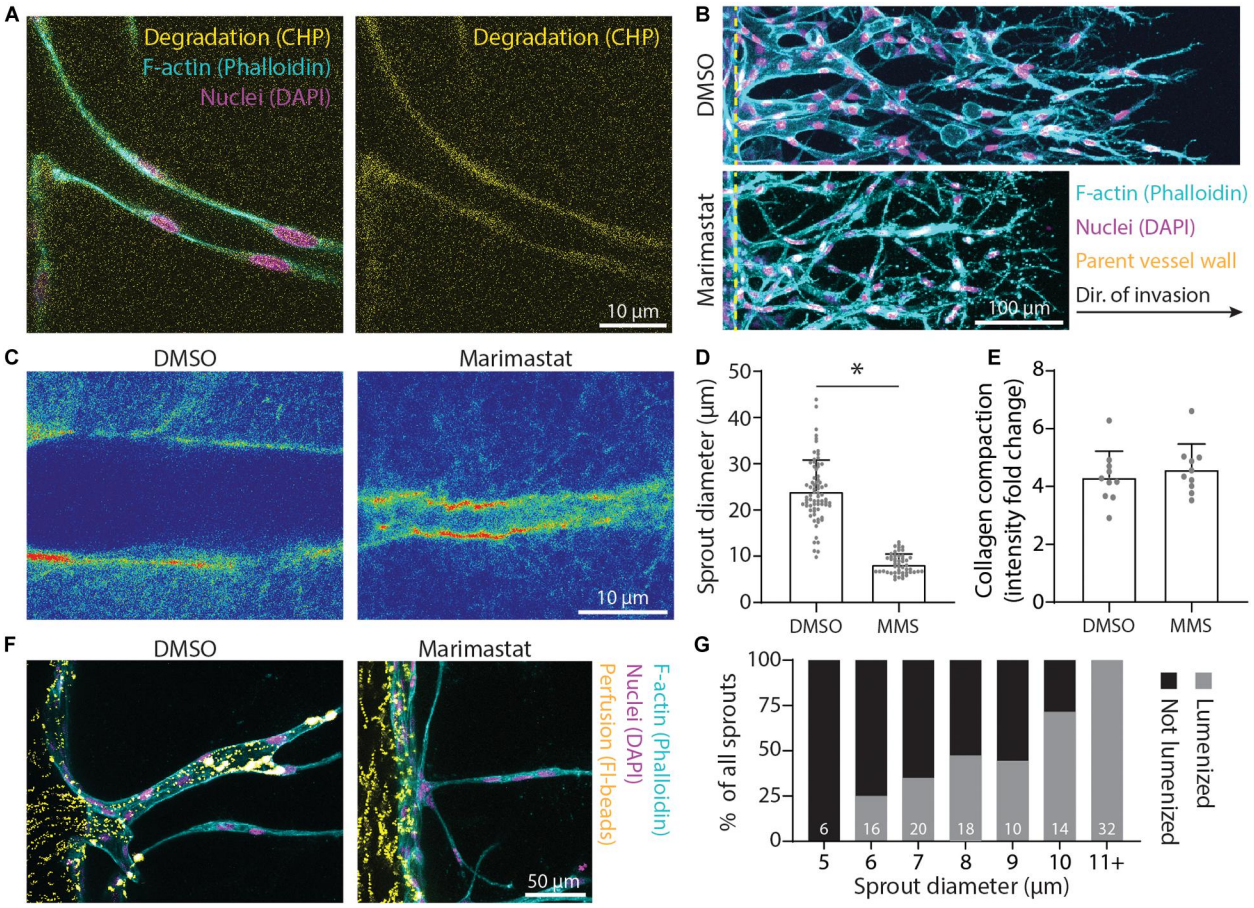

Figure 6.7: Matrix proteolysis is required for larger sprout diameters that are lumenized. **a)** Representative image (individual *z*-slices) of collagen degradation along sprout stalk cells. *F*-actin (cyan), nuclei (magenta), collagen hybridization peptide (CHP; yellow). **b)** Representative images (max intensity projections) of marimastat (MMS) treatment (1 µM) of sprouts cultured over 5 days with 250 nM sphingosine 1-phosphate (S1P) and 25 ng ml^{-1} phorbol 12-myristate 13-acetate (PMA) within 3 mg ml^{-1} collagen. **c)** Representative images (single z-slice) of fluorescently labeled collagen (intensity heat map) with MMS treatment (1 µM) of sprouts cultured over 3 days with 250 nM S1P and 25 ng ml^{-1} PMA within 3 mg ml^{-1} collagen. **d-e)** Quantifications of sprout diameter and collagen compaction from MMS treatment (1 µM). For sprout diameter: $n \geq 50$ per condition and for collagen compaction: $n \geq 10$ per condition. **f-g)** Assessment of lumenization as a function of sprout diameter by parent vessel perfusion of 1 µm-diameter microsphere. Sample size for total sprouts analyzed for each group is indicated in bar plot. All data presented as mean ± SD; *indicates a statistically significant comparison with $P < 0.05$ (two-tailed Student's *t*-test).

6.5 Discussion

The relationship between microenvironmental cues, angiogenic sprout morphology, and subsequent neovessel function remains relatively understudied. Our group recently established that the multicellularity of invading ECs dictates the subsequent function (perfusability and permeability) of formed neovessels (Trappmann et al., 2017; Wang et al., 2020). The work presented here builds upon this structure–function relationship, highlighting how cytoskeletal and proteolytic machinery of sprout stalk cells enzymatically remodel and mechanically compact the surrounding ECM to create sufficient space to laterally expand sprout stalks and enable lumenization. With increased collagen matrix density or stiffening from GA cross-linking, stalk cell-mediated collagen compaction decreased as cell-generated forces were likely insufficient to compact a more mechanically resistant ECM, thus yielding smaller sprout diameters **(Figure 6.3)**. Additionally, increasing matrix density or stiffening with GA cross-linking led to a stiffer ECM more resistant to proteolysis, thus requiring enhanced MMP activity and/or cell-generated forces to generate open space for growing sprouts. Modulating EC proliferation with PMA, we found sprout diameters increased with increases in stalk cell proliferation **(Figure 6.2)**; we anticipate cell-generated forces and proteolysis are likely cell density dependent, where increased cell density may lead to locally higher levels of multicellular force generation and higher rates of proteolysis, thus resulting in enhanced ECM degradation and compaction that afford more space for larger sprout diameters. Lastly, cytoskeletal forces and proteolysis remodeled the ECM more drastically over longer timescales (days) **(Figure 6.4)**; modulating sprouting speed with soluble chemoattractants resulted in faster invasion speeds and decreased sprout diameters, which may spatiotemporally limit physical and proteolytic interactions between stalk cells and adjacent matrix **(Figure 6.1)**.

Toward the design of pro-angiogenic biomaterials that promote host angiogenesis, this work highlights a critical need for biomaterial cues that promote sprout stalk cell-mediated increases in diameter and subsequent lumenization. While natural materials such as collagen and fibrin hydrogels offer sufficient microporosity and enable cell-mediated remodeling to create space, following implantation, these materials are rapidly resorbed and lose their initial structural integrity (Thomson et al., 2013; Vigen et al., 2014). Thus, a major focus in the design of pro-angiogenic biomaterials has been placed on designing tunable synthetic hydrogels with enhanced specificity over degradative mechanisms and tunability over resorption rates to retain integrity upon implantation (Li et al., 2017a). Facilitating sprout-mediated matrix remodeling by modulating synthetic hydrogel degradability could augment sprout diameters *via* proteolysis but at the cost of also enhancing resorption rates. Viscoelastic hydrogels could take advantage of proteolysis-independent methods of space generation *via* cell force-mediated pushing forces, as previous studies have demonstrated plastic deformation of hydrogels with viscoelastic behavior (Chaudhuri et al., 2020; Wei et al., 2020). As increased EC proliferation resulted in enhanced sprout diameters, incorporating matrix cues that additionally enhance proliferation in 3D synthetic hydrogel settings would also be beneficial. While matrix stiffness in 2D settings enhances proliferation, increased stiffness in 3D has been shown to decrease cell proliferation and spreading likely due to the confinement of cells in typically nanoporous synthetic hydrogels and the requirement for significant degradation prior to cell spreading, which appears to be a prerequisite for proliferation of adherent cells (Khetan et al., 2013). As native ECM is primarily composed of fibrillar collagens, recent work from our group has designed composite materials composed of stiff, microscale fibers embedded within soft bulk hydrogels (Matera et al., 2019, 2020). These composite hydrogels containing stiff adhesive structures that promote cell spreading and

proliferation could have utility for angiogenesis. Lastly, generating sufficient space within nanoporous synthetic hydrogels can be approached with subtractive materials engineering methods rather than a cell-mediated process. Recent techniques in 3D printing vessel conduits, photoablation of microtracks, and microporous annealed particles are capable of generating material porosity at various length scales to enhance vascularization (Arakawa et al., 2020; Griffin et al., 2015; Mirabella et al., 2017). The continued advancement of synthetic biomaterials and careful consideration of dynamic sprout-mediated matrix reorganization will be critical for the future development of pro-angiogenic biomaterial implants.

While much progress has been made on understanding how matrix properties regulate sprouting angiogenesis, only recently have we begun to appreciate the dynamic bidirectional interactions between ECM and collectively invading EC sprouts (Helvert et al., 2018). Most studies define and characterize the initial matrix state and then measure the subsequent cell response. However, as highlighted by this work, EC sprouts dynamically reorganize and remodel ECM structure and mechanics using cytoskeletal forces and proteolytic activity over extended timescales required for complex morphogenetic processes. To understand how cell-altered ECM iteratively and reciprocally influences cell processes requires advances in characterization techniques that probe cell–matrix interactions across space and time. Here, we employed live time-lapse imaging of fluorescently labeled ECM to characterize matrix compaction mirroring sprout morphology fluctuations over short timescales (minutes) and matrix degradation and compaction corresponding to increases in sprout diameter over longer timescales (days). To more closely examine how cells may dynamically alter the matrix state, future work could integrate recent advances in metabolic labeling of secreted proteins to examine matrix deposition (Loebel, C, Mauck, RL, Burdick, 2019), fluorescence resonance energy transfer (FRET)-based protease

microgels to assess protease activity (Shin et al., 2018), and techniques such as magnetic bead microrheology to spatially characterize matrix stiffness (Juliar et al., 2018). Coupling these matrix state analysis techniques with cell state measurement techniques such as fluorescent fusion-tagged proteins, FRET-based reporters of forces across cytoskeletal proteins (Grashoff et al., 2010; Ham et al., 2019), and transcription factor activity reporters (Aguado et al., 2015) would provide new insights on the dynamic and bidirectional relationships between cells and surrounding matrix. The continued development and deployment of such techniques will be essential in further elucidating critical aspects of cell–matrix reciprocity during the complex and dynamic process of sprouting angiogenesis.

6.6 Materials and Methods

6.6.1 Reagents

All reagents were purchased from Sigma-Aldrich and used as received, unless otherwise stated.

6.6.2 Microfluidic device fabrication

The 3D printed molds were designed in AutoCAD and printed *via* stereolithography by Protolabs (Maple Plain, MN, United States). Polydimethylsiloxane (PDMS, 1:10 cross-linker:base ratio) devices were replica casted from 3D printed molds, cleaned with isopropyl alcohol and ethanol, and bonded to glass coverslips activated by a plasma etcher. Devices were treated with 0.01% (w/v) poly-L-lysine and 0.5% (w/v) L-glutaraldehyde sequentially for 1 h each (with Milli-Q rinses in between) to promote ECM attachment to the PDMS housing, thus preventing potential hydrogel compaction from cell-generated forces. To generate patent microchannels, 300 μm stainless steel acupuncture needles (Lhasa OMS, Weymouth, MA, United States) were dip-coated

with 1% (w/v) gelatin to enable eventual hydrogel release, inserted into each device and sterilized by UV ozone. Hydrogel precursor solution was then injected into each device and polymerized around each set of needles. Hydrogels were hydrated in Endothelial cell growth medium-2 (EGM2) containing 50 mM glycine [to quench unreacted glutaraldehyde (GA)] and incubated at 37°C overnight to dissolve the gelatin layer. Needles were subsequently removed, yielding 3D microchannels fully embedded within a collagen hydrogel positioned 400 μm away from PDMS and glass boundaries **(Figure 6.1a)**.

6.6.3 Collagen hydrogel formulation

Type I rat tail collagen hydrogels (Corning, Corning, NY, United States) were prepared on ice with a reconstitution buffer (10 mM HEPES, 0.035% w/v sodium bicarbonate, 1 × M199), titrated to a pH of 7.6 with 1 M NaOH, and brought to a final concentration of 2, 3, or 6 mg ml^{-1} collagen. Collagen hydrogels were cross-linked for 30 min at 37°C. All hydrogels were hydrated in EGM2 media after cross-linking. Fluorescently labeled collagen was prepared as in (Doyle, 2016) and incorporated at 2 wt.% of the total collagen content (1:50 dilution in unlabeled collagen).

6.6.4 Device cell seeding and culture

Human umbilical vein ECs (HUVECs; Lonza, Switzerland) were cultured in endothelial growth media (EGM2; Lonza). HUVECs were passaged upon achieving confluency at a 1:4 ratio and used in studies from passages 4–9. A 20 μl solution of suspended HUVECs was added to one reservoir of the endothelial channel and inverted for 30 min to allow cell attachment to the top half of the channel, followed by a second seeding with the device upright for 30 min to allow cell

attachment to the bottom half of the channel. HUVEC solution density was varied with collagen density as attachment efficiency was dependent on collagen density (Wang et al., 2020). HUVEC seeding densities were determined experimentally to achieve parent vessels with consistent cell densities across each hydrogel formulation (1.5 M ml^{-1} for 2 mg ml^{-1}, 2 M ml^{-1} for 3 mg ml^{-1}, and 5 M ml^{-1} for 6 mg ml^{-1}). HUVECs reached confluency and self-assembled into stable parent vessels over 24 h. Media and chemokines were refreshed every 24 h, and devices were cultured with continual reciprocating flow utilizing hydrostatic pressure-driven flow on a seesaw rocker plate at 0.33 Hz. For pharmacological studies, 25 μM blebbistatin (Santa Cruz Biotechnology, Dallas, TX, United States), 50 ng ml^{-1} nocodazole, and 1 μM marimastat were added to both endothelial and chemokine channel media and refreshed every 24 h.

6.6.5 Fluorescent staining

Samples were fixed with 4% paraformaldehyde and permeabilized with a phosphate-buffered saline (PBS) solution containing Triton X-100 (5% v/v), sucrose (10% w/v), and magnesium chloride (0.6% w/v) for 1 h each at room temperature. AlexaFluor 488 phalloidin (diluted 1:500; Life Technologies, Carlsbad, CA, United States) was utilized to visualize *F*-actin. In addition, 4′,6-diamidino-2-phenylindole (DAPI; 1 μg ml^{-1}) was utilized to visualize cell nuclei. For proliferation studies, 5-ethynyl-2′-deoxyuridine (EdU) was applied for the final 24 h prior to fixation of each study. EdU fluorescent labeling was performed following the manufacturer's protocol (ClickIT EdU, Life Technologies). DyLight 649 labeled Ulex Europaeus Agglutinin-1 (UEA, 1:200, Vector Labs, Burlingame, CA, United States) was utilized to visualize EC morphology in samples stained with EdU due to the incompatibility of EdU ClickIT chemistry with phalloidin staining. To visualize α-tubulin, samples were sequentially blocked in bovine

serum albumin (0.3% w/v), incubated with primary mouse monoclonal anti-α-tubulin (1:200, Invitrogen), and incubated with secondary AlexaFluor 647 goat anti-mouse IgG (H+L) (1:1,000; Life Technologies) each for 8 h at room temperature. To visualize collagen degradation, collagen hybridizing peptide (5 μM; 3 Helix, Salt Lake City, Utah) was heated to 80°C for 5 min, then chilled in an ice-water bath for 30 s, and added to samples for 8 h.

6.6.6 Microscopy and image analysis

Fluorescent images were captured on a Zeiss LSM800 confocal microscope. Time-lapse imaging was performed on sprouts after 2 days of culture in an environmentally controlled chamber (37°C, 5% CO_2, and 100% humidity) with images acquired every 20 min over 8 h. For time-lapse imaging with 24-h frame intervals, devices were cultured in the incubator and transported to the microscope stage for daily imaging in a custom stage holder such that specific regions of interest were maintained over the 5-day imaging period. EC density and proliferation (EdU-positive nuclei) within sprouts were quantified by counting DAPI and EdU-positive cell nuclei. Invasion depth was quantified as the distance from the parent vessel edge to each sprout's tip cell and measured manually in FIJI at 100 μm intervals along the parent vessel. Sprout diameter measurements were taken orthogonal to the long axis of the sprout, 30–50 μm away from the parent vessel edge. Collagen compaction analyses were performed by acquiring intensity profiles along the sprout stalk region orthogonal to the long axis of the sprout, 30–50 μm away from the parent vessel edge (i.e., identical region to sprout diameter measurements). Given differences in fluorescent intensity as a function of initial collagen hydrogel density, images of acellular regions were used to determine baseline collagen intensity to normalize measurements following

remodeling. The intensity fold change of the compacted collagen area (sprout periphery) compared to the baseline collagen intensity was utilized as a relative measure of collagen compaction.

6.6.7 Statistics

Statistical significance was determined by one-way analysis of variance (ANOVA), two-sided Student's *t*-test, or Pearson's correlation where appropriate, with significance indicated by $P < 0.05$. Pearson's correlation was performed on sample mean values for each group without accounting for total sample size; a strong correlation was defined as $R^2 > 0.7$. Sample size is indicated within corresponding figure legends, and all data are presented as mean ± standard deviation.

6.7 Supplementary Material

Supplementary Movie 6.1: Time-lapse imaging of sprout-ECM dynamics cultured in 250 nM S1P and 50 ng ml^{-1} PMA within 3 mg ml^{-1} fluorescently labeled collagen hydrogel. Time-lapse imaging was initiated after 48 h of sprouting. Transmitted light (top), fluorescent collagen (middle), and merge (bottom).
https://www.frontiersin.org/articles/10.3389/fbioe.2021.620128/full#supplementary-material

Supplementary Movie 6.2: Time-lapse imaging of nocodazole treated sprouts. Sprouts were cultured in 250 nM S1P and 25 ng ml^{-1} PMA within 3 mg ml^{-1} collagen hydrogel. 50 ng ml^{-1} nocodazole was first administered to sprouts along with the initiation of time-lapse imaging after 48 h of sprouting.
https://www.frontiersin.org/articles/10.3389/fbioe.2021.620128/full#supplementary-material

Supplementary Movie 6.3: Time-lapse imaging of podophyllotoxin treated sprouts. Sprouts were cultured in 250 nM S1P and 25 ng ml^{-1} PMA within 3 mg ml^{-1} collagen hydrogel. 100 nM podophyllotoxin was first administered to sprouts along with the initiation of time-lapse imaging after 48 h of sprouting.
https://www.frontiersin.org/articles/10.3389/fbioe.2021.620128/full#supplementary-material

Chapter 7: Direct Comparison of Angiogenesis in Natural and Synthetic Biomaterials Reveals Matrix Porosity Regulates Endothelial Cell Invasion Speed and Sprout Diameter

7.1 Authors

William Y. Wang, Robert N. Kent III, Stephanie A. Huang, Evan H. Jarman, Eve H. Shikanov, Christopher D. Davidson, Harrison L. Hiraki, Daphne Lin, Monica A. Wall, Jae-Won Shin, William J. Polacheck, Ariella Shikanov, Brendon M. Baker

7.2 Abstract

Vascularization of large, diffusion-hindered biomaterial implants requires an understanding of how extracellular matrix (ECM) properties regulate angiogenesis. Sundry biomaterials assessed across many disparate angiogenesis assays have highlighted ECM determinants that influence this complex multicellular process. However, the abundance of material platforms, each with unique parameters to model endothelial cell (EC) sprouting presents additional challenges of interpretation and comparison between studies. In this work we directly compared the angiogenic potential of commonly utilized natural (collagen and fibrin) and synthetic dextran vinyl sulfone (DexVS) hydrogels in a multiplexed angiogenesis-on-a-chip platform.

Modulating matrix density of collagen and fibrin hydrogels confirmed prior findings that increases in matrix density correspond to increased EC invasion as connected, multicellular sprouts, but with decreased invasion speeds. Angiogenesis in synthetic DexVS hydrogels, however, resulted in fewer multicellular sprouts. Characterizing hydrogel Young's modulus and permeability (a measure of matrix porosity), we identified matrix permeability to significantly correlate with EC invasion depth and sprout diameter. Although microporous collagen and fibrin hydrogels produced lumenized sprouts *in vitro*, they rapidly resorbed post-implantation into the murine epididymal fat pad. In contrast, DexVS hydrogels proved comparatively stable. To enhance angiogenesis within DexVS hydrogels, we incorporated sacrificial microgels to generate cell-scale pores throughout the hydrogel. Microporous DexVS hydrogels resulted in lumenized sprouts *in vitro* and enhanced cell invasion *in vivo*. Towards the design of vascularized biomaterials for long-term regenerative therapies, this work suggests that synthetic biomaterials offer improved size and shape control following implantation and that tuning matrix porosity may better support host angiogenesis.

7.3 Introduction

The vascularization challenge remains a major hurdle to the clinical translation of engineered tissue repair and organ replacement therapies (Novosel et al., 2011; Rouwkema et al., 2009). A major focus has been placed on engineering microscale vessels within implantable biomaterials, as nearly all tissues *in vivo* are supplied with oxygen and nutrients by a hierarchical vascular network of larger diameter arterioles and venules bridged by dense microscale capillary beds (Pellegata et al., 2018). An emerging strategy to engineer microvasculature lies in the design of implantable biomaterials that support angiogenesis, the invasive biological process by which pre-existing microvasculature extends. Biomaterials capable of initiating angiogenesis

from the host vasculature and recruiting invasive microvessels could ensure circulation between the host and implant. Angiogenesis is generally accepted to be a multi-step process involving 1) chemokine gradients that promote tip cell formation, 2) collective migration of multicellular sprouts through a surrounding 3D extracellular matrix (ECM), and 3) subsequent microvessel maturation that commences with neovessel lumenization (Francavilla et al., 2009; Potente et al., 2011). Although the timely formation of perfused host microvasculature should enhance the viability of cell-laden biomaterials (Cheng et al., 2011), the angiogenic process driven too rapidly or in a dysregulated fashion negatively impacts microvasculature quality and function (Siemann, 2011; Wang et al., 2020). The informed design of biomaterials that support functional angiogenesis therefore critically requires an understanding of how specific soluble and physical microenvironmental cues regulate this complex process (Crosby and Zoldan, 2019; Wang et al., 2020).

In vitro models that can help extend our understanding of how the microenvironment regulates angiogenesis require two essential components: 1) the surrounding 3D material through which multicellular endothelial sprouts navigate, and 2) an appropriate culture platform that defines physical and soluble boundary conditions and enables facile assessment of the angiogenic process (Caliari and Burdick, 2016; Li et al., 2017a; Nowak-Sliwinska et al., 2018). The first angiogenic biomaterial hydrogels were formed from reconstituted ECM proteins harvested and purified from animals. In particular, reconstituted type I collagen and fibrin hydrogels have long been used to model stromal and wound healing ECM, respectively (Levental et al., 2009; Scott, 1988; Tonnesen et al., 2000). To examine how matrix properties influence angiogenesis, a common perturbation for naturally-derived hydrogels (e.g. collagen and fibrin) is to modulate protein concentration. Across a variety of studies, increasing matrix

density results in decreased endothelial cell (EC) sprouting (Ghajar et al., 2008; Shamloo and Heilshorn, 2010; Vernon and Sage, 1999; Wang et al., 2020). However, increases in matrix density simultaneously decreases porosity, while increasing stiffness and ligand density. Towards understanding how individual matrix properties influence angiogenesis, numerous biomaterials have been designed to possess orthogonally tunable properties (Li et al., 2017a; Vining and Mooney, 2017). A wide range of synthetic and semi-synthetic hydrogel systems, including functionalized polyethylene glycol, hyaluronic acid, alginate, and dextran, have been created to examine the influence of matrix stiffness, porosity, degradability, viscoelasticity, and ligand engagement on cell behavior (Griffin et al., 2015; Li et al., 2017b; Martino et al., 2015; Sokic and Papavasiliou, 2012; Trappmann et al., 2017; Wei et al., 2020; Wisdom et al., 2018). Despite the wealth of available synthetic biomaterials, robust angiogenesis within synthetic hydrogels is lacking relative to angiogenesis observed in naturally-derived biomaterials such as collagen and fibrin. Identifying critical matrix properties that regulate angiogenesis in natural materials and imbuing synthetic hydrogels with these features will be critical to achieving engineering control over biomaterial implant vascularization.

The second essential element is the culture platform used to drive the angiogenic process and quantitatively assess resulting microvasculature that forms. The culture platform houses the biomaterial and may define its architecture, dictates the cellular constituents and their initial positions, imposes external mechanical and soluble boundary conditions, and defines the directionality and imaging plane of formed vasculature, critical to robust quantitative morphometrics. An existing challenge to selecting an ideal angiogenic biomaterial stems from cross-comparison between studies employing distinct angiogenesis platforms (e.g. 2D scratch assays, 3D spheroid outgrowth, or microfluidics), each with unique parameters to model and

interpret EC sprouting morphogenesis (Nowak-Sliwinska et al., 2018). EC outgrowth assays from microcarrier beads or cell spheroids embedded within 3D ECM have been instrumental in recapitulating 3D sprouting morphogenesis (Boucher et al., 2017; Heiss et al., 2015). However, across studies, the methods to induce EC outgrowth has varied considerably as sprouting morphogenesis has been shown to be sensitive to the addition of exogenous chemokines and undefined cell-secreted factors from the addition of secondary support cells. Furthermore, the addition of secondary support cells have varied in cell identity (e.g. fibroblasts, mesenchymal stem cells, or cancer cells) as well as location as a 2D feeder layer, embedded in 3D, or intermixed with ECs in spheroids (Ghajar et al., 2008; Kosyakova et al., 2020; Margolis et al., 2021; Turturro et al., 2013). More recently, advances in biomicrofluidics and efforts to develop tissue-on-a-chip platforms have generated models of human engineered microvessels fully embedded within user-defined ECM in which EC sprouting can be initiated with well-defined gradients of pro-angiogenic factors (Akbari et al., 2017; Nguyen et al., 2013; Polacheck et al., 2017; Wang et al., 2020). While previous microfluidics-based angiogenesis assays suffer from complicated and low-throughput device assembly, our group has recently established a multiplexed, single-layer fabrication approach affording higher throughput investigation of large parameter spaces such as the wide range of available biomaterials (Wang et al., 2020).

The following work serves to directly compare commonly utilized biomaterials in a microfluidics-based platform that recapitulates key features of physiologic angiogenesis, namely a chemokine-directed 3D invasion of ECs from a lumenized parent vessel into a surrounding, user-defined biomaterial. Employing type I collagen, fibrin, and synthetic dextran hydrogels, we directly compare 3D EC sprouting morphogenesis within these distinct biomaterials varying in material properties. As a quantitative measure of matrix porosity, we developed a fluorescent recovery after

photobleaching method to extract an intrinsic material property related to matrix pore size and structure, matrix permeability. Interestingly, we found that matrix permeability significantly correlates with EC invasion depth and sprout diameter. While the nanoscale pore size of dextran hydrogels restricted EC proliferation and sprout diameter resulting in non-lumenized sprouts *in vitro*, upon implantation we note better retention of the size and shape of synthetic hydrogel implants in the mouse epididymal fat pad as compared to collagen and fibrin grafts which rapidly resorb. To enhance pore size within synthetic dextran hydrogels, we employed a composite materials approach embedding pore-generating, sacrificial gelatin microgels. Synthetic hydrogels imbued with microporosity resulted in increased sprout diameter and the formation of lumenized, multicellular EC sprouts. Through the direct comparison of natural and synthetic hydrogels, we identified matrix permeability as a critical regulator of angiogenesis and introduce a new materials approach that tunes porosity to enhance the angiogenic potential of synthetic biomaterials.

7.4 Results

7.4.1 Generation of consistent parent vessels in collagen and fibrin hydrogels

We employed a multiplexed, organotypic model that recapitulates 3D EC sprouting morphogenesis from a stable, quiescent endothelium to assess angiogenesis into commonly used natural biopolymer-based hydrogels as a function of matrix density **(Figure 7.1a)** (Wang et al., 2020). Specifically, we investigated collagen and fibrin hydrogels over a range of matrix densities explored previously in various models of angiogenesis (Bordeleau et al., 2017; Ghajar et al., 2008). To fabricate patent arteriole-scale channels, hydrogel precursor solution was injected into micromolded silicone devices and polymerized around acupuncture needles (300 μm diameter) **(Figure 7.1a).** Needle removal yields hollow channels fully embedded within the user-defined

hydrogel, with each device containing a pair of channels connected to media reservoirs. One channel was seeded with a suspension of ECs that adhered and self-assembled into the parent vessel, with VE-cadherin localized to cell-cell junctions 24 hours after seeding **(Figure 7.1b-c)**. The resultant parent vessels across collagen and fibrin hydrogel demonstrated no difference in vessel diameter and cell density **(Figure 7.1b-d)**. To isolate the interactions between ECs and the ECM, the parent vessels modeled in this work did not include supporting mural cells; however, these devices have the potential to incorporate mural cells outlining the endothelialized channel as demonstrated in previous work (Alimperti et al., 2017).

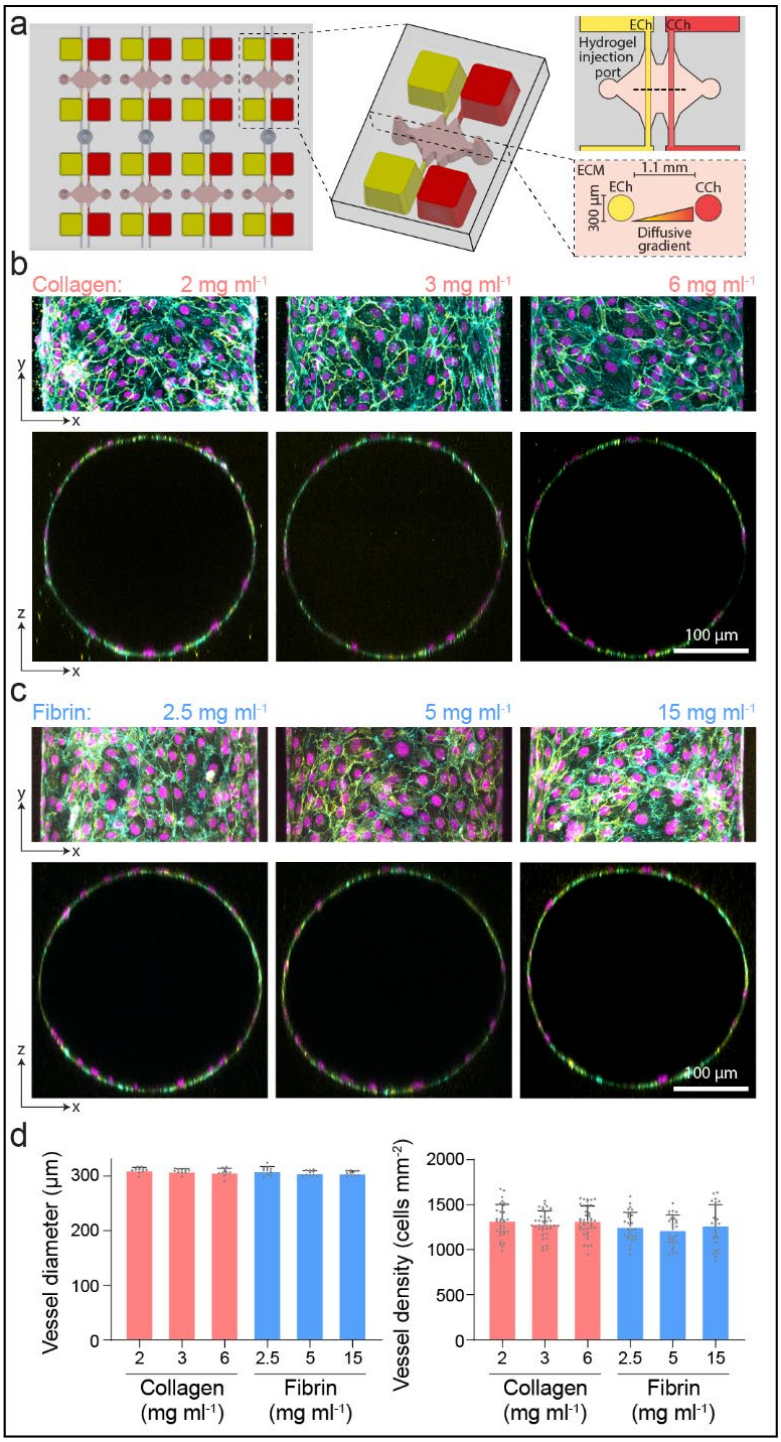

Figure 7.1: Multiplexed angiogenesis-on-a-chip.
a) Schematic of microfluidic-based device to study 3D endothelial cell sprouting from an endothelialized parent channel. Endothelial channel (ECh) and chemokine channel (CCh). **b-c)** Representative images of x-y projection (top) and x-z orthogonal slice (bottom) of parent channels formed within collagen (b) and fibrin (c) hydrogels of varying matrix density. F-actin (cyan), nuclei (magenta), VE-cadherin (yellow). **d)** Quantifications of diameter (n = 10) and cell density ($n \geq 28$) of parent channels from conditions in (b-c). All data presented as mean ± s.d.

We next characterized properties of collagen and fibrin hydrogels as a function of matrix density (i.e. protein concentration of the gel precursor solution). Utilizing fluorescently labelled ECM proteins, we qualitatively observed increases in matrix density concurrent with decreases in pore size **(Figure 7.2a-b)**. Image analysis approaches have been used to assess matrix porosity, but these methods rely on assumptions of equivalence in fluorophore conjugation efficiency and distribution between different ECM proteins. As such, we employed a fluorescent recovery after photobleaching method to assess matrix permeability as a measurable output of matrix porosity. Briefly, devices with each hydrogel composition were saturated with fluorescently labelled 70 kDa dextran overnight. Next, a hydraulic pressure head was applied across the two channels (ECh and CCh) and a region of interest (ROI) was photobleached using a confocal microscope and subsequently imaged to calculate the fluid velocity into the ROI. With a known hydraulic pressure difference and measured fluid velocity, permeability was calculated using Darcy's law (Equation 2). Employing this assay, we find that increasing matrix density results in decreased levels of permeability **(Figure 7.2c)**. Additionally, performing nanoindentation with an atomic force microscope and assuming Hertzian contact, we found increases of matrix stiffness with matrix density confirming previous findings **(Figure 7.2d)** (Bordeleau et al., 2017; Duong et al., 2009). Having characterized two key matrix properties of fibrin and collagen hydrogels previously implicated in angiogenesis (Crosby and Zoldan, 2019), we next sought to directly compare angiogenic sprouting in these two biomaterials as a function of matrix density.

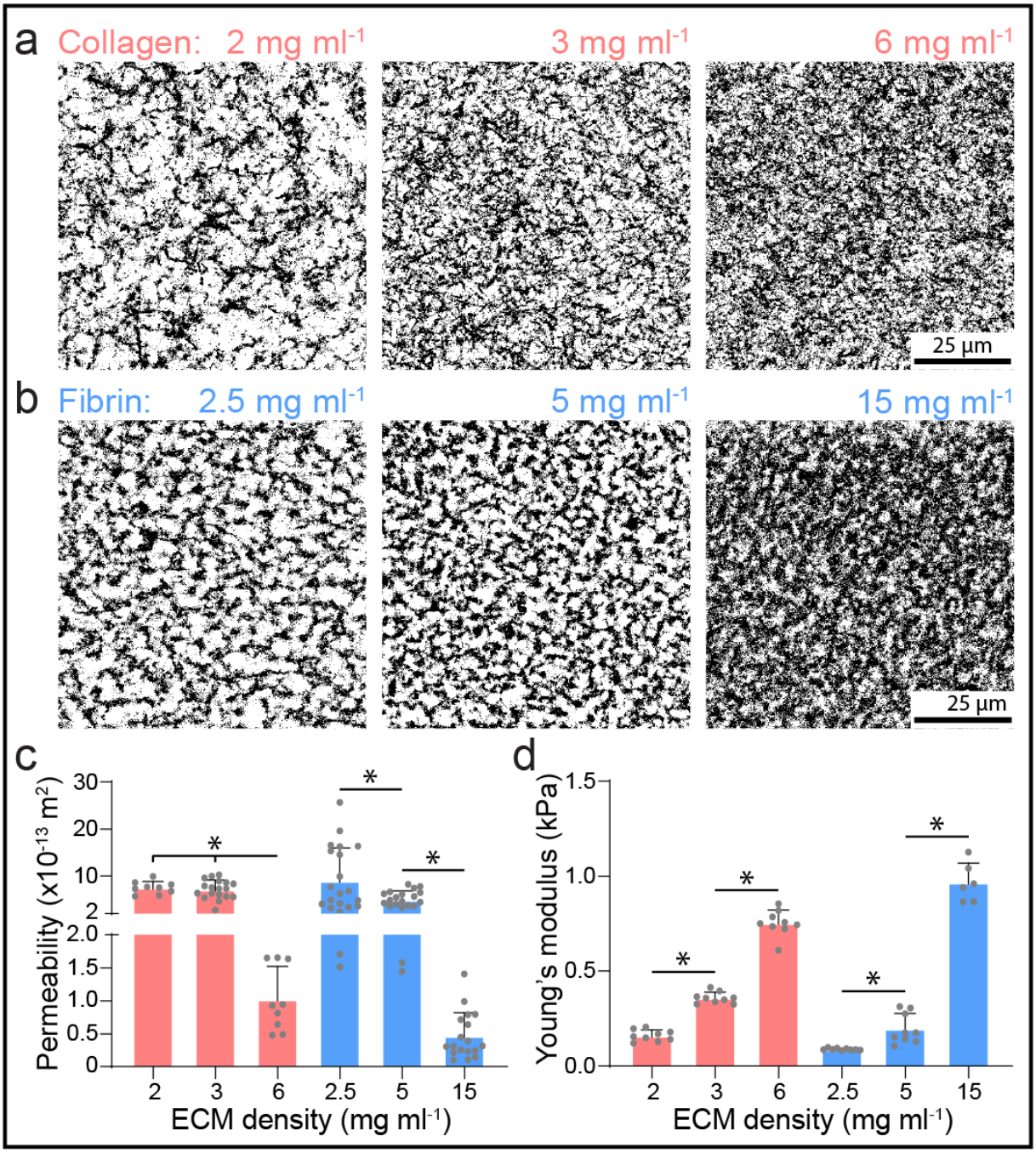

Figure 7.2: Matrix stiffness and pore size as a function of matrix density.
a-b) Representative images (max intensity projection) of fluorescently labelled collagen (a) and fibrin (b) hydrogels of varying matrix density. **c-d)** Matrix permeability (c) and stiffness (d) as a function of matrix density for collagen and fibrin hydrogels; $n \geq 9$ (c) and $n \geq 6$ (d). All data presented as mean ± s.d.; * indicates a statistically significant comparison with $P<0.05$ (one-way analysis of variance).

To induce 3D EC invasion into each ECM composition, we utilized well-established pro-angiogenic factors (250 nM sphingosine 1-phosphate (S1P) and 50 ng ml^{-1} phorbol 12-myristate 13-acetate (PMA)) that promote EC migration and proliferation (Nguyen et al., 2013; Trappmann et al., 2017; Wang et al., 2020). S1P chemoattractant was added only to the CCh, thus generating a diffusive gradient to initiate EC invasion into the ECM, while pro-mitogenic PMA was supplemented to EGM2 media in both the ECh and CCh **(Figure 7.1a)**. To confirm the generation of an increasing S1P gradient, we tracked FITC diffusion from the CCh through each hydrogel condition. Early timepoints of FITC diffusion displayed a logarithmic profile as the gradient was forming (5-90 seconds) **(Supplementary Figure 7.1a-b)**. However, FITC diffusion profiles became more linear with time (60-685 seconds). Although the linear diffusion profile was achieved at varying timepoints across the hydrogel conditions, this timescale is orders of magnitude smaller than the duration of the cell invasion response (hours to days) **(Supplementary Figure 7.1c-d)**. We tracked EC sprout invasion depth over 3 days across each ECM composition, and as expected, invasion depth increased incrementally with culture time **(Figure 7.3a-d)**. Across both collagen and fibrin hydrogels, increases in matrix density resulted in decreased invasion depth by 3 days of culture **(Figure 7.3c-d and Figure 7.4c)**.

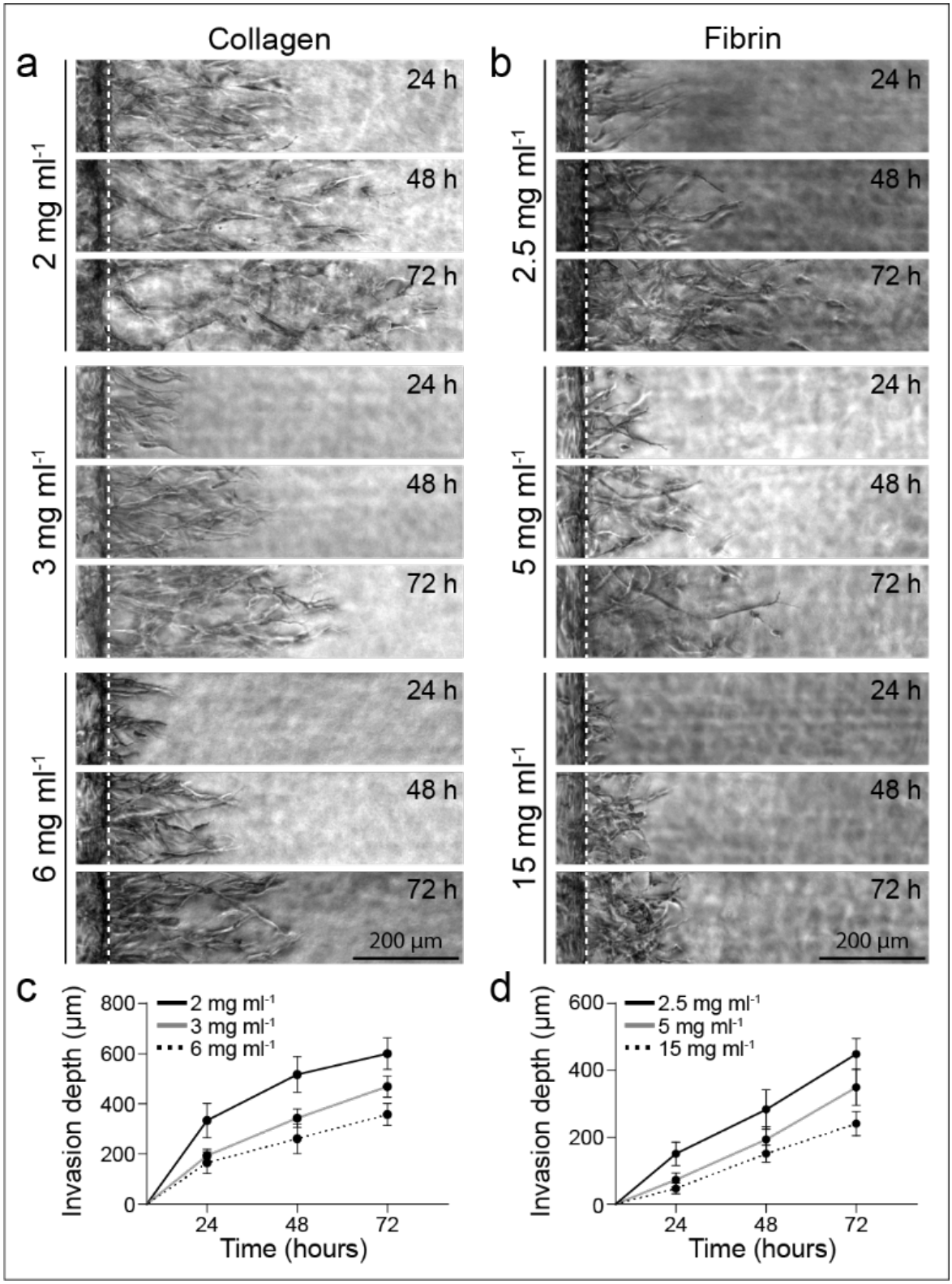

Figure 7.3: EC sprouting time course.
a-b) Representative time course images (brightfield) of invading endothelial cells into collagen (a) and fibrin (b) hydrogels with varying matrix densities as indicated. **c-d)** Quantifications of invasion

depth over 72 hours for collagen (c) and fibrin (d) hydrogels with varying matrix densities; $n \geq 16$. All data presented as mean ± s.d.

7.4.2 Endothelial cell sprout morphology in natural and synthetic biomaterials

In addition to sprout invasion depth, we imaged sprouts at the final day 3 timepoint by confocal fluorescence microscopy **(Figure 7.4a, c)** and quantified EC proliferation and sprout morphometrics as a function of matrix density. We found that matrix density did not influence proliferation rates, as assayed by EdU incorporation, perhaps due to soluble PMA's potent enhancement of proliferation in line with prior findings **(Figure 7.4d)** (Wang et al., 2020). However, invaded ECs were more proliferative in collagen compared to fibrin hydrogels **(Figure 7.4a, d)**. Prior work from our group has demonstrated that increasing sprout multicellularity produces functional angiogenesis, namely perfusable neovessels with appropriate barrier function (Wang et al., 2020). Performing similar morphologic analyses here, ECs were categorized as isolated single cells or multicellular sprouts, and the ratio of sprouts to single cells served as a metric of invasion multicellularity **(Supplementary Figure 7.2a)**. Due to variations in invasion depth across conditions, we defined sprouts as contiguous multicellular structures with a length greater than half the max invasion depth. We quantified all invaded single cells, which were most abundant at the leading invasive front. Analyzing the morphology of invaded ECs, increasing matrix density in both collagen and fibrin hydrogels resulted in a decrease in the number of single cells, increase in multicellular sprouts, and therefore an increase in sprout:single ratio **(Figure 7.4a-b, e-g and Supplementary Figure 7.2b)**. Furthermore, increasing matrix density of both collagen and fibrin hydrogels resulted in decreased sprout diameters **(Figure 7.4a-b, h and Supplementary Figure 7.2b)**. In general, sprouts formed in fibrin hydrogels were smaller in diameter compared to collagen, potentially due to less cell proliferation and thus reduced lateral

expansion of the sprout stalk. To assess whether sprouts in each condition were lumenized, we perfused a solution of 1 μm diameter fluorescent microspheres into the endothelial channel and analyzed whether microspheres flowed into invading sprouts. Interestingly, the number of lumenized sprouts increased with matrix density in collagen hydrogels, following the observed increase of multicellular sprouts **(Figure 7.4f and Supplementary Figure 7.3a-b)**. However, in fibrin hydrogels, increasing matrix density resulted in less lumenized sprouts, despite having increased levels of multicellular sprouts **(Figure 7.4f and Supplementary Figure 7.3a-b)**. As sprout diameter was found to be decreased in fibrin hydrogels, it is likely that despite matrix density promoting more collective EC invasion, these multicellular sprouts did not reach a sufficient diameter to lumenize **(Figure 7.4f, h and Supplementary Figure 7.3a-b)**.

Altering matrix density in collagen and fibrin hydrogels yields concurrent changes in stiffness, porosity, and adhesive ligand density. To further investigate how matrix density in natural hydrogels influences EC sprouting morphogenesis, we next employed synthetic hydrogels that provide orthogonal control over material properties. In previous work, we found that increasing matrix stiffness in synthetic dextran-based hydrogels reduces multicellular sprouting (Trappmann et al., 2017). Thus, here we generated synthetic dextran hydrogels on the lower end of matrix stiffness (while still affording robust hydrogel formation) and altered ligand presentation to probe its influence on EC sprouting morphogenesis. We functionalized dextran, a protein-resistant polysaccharide, with pendant vinyl sulfone groups amenable to peptide conjugation via thiol-ene click chemistry (Matera et al., 2020). Unlike other synthetic hydrogel polymers (e.g. polyethylene glycol and hyaluronic acid), dextran-based hydrogels are non-swelling and afford integration with microfluidic devices to maintain the desired device geometries (Trappmann et al., 2017). Dextran vinyl sulfone (DexVS) was crosslinked with an MMP-labile peptide, and

functionalized with cell adhesive RGD and heparin-binding peptide. Hydrogel functionalization with heparin-binding peptide enables the incorporation of heparin and subsequently, heparin-binding proteins including collagen and fibrinogen (Martino et al., 2013). Parent vessels formed within DexVS hydrogels had equivalent cell density to pure collagen and fibrin hydrogels and was unaffected by enrichment with collagen or fibrin **(Figure 7.1b-d and Figure 7.5a)**. Additionally, enrichment with collagen or fibrinogen did not influence the stiffness nor permeability of DexVS hydrogels **(Figure 7.5b)**. The Young's moduli of DexVS hydrogels was comparable to 6 mg/ml collagen and 15 mg/ml fibrinogen, however, permeability was more than 2 orders of magnitude lower than either natural material **(Figure 7.2c-d and Figure 7.5b)**. Analyzing sprout morphometrics after 3 days of S1P- and PMA-driven sprouting, we found that the incorporation of collagen or fibrinogen into synthetic DexVS hydrogels did not influence invasion depth, proliferation, sprout multicellularity, or diameter **(Figure 7.5c-j)**. Compared to sprouts in 6 mg/ml collagen or 15 mg/ml fibrin, sprouts in DexVS hydrogels infrequently contained proliferating ECs, possessed limited multicellularity and an abundance of single invading cells, and had smaller diameters **(Supplementary Figure 7.4)**.

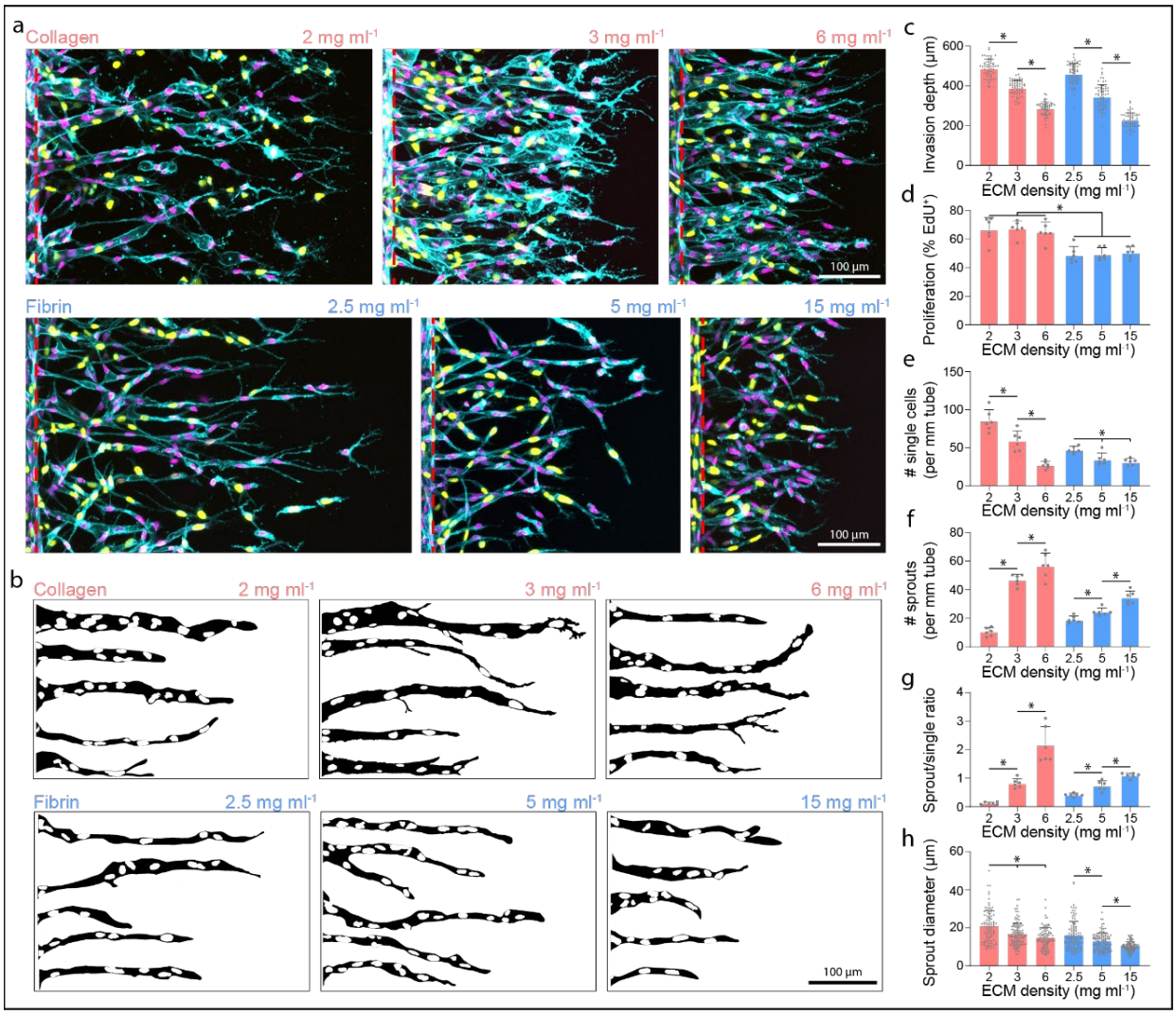

Figure 7.4: Sprout morphometrics in collagen and fibrin hydrogels.
a) Representative images (max intensity projections) of invading endothelial cells into collagen and fibrin hydrogels with varying matrix densities as indicated. UEA (cyan), nucleus (magenta), EdU (yellow). **b)** Representative sprout outlines from conditions in (a). **c-h)** Quantifications of invasion depth ($n \geq 60$), proliferation ($n = 6$), morphology of invading endothelial cells as single cells or multicellular sprouts ($n = 6$), and sprout diameter ($n \geq 100$). All data presented as mean ± s.d.; * indicates a statistically significant comparison with $P<0.05$ (one-way analysis of variance).

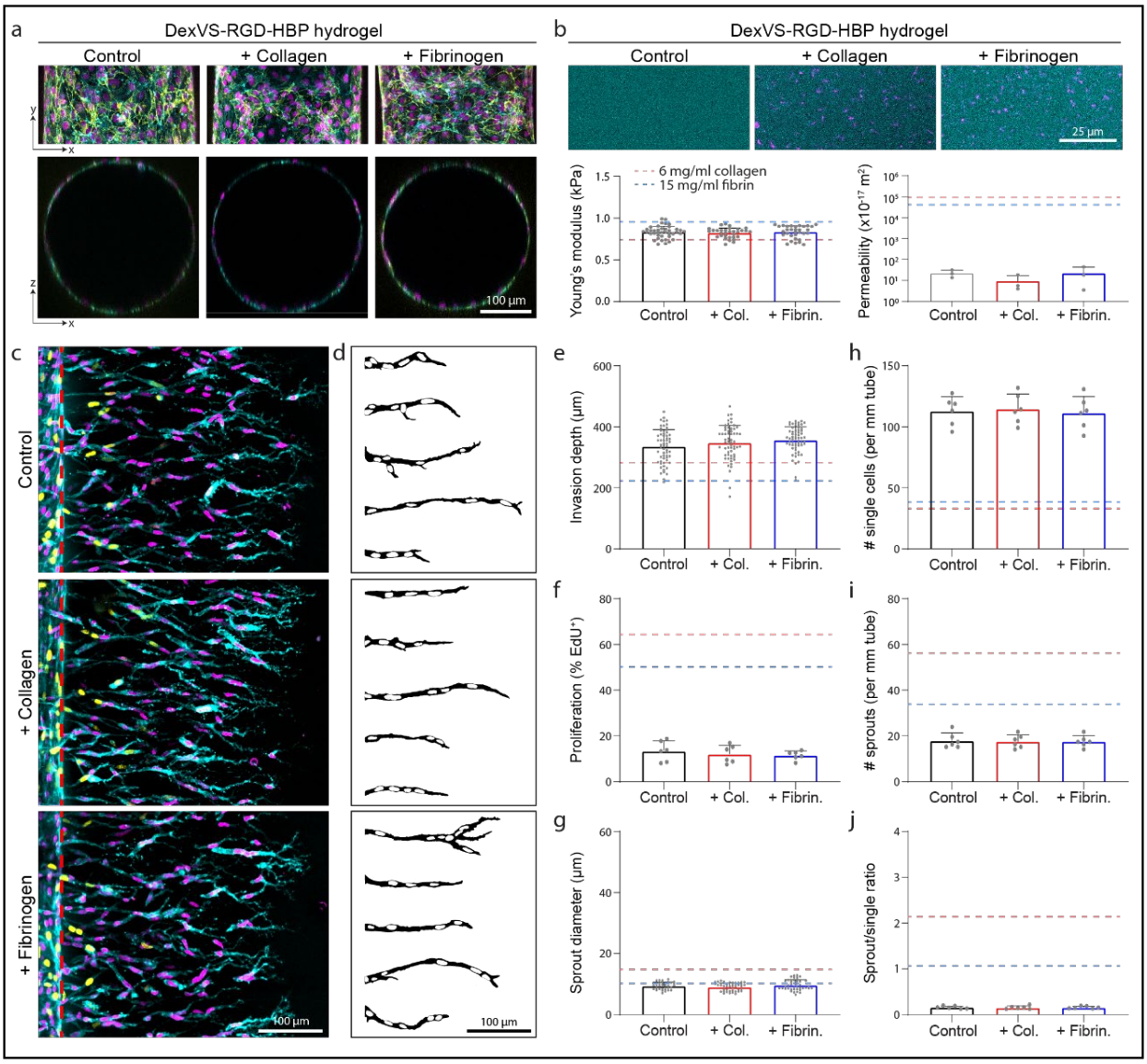

Figure 7.5: Sprout morphometrics in DexVS hydrogels.
a) Representative images of x-y projection (top) and x-z orthogonal slice (bottom) of parent channels formed within DexVS hydrogels enriched with ECM proteins. F-actin (cyan), nuclei (magenta), VE-cadherin (yellow). **b)** Fluorescent images and quantifications of matrix stiffness and permeability. **c)** Representative images (max intensity projections) of invading endothelial cells into DexVS hydrogels enriched with ECM proteins as indicated. UEA (cyan), nucleus (magenta), EdU (yellow). **d)** Representative sprout outlines from conditions in (d). **e-j)** Quantifications of invasion depth ($n \geq 60$), proliferation ($n = 6$), sprout diameter ($n \geq 33$), and morphology of invading endothelial cells as single cells or multicellular sprouts ($n = 6$). Dashed lines in (b, e-j) indicate values from 6 mg/ml collagen and 15 mg/ml fibrin studies. All data presented as mean ± s.d.

7.4.3 Enhancing angiogenesis in synthetic DexVS hydrogels

To examine relationships between key sprout morphometrics and matrix porosity or stiffness, we performed Pearson's correlation analyses between matrix permeability and modulus with sprout invasion depth, diameter, multicellularity, and proliferation **(Figure 7.6a-h)**. Of all analyses across collagen, fibrin and DexVS hydrogels, we found matrix permeability to significantly, positively correlate with both invasion depth and sprout diameter **(Figure 7.6a-b)**. Young's modulus significantly anti-correlated only with invasion depth **(Figure 7.6e)**. This correlation is in line with the previous observations that matrix density and crosslinking (which both contribute to hydrogel stiffness) hamper angiogenic invasion. Performing these analyses with only natural-derived material conditions resulted in significant correlations between matrix permeability with invasion depth and Young's modulus with invasion depth **(Supplementary Figure 7.5)**.

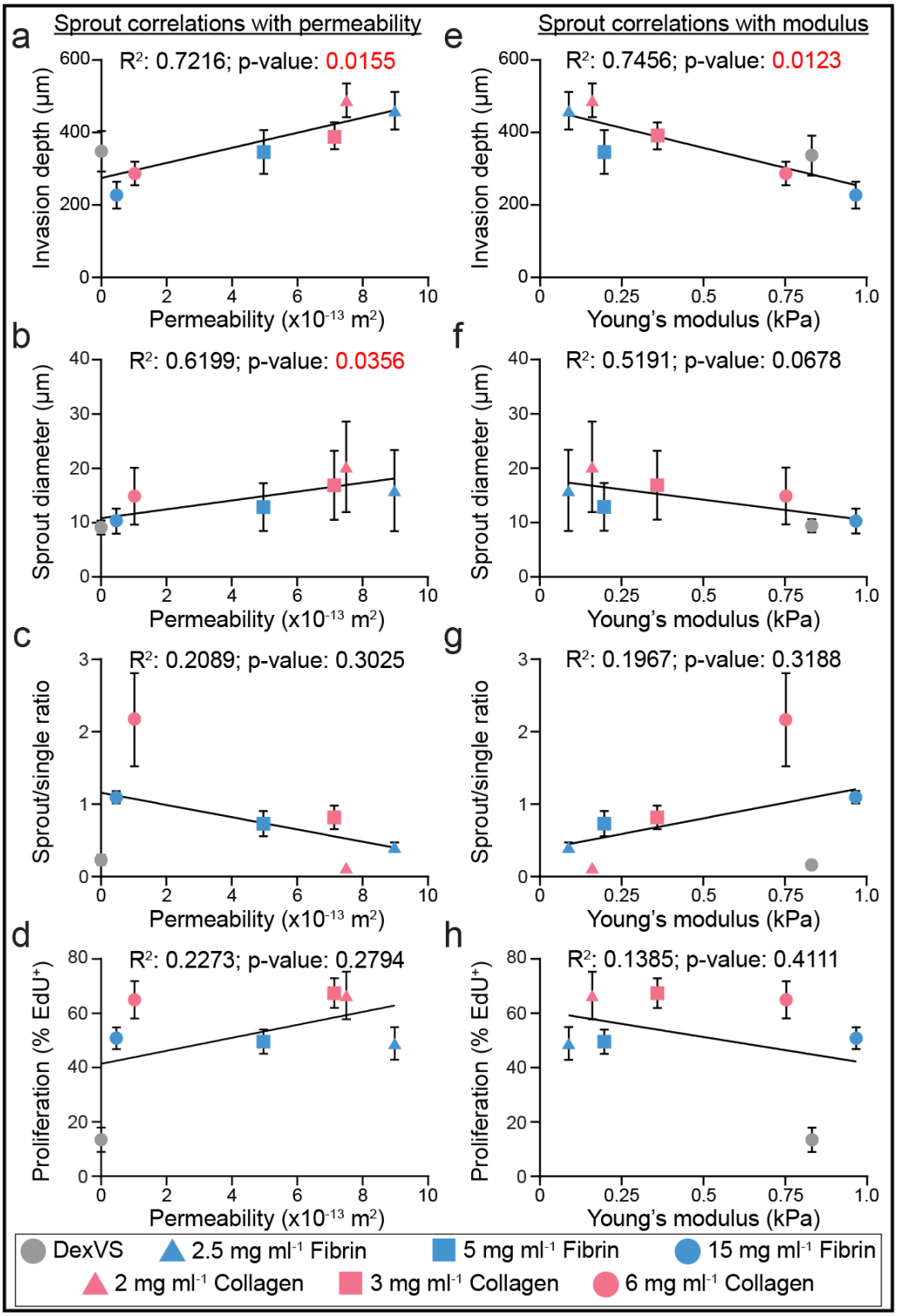

Figure 7.6: Pearson's correlations between matrix permeability and modulus with sprout morphometrics.

a-d) Pearson's correlations between matrix permeability and sprout morphometrics. **e-h)** Pearson's correlations between matrix stiffness and sprout morphometrics. R^2 and p-values indicated within each plot.

We next investigated whether matrix porosity would have a similar influence on cell invasion in an *in vivo* context. We implanted collagen, fibrin, and DexVS hydrogels into murine epididymal fat pads and assessed cell invasion into hydrogel implants retrieved after 7 days. Hydrogels of the highest matrix density explored in these studies were selected for implantation (collagen: 6 mg/ml, fibrin: 15mg/ml), as their moduli were most similar to DexVS hydrogels. After 7 days of implantation, collagen and fibrin hydrogel implants contained numerous invading cells with a subset of isolectin B4 (IB4) positive ECs, while DexVS implants possessed cells exclusively restricted to the hydrogel periphery **(Figure 7.7c-d and Supplementary Figure 7.6)**. Cell invasion is a requirement for angiogenesis, and these results support previous observations that both natural materials are angio-conductive. However, we found that even when formulated at high density, collagen and fibrin hydrogels rapidly resorbed *in vivo*, evident in a marked reduction in the projected area of initially cylindrical implants **(Figure 7.7a-b)**. In contrast, synthetic DexVS hydrogels resorbed more slowly and better maintained initial implant cross-sectional area and overall geometry **(Figure 7.7a-b)**. As degradation mechanism and kinetics of synthetic hydrogels can be readily tuned, this class of biomaterials is attractive for applications that require longer-term shape/size control.

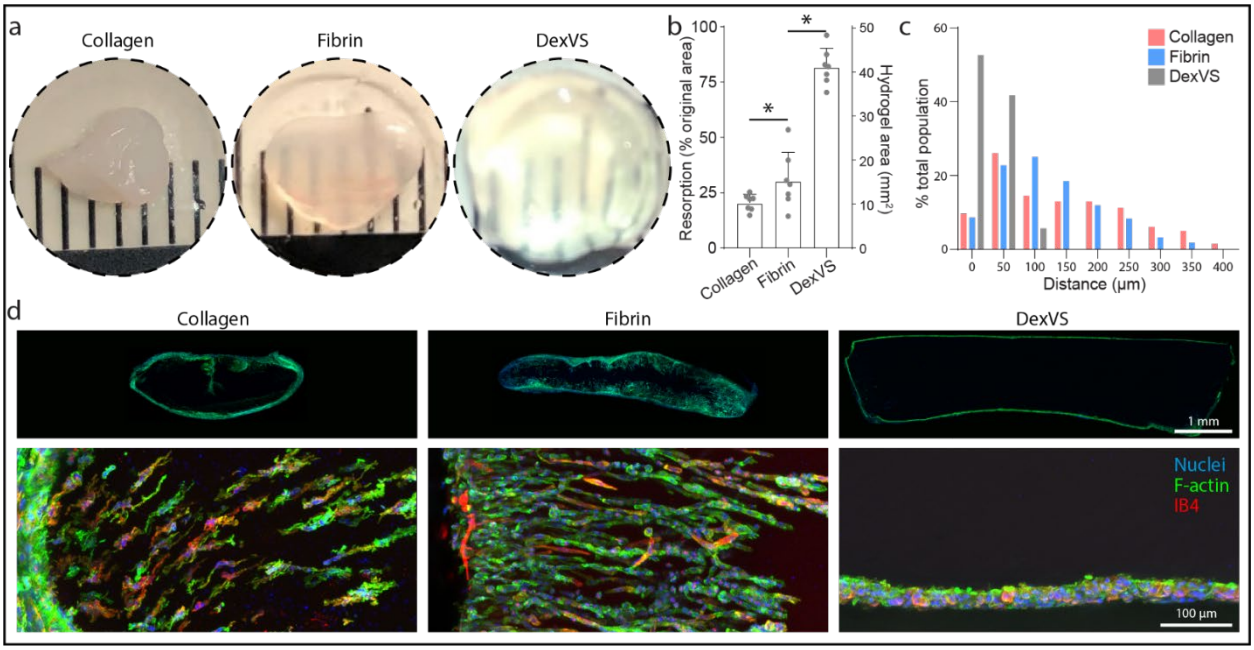

Figure 7.7: *In vivo* cell migration response.
a) Images of hydrogel explants after 7 days implantation into fat pad. **b)** Quantification of hydrogel resorption and final hydrogel area (n = 7). **c)** Quantification of cell migration into implanted hydrogels. **d)** Images of vibratome sections of whole implants (top row) and cell invasion (bottom row). Nuclei (blue), Actin (green), Isolectin B4 (red). All data presented as mean ± s.d.; * indicates a statistically significant comparison with $P<0.05$ (one-way analysis of variance).

As the resorption rate of natural materials cannot be easily tuned without influencing properties that inhibit EC invasion, we instead focused on improving lumenized sprout formation in DexVS hydrogels by introducing microporosity into an otherwise nanoporous bulk hydrogel. We employed an established technique to generate gelatin microgels with defined diameter using a microfluidic droplet generator **(Figure 7.8a)** (Mao et al., 2017). 20 μm diameter gelatin microgels were generated and swelled to 27.85 ± 1.32 μm, upon equilibrium swelling in PBS after the liquid-oil emulsion phase was broken. This diameter was selected based on prior work utilizing photoablation of collagen hydrogels (Arakawa et al., 2020) and were of similar caliber to lumenized sprout diameters **(Figure 7.8b-d)**. To incorporate gelatin microgels into DexVS hydrogels, we added a chilled solution of gelatin microgels into the precursor hydrogel to occupy

7.3% v/v space and subsequently melted the gelatin microgels upon incubation at 37°C, leading to micro-scale pore formation throughout the synthetic hydrogel **(Figure 7.8e)**. Performing *in vitro* sprouting studies over 3 days, we found that DexVS hydrogels imbued with microporosity increased endothelial sprout diameter, but not invasion depth **(Figure 7.8f-h)**. Larger sprout diameters in microporous DexVS coincided with sprout lumenization, as evidenced by the entry of fluorescent microspheres (Ø=1 μm) into sprouts upon addition to the parent vessel. In stark contrast, microspheres did not enter sprouts in nanoporous DexVS controls **(Figure 7.8f)**. Lastly, to assess the impact of gel porosity on endothelial invasion *in vivo*, we implanted control or microporous DexVS hydrogels for 7 days in murine epididymal fat pad. We noted no difference in the degree of resorption between control and porous DexVS hydrogels, with both maintaining overall implant shape and size **(Figure 7.8i-j)**. However, cell invasion was enhanced in microporous DexVS hydrogels, with some cells positive for IB4 **(Figure 7.8k-l, Supplementary Figure 7.6 and Supplementary Figure 7.7)**. Overall, utilizing a composite materials approach to enhance porosity of synthetic DexVS hydrogels with gelatin microgels increased sprout diameter and lumenization *in vitro* and cell invasion *in vivo*.

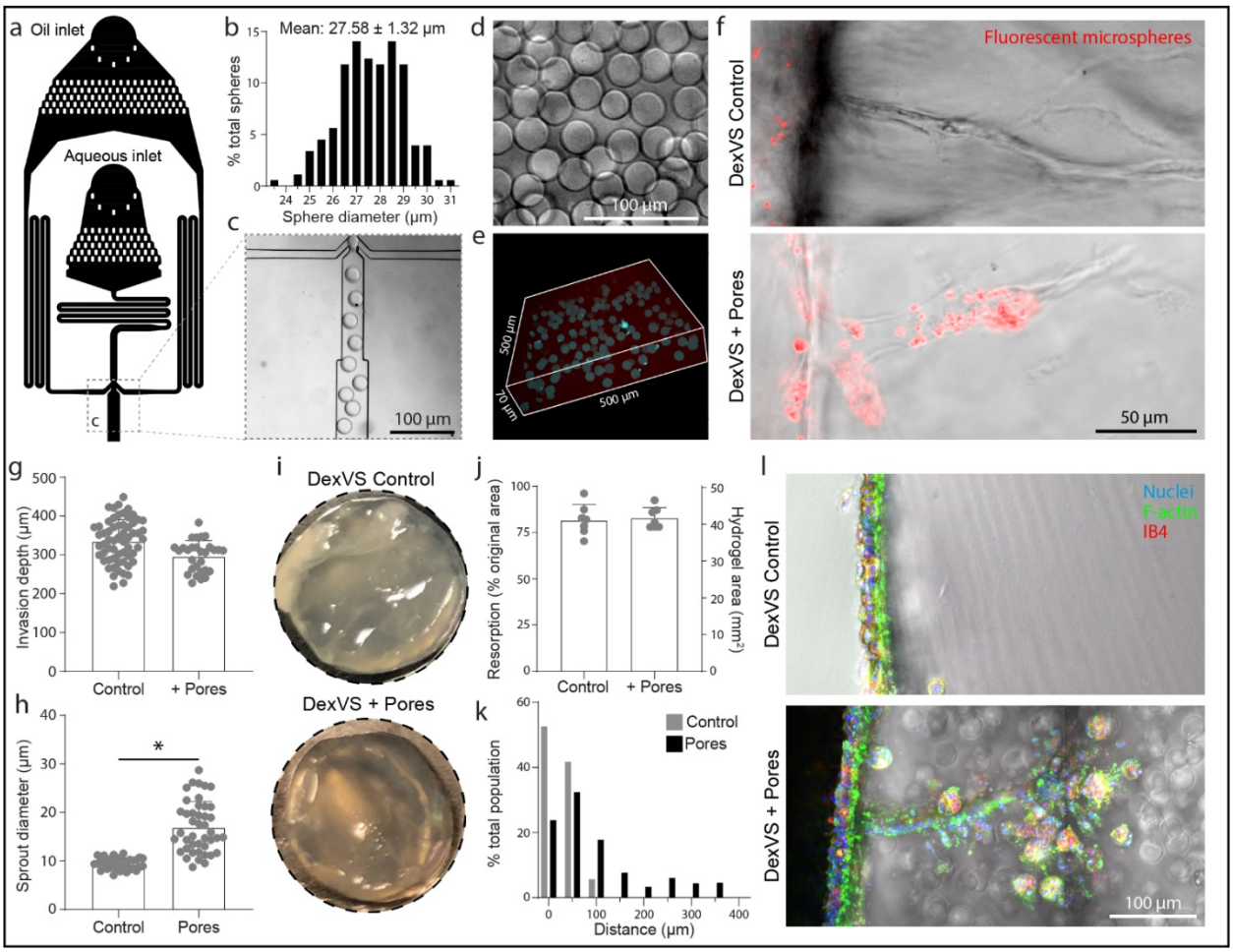

Figure 7.8: Sacrificial gelatin microgels to enhance microporosity increase sprout diameter *in vitro* and cell invasion *in vivo*.
a) Schematic of microfluidic droplet generator with oil and aqueous inlets. **b)** Inset of oil and aqueous junction. **c)** Histogram of gelatin microgel diameter. **d-e)** image of a solution of gelatin microgels (d) and encapsulated in 3D DexVS hydrogel (e). f) Images of endothelial cell invasion into control and microporous DexVS hydrogels *in vitro* after 3 days of sprouting. **g-h)** Quantifications of invasion depth ($n \geq 29$) and sprout diameter ($n \geq 33$) from conditions in (f). **i)** Images of hydrogel explants after 7 days implantation into fat pad. **j)** Quantification of hydrogel resorption and final hydrogel area ($n = 7$). **k)** Quantification of cell migration into implanted hydrogels. **l)** Images of vibratome sections of cell invasion. Nuclei (blue), Actin (green), Isolectin B4 (red). All data presented as mean ± s.d.; * indicates a statistically significant comparison with $P<0.05$ (two-sided student's t-test).

7.5 Discussion

To identify physical properties of biomaterials that influence angiogenesis, we utilized a recently established multiplexed angiogenesis-on-a-chip platform to compare EC sprouting morphogenesis in natural and synthetic hydrogels. We measured the Young's modulus and hydraulic permeability of type I collagen, fibrin, and DexVS hydrogels while also quantifying morphometrics of EC sprouting into these materials. We found that matrix permeability significantly positively correlated with EC invasion depth and sprout diameter, while hydrogel stiffness significantly anti-correlated with EC invasion depth. Nanoporous synthetic DexVS hydrogels with low permeability prevented sprout lumenization *in vitro* and cell infiltration *in vivo*, although implanted DexVS hydrogels maintained their initial shape better than natural materials – a critical feature for the long-term function of tissue engineered implants. To address the impaired sprouting and limited cell infiltration of this synthetic hydrogel, we developed a composite materials approach to generate microporosity using sacrificial gelatin microgels. Incorporating microporosity into nanoporous DexVS hydrogels enhanced sprout diameter in our *in vitro* angiogenesis model and enhanced cell invasion upon hydrogel implantation *in vivo*. These studies highlight porosity as a critical physical feature of hydrogels required for the invasion of angiogenic sprouts and establish a promising approach that will extend the application space of synthetic hydrogels. These efforts add to the rapidly growing set of critical design features and strategies to tune synthetic hydrogel properties that can address the outstanding challenge of vascularizing implantable, engineered tissues and organs.

Natural biopolymers such as type I collagen and fibrin hydrogels have been extensively explored for supporting neovascularization (Bordeleau et al., 2017; Ghajar et al., 2008; Wang et al., 2020). These materials readily support the recruitment of cells that mediate wound repair (e.g.

mesenchymal, endothelial, and immune cells) followed by subsequent matrix resorption and remodeling that replaces the implanted material with cell-produced matrix. Rapid revision and replacement of the implant may be ideal in contexts such as wound repair, but these features are likely suboptimal for tissue or organ replacement therapies that require long-term persistence of the biomaterial-based implant. For example, recent advances in biomaterial and stem cell technologies indicate promise for engineering β-cell-containing, extra-pancreatic implants to treat type I diabetes (Headen et al., 2018; Weaver et al., 2018). However, the post-implantation survival, vascular integration, and long-term function of such implants requires careful balance between (1) hydrogel degradation to support host angiogenesis and (2) maintenance of mechanical stability to support incorporated parenchymal cells such as stem cell-derived β-cells or donor islets (Bowers et al., 2019). By virtue of their tunable degradative mechanisms and kinetics, synthetic hydrogels provide a potential route to striking such a balance. However, angiogenesis within synthetic hydrogels has in general been limited due to the nanoscale pore size of this class of materials, which hampers cell migration.

Towards the development of synthetic hydrogels that robustly support neovascularization, we employed a composite hydrogel approach to decouple hydrogel porosity from crosslinking and stiffness. We utilized cell-scale sacrificial gelatin microgels to produce hydrogel micropores (27 μm diameter, 7.3 % v/v) within synthetic DexVS hydrogels. Microporous DexVS hydrogels supported sprout lumenization in our *in vitro* model of angiogenesis and promoted cell invasion following implantation to the mouse fat pad. Future studies exploring the large parameter space of porogen properties (e.g. size, shape, and volume fraction) will be essential to realizing the full potential of this approach.

A variety of strategies have previously been implemented to enhance the porosity of synthetic hydrogels. Gas-foaming and salt-leaching techniques within PLGA scaffolds produce pore sizes on the larger length-scale (100-500 μm); such approaches have indicated heparin or growth factor functionalized PLGA scaffolds promotes localized angiogenesis (Chung et al., 2006; Elcin and Elcin, 2006). At smaller length-scales, microporous annealed particle (MAP) hydrogels consisting of annealed microgels with interconnected pore space have shown promise for enhancing angiogenesis during dermal wound repair (Griffin et al., 2015). With either of these techniques, the resulting pores are heterogenous. Salt-leaching or gas foaming result in heterogeneously sized pores while the pore space in MAP gels lying between microgels possess poorly defined shapes. An overall challenge in connecting porosity to angiogenesis lies in both consistently generating and accurately measuring porosity and pore properties. Aspects including pore size, volume fraction, connectivity, shape, and even orientation all likely converge to dictate the cell response (Dumont et al., 2019; Ilina et al., 2020; Kang et al., 2020; Tien et al., 2020). For example, consider the impact of equal volume fractions of disconnected larger diameter pores versus smaller, interconnected pores on cell invasion. Here, we developed an alternative approach to changing hydrogel porosity by quantifying matrix permeability, which incorporates both pore size and geometry to produce an effective resistance. Indeed, matrix permeability has been well-characterized as a biologically significant parameter governing cartilage deformation, lymphatic drainage and cytoskeletal dynamics (Mitchison et al., 2008; Moeendarbary et al., 2013; Quinn et al., 2001; Swartz et al., 1999). In this work, matrix permeability significantly correlated with EC invasion depth and sprout diameter, and may be an additional matrix property to consider in the design of pro-angiogenic biomaterials to promote collective cell invasion, a process that has recently been linked to a fluid-like phase transition (Kang et al., 2020).

Beyond matrix porosity, other matrix properties have been shown to influence cell behavior including during sprouting morphogenesis. This work also identified matrix stiffness to significantly anti-correlate with EC invasion depth (Fig. 6e), while previous work modulating collagen hydrogel stiffness has shown conflicting responses (Berger et al., 2017; Bordeleau et al., 2017; Kuzuya et al., 1998; Lee et al., 2013). Increasing matrix stiffness via glutaraldehyde reduces sprout response while increasing matrix stiffness with ribose pre-glycation increases the sprout response. Underlying these methods to increase collagen stiffness are changes to the susceptibility of matrix degradation, where glutaraldehyde introduces non-enzymatically degradable crosslinks thus hampering cell-mediated proteolysis. Indeed, previous work from our group utilizing synthetic dextran-based hydrogels has parsed the roles of matrix stiffness and degradability highlighting that multicellular sprouting requires a balance between these two parameters (Trappmann et al., 2017). In addition to stiffness, viscoelastic and non-linear mechanical properties have recently been demonstrated to influence cell migration and vasculogenic self-assembly of EC networks (Davidson et al., 2020a; Wei et al., 2020).

Lastly, one should take into account that most studies only define and characterize initial ECM properties; however, cell-mediated processes such as proteolysis, matrix synthesis, and contractility dynamically alter the biochemical and biophysical properties of ECM immediately upon contact between cells and material (Helvert et al., 2018). These dynamic changes to the ECM are likely accelerated and even more complex *in vivo,* where cell densities and the number of different cell populations are comparatively greater. Characterization of these dynamic ECM changes and their influence on angiogenesis requires the integration of recent enabling technologies such as metabolic labelling of secreted proteins to examine matrix deposition and ligand presentation (Loebel, C, Mauck, RL, Burdick, 2019), FRET-based protease microgels to

assess matrix proteolysis (Shin et al., 2018), magnetic bead microrheology to spatially map matrix stiffness (Juliar et al., 2018; Krajina et al., 2021), and acoustically responsive scaffolds to spatiotemporally control the generation of pores (Aliabouzar et al., 2020). Integrating such technologies with tunable synthetic biomaterials will elucidate new cell-matrix interactions that govern sprouting angiogenesis towards enhancing the vascularization of biomaterial implants for tissue engineering and regenerative medicine.

7.6 Materials and methods

7.6.1 Reagents

All reagents were purchased from Sigma-Aldrich and used as received, unless otherwise stated.

7.6.2 Microfluidic device fabrication

3D printed moulds were designed in AutoCAD and printed via stereolithography from Protolabs (Maple Plain, MN). Polydimethylsiloxane (PDMS, 1:10 crosslinker:base ratio) devices were replica casted from 3D printed moulds, cleaned with isopropyl alcohol and ethanol, and bonded to glass coverslips with a plasma etcher. Devices were treated with 0.01% (w/v) poly-l-lysine and 0.5% (w/v) L-glutaraldehyde sequentially for 1 hour each to promote ECM attachment to the PDMS housing, thus preventing potential hydrogel compaction from cell-generated forces. 300 μm diameter stainless steel acupuncture needles (Lhasa OMS, Weymouth, MA) were dip-coated with 1% (w/v) gelatin to reduce hydrogel fracture, inserted into each device, and sterilized. Hydrogel precursor solution was then injected into each device and polymerized around each set of needles. Hydrogels were hydrated in EGM2 media at 37℃ overnight (or greater than 12 hours)

to dissolve the gelatin layer and needles were removed to form 3D hollow channels fully embedded within a crosslinked hydrogel and positioned 400 μm away from PDMS and glass boundaries.

7.6.3 Dextran vinyl sulfone polymer synthesis

Dextran (molecular weight 86,000 Da, MP Biomedicals, Santa Ana, CA) was modified with vinyl sulfone groups as in (Matera et al., 2019, 2020; Yu and Chau, 2012). Dextran (5 g) was dissolved in 0.1 M sodium hydroxide solution (250 mL) at room temperature. Divinyl sulfone (3.875 ml, Thermo Fisher Scientific, Waltham, MA) was added and the reaction was carried out for 4 minutes with vigorous stirring (1500 RPM) at room temperature. The reaction was terminated by adjusting the pH to 5.0 with the addition of hydrochloric acid. The reaction product was dialyzed against milli-Q water for 3 days with two solvent exchanges daily. The dialyzed reaction product was then lyophilized for 3 days to obtain the pure product, which was then characterized by ^{1}H-nuclear magnetic resonance spectroscopy in D_2O. The degree of vinyl sulfone functionalization was calculated as the ratio of the proton integral (6.91 ppm) and the anomeric proton of the glucopyranosyl ring (5.166 and 4.923 ppm); here a vinyl sulfone/dextran repeat unit ratio of 0.16 was determined.

7.6.4 Hydrogel formulations

Dextran vinyl sulfone hydrogels were formed via a thiol-ene click reaction at 3.25 %w/v (pH 7.4, 37℃, 1 hour) solubilized in PBS containing 50 mM HEPES with 12.5 mM MMP-labile crosslinker (GCRDVPMS↓MRGGDRCG, Genscript, Piscataway, NJ) in the presence of argininyl-glycyl-aspartic acid (RGD, CGRGDS, 2 mM, Genscript), heparin-binding peptide (GCGAFAKLAARLYRKA, 1 mM, Genscript), and cysteine (0.5 mg ml^{-1}). As indicated in

experiments, collagen (100 μg ml^{-1}) or fibrinogen (100 μg ml^{-1}) proteins were incorporated in the dextran vinyl sulfone precursor solution during crosslinking. For microporous DexVS hydrogels, 31 μl of a gelatin microgel solution (22.8 x 10^6 microgels/ml density) were added for every 100 μl of total hydrogel volume resulting in a 7.3% volume occupied by microgels. Gelatin microgels were then melted at 37℃ with excess PBS over 24 hours. Type I rat tail collagen hydrogels (Corning, Corning, NY) were prepared on ice with a reconstitution buffer (10 mM HEPES, 0.035 %w/v sodium bicarbonate), M199, and titrated to a pH of 7.6 with 1 M NaOH and brought to a final concentration of 2, 3, or 6 mg ml^{-1} collagen with Milli-Q water. Collagen hydrogels were crosslinked for 30 minutes at 37℃. Fibrin hydrogels were prepared with fibrinogen from bovine plasma dissolved in PBS at 50 mg ml^{-1} stock concentrations. Fibrinogen (2.5, 5, and 15 mg ml^{-1}) was prepared on ice in PBS and crosslinked with thrombin (6 units per mg of fibrinogen) for 20 minutes at 37℃. All hydrogels were hydrated in EGM2 media after crosslinking.

7.6.5 Microfluidic droplet generator

Gelatin microgels were generated from a droplet-based microfluidic device. The pattern was designed in AutoCAD, and a master mold was fabricated using a SU-8 negative photoresist (Kayaku, Westborough, MA). PDMS (1:10 crosslinker:base ratio) was cast, cleaned, and bonded to glass. An aqueous phase containing 2.5 %w/v gelatin was prepared in addition to an oil phase comprised of 1 %w/v perfluoropolyethylene (Ran Biotechnologies, Beverly, MA) in HFE-7500 (3M, St. Paul, MN), a perfluorinated mineral oil. A syringe pump was used to flow the aqueous and oil phases through the microfluidic device at 0.5 and 1.0 mL/hr, respectively, to generate water-in-oil droplets with a high degree of monodispersity (Fig. 8a-d). During droplet generation, the syringe containing the aqueous phase was warmed with a heating lamp, and the microfluidic

device was placed on a hotplate set to 75℃. The resulting emulsion was collected, refrigerated at 4℃ for 30 minutes to ensure gelation of the aqueous phase, and then broken by the addition of PBS and 20 %v/v perfluorooctanol (PFO, Alfa Aesar, Haverhill, MA). Oil phase components and PFO were washed from the microgels via centrifugation for 3 minutes at 400 g and replaced with PBS. Microgels swelled from 20 µm to 27.85 µm diameter after the liquid-oil phase emulsion was broken and achieved equilibrium swelling in PBS. A 1:10 dilution of the resulting suspension was loaded onto a hemocytometer to count microgel density.

7.6.6 Device cell seeding and culture

Human umbilical vein endothelial cells (HUVECs; Lonza, Switzerland) were cultured in endothelial growth media (EGM2, Lonza). HUVECs were passaged upon achieving confluency at a 1:4 ratio and used in studies from passages 4 to 9. A 20 µl solution of suspended HUVECs was added to one reservoir of the endothelial channel and inverted for 30 minutes to allow cell attachment to the top half of the channel followed by a second seeding with the device upright for 30 minutes to allow cell attachment to the bottom half of the channel. HUVEC solution density was varied with ECM composition as attachment efficiency was dependent on ECM composition. HUVEC seeding densities were determined experimentally to achieve parent vessels with consistent cell densities across each hydrogel formulation (Fig. 1). Collagen: 1.5 M ml^{-1} for 2 mg ml^{-1}, 2M ml^{-1} for 3 mg ml^{-1}, and 5 M ml^{-1} for 6 mg ml^{-1}. Fibrin: 5 M ml^{-1} for 2.5 mg ml^{-1}, 10 M ml^{-1} for 5 mg ml^{-1}, and 15 M ml^{-1} for 15 mg ml^{-1}. DexVS: 20 M ml^{-1}. HUVECs reached confluency and self-assembled into stable parent vessels over 24 hours. Media and chemokines were refreshed every 24 hours and devices were cultured with continual reciprocating flow utilizing gravity-driven flow on a seesaw rocker plate at 0.33 Hz.

7.6.7 Mechanical testing

Young's modulus of each hydrogel was measured using atomic force microscopy (AFM; Nanosurf, Liestal, Switzerland) in contact mode. Indentations were made at a loading rate of 2 μm/s with silicon nitride cantilevers (AppNano, Mountain View, CA) with a nominal spring constant of 0.046 N/m and a 5 μm diameter spherical glass bead. Force-displacement curves were taken at a minimum of 3 regions on each hydrogel and fit to the Hertz model assuming a Poisson's ratio of 0.5 to estimate the elastic modulus.

7.6.8 Quantification of hydrogel permeability

For fibrin and collagen hydrogels**:** Following fabrication of microfluidic devices and hydrogels as described above, 125 μg/ml 70 kDa conjugated with fluorescein isothiocyanate (FITC, ThermoFisher, Waltham, MA, D-1823) in PBS was added to each of the 4 ports on the device and incubated overnight at 37°C to allow the fluorescent dextran to permeate the gel. FITC-dextran containing PBS was then removed from all ports, and glass reservoirs (4 mm inner diameter, 20 mm in height, Chemglass, Vineland, NJ, CG-700-05L) were inserted into the ports of the endothelial channel (ECh). A hydrostatic pressure gradient across the hydrogel was applied by adding fresh 70 kDa FITC dextran solution to the glass reservoirs and maintaining the chemokine channel (CCh) at atmospheric pressure. The pressure induced by a given height of fluid was calculated using the equation for hydrostatic pressure:

$$P = \rho g h \qquad (1)$$

Where P is the hydrostatic pressure, ρ is the density of the fluid (assumed to be that of water, 10^3 kg/m^3), g is the acceleration due to gravity, and h is the height of fluid in the reservoir. The fluid velocity between the two channels was measured using a modified fluorescence recovery

after photobleaching (FRAP) procedure (Bonvin et al., 2010). Using a laser scanning confocal microscope (Olympus FV3000), a 124 μm diameter circle of FITC-dextran was bleached for 2.161 seconds in the interstitial region between the two channels using a 488 nm, 20 mW laser at 60% power at 20x magnification. Immediately after bleaching, the bleached region and a surrounding region of interest (ROI) was imaged every second for a total of 30s. The velocity of the fluid was measured using a custom MATLAB (MathWorks, Natick, MA) script to measure displacement of the center of mass of the bleached circle as a function of time. With the known input pressure and measured fluid velocity, the permeability of the hydrogel was calculated using Darcy's Law in one dimension (Deen, 1998):

$$k = \frac{-\mu L v}{\Delta P} \qquad (2)$$

Where k is the permeability of the gel, μ is the viscosity of the fluid (assumed to be the viscosity of water at 37°C, 10^{-3} Pa s), L is the distance between the channels in the direction of flow (4 mm), v is the velocity of flow across the gel, and ΔP is the difference in pressure across the two channels calculated from (equation 1).

For DexVS hydrogels: Given the low hydraulic permeability values of dextran hydrogels reported previously (Trappmann et al., 2017), the Peclet number for experimentally feasible pressure gradients is << 1, precluding the use of FRAP for determining fluid velocity magnitude. Therefore, we modified a mass flux-based approach we developed previously (Polacheck et al., 2019) to measure the fluid velocity magnitude for a given pressure gradient and thus determine the hydraulic permeability. Briefly, the total mass flux of fluorescent dextran into a ROI bounded by a source channel with a constant concentration of fluorescent dextran can be determined by

measuring the change in fluorescence intensity within the ROI and the fluorescence intensity of the source channel, as previously described (Polacheck et al., 2019). Therefore, to determine the flux due to convection and the fluid velocity magnitude, we first measured flux into the DexVS hydrogel with an imposed pressure gradient (J_{tot} = total flux), followed by measuring flux with uniform pressure (J_{diff} = diffusive flux). Fluid velocity magnitude can then be determined from the definition of mass flux (Deen, 1998):

$$v = \frac{(J_{tot} - J_{diff})LDz}{I_0} \qquad (3)$$

where I_0 is the total pixel intensity within the source channel (assumed to be constant, and verified experimentally as described below), L is the length of the source channel, D is the diameter of the channel, and z is the optical thickness as determined by the point spread function of optical setup.

Two sequential flux measurements were made to determine J_{tot} and J_{diff}. First, 125 µg/ml 70 kDa dextran conjugated with Texas Red (TR, ThermoFisher, Waltham, MA, D-1830) in PBS was added to the glass reservoirs to induce a 400 Pa pressure drop across the hydrogel, as described above. The input channel was centered in the field of view and imaged at 4x magnification every 5 minutes for 2 hours to determine J_{tot}. Subsequently, the glass reservoirs were removed, TR-dextran was removed from all ports, and 50 µl of 125 µg/ml 70 kDa FITC-dextran in PBS was added to all ports to maintain constant pressure. The ROI was then re-imaged with the same parameters as the total flux measurement to determine diffusive flux.

The two time-resolved image sets were then analyzed using ImageJ to determine total flux and diffusive flux, respectively. Briefly, a rectangular ROI along the length of the channel was drawn in the hydrogel adjacent to the source channel. The change in total pixel intensity within the ROI was measured over time for TR-dextran and FITC-dextran along with the intensity in the

source channel (to justify the constant concentration assumption). With these measurements, J_{tot} and J_{diff} were calculated as previously described (Polacheck et al., 2019), and equation 3 was used to determine fluid velocity magnitude. With the measured velocity magnitude and known input pressure gradient, equation 2 was used to determine the hydraulic permeability.

7.6.9 Mouse implantation

Hydrogels for mouse implantation were formed in 8 mm diameter PDMS gaskets with 100 µl of hydrogel precursor solution resulting in cylindrical-shaped implants upon PDMS gasket removal. Hydrogels were hydrated for 16 hours in VEGF165 (100 ng ml^{-1}, Peprotech, Rocky Hill, NJ) to promote EC invasion. The Institutional Animal Care and Use Committee (IACUC) guidelines for survival surgery in rodents and the IACUC Policy on Analgesic Use in Animals Undergoing Surgery were followed for all the procedures. Animal experiments for this work were performed in accordance with the protocol approved by the IACUC at the University of Michigan (PRO00007716). Male mice (F1 C57Bl/6XCBA) 12–16 weeks old were anesthetized by isoflurane and treated with Carprofen (5mg/kg, subcutaneously, Rimadyl, Zoetis) for analgesia. The intraperitoneal space and the epididymal fat pad were exposed through a midline incision and secured using an abdominal retractor. The hydrogels (one on each side) were wrapped within fat tissue, sutured in place with 10-0 Nylon sutures, and returned to the abdominal cavity. The muscle and skin layers of the abdominal wall were closed with 5/0 absorbable sutures (AD Surgical). The mice recovered in a clean warmed cage and received another dose of Carprofen 24 hours post recovery or as needed. Hydrogels were retrieved after 7 days. Upon explant, isolated hydrogels were imaged and measured for their cross-sectional area and fixed with 4% paraformaldehyde solution.

7.6.10 Vibratome processing

Vibratome sections were processed using a VF-310-0Z Compresstome (Precisionary Instruments, Natick, MA) per manufacturer's protocol. In brief, hydrogel explant samples were affixed to a specimen column and embedded with 2% w/v agarose. Sections were taken at 200 μm thickness with a speed and oscillation setting of 3 and 4, respectively.

7.6.11 Fluorescent staining

Samples were fixed with 4% paraformaldehyde and permeabilized with a PBS solution containing Triton X-100 (5% v/v), sucrose (10% w/v), and magnesium chloride (0.6% w/v) for 1 hour each at room temperature. AlexaFluor 488 phalloidin (Life Technologies, Carlsbad, CA) was utilized to visualize F-actin. 4', 6-diamidino-2-phenylindole (DAPI, 1 μg ml^{-1}) was utilized to visualize cell nucleus. For proliferation studies, EdU was applied for the final 24 hours prior to fixation for each study. EdU fluorescent labelling was performed following the manufacturer's protocol (ClickIT EdU, Life Technologies). DyLight 649 labelled Ulex Europaeus Agglutinin-1 (UEA, 1:200, Vector Labs, Burlingame, CA) was utilized to visualize endothelial cell morphology in samples stained with EdU due to EdU ClickIT incompatibility with phalloidin staining. To visualize VE-cadherin, samples were sequentially blocked in bovine serum albumin (0.3% w/v), incubated with primary mouse monoclonal anti-VE-cadherin (1:1000, Santa Cruz Biotechnology), and incubated with secondary AlexaFluor 647 goat anti-mouse IgG (H+L) (1:1000, Life Technologies) each for 1 hour at room temperature. To visualize mouse endothelial cells in explant hydrogels, samples were stained with Griffonia Simplicifolia Lectin I isolectin B4, DyLight 649 (1:200, Vector Labs).

7.6.12 Microscopy and image analysis

Fluorescent images were captured on a Zeiss LSM800 confocal microscope. Parent vessel endothelial cell density and EdU proliferation was quantified by counting DAPI and EdU positive cell nuclei. Invasion depth was quantified as the distance from the parent vessel edge to the tip cell and measured in FIJI. Invasion depth measurements were performed at 100 µm intervals along the parent vessel. Sprout diameter measurements were taken 50 µm away from the parent vessel edge.

7.6.13 Single vs. multicellular sprout analysis

Single cell and multicellular sprout analyses were performed manually in FIJI utilizing fluorescent markers of nuclei and UEA. This analysis was performed utilizing single z-slices within a 300 µm z-stack. Single cells were quantified as the number of isolated single cells without connections to other cells. Sprouts were quantified as the number of connected multicellular sprouts with UEA connections from the parent vessel edge to tip cell and a length greater than half the maximum invasion depth per condition. The parent vessel edge was clearly distinguished utilizing single z-slice views.

7.6.14 FITC diffusion

To model the diffusion profile of S1P (379 g/mol), fluorescein isothiocyanate (FITC; 389 g/mol) was selected due to the similarity in molecular weight. 50 µl of PBS was first added to the right-hand channel of the angiogenesis-on-a-chip model and then 50 µl of FITC (20 µg/ml diluted in PBS) was added to the left-hand channel such that FITC diffusion flowed from left to right. Timelapse imaging was performed at 5 second intervals to capture fluorescent FITC diffusion through each hydrogel condition.

7.6.15 Fluorescent microsphere perfusion

To assess sprout lumenization, a 50 µl solution of 1 µm diameter fluorescent microspheres (1:10,000, ThermoFisher) was added to the endothelial cell channel with 10 µl of PBS added to the chemokine channel to promote microsphere perfusion into sprouts. Sprouts that contained fluorescent microspheres were considered to be lumenized.

7.6.16 Statistics

Statistical significance was determined by one-way analysis of variance (ANOVA), two-sided Student's t-test, or Pearson's Correlation where appropriate, with significance indicated by $p<0.05$. Pearson's Correlation was performed on sample mean values for each group without accounting for total sample size. Sample size is indicated within corresponding figure legends and all data are presented as mean ± standard deviation.

7.7 Supplementary material

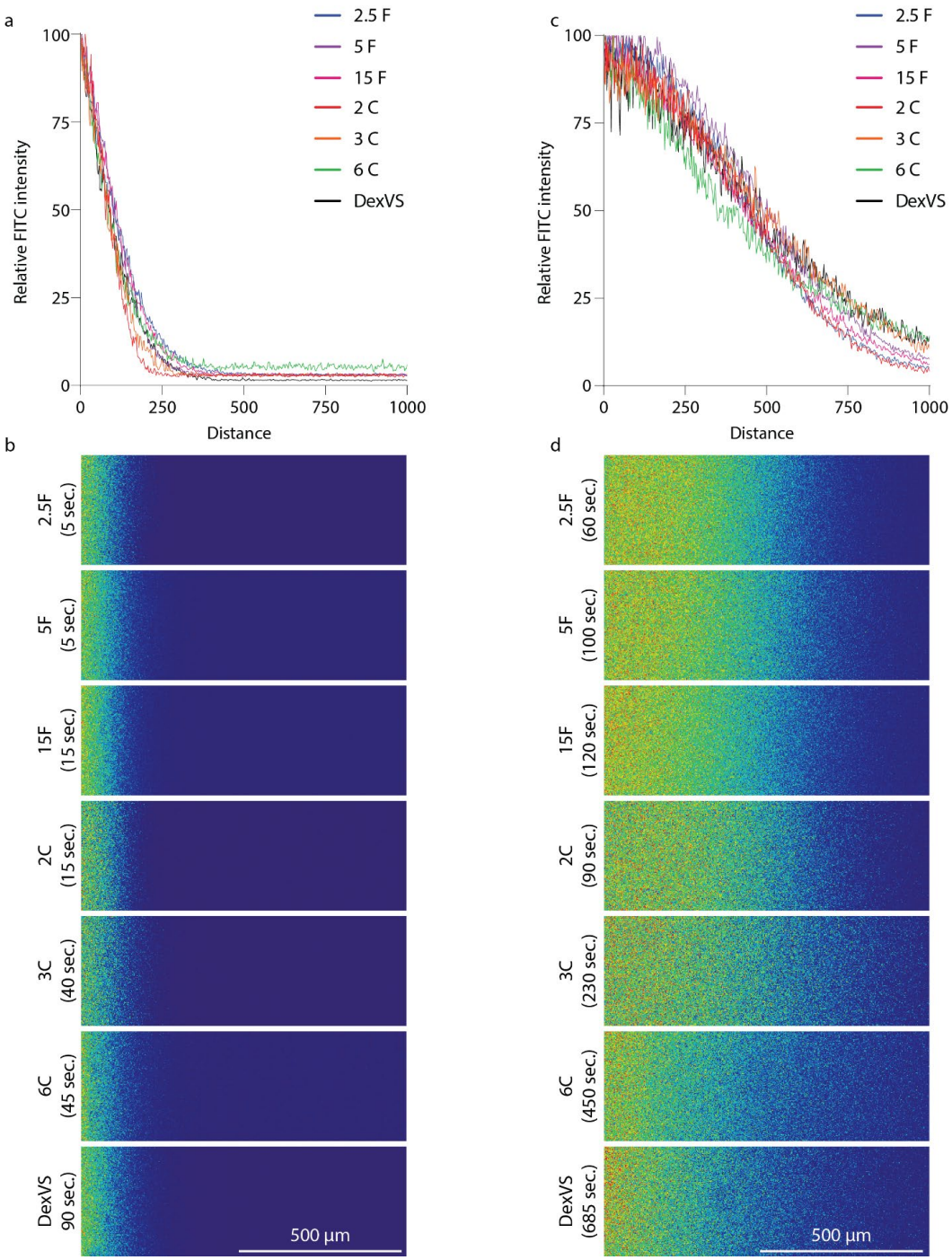

Supplementary Figure 7.1: FITC diffusion within natural and synthetic hydrogels. **a-b)** Quantification and images of the forming FITC diffusion profile in 2.5, 5, and 15 mg/ml fibrin (2.5F, 5F, 15F), 2, 3, and 6 mg/ml collagen (2C, 3C, 6C), and dextran vinyl sulfone (DexVS) hydrogels at the indicated timepoints. **c-d)** Quantification and images of the linear FITC diffusion profile within indicated hydrogel conditions and timepoints. FITC (389 g/mol) was selected to model the diffusion profile of S1P (379 g/mol) due to their similar molecular weights. See methods section 7.2.15. for experimental details.

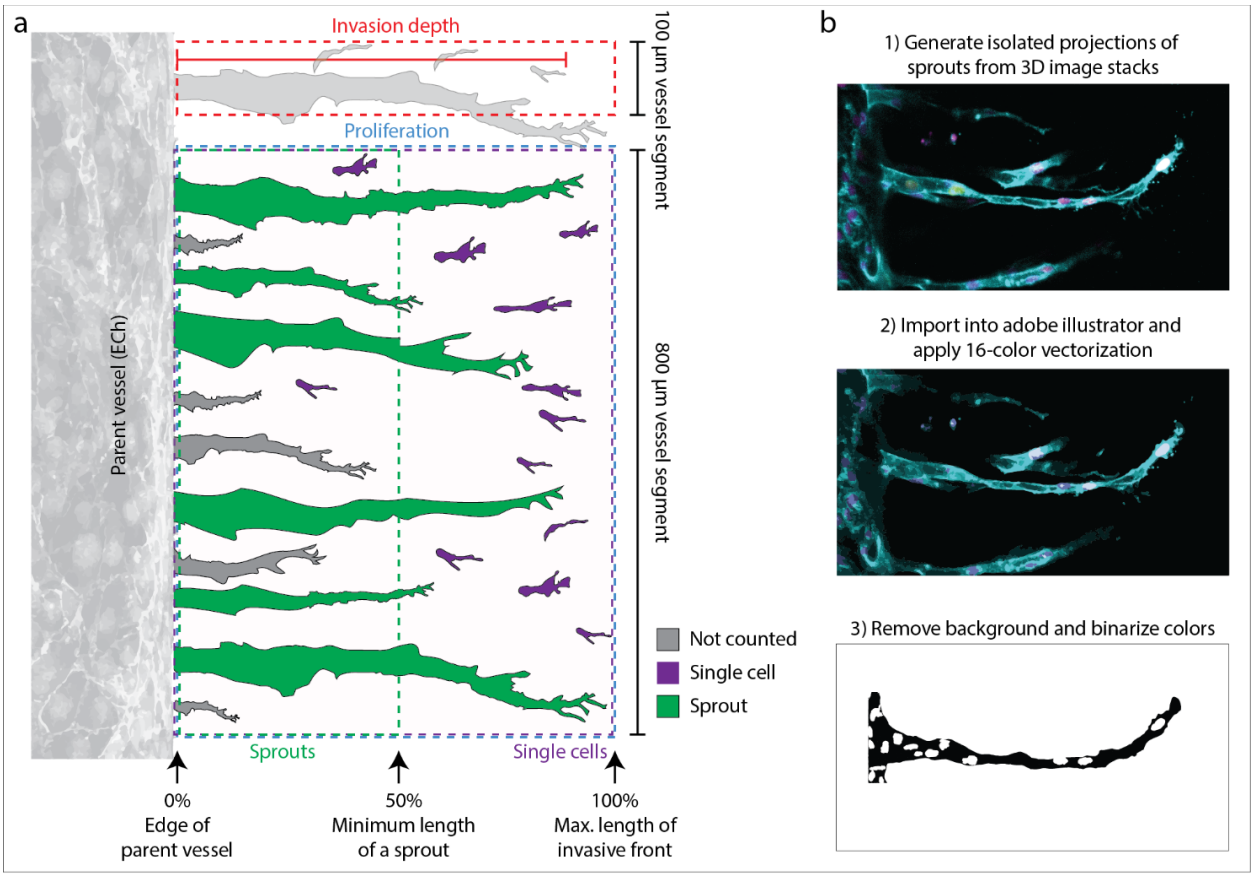

Supplementary Figure 7.2: Schematic of quantification metrics.
a) To quantify EC invasion morphology, ECs were categorized morphologically as either single cells or multicellular sprouts. Single cells were quantified as the number of isolated single cells without connections to other cells. Sprouts were quantified as the number of connected multicellular structures with UEA connections from the parent vessel edge to the tip cell with an overall invasion depth grater than half the maximum invasion depth per condition. This analysis was performed on single z-slices within a 300 µm z-stack to better assess cellular connectivity. **b)** Sproutlines were generated by projecting only the z-range of a given sprout to produce images of isolated sprouts. These isolated sprout projections were imported into adobe illustrator and vectorized using the 16-color function. From here, the background was removed, and sprouts were binarized to black and white corresponding to the cell body and nuclei, respectively.

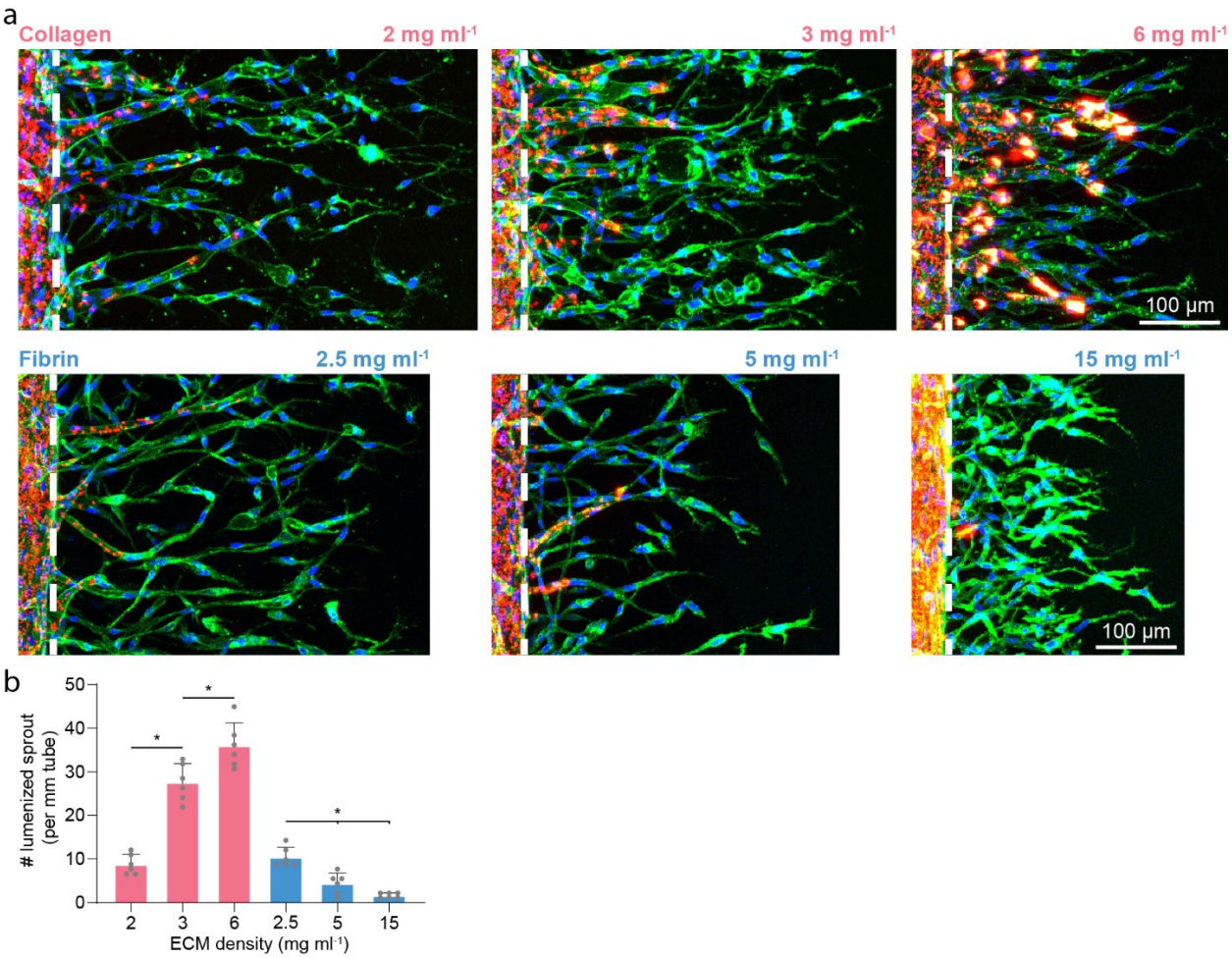

Supplementary Figure 7.3: Fluorescent microsphere perfusion to assess sprout lumenization. **a)** Representative images (max intensity projections) of fluorescent 1 µm diameter microsphere perfusion into invading endothelial cells to assess lumenized sprouts. Microspheres (red), UEA (green), nuclei (blue), white dashed lines indicate parent vessel edge. **b)** Quantification of lumenized sprouts from conditions in (a). All data presented as mean ± s.d.; * indicates a statistically significant comparison with $P<0.05$ (one-way analysis of variance).

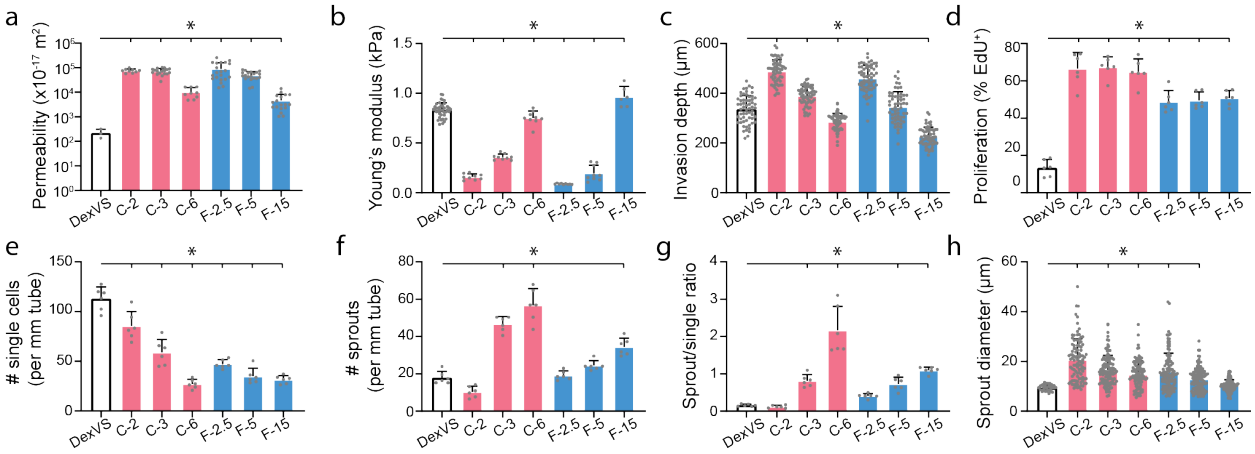

Supplementary Figure 7.4: Direct comparison of matrix properties and endothelial cell invasion response across natural and synthetic hydrogels.
a-h) Data generated from Figures 7.4 and 7.5 are reproduced here to provide direct comparisons. All data presented as mean ± s.d.; * indicates a statistically significant comparison to DexVS condition with $P<0.05$ (one-way analysis of variance).

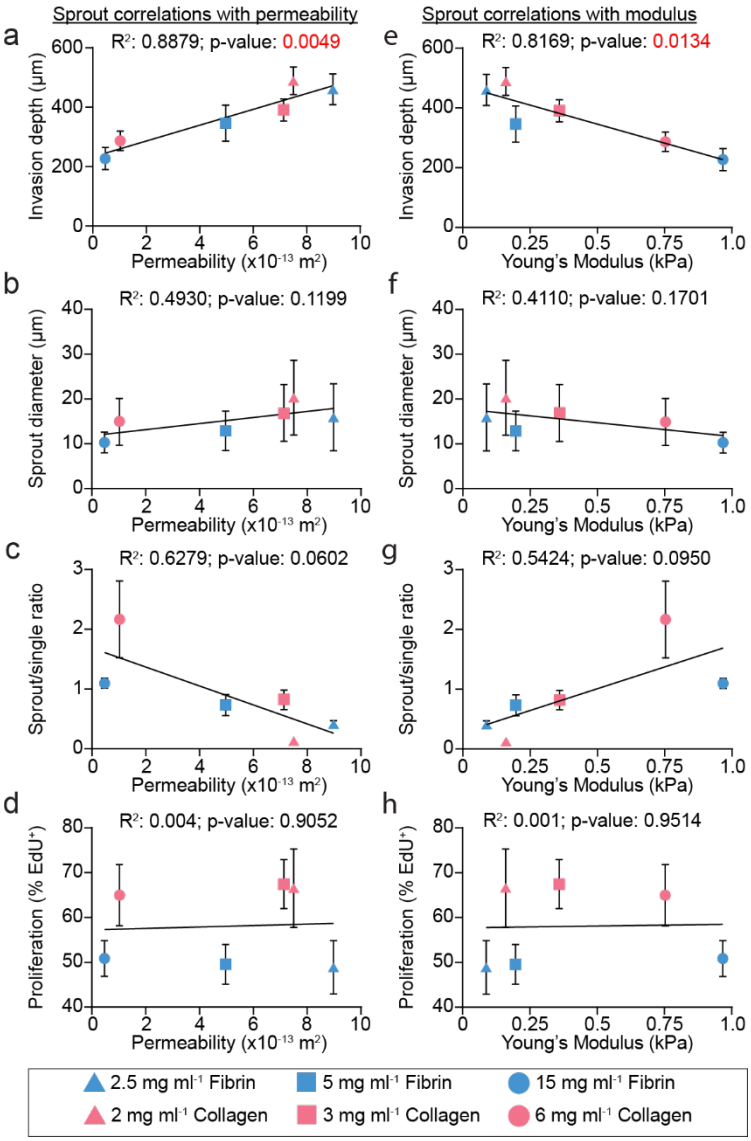

Supplementary Figure 7.5: Pearson's correlations between matrix permeability and modulus with sprout morphometrics for collagen and fibrin hydrogels.

a-d) Pearson's correlations between matrix permeability and sprout morphometrics. **e-h)** Pearson's correlations between matrix stiffness and sprout morphometrics. R^2 and p-values indicated within each plot. Data reproduced from Figure 7.5, but without the inclusion of DexVS conditions.

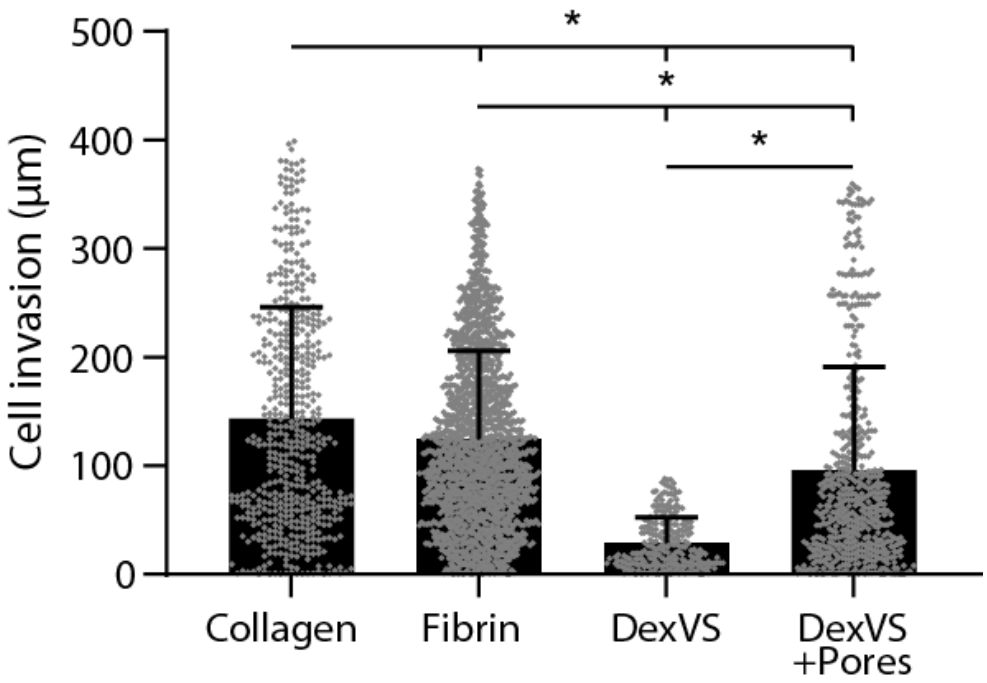

Supplementary Figure 7.6: Direct comparison of *in vivo* cell invasion across natural and synthetic hydrogels.
Quantification of cell migration into implanted hydrogels. Data is reproduced from Figures 7.7 and 7.8 cell invasion histograms and presented here as mean ± s.d.; * indicates a statistically significant comparison with $P<0.05$ (one-way analysis of variance).

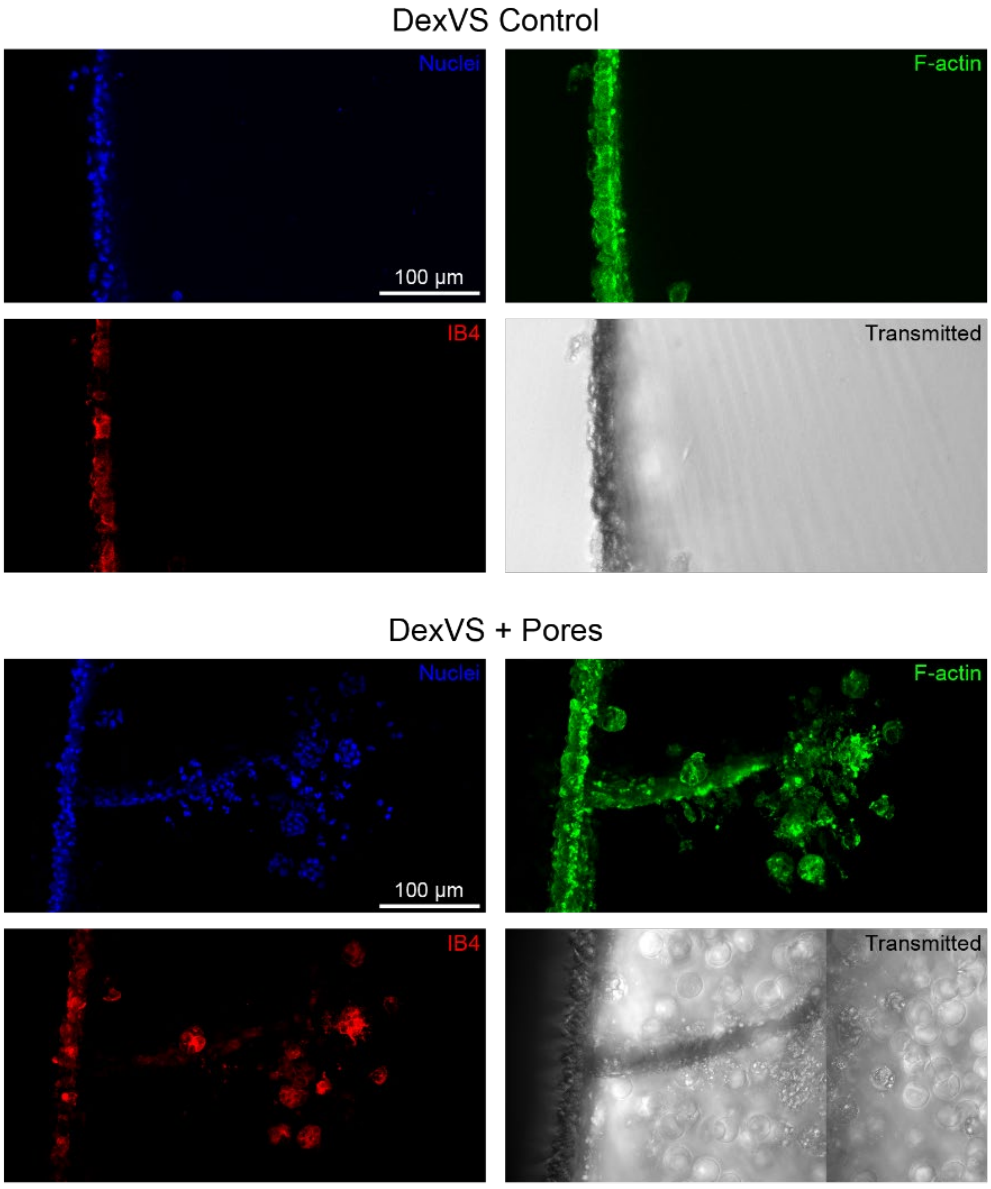

Supplementary Figure 7.7: Immunofluorescence of DexVS and DexVS + micropores implantation hydrogels.
a) Single fluorescent channel images of vibratome sections of cell invasion. Nuclei (blue), Actin (green), Isolectin B4 (red), transmitted light (gray).

Chapter 8: Fiber Density Promotes Endothelial Tip Cell Formation via Mesenchymal Transition Pathways and Propagates Pro-Fibrotic Endothelial Cell Phenotypes

Note: this chapter contains unpublished work in preparation for submission

8.1 Authors

William Y. Wang, Daphne Lin, Evan H. Jarman, Daniel L. Matera, Christopher D. Davidson, Kristen Loesel, Harrison L. Hiraki, Xiaotian Tan, Robert N. Kent III, Eve H. Shikanov, Carole Parent, Xudong Fan, Ariella Shikanov, Matthew L. Kutys, Brendon M. Baker

8.2 Abstract

Tip cell formation marks the onset of angiogenesis and while soluble biochemical factors have long been understood to regulate this process, the role of biophysical extracellular matrix cues are currently uncharacterized. As angiogenesis plays a critical role in both physiologic and pathologic processes, namely fibrosis, where fibrillar collagen type I proteins accumulate over time, an improved understanding of how fibrillar matrix properties regulate tip cell formation may help identify new drivers of fibrotic disease. Here, we model fibrotic matrix architecture utilizing tunable, synthetic fiber segments embedded within 3D hydrogels. Integrating this fibrotic matrix mimetic within microphysiologic devices that model sprouting angiogenesis, we explore how fiber

density activates endothelial cells into invasive tip cells via mesenchymal transition pathways towards a fibrosis propagating phenotype.

8.3 Introduction

Fibrotic diseases are often characterized as wounds that never heal. While the myofibroblast has been identified as the main cellular driver of fibrosis and primary focus of therapeutic targeting, accumulating evidence has highlighted the role of endothelial cells (ECs) as an additional cellular driver of fibrosis. Indeed, several *in vivo* lineage tracing studies in murine models of fibrotic disease (cardiac, cancer, lung, liver, kidney) have identified as many as 30% of myofibroblasts originate from endothelial cells that undergo endothelial to mesenchymal transition (EndMT) (Dejana et al., 2017; Hultgren et al., 2020; Jimenez and Piera-Velazquez, 2016; Piera-Velazquez et al., 2011; Potenta et al., 2008; Welch-Reardon et al., 2015; Zeisberg et al., 2007). Additionally, angiocrine signaling from ECs have been shown to control tissue regeneration vs fibrotic progression in acute injury models of lung and liver fibrosis (Cao et al., 2016, 2017b; Ding et al., 2014). Thus, understanding how biophysical changes that occur over fibrotic progression (i.e. accumulation of fibrillar collagen proteins) influence EC function as disease-contributing cells may identify novel therapeutic targets to treat fibrotic diseases.

In this work, we employ a microphysiologic model to recapitulate fibrotic matrix settings and affords investigation of matrix-vasculature interactions, specifically the quiescent to invasive transition of endothelial tip cells. We identify that fiber density destabilizes endothelium adherens junctions, decreases barrier function and increases tip cell formation via mesenchymal transition pathways. Transcriptomic and secretomic characterization of fiber-induced tip ECs reveal these cells transition towards a fibrosis propagating phenotype and source of TGFβ2. Lastly, we describe

a VE-cadherin dependent TGFβ receptor-2 signaling pathway that regulates the susceptibility of ECs to TGFβ2-induced apoptosis.

8.4 Results

8.4.1 *In vitro* platform to characterize fibrotic ECM properties on angiogenesis

To better understand the underlying mechanisms that drive the co-evolution of matrix and microvasculature over fibrosis (Ehling et al., 2014), we adapted an *in vitro* model of angiogenesis and specifically investigated how fibrotic matrix signatures influence the initiation of angiogenesis (i.e. tip cell formation) (Wang et al., 2020). This model is composed of two parallel channels fully embedded within user-defined ECM **(Figure 8.1a)**. Here, we utilized 10 mg/ml fibrin hydrogels, commonly employed to model wound healing ECM, as fibrosis is often associated as a chronic wound that fails to resolve (Tonnesen et al., 2000). One channel is seeded with ECs that self-assemble into an arteriole-scale parent vessel overnight (16 hours post cell seeding) with a 150 μm diameter **(Figure 8.1a and Supplementary Figure 8.1a-b)**. Chemokines can be added to the parallel channel to generate a diffusive chemoattractant gradient to drive tip cell formation via soluble factors **(Figure 8.1a)**. To confirm this assay is amenable to assessing tip cell formation, we introduced a well-established chemoattractant, sphingosine-1-phosphate (S1P) (Paik et al., 2001; Wang et al., 2020), to the chemokine channel at varying concentrations. Indeed, tip cell formation increased with S1P concentration as indicated by an increasing number of tip cells and their invasion distance **(Figure 8.1b-d)**.

As individual properties of fibrin hydrogels are challenging to decouple, namely fiber density and stiffness, we implemented a recently established composite materials technique that imbues hydrogels with defined fiber segments that have been recently shown to mimic collagen

fibrils in idiopathic pulmonary fibrosis settings (Matera et al., 2020). Fiber segments are generated via electrospinning of a synthetic polymer solution, dextran vinyl sulfone (DexVS), into fiber matrices. Fiber matrices are then photopatterned into defined lengths, collected in solution, and functionalized with cell adhesive RGD peptides. DexVS fiber segments are incorporated into hydrogel precursor solution at varying concentrations to tune the resultant hydrogel fiber density (0 - 2 vol%) and was found to be independent of the Young's Modulus over this range **(Figure 8.1e-f)**. Decoupling fiber density with matrix stiffness affords improved mechanistic studies to identify how ECs respond to increases in matrix fibril density observed over fibrotic progression.

Additionally, to model collagen alignment observed in fibrosis, we employed a flow-induced fiber alignment methodology as previously performed with collagen fibrils (Gong et al., 2020; Riching et al., 2015). To generate fiber alignment perpendicular to the long axis of the parent vessel (0° alignment), hydrogel precursor solution is injected across inserted acupuncture needles which generates a fluid flow profile that aligns fibers in the direction of flow. To generate fiber alignment parallel to the long axis of the parent vessel (90° alignment), hydrogel precursor solution is first injected into the device and subsequent insertion of acupuncture needles generates fluid flow profiles to align the fibers in the direction of needle insertion **(Figure 8.1g)**. Prior to cell seeding, basement membrane proteins are coated along the channel's surface, to promote more equivalent initial matrix topography cells adhere to within hydrogel conditions of varying fiber density. Indeed, 16 hours post cell seeding, parent vessels in control vs fibrous hydrogels possess no difference in vessel diameter, cell density, nor permeability **(Supplementary Figure 8.1a-b, d)**. However, extending the culture duration an additional 3 days, parent vessels in fibrous hydrogels displayed a 5-fold increase in permeability compared to control **(Supplementary**

Figure 8.1c-d). As increased permeability has been associated with tip cell formation, we next more closely examined the influence of fiber density on tip cell formation.

Without the addition of soluble S1P gradients, increasing fiber density resulted in increased tip cell formation as quantified by the number of tip cells and their invasion distance **(Figure 8.1h-j)**. However, fiber alignment parallel to the parent vessel axis (90° alignment), significantly reduced the influence of fiber density on tip cell formation **(Figure 8.1h-j)**. Together, both the density and alignment of matrix fibrils regulate tip cell formation.

We selected to use human umbilical vein ECs as our model EC due to their ubiquitous use in the literature. To assess whether other tissue-specific ECs respond to fiber-induced tip cell formation, we utilized human liver, lung and dermal ECs. Fibrous ECM increased tip cell formation in liver and lung specific ECs, however, dermal ECs did not invade in response to fibrous ECM **(Supplementary Figure 8.2a-c).** As a material control for the synthetic DexVS fiber segments utilized here, we adapted a recently established approach to generate larger collagen bundles that more closely mimic the length scale of native collagen fibrils compared to traditional collagen hydrogels (Gong et al., 2020; Matera et al., 2020). Collagen bundles were isolated and suspended within fibrin hydrogels and also produced fiber-induced tip cell formation **(Supplementary Figure 8.3)**. Lastly, endothelial channels were coated with adipose-derived human mesenchymal stem cells (MSC) to model a mural cell-lined endothelium (Alimperti et al., 2017). Again, fibrous hydrogels resulted in endothelial tip cell formation, in addition to increased MSC divestment and polarized migration into the matrix **(Supplementary Figure 8.4)**.

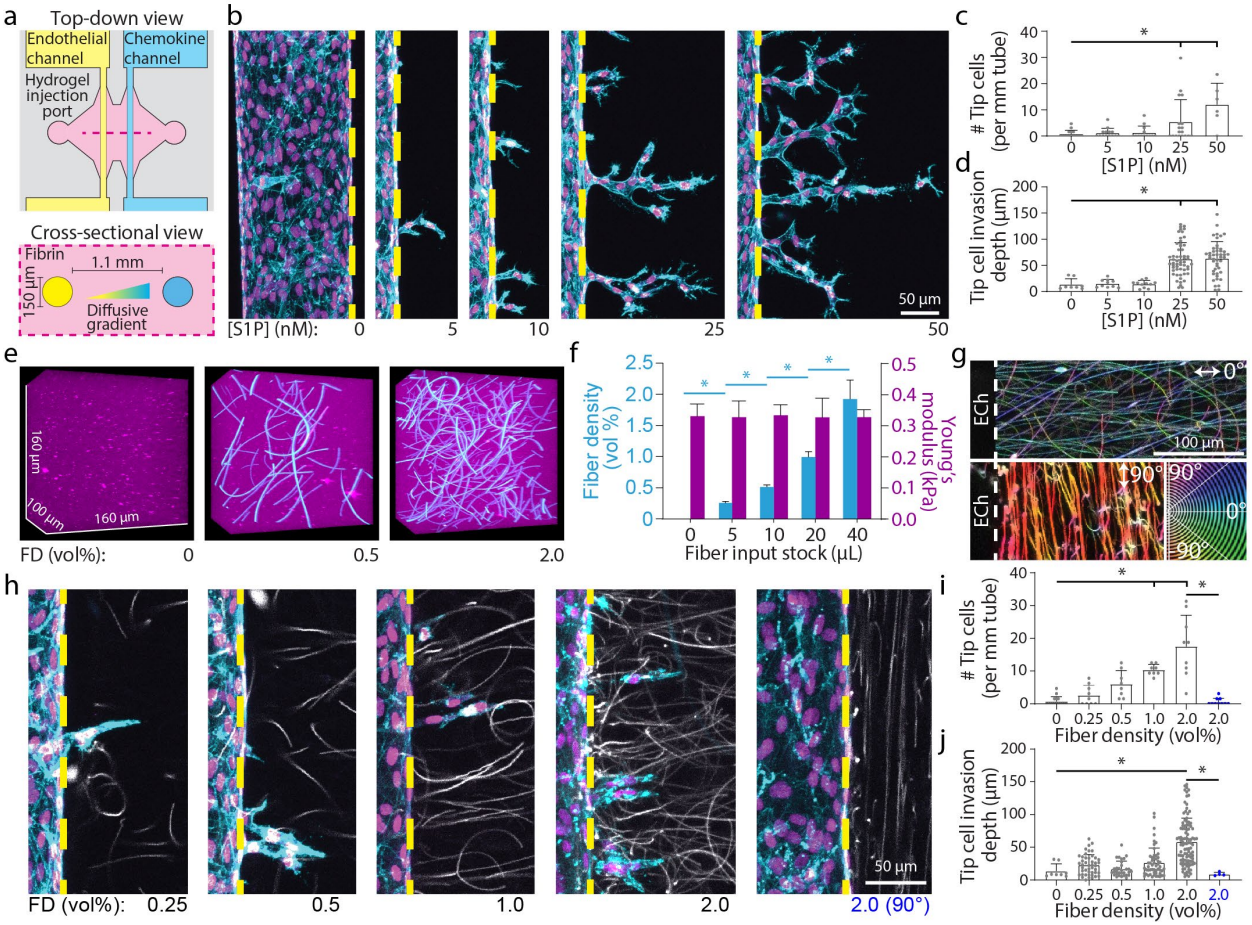

Figure 8.1: Tunable biomaterial platform to assess fiber-induced tip cell formation.
a) Schematic of tip cell formation assay. **b)** S1P-induced tip cell formation over 4-days within 10 mg/ml fibrin hydrogels at indicated [S1P]. Nuclei (magenta), F-actin (cyan), yellow dashed lines indicate parent vessel edge. **c-d)** Quantification of number of tip cells and tip cell invasion depth as a function of [S1P] from (b). **e)** 3D rendering of fiber-embedded fibrin hydrogels. Synthetic DexVS fiber segments (cyan), fluorescently-labelled fibrin hydrogel (magenta). **f)** Quantification of fiber density and Young's modulus as a function of input fiber stock volume. **g)** Flow-induced fiber alignment perpendicular (0°) or parallel (90°) to the long axis of the parent vessel. **h)** Fiber-induced tip cell formation (with no S1P added to the chemokine channel) over 4-days within 10 mg/ml fibrin hydrogels and indicated fiber density. Nuclei (magenta), F-actin (cyan), fibers (white), yellow dashed lines indicate parent vessel edge. **i-j)** Quantification of number of tip cells and tip cell invasion depth as a function of fiber density. Blue indicates 90° fiber alignment. All data presented as mean ± std.; * indicates a statistically significant comparison with $P<0.05$ (one-way analysis of variance).

8.4.2 VE-cadherin destabilization decreases barrier function and promotes tip cell invasion

As fibrous hydrogels resulted in a 5-fold increase of permeability by day 4 of culture, we next investigated whether fibrous topography influenced VE-cadherin, a major component of

adherens junctions known to regulate endothelium barrier function (Polacheck et al., 2017). To achieve sufficient cell quantity for protein isolation and western blot analysis, we first assessed VE-cadherin of EC monolayers cultured on 'flat' tissue culture plastic compared to fibrous matrices of electrospun DexVS (Davidson et al., 2020b; Depalma et al., 2021). In line with decreased barrier function as assessed with permeability measurements, EC monolayers cultured on fibrous topography resulted in decreased VE-cadherin levels **(Figure. 8.2a-b)**. Additionally, immunofluorescence analysis confirmed western blotting results as EC monolayers cultured on fibrous matrices resulted in decreased VE-cadherin intensity and junctional thickness **(Figure. 8.2c-d, f)**. Furthermore, towards understanding the dynamics of VE-cadherin stability, we pulsed a fluorescently tagged anti-VE-cadherin antibody that binds to the extracellular domain, thus allowing for live cell labeling, and found that after 2-day culture, EC monolayers on fibrous matrices expressed decreased pulse VE-cadherin signal intensity **(Figure. 8.2c, e)**. This suggests that the decreased VE-cadherin observed in EC monolayers on fibrous topography may be due in part to increased rates at which VE-cadherin is internalized and recycled at junctions.

To further understand the role of VE-cadherin destabilization on tip cell formation, we utilized three well-accepted permeability agonists: VEGF, TNFα, and Thrombin (Huynh et al., 2011; Mehta and Malik, 2006; Van Nieuw Amerongen et al., 2007). Indeed, VEGF, TNFα, and Thrombin resulted in decreased VE-cadherin protein levels assessed via western blotting, decreased VE-cadherin signal intensity, junctional width, and pulsed VE-cadherin signal intensity via immunofluorescence **(Figure 8.2i-l)**. Employing the angiogenesis-on-a-chip platform, treatment of parent vessels within control or fibrous hydrogels with EGM2 control, or supplemented with VEGF, TNFα, or Thrombin resulted in increased diffusive permeability **(Figure. 8.2m-n)**. Within fibrous hydrogels, treatment with these three permeability agonists that

destabilized VE-cadherin further increased fiber-induced tip cell formation **(Figure. 8.2o-p).** Furthermore, ECs treated with a VE-cadherin CRISPR-cas9 knockout (VECKO) resulted in increased fiber-induced tip cell formation **(Figure 8.3a-d)**. Taken together, VE-cadherin destabilization, either through fibrous topography, soluble factors or genetic deletion, resulted in decreased barrier function and increased tip cell invasion.

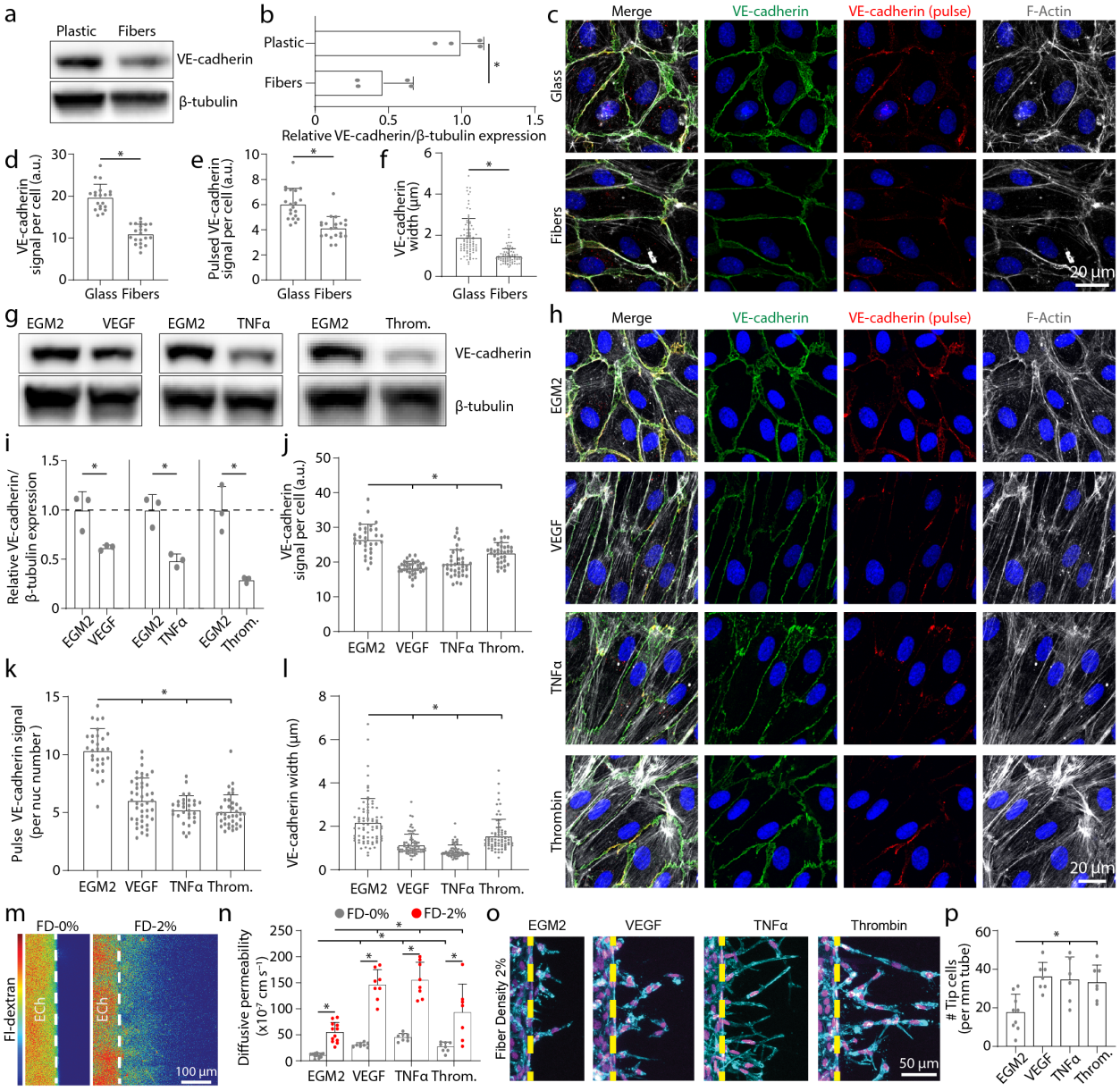

Figure 8.2: VE-cadherin destabilization increases vessel permeability and tip cell invasion. **a-b)** VE-cadherin western blot analysis from endothelial cell monolayers cultured on tissue culture plastic or electrospun DexVS fiber matrices for 2 days. **c)** Representative images of endothelial cell monolayers cultured for 2 days on glass coverslips or electrospun DexVS fiber matrices. Nuclei (blue), VE-cadherin (green), pulsed VE-cadherin (red), F-actin (white). **d-f)** Quantifications of VE-cadherin signal per cell (d), pulsed VE-cadherin signal per cell (e), and VE-cadherin width (f). **g, i)** VE-cadherin western blot analysis from endothelial cell monolayers cultured on tissue culture plastic treated with EGM2 control media or EGM2 media supplemented with 50 ng/ml VEGF, 50 ng/ml TNFα, or 2 U/ml Thrombin for 2 days. **h)** Representative images of endothelial cell monolayers cultured for 2 days on glass coverslips treated with identical conditions as in (g). Nuclei (blue), VE-cadherin (green), pulsed VE-cadherin (red), F-actin (white). **j-l)** Quantifications of VE-cadherin signal per cell (j), pulsed VE-cadherin signal per cell (k), and VE-cadherin width (l) from conditions in (h). **m-n)** Diffusive permeability assessment within

parent vessels cultured for 4 days in control or fibrous hydrogels with EGM2 control, or EGM2 supplemented with 50 ng/ml VEGF, 50 ng/ml TNFα, or 2 U/ml Thrombin. White dashed lines indicate parent vessel edge (m). **o-p)** Tip cell formation assessment within fibrous hydrogels with indicated treatment groups identical to (n). Nuclei (magenta), F-actin (Cyan), yellow dashed lines indicate parent vessel edge (o). All data presented as mean ± std.; * indicates a statistically significant comparison with $P<0.05$ (b, d-f, i: two-sided student's t-test, j-l, n, p: one-way analysis of variance).

8.4.3 Requirements of fiber induced tip cell formation crossover with EndMT processes

The transition of quiescent vessel-lining ECs into invasive tip cells has previously been hypothesized to follow endothelial-mesenchymal transition (EndMT) programming (Hultgren et al., 2020; Welch-Reardon et al., 2014, 2015). Towards identifying key molecular regulators of fiber-induced tip endothelial cells (FIT-ECs), we utilized a panel of pharmacologic inhibitors targeting EndMT-associated pathways. Beyond destabilization or CRISPR-cas9 deletion of VE-cadherin **(Figure 8.2o-p and Figure 8.3a-d)**, we also investigated the requirements of proteolysis and actomyosin contractility. Treatment with marimastat, a broad-spectrum inhibitor of proteolysis, decreased both the number of tip cells and their invasion depth as ECs were unable to degrade matrix to generate sufficient space to invasion **(Figure 8.3e-g)**. Treatment with a myosin II inhibitor (blebbistatin) or ROCK inhibitor (Y27) resulted in decreased tip cell formation as these are critical regulators of actomyosin contractility required for cell migration **(Figure 8.3e-g)**. As protrusions of FIT-ECs were observed to track along ECM fibrils (contact guidance), we next tested whether adhesion to matrix fibers were critical. Indeed, removing RGD, the cell adhesive peptide functionalized to fiber segments, reduced tip cell formation **(Figure 8.3h-j)**. Lastly, recent studies have highlighted the role of electrospun fiber matrices promoting YAP/TAZ signaling in EC monolayers to promote cell migration (Mascharak et al., 2016). To test whether YAP/TAZ signaling was at play, we treated ECs with dimethyl fumarate, an inhibitor of YAP/TAZ signaling pathway, and resulted in decreased tip cell formation **(Figure 8.3h-j)**. Overall, these

pharmacologic inhibitor studies highlight that proteolysis, actomyosin contractility, cell-matrix adhesion, and YAP/TAZ signaling are all required for FIT-ECs. Additionally, immunofluorescent imaging of EndMT markers also support that mesenchymal transition pathways regulate tip cell formation as tip cells were observed to express decreased junctional VE-cadherin, and increased expression of YAP/TAZ, SNAI1, and vimentin **(Figure 8.3k-m)**.

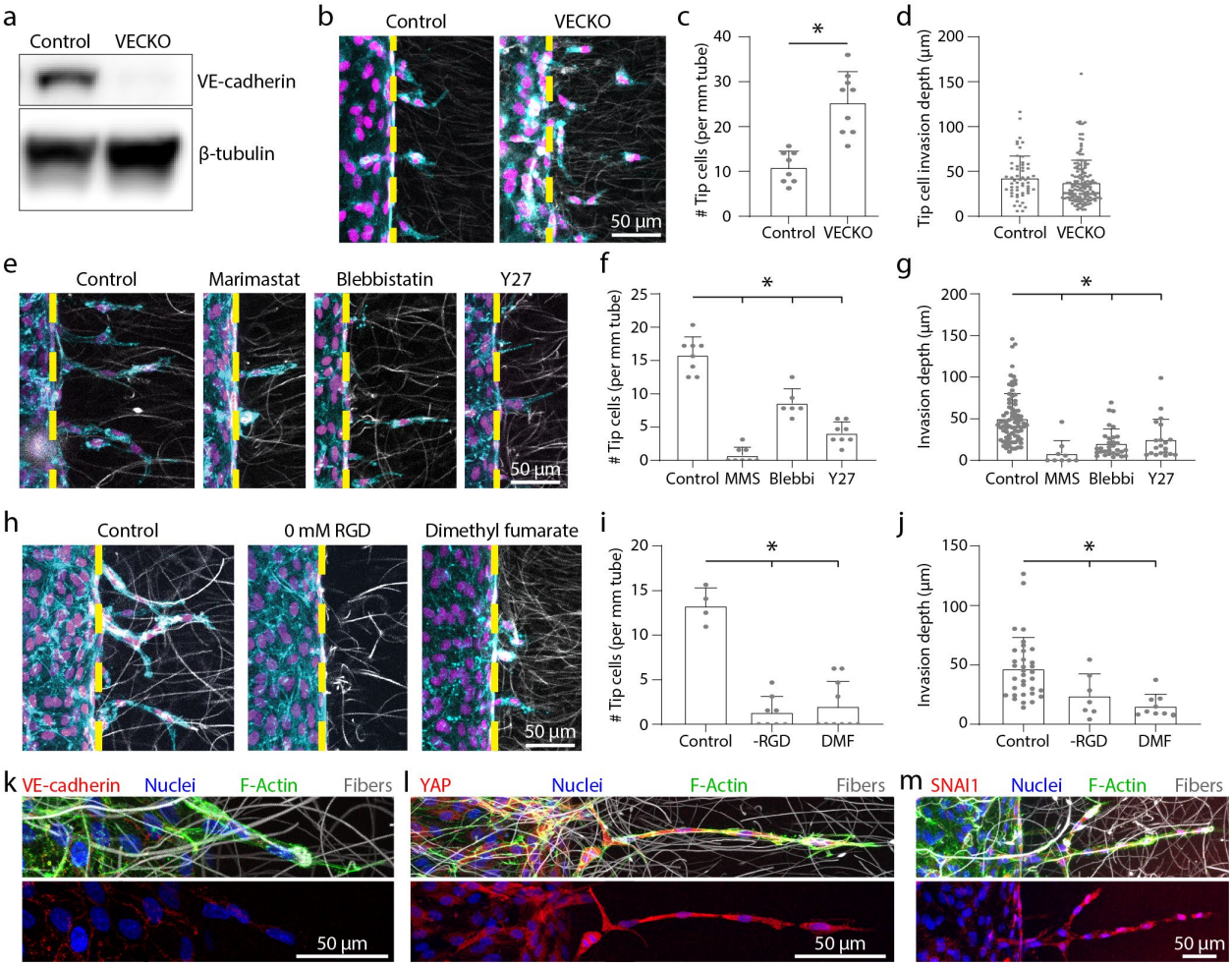

Figure 8.3: Requirements of fiber-induced tip cell formation crossover with EndMT processes.

a) Western blot confirmation of VE-cadherin CRISPR knockout (VECKO) endothelial cells. **b-d)** Representative images (b) of control vs VECKO tip cell invasion in fibrous hydrogels over 4 days and quantification of number of tip cells (c) and invasion depth (d). Nuclei (magenta), F-actin (cyan), yellow dashed lines indicate parent vessel edge. **e-g)** Representative images (e) of control, marimastat, blebbistatin, or Y27 treated endothelial cells within fibrous hydrogels over 4 days and quantification of number of tip cells (f) and invasion depth (g). **h-j)** Representative images (h) of control, 0 mM RGD coupled fibers, and dimethyl fumarate treated endothelial cells within fibrous hydrogels over 4 days and quantification of number of tip cells (i) and invasion depth (j). **k-m)** Relative localization of VE-cadherin (k), YAP (l), and SNAI1 (m) in fiber-induced tip cells vs parent vessel within fibrous hydrogels cultured over 4 days. All data presented as mean ± std.; * indicates a statistically significant comparison with $P<0.05$ (two-sided student's t-test compared to control condition).

8.4.4 Fiber-induced tip endothelial cells exhibit fibrosis propagating phenotype

To further characterize potential changes in FIT-ECs, microarray analysis was utilized to characterize changes in gene expression in response to fibrous topography. To achieve sufficient cell specificity (isolating tip cells from parent vessel cells) and sample size for gene expression measurements, we employed a 3D encapsulation of isolated ECs in control vs fibrous hydrogels to model the more isolated tip cell compared to a cell-dense monolayer of cells that reside in the parent vessel. 3D encapsulated ECs cultured over 3 days were observed to increase in cell spread area and were more polarized, likely due to contact guidance cues provided by ECM fibers **(Figure 8.4a-b)**. Samples submitted for microarray analysis included confluent EC monolayers cultured on tissue culture plastic, confluent EC monolayers cultured within 10 mg/ml fibrin channels (vessel), 3D embedded ECs within 10 mg/ml fibrin and 3D embedded ECs within 10 mg/ml fibrin containing FD2% fibers **(Figure 8.4c)**. All conditions were cultured for 3 days upon which nattokinase (a fibrinolytic enzyme) was utilized to digest fibrin hydrogels affording cell isolation. RNA lysates were extracted from each condition and submitted for microarray analysis **(Figure 8.4c)**.

Compared to 2D EC monolayers, gene expression was largely unchanged in EC monolayers organized within a channel (parent vessel) **(Figure 8.4d)** while ECs cultured in 3D FD0% and FD2% hydrogels resulted in 294 and 1071 differentially expressed genes **(Figure 8e-f)**. For FD2% conditions modeling FIT-ECs, several Gene Ontology terms were significantly changed corresponding to the enhanced tip cell invasion observed in previous studies such as cell migration, cell adhesion, angiogenesis, and positive regulation of EMT (**Figure 8.4g)**. Supporting the observed increase of SNAI1 expression in fiber-induced tip cells, SNAI1 was observed to also significantly increase at the transcriptomic level along with several other EndMT-associated genes

such as MMP14 and TGFβ-signaling associated genes (TGFβ2, BMP2, SMAD3) **(Figure 8.4h and Supplementary Figure 8.5)**. However, microarray analysis also resulted in decreased genes associated with collagen secretion and periostin, two well-accepted markers of myofibroblasts, which may suggest FIT-ECs may only adopt a partial EndMT phenotype in lieu of the observed full EndMT differentiation into myofibroblasts that may require a defined cocktail of soluble factors not introduced in these studies (Medici et al., 2011; Welch-Reardon et al., 2015; Zeisberg et al., 2007). Interestingly, we observed TGFβ2 gene expression was uniquely upregulated in ECs cultured in FD 2% hydrogels **(Figure 8.4h)**. As the family of TGFβ growth factors has been implicated as a main driver of fibrosis, we employed a microfluidic ELISA assay to quantitatively measure TGFβ2 secretion levels. Indeed, TGFβ2 secretion was observed to be elevated only in FD 2% hydrogel conditions **(Figure 8.4i)**. Furthermore, we utilized a cytokine antibody membrane array to detect whether other fiber-induced cell secreted cytokines were elevated. An inflammation-based cytokine membrane array identified elevated levels of MCP1 (CCL2) and IL8 (CXCL8) to be increased in FD2% hydrogels compared to ECs cultured as parent vessels **(Figure 8.4j and Supplementary Figure 8.6a-b)**. Additionally, both CCL2 and CXCL8 were observed to be significantly upregulated at the transcriptomic level supporting the findings of the upregulated cytokine secretion **(Figure 8.4h)**. Taken together, our data demonstrates fiber-induced tip cells present accepted EndMT markers, express differential changes at the gene expression level, and increase secretion of pro-fibrotic cytokines leading us to believe FIT-ECs have transitioned towards a disease propagating phenotype, but not into bona fide myofibroblasts.

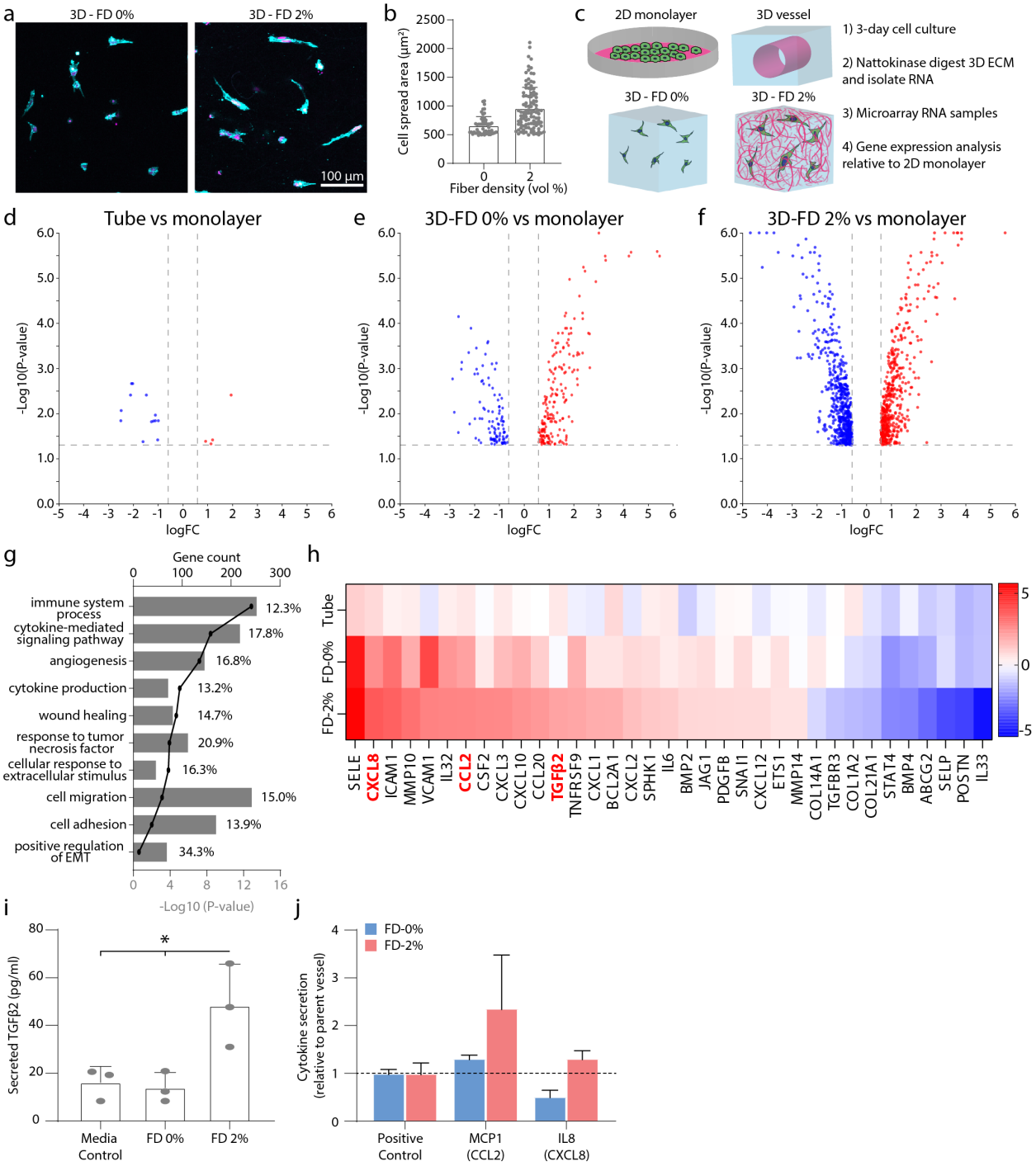

Figure 8.4: Transcriptomic and secretomic analyses of fiber-induced tip cells.
a) 3D embedded ECs within control or fibrous hydrogels cultured over 3 days to model isolated tip cells. **b)** Quantification of projected cell spread area in conditions from (a). c) Microarray study schematic. **d-f)** Volcano plots to visualize differentially expressed genes of RNA lysates collected from ECs culture for 3 days as a vessel (d), 3D embedded within FD 0% hydrogels (e), or 3D embedded within FD 2% hydrogels (f). **g)** Significant Gene Ontology terms for FD 2% vs monolayer. **h)** Curated genes of interest differentially expressed in FD 2% vs monolayer conditions. **i)** Microfluidic ELISA quantification of TGFβ2 secretion. **h)** Cytokine antibody

membrane array detection of MCP1 (CCL2) and IL8 (CXCL8). b, i: Data presented as mean ± std; * indicates statistically significant comparison with $P<0.05$ (b: two-sided student's t-test. i: one-way analysis of variance).

8.4.5 VE-cadherin dependent TGFβ2-induced apoptosis underlies microvasculature rarefaction in late-stage fibrosis

Our transcriptomic and secretomic analyses implicate FIT-ECs as a fibrosis propagating phenotype and a source of TGFβ2 which may promote MF differentiation of other tissue resident cells (i.e. fibroblasts) and subsequent increases of TGFβ2 over the course of fibrosis. To understand how increased TGFβ2 may influence arteriole-scale vasculature, we treated parent vessels in control and fibrous hydrogels with 10 ng/ml TGFβ2. We found that TGFβ2 treatment significantly reduced vessel cell density in both control and fibrous conditions compared to untreated vessels through TGFβ2-induced apoptosis **(Figure 8.5a-b)** (Leight et al., 2012). However, TGFβ2-induced apoptosis was observed to be more potent in parent vessels within fibrous conditions, with increased cells expressing cleaved-caspase-3 **(Figure 8.5a-b)**. As our previous studies demonstrated fibrous topography destabilizes VE-cadherin, and because VE-cadherin stability has previously been shown to regulate downstream signaling and cell response to growth factors (e.g. VEGF and VEGFR2 on cell proliferation vs survival) (Dejana, 2004), we hypothesized that TGFβ2 signaling may be influenced in a VE-cadherin dependent manner.

To test the hypothesis that TGFβ2 signaling is altered by VE-cadherin stability, we first modulated VE-cadherin levels of EC monolayers seeded on 10 mg/ml fibrin hydrogels with varying cell density where confluent monolayers possessed high levels of VE-cadherin and decreased with cell density **(Figure 8.5c-d)**. To assess TGFβ2 signaling, we dosed these conditions with TGFβ2 and measured nuclear SMAD3 localization as TGFβ2 binding to TGFβ receptor (TGFβR) -1 and TGFβR-2 leads to downstream nuclear translocation of SMAD transcription

factor complexes (Weiss and Attisano, 2013). Indeed, lower cell density conditions with decreased VE-cadherin resulted in increased SMAD3 nuclear localization **(Figure 8.5c-d)**. Combining all cell density conditions together, Pearson's correlation analyses result in a significant, negative correlation between VE-cadherin and nuclear SMAD3 **(Figure 8.5e)**. As varying cell density may lead to confounding factors, such as variable paracrine signaling, we next performed mosaic studies with control and VECKO ECs at varying ratios as a method to control VE-cadherin stability independent of cell density. Increased ratios of VECKO:control ECs resulted in decreased VE-cadherin and increased nuclear SMAD3 falling in line with our variable cell density results **(Supplementary Figure 8.7a-c)**. Additionally, we employed a scratch wound assay to achieve variable VE-cadherin stability within the same samples. In scratched regions of the sample, invading cells were less dense with decreased VE-cadherin and increased nuclear SMAD3 compared to regions distanced from the scratch which were more cell dense with increased VE-cadherin and decreased nuclear SMAD3 **(Supplementary Figure 8.8a-c)**. Lastly, we performed these studies comparing control hydrogels with fibrous hydrogels and found that fibrous topography without addition of TGFβ2 led to increased nuclear SMAD3 expression and was further increased with TGFβ2 treatment **(Figure 8.5g-i)**.

Towards identifying how VE-cadherin may be influencing TGFβ signaling, we utilized a protein-proximity labeling technique (BioID) to identify protein-protein interactions with VE-cadherin (data not included in current version). Protein lysates from ECs containing VE-cadherin-BIRA-HA (VE-BioID) were collected and biotinylated VE-cadherin protein complexes were extracted with streptavidin. Interestingly, TGFβR2 was identified as a top 15 most abundant binding partner with VE-cadherin. This finding may suggest that VE-cadherin inactivates downstream TGFβ signaling by directly binding to TGFβR2 therefor offering a protective effect

from TGFβ2-induced apoptosis. Overall, these studies demonstrate that high levels of VE-cadherin inhibit downstream TGFβ2 signaling, resulting in decreased nuclear SMAD3 expression. Fibrous topography destabilizes VE-cadherin, rendering ECs to be more susceptible to TGFβ2-induced apoptosis. A common observation in various animal models of fibrosis is microvasculature rarefaction towards the late-stage of the disease where both fiber density and TGFβ are heightened (Goligorsky, 2010; Magro et al., 2006; Mohammed et al., 2015). Although more studies at the proteomic level are required, the identification that VE-cadherin confers protective shielding from TGFβ-induced apoptosis may offer a promising therapeutic approach to prevent microvasculature rarefaction, and subsequent tissue hypoxia and nutrient deficiency in fibrotic diseases.

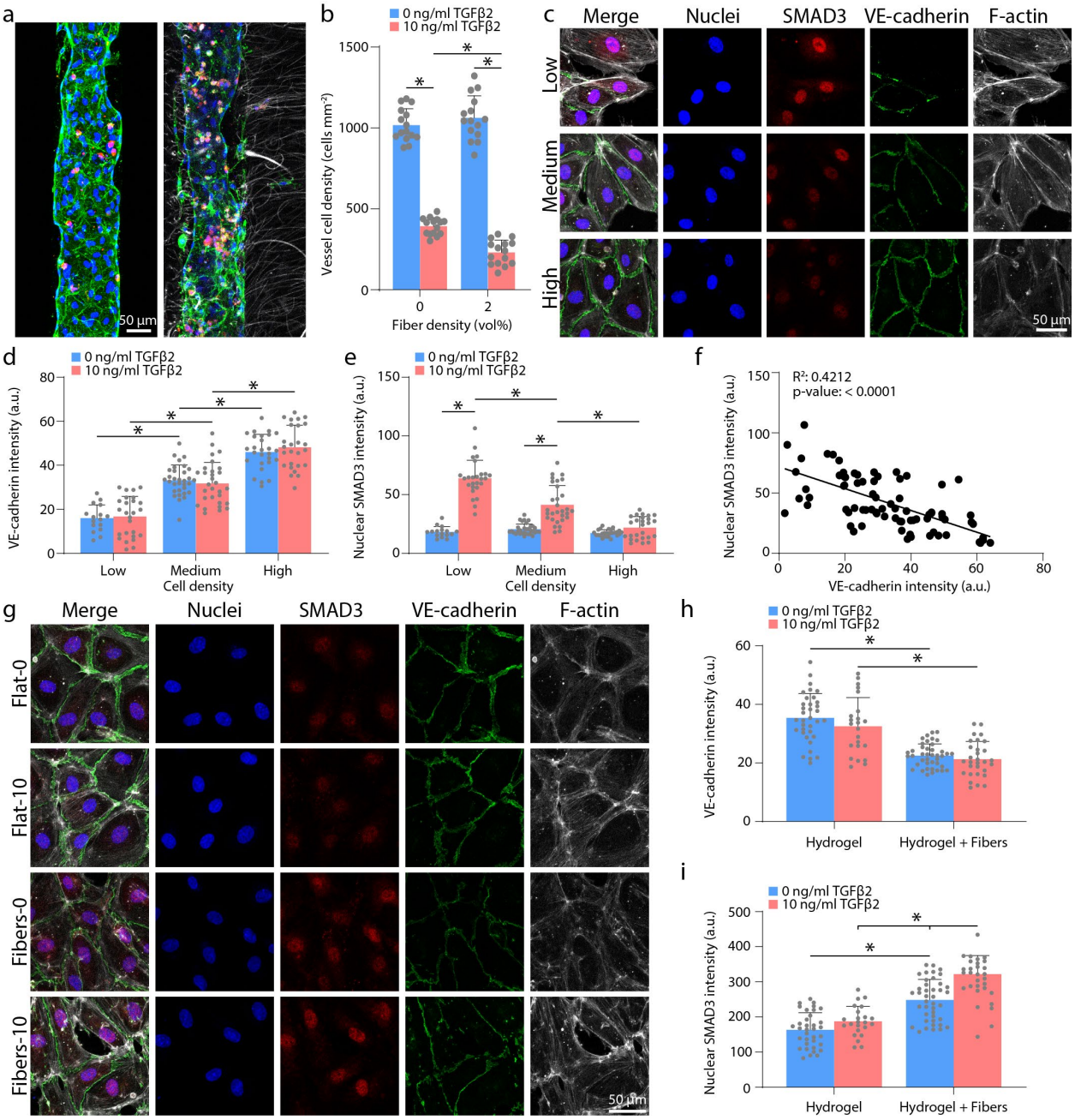

Figure 8.5: VE-cadherin dependent TGFβ2 signaling.

a) Parent vessels in control or fibrous hydrogels treated with 10 ng/ml TGFβ2 for 4 days. Nuclei (blue), F-actin (green), cleaved-caspase-3 (red). **b)** Quantification of vessel cell density within control or fibrous hydrogels treated with or without 10 ng/ml TGFβ2. **c)** Variable EC monolayer seeding density on 10 mg/ml fibrin hydrogels treated with 10 ng/ml TGFβ2 for 2 days on VE-cadherin and SMAD3. Nuclei (blue), SMAD3 (red), VE-cadherin (green), F-actin (white). **d-f)** Quantifications of VE-cadherin intensity (d), nuclear SMAD3 (e), and correlation between VE-cadherin and SMAD3 (f) for conditions in (c) with or without 10 ng/ml TGFβ2. **g)** EC monolayers cultured on 10 mg/ml fibrin hydrogels with or without an overlying fibrous matrix and with or without 10 ng/ml TGFβ2 for 2 days. **h-i)** Quantifications of VE-cadherin (h) and SMAD3 (i) for

conditions in (g). All data presented as mean ± std.; * indicates a statistically significant comparison with $P<0.05$ (one-way analysis of variance).

8.5 Discussion

While myriad soluble factors have been identified to activate and direct endothelial tip cell invasion (Potente et al., 2011), the role of physical cues presented by the ECM has not been well-characterized. As tip cell activation and changes in ECM properties, such as fibrillar collagen density and organization, have been observed to occur concurrently over physiologic and pathologic processes such as fibrosis, this work establishes how specific physical ECM cues may regulate tip cell activation. We integrated a recently established microphysiologic model of sprouting angiogenesis with a materials fabrication technique to imbue collagen fibril mimetic synthetic fibers within 3D hydrogels and identified fiber density destabilizes VE-cadherin cell-cell junctions, decreases endothelium barrier function, and increases tip cell activation and invasion via mesenchymal transition pathways. Performing microarray and cytokine detection assays, we identified that fibrous topography transition endothelial tip cells towards a fibrosis propagating phenotype serving as a source of TGFβ2 and inflammatory cytokines. Lastly, this work identified how endothelium responds to excessive TGFβ2 in a VE-cadherin dependent manner, where increased VE-cadherin stability offers a protective effect from TGFβ2-induced apoptosis by directly binding to TGFβR2. In late-stage fibrosis settings, where TGFβ2 and fibrillar collagen density are elevated, these studies provide insight to the molecular mechanisms that underlie the common observation of microvasculature rarefaction where fibrous topography of perivascular ECM disrupt protective VE-cadherin in endothelium allowing for the release of VE-cadherin-TGFβR2 complexes and increased TGFβ2-induced endothelial cell apoptosis.

8.6 Materials and Methods

8.6.1 Reagents

All reagents were purchased from Sigma-Aldrich and used as received, unless otherwise stated.

8.6.2 Microfluidic device fabrication

3D printed moulds were designed in AutoCAD and printed via stereolithography from Protolabs (Maple Plain, MN). Polydimethylsiloxane (PDMS, 1:10 crosslinker:base ratio) devices were replica casted from 3D printed moulds, cleaned with isopropyl alcohol and ethanol, and bonded to glass coverslips with a plasma etcher. Devices were treated with 0.01% (w/v) poly-l-lysine and 0.5% (w/v) L-glutaraldehyde sequentially for 1 hour each to promote ECM attachment to the PDMS housing, thus preventing potential hydrogel compaction from cell-generated forces. 160 μm stainless steel acupuncture needles (Lhasa OMS, Weymouth, MA) were dip-coated with 1% (w/v) gelatin to reduce hydrogel fracture, inserted into each device and sterilized. Hydrogel precursor solution was then injected into each device and polymerized around each set of needles. Hydrogels were hydrated in EGM2 media at 37℃ overnight (or greater than 12 hours) to dissolve the gelatin layer and needles were removed to form 3D hollow channels fully embedded within a crosslinked hydrogel and positioned 500 μm away from PDMS and glass boundaries. A chilled solution of 100 μg/ml matrigel diluted in PBS was added to endothelial channels and allowed to adsorb onto the hydrogel channel surface at 4°C overnight. Matrigel solution was then rinsed with PBS twice followed by incubation in EGM2 media.

8.6.3 Dextran vinyl sulfone polymer synthesis

Dextran (molecular weight 86,000 Da, MP Biomedicals, Santa Ana, CA) was modified with vinyl sulfone groups as in (Matera et al., 2019, 2020; Yu and Chau, 2012). Dextran (5 g) was dissolved in 0.1 M sodium hydroxide solution (250 mL) at room temperature. Divinyl sulfone (3.875 ml, Thermo Fisher Scientific, Waltham, MA) was added and the reaction was carried out for 4 minutes with vigorous stirring (1500 RPM) at room temperature. The reaction was terminated by adjusting the pH to 5.0 with the addition of hydrochloric acid. The reaction product was dialyzed against milli-Q water for 3 days with two solvent exchanges daily. The dialyzed reaction product was the lyophilized for 3 days to obtain the pure product, which was then characterized by ^{1}H-nuclear magnetic resonance spectroscopy in D_2O. The degree of vinyl sulfone functionalization was calculated as the ratio of the proton integral (6.91 ppm) and the anomeric proton of the glucopyranosyl ring (5.166 and 4.923 ppm); here a vinyl sulfone/dextran repeat unit ratio of 0.16 was determined.

8.6.4 Fiber segment fabrication

DexVS fiber segments were generated as in (Matera et al., 2020). DexVS was dissolved at 0.6 g ml^{-1} in a 1:1 mixture of Milli-Q water and dimethylformamide with 0.015% Irgacure 2959 photoinitiator and 0.5 mM methacrylated rhodamine (Polysciences Inc., Warrington, PA). This polymer solution was utilized for electrospinning within an environment-controlled glovebox held at 21°C and 30% relative humidity. Electrospinning was performed at a flow rate of 0.3 ml hour^{-1}, gap distance of 5 cm, and voltage of −10.0 kV onto a grounded collecting surface attached to a linear actuator. Fiber layers were collected on glass slabs and primary cross-linked under ultraviolet light (100 mW cm^{-2}). After polymerization, fiber segments were resuspended in a

known volume of phosphate-buffered saline (PBS) (3 ml). The total volume of fibers was then calculated via a conservation of volume equation: total resulting solution volume = volume of fibers + volume of PBS. After calculating total fiber volume, solutions were re-centrifuged, supernatant was removed, and fiber pellets were resuspended to create a 10 volume % fiber solution, which were then aliquoted and stored at 4°C. To support cell adhesion, 2 mM arginylglycylaspartic acid (RGD, CGRGDS; GenScript, George Town, KY) was coupled to vinyl sulfone groups along the DexVS backbone via Michael-type addition chemistry for 30 min, followed by quenching of excess VS groups in a 300 mM cysteine solution for 30 min.

8.6.5 Hydrogel formulations

Fibrin hydrogels were prepared with fibrinogen from bovine plasma dissolved in PBS at 50 mg ml^{-1} stock concentrations. 10 mg ml^{-1} fibrinogen was prepared in PBS and crosslinked with thrombin (6 units per mg of fibrinogen) for 20 minutes at 37℃. For fibrous hydrogels, DexVS fiber segments were incorporated within the fibrin hydrogel precursor solution over a 0-2% v/v density. To generate fiber alignment perpendicular to the long axis of the parent vessel (0° alignment), fibrin precursor solution containing fibers were injected such that flow across acupuncture needles (rigid cylinder) generated a flow profile that aligned fibrils in the direction of flow. To generate fiber alignment parallel to the long axis of the parent vessel (90° alignment), fibrin precursor solution containing fibers were first injected into the device. Subsequent insertion of acupuncture needles generated flow profiles to align fibers in the direction of needle insertion. To generate collagen bundle-embedded fibrin hydrogels, type I collagen rat tail (4.8 mg ml^{-1}) was adjusted to a pH of 7.4 with sodium hydroxide and PBS on ice. Next, 80°C MQ water was added in a 1:1 ratio (2.4 mg ml^{-1} final concentration) and immediately vortexed for 30 seconds. Collagen

bundles form immediately during vortexing and were isolated via centrifugation (500 g for 4 minutes).

8.6.6 Mechanical testing

Young's modulus of each hydrogel condition was measured using atomic force microscopy (AFM; Nanosurf, Liestal, Switzerland) in contact mode. Indentations were made at a loading rate of 2 μm/s with silicon nitride cantilevers (AppNano, Mountain View, CA) with a nominal spring constant of 0.046 N/m and a 5 μm diameter spherical glass bead. Force-displacement curves were taken at a minimum of 3 regions on each hydrogel and fit to the Hertz model assuming a Poisson's ratio of 0.5 to estimate the elastic modulus.

8.6.7 Device cell seeding and culture

Human umbilical vein, liver, lung, and dermal endothelial cells (Lonza, Switzerland) were cultured in endothelial growth media (EGM2, Lonza). HUVECs were passaged upon achieving confluency at a 1:4 ratio and used in studies from passages 4 to 9. Liver, lung, and dermal ECs were passaged at a 1:4 ratio and used in studies from passages 2 to 6. A 10 μl solution of suspended ECs (10 million cells ml^{-1} density) was added to one reservoir of the endothelial channel and inverted for 30 minutes to allow cell attachment to the top half of the channel, followed by a second seeding with the device upright for 30 minutes to allow cell attachment to the bottom half of the channel. ECs reached confluency and self-assembled into stable parent vessels over 24 hours. Media and chemokines were refreshed every 24 hours and devices were cultured with continual reciprocating flow utilizing gravity-driven flow on a seesaw rocker plate at 0.33 Hz. S1P-induced tip cell formation was performed with 0-50 nM S1P diluted in EGM2 media and was added only

to the chemokine channel for 3 days after 16 hours post cell seeding. Fiber-induced tip cell formation studies were cultured in EGM2 media alone for 3 days after 16 hours post cell seeding. Agents for permeability agonist and pharmacologic dosing studies were incorporated into EGM2 media and added to both the endothelial and chemokine channels for 3 days after 16 hours post cell seeding. Human mesenchymal stem cells were cultured in high-glucose DMEM containing 5% fetal bovine serum and 1% P/S and were passaged upon achieving confluency at a 1:3 ratio and used from passages 3-6. hMSCs were first seeded into device channels as described above, at a 10 µl solution of 1.5 million cells ml^{-1}. Endothelial cells were seeded as described above 1 hour after hMSCs seeding and attachment.

8.6.8 Diffusive permeability measurements

Diffusive permeability was quantified as in (Polacheck et al., 2017, 2019). Briefly, fluorescent dextran (70 kDa Texas Red, Thermo Fisher) was incorporated into EGm2 media at 12.5 µg ml^{-1} and dextran diffusion was imaged at 1 second intervals to measure flux of dextran from endothelium into the ECM. The resulting diffusion profile was fitted to a dynamic mass-conservation equation as in (Adamson et al., 1994) with the diffusive-permeability coefficient (P_D) defined by $J = P_D(c_{vessel} - c_{ECM})$, where J is the mass flux of dextran, c_{vessel} is the concentration of dextran in the vessel, and c_{ECM} is the concentration of dextran in the perivascular ECM.

8.6.9 Western blotting

Samples for western blotting were collected from confluent EC monolayers cultured on tissue culture plastic or electrospun fiber matrices for 2 days after cell seeding and were treated with either EGM2 media, or EGM2 media containing 50 ng ml^{-1} VEGF (peprotech), 50 ng ml^{-1}

TNFα, or 2 U ml^{-1} Thrombin. To collect protein lysates, cells were collected with a cell scraper in chilled PBS solution and centrifuged to generate cell pellet. PBS supernatant was removed and replaced with RIPA buffer containing protease and phosphatase inhibitors. Following freeze fracture of cell membranes (10 minutes at -80°C), samples were centrifuged for 10 minutes at 20,000 g, and the supernatant was collected containg the purified protein lysate. Protein lysate concentrations were measured using a BCA assay, and 30 μg ml^{-1} protein was loaded into a 4-20% Tris-Glycine Novex wedge well. Proteins were separated with electrophoresis for 90 minutes at 120V in running buffer. Protein gels were then transferred to a PVDF membrane for 60 minutes at 20V in transfer buffer at 4°C. PVDF membranes were then blocked in 5% w/v blocking grade milk buffer, and stained with primary antibodies [VE-cadherin (1:1,000, santa crux biotechnology) and β-tubulin (1:10,000, Proteintech)] overnight on an orbital shaker at 4°C. Membranes were then rinsed in TBST and stained with HRP and imaged on a blot dock.

8.6.10 Transcriptomic analysis

Samples for microarray analysis included 1) confluent EC monolayers cultured on tissue culture plastic, 2) confluent EC monolayers cultured within 10 mg ml^{-1} fibrin hydrogel channels within the angiogenesis-on-a-chip device, 3) single, 3D embedded ECs within FD 0% 10 mg ml^{-1} fibrin hydrogels and 4) single, 3D embedded ECs within FD 2% 10 mg ml^{-1} fibrin hydrogels. All conditions were cultured for 3 days upon which nattokinase (100 fibrinolytic units ml^{-1}) was incorporated into EGM2 media for 15 minutes to digest the surrounding fibrin hydrogel. ECs were pelleted and RNA isolation was performed via RNeasy mini kit per manufacturer's protocol. Purified RNA samples were submitted to the University of Michigan Sequencing Core for

microarray analysis. Gene expression data was analyzed utilizing Advaita Bioinformatics software.

8.6.11 Secretomic analysis

To assess how fibrous topography influenced EC cytokine secretion, we employed a recently established microfluidic ELISA and an antibody cytokine detection array membrane. For both assays, samples were cultured for 7 days, with supernatant media refreshed every 2 days. Thus, conditioned media collected for analysis contained 2 days of cell secreted factors (i.e. days 5-7). As cell-secreted factors, such as TGFβ2 may secreted and bound to the extracellular matrix (i.e. latent TGFβ complexes), the fibrin hydrogel was digested utilizing nattokinase as described above. To stabilize TGFβ2 cytokines, hydrochloric acid was added to conditioned media to pH5 only for TGFβ2 measurements. All samples were stored at -80°C and thawed immediately prior to cytokine detection assays. Microfluidic ELISA was performed as previously described in detail in (Tan et al., 2017). Antibody cytokine detection array membrane was performed per manufacturer protocol.

8.6.12 VE-cadherin dependent TGFB2 signaling studies

For all SMAD3 studies ECs were first treated with mitomycin C (20 μg ml^{-1} for 2 hours) to inhibit cell proliferation and control cell density. For variable cell density SMAD3 studies, ECs were seeded onto 2D 10 mg ml^{-1} fibrin hydrogels (18 mm coverslips treated with poly-l-lysine and l-glutaraldehyde) at a low (25 K cells cm^{-2}), medium (50 K cells cm^{-2}) and high (100 K cells cm^{-2}) cell density. The following day, samples were treated with 0 or 10 ng ml^{-1} TGFβ2 (Peprotech) in EGM2 media (without serum or fibroblast growth factor (FGF) as FGF has previously been

shown to inhibit TGFβ signaling) for two days with media refreshed daily. For mosaic SMAD3 studies, control and VECKO ECs were seeded at varying ratios (0, 50, 75, and 100% VECKOs) at a constant 100 K cells cm^{-2} density on 2D 10 mg ml^{-1} fibrin hydrogels. TGFβ2 treatment was identical as described above. For fibrin hydrogel vs fibrin hydrogel + fibers studies, fibrin hydrogel + fibers conditions were generated by electrospinning DexVS fiber matrices onto a dried gelatin-coated coverslip. A solution of fibrin hydrogel was then added to the DexVS fiber matrix with a second glutaraldehyde treated coverslip placed on top. After fibrin polymerization and hydration, the dried-gelatin coverslip was removed, resulting in a DexVS fiber matrix adhered on top of a fibrin hydrogel-coated glutaraldehyde coverslip. ECs were seeded on to fibrin and fibrin+fibers hydrogels at a 100 K cells cm^{-2} density and dosed with TGFβ2 identical as described above. For scratch wound studies, glass coverslips were seeded with ECs at 100 K cells cm^{-2} density and scratched with a P1000 tip the following day and dosed with TGFβ2 identical as described above except only for 1 day as at longer timepoints ECs were observed to close the scratch region.

8.6.13 Fluorescent staining

Samples were fixed with 4% paraformaldehyde and permeabilized with a PBS solution containing Triton X-100 (5% v/v), sucrose (10% w/v), and magnesium chloride (0.6% w/v) for 1 hour each at room temperature. AlexaFluor 488 phalloidin (Life Technologies, Carlsbad, CA) was utilized to visualize F-actin. 4', 6-diamidino-2-phenylindole (DAPI, 1 μg ml^{-1}) was utilized to visualize cell nucleus. To visualize VE-cadherin, YAP, SNAI1, vimentin, or SMAD3, samples were sequentially blocked in bovine serum albumin (0.3% w/v), incubated with primary antibody [mouse monoclonal anti-VE-cadherin (1:500, Santa Cruz Biotechnology), mouse monoclonal anti-YAP (1:500, Santa Cruz Biotechnology), rabbit monoclonal anti-SNAI1 (1:500, Cell Signaling

Technologies), mouse monoclonal anti-vimentin (1:500) rabbit monoclonal anti-SMAD3 (1:500, Cell Signaling Technologies)], and incubated with secondary AlexaFluor 647 goat anti-mouse or anti-rabbit IgG (H+L) (1:1000, Life Technologies) each for 1 hour at room temperature. For VE-cadherin pulse studies, a mouse monoclonal anti-VE-cadherin antibody (55-7H1 clone) pre-conjugated with AlexaFluor 647 was added to cell culture media (1:500) for 30 minutes followed by media rinses as described in (Neto et al., 2018).

8.6.14 Microscopy and image analysis

Fluorescent images were captured on a Zeiss LSM800 confocal microscope. To quantify tip cell formation, the number and distance of tip cells were measured in FIJI. Tip cells were defined morphologically as the leading cell of an invading strand or as a single invading cell. VE-cadherin signal intensity was quantified by summing the total VE-cadherin signal and normalizing to the number of cells in each field of view. Nuclear SMAD3 intensity was quantified by first masking the SMAD3 signal with a nuclear mask, then summing SMAD3 intensity and normalizing to the number of cells in each field of view. Performing these analyses on a field of view basis allowed for Pearson's correlation analysis between nuclear SMAD3 and VE-cadherin. Measurements of VE-cadherin junctional width was performed as described previously (Bordeleau et al., 2017; Huynh et al., 2011; Van Nieuw Amerongen et al., 2007). Briefly, high resolution images of VE-cadherin were acquired on a confocal microscope. Images across conditions were thresholded under the same parameters. A line orthogonal to the long axis of the junction was drawn to measure the intensity profile and obtain VE-cadherin junction width.

8.6.15 Statistics

Statistical significance was determined by one-way analysis of variance (ANOVA) or two-sided student's t-test where appropriate, with significance indicated by $p<0.05$. Sample size is indicated within corresponding figure legends and all data are presented as mean ± standard deviation.

8.6.16 Data availability

The data that support the findings of this study are available from the corresponding author upon reasonable request.

8.7 Supplementary Material

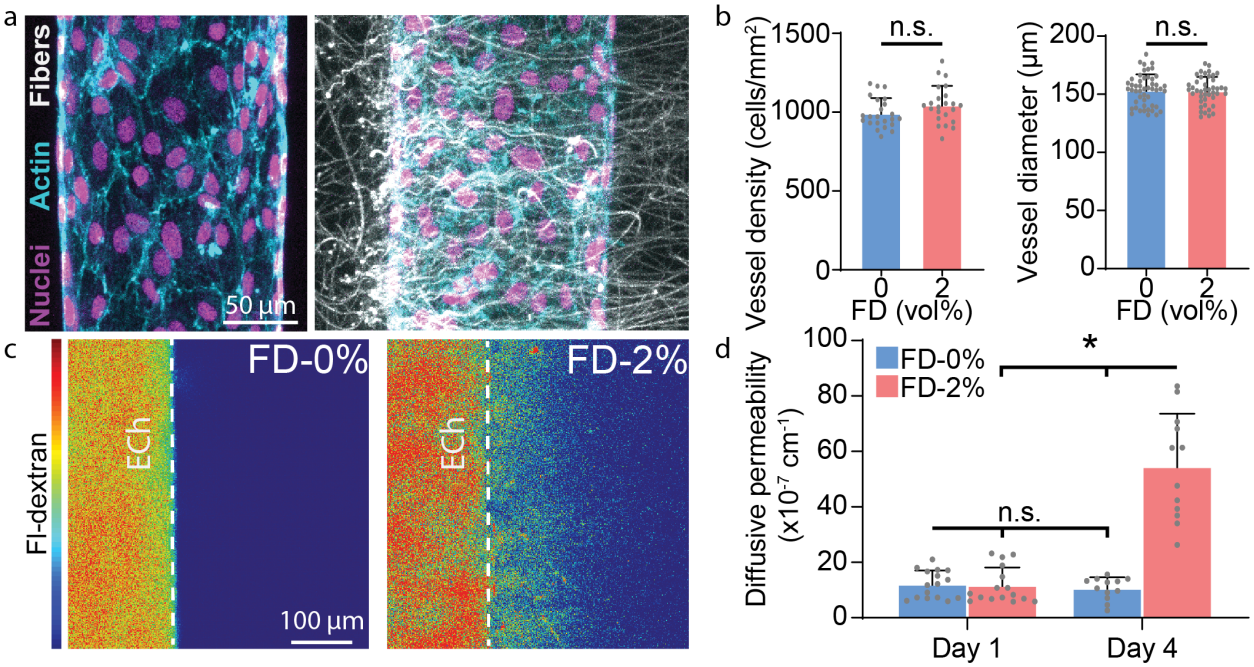

Supplementary Figure 8.1: Consistent parent vessels in control vs fibrous ECM after 16 hours of cell seeding.
a) Representative images (max intensity projection) of parent vessels cultured in control vs FD 2% hydrogels with channels coated in basement membrane proteins. **b)** Quantification of vessel cell density and diameter. **c)** Fluorescent dextran diffusion in control vs FD 2% hydrogels on Day 4 culture. **d)** Quantification of diffusive permeability of control and FD 2% hydrogels on Day 1 and

4. All data presented as mean ± std.; * indicates a statistically significant comparison with P<0.05. n.s. indicates a non-statistically significant comparison (b: two-sided student's t-test and d: one-way analysis of variance).

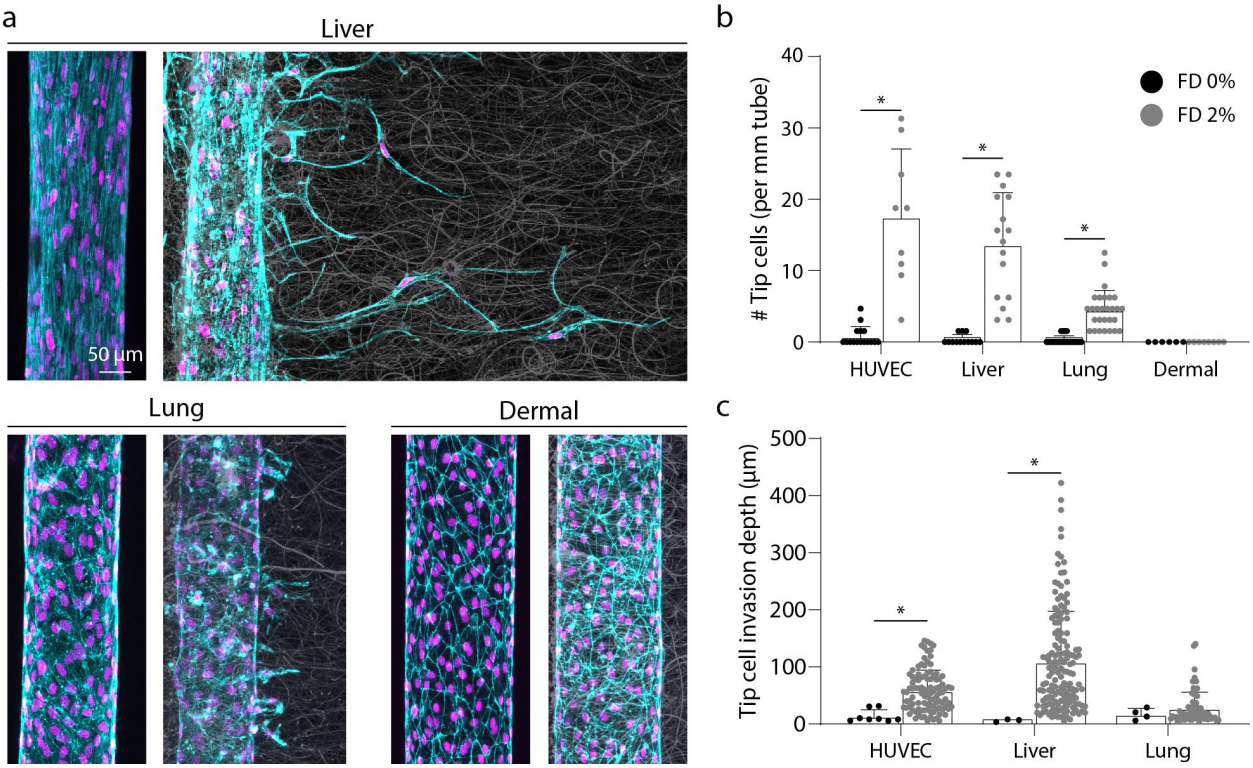

Supplementary Figure 8.2: Fiber density promotes tip cell formation in liver and lung, but not dermal endothelial cells.

a) Representative images (max intensity projection) of liver, lung, and dermal endothelial cells cultured over 4-days in control or FD 2% hydrogels. Nuclei (magenta), F-actin (cyan). **b-c)** Quantification of number of tip cells and tip cell invasion depth for conditions in (a). All data presented as mean ± std.; * indicates a statistically significant comparison with P<0.05 (two-sided student's t-test).

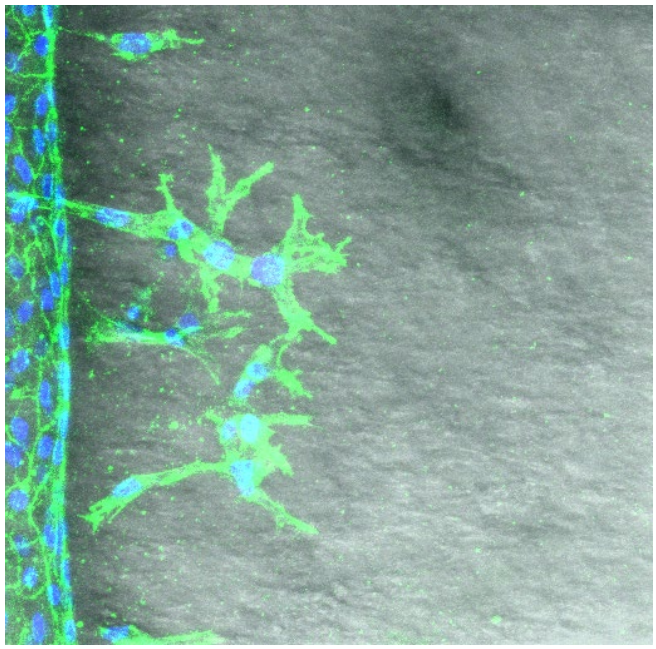

Supplementary Figure 8.3: Isolated collagen bundles embedded within fibrin hydrogels.
a) Collagen bundles were generated as in (Gong et al., 2020), isolated with centrifugation and embedded within 10 mg/ml fibrin hydrogels. Endothelial cells were cultured for 6 days. Nuclei (blue), F-actin (green), transmitted light (grey).

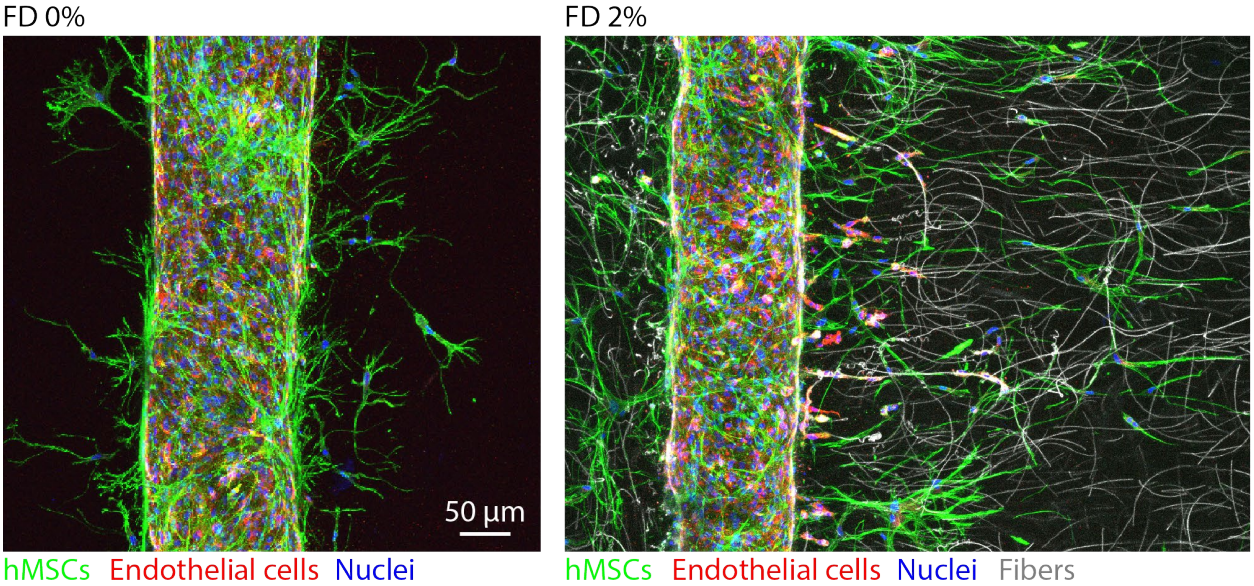

Supplementary Figure 8.4: Fiber density promote tip cell formation with hMSC-coated endothelium.
Representative images (max intensity projection) of hMSCs and endothelial cells cultured over 4-days in control or FD 2% hydrogels.

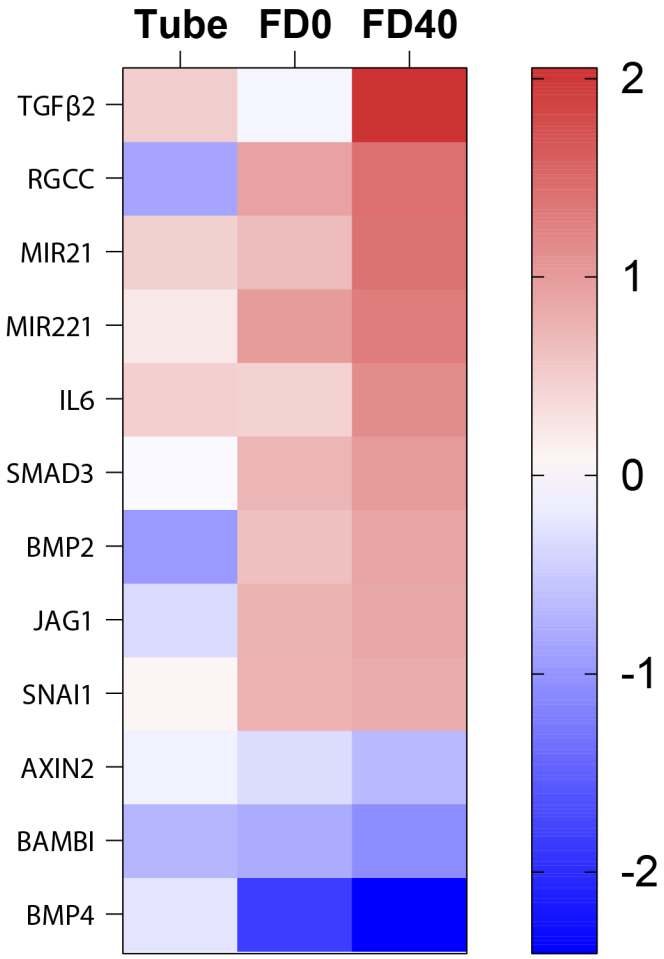

Supplementary Figure 8.5: Differentially expressed genes under "positive regulation of epithelial to mesenchymal transition" Gene Ontology category.

a

	A	B	C	D	E	F	G	H	I	J	K	L
1	Pos	Pos	Neg	Neg	Eotaxin	Eotaxin-2	GCSF	GM-CSF	ICAM-1	IFN-g	I-309	IL-1a
2	Pos	Pos	Neg	Neg	Eotaxin	Eotaxin-2	GCSF	GM-CSF	ICAM-1	IFN-g	I-309	IL-1a
3	IL-1b	IL-2	IL-3	IL-4	IL-6	IL-6sR	IL-7	IL-8	IL-10	IL-11	IL-12p40	IL-12p70
4	IL-1b	IL-2	IL-3	IL-4	IL-6	IL-6sR	IL-7	IL-8	IL-10	IL-11	IL-12p40	IL-12p70
5	IL-13	IL-15	IL-16	IL-17	IP-10	MCP-1	MCP-2	M-CSF	MIG	MIP-1a	MIP-1B	MIP-1s
6	IL-13	IL-15	IL-16	IL-17	IP-10	MCP-1	MCP-2	M-CSF	MIG	MIP-1a	MIP-1B	MIP-1s
7	RANTES	TGF-B1	TNFa	TNF-B	s TNF RI	s TNF RII	PDGF-BB	TIMP-2	Blank	Blank	Neg	Pos
8	RANTES	TGF-B1	TNFa	TNF-B	s TNF RI	s TNF RII	PDGF-BB	TIMP-3	Blank	Blank	Neg	Pos

b

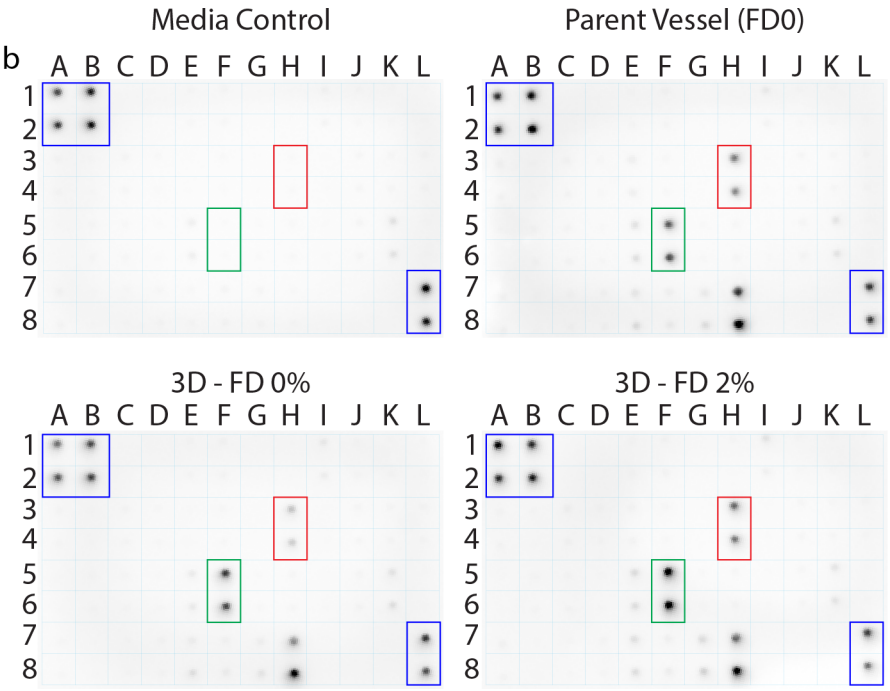

Supplementary Figure 8.6: Human inflammation antibody membrane array.
a) Membrane array cytokine map. **b)** Intensity-based response of captured antibodies from media control, or conditioned media collected from cells cultured as a parent vessel, 3D embedded within control or fibrous hydrogels.

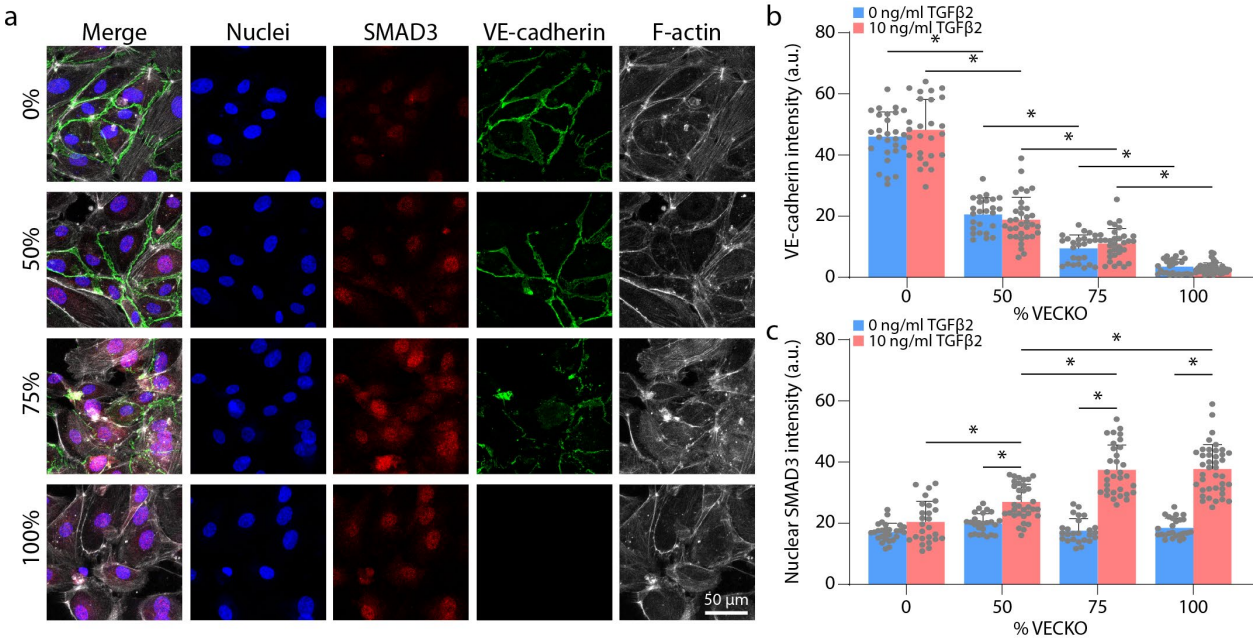

Supplementary Figure 8.7: Mosaic EC monolayers to modulate VE-cadherin stability.
a) High cell density EC monolayers of control and VECKO ECs at varying ratios (indicated as % VECKOs) treated with 10 ng/ml TGFβ2 for 2 days and seeded on 10 mg/ml fibrin hydrogels. Nuclei (blue), SMAD3 (red), VE-cadherin (green), F-actin (white). **b-c)** Quantification of VE-cadherin and nuclear SMAD3 expression for mosaic control and VECKO monolayers treated with or without 10 ng/ml TGFβ2. All data presented as mean ± std.; * indicates a statistically significant comparison with P<0.05 (one-way analysis of variance).

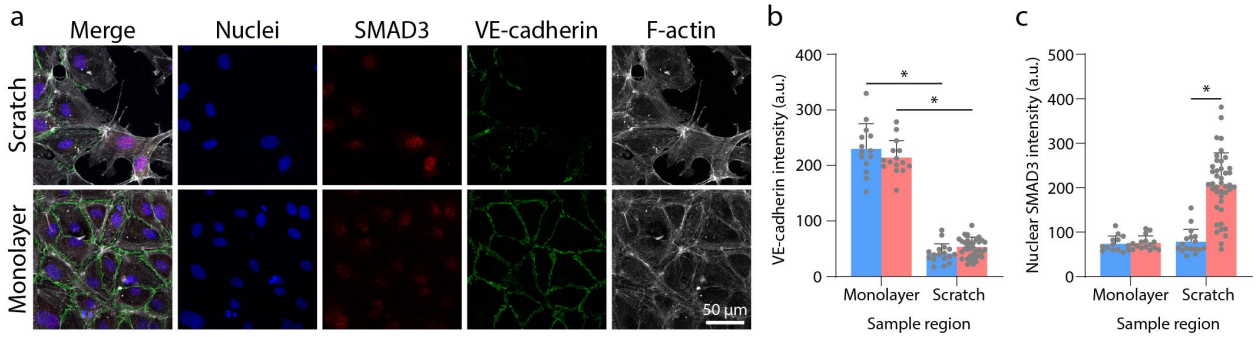

Supplementary Figure 8.8: Scratch wound assay to modulate VE-cadherin stability.
a) Monolayer vs scratch regions within the same sample treated with 10 ng/ml TGFβ2 for 1 day. Nuclei (blue), SMAD3 (red), VE-cadherin (green), F-actin (white). **b-c)** Quantification of VE-cadherin and nuclear SMAD3 expression in monolayer vs scratch regions treated with or without 10 ng/ml TGFβ2. All data presented as mean ± std.; * indicates a statistically significant comparison with P<0.05 (one-way analysis of variance).

Chapter 9: Conclusions and Future Directions

9.1 Summary of findings

Cell migration is an iterative and adaptive process that involves intimate interactions with dynamically changing extracellular matrix (ECM) microenvironments. Chapter 2 highlighted the diversity of both cell migration modes and native tissue structures and their interdependency observed in *in vivo* contexts. As controlling cell migration and ECM properties is challenging *in vivo*, the cell migration field has turned towards a long history of *in vitro* cell migration platforms that have iteratively increased in complexity to better recapitulate cell migration in physiologic contexts. A critical missing ingredient in previous standard cell migration assays has been the lack of tunable biomaterials that incorporate the fibrous architecture of native tissues. As fibrillar matrix proteins, such as collagen type I, are the predominant ECM component in native tissues, this thesis focused on designing biomimetic microsystems that incorporated this key matrix feature.

This thesis employed various microsystems that ranged in complexity from 2D micropatterned lines, 3D synthetic fiber matrices, and microphysiologic devices of sprouting angiogenesis composed of natural-derived hydrogels (collagen and fibrin), synthetic DexVS hydrogels with tunable micropores, and synthetic fibrous hydrogel composites (electrospun fiber segments embedded within 3D hydrogels). Overall, using such microsystems, this thesis examined cell migration mechanoreciprocity over various timescales. Over shorter timescales (minutes to hours), Chapters 3-4 examined cell migration mechanoreciprocity of fibroblasts and cancer cells

(Wang et al., 2018, 2019). Over intermediate timescales (hours to days), Chapters 5-7 examined cell migration mechanoreciprocity of collective endothelial cell migration during angiogenesis (Wang et al., 2021a, 2020, 2021b). Over longer timescales (days to months), Chapter 8 examined how changes in fibrotic matrix signatures influence the activation of endothelial tip cell formation and their transition towards a fibrosis propagating phenotype. Overall, with improved understanding of how cell and matrix states spatiotemporally coevolve during cell migration will provide new insights to promote fibroblasts to repair wound sites, direct endothelial cell sprouts to vascularize ischemic or engineered tissue grafts and inform new therapeutic strategies to confine otherwise metastatic cancer cells to the primary tumor.

9.2 Future directions

9.2.1 3D printing approaches to engineer microvasculature

The vascularization challenge remains an outstanding hurdle for the clinical translation of large, engineered tissue replacement therapies (Kim et al., 2021; Novosel et al., 2011). With increasing size (>500 μm thickness), engineered tissue grafts are diffusion-limited resulting in hypoxic microenvironments unsuitable for cell survival and function. Through Chapters 5-7, this thesis employed a cell migration and biomaterials approach to address the vascularization challenge by identifying critical ECM design criteria that promote functional angiogenesis. However, a key finding from these chapters is that vascularization via sprouting angiogenesis requires a slow and steady approach to generate perfusable, anastomosed neovessels (around 100-150 micron invasion per day) (Wang et al., 2020). Thus, the time required to vascularize large tissue engineered constructs relying solely on host angiogenesis may bypass the time window to rescue cell viability upon implantation.

Recent advances in 3D printing approaches have demonstrated that the incorporation of perfusable channels within cell-dense tissue constructs can rescue cell viability (Grigoryan et al., 2019; Miller et al., 2012; Skylar-Scott et al., 2019). Approaches such as Sacrificial Writing Into Functional Tissue (SWIFT) utilize sacrificial ink to 3D print various channel architectures such as straight, helical, or branched channels with a minimum channel diameter resolution of 400 μm (Skylar-Scott et al., 2019). However, a major limitation of current 3D printing approaches is the lack of micron-scale resolution as the majority of nutrient/waste exchange occurs most efficiently at the microvascular length scale (Huxley and Rumbaut, 2000). Thus, an approach that integrates angiogenesis from 3D printed arteriole-scale parent vessels, similar to the length scale modeled in Chapters 5-7 (300 μm diameter), may be a suitable future approach to rapidly generating microvasculature in large tissue grafts. For example, an array of arteriole-scale channels printed at defined distances with alternating endothelial and chemokine source channels to drive angiogenesis and microvascular formation within stromal spaces in between and could be scaled to achieve large, microvascularized tissue constructs.

Another current limitation of many 3D printing approaches is the biomaterial. Most 3D printing materials employ natural-derived materials that are more susceptible to resorption upon *in vivo* implantation as identified in Chapter 7. While this rapid resorption may be desirable in some applications, for example in wound healing contexts where the implanted material is eventually replaced by cell-derived matrix, in other contexts such as the design of β-cell containing, extra-pancreatic implants to treat type I diabetes, longer term implant stability is required (Headen et al., 2018; Weaver et al., 2018). Thus, a major next step in 3D printing vasculature may lie in identifying compatible synthetic biomaterials with tunable degradation rates.

9.2.2 Advancing pro-angiogenic synthetic biomaterials

Synthetic hydrogels with sets of orthogonally tunable properties have driven the mechanobiology field forward by affording mechanistic studies on how specific matrix properties regulate cell function (Li et al., 2017a; Vining and Mooney, 2017). However, many current synthetic biomaterials fail to accurately recapitulate the fibrous and microporous architecture of native tissues (Weigelin et al., 2012). As highlighted in this thesis, matrix fibrils critically influence how cells sense, polarize, exert forces, remodel matrix, alter gene expression, and directionally migrate within ECM. Continued advancement of composite, synthetic hydrogels that incorporate fibrillar and/or microporous properties will help inform how cells interact with ECM in more physiologic contexts. In this thesis, composite hydrogels containing either fibrillar ECM or micropores (sacrificial microgels) were employed. An immediate next step is incorporating both fibrillar and micropore features towards enhancing functional angiogenesis in synthetic hydrogels. Chapter 8 identified that fibrous cues promote the activation of quiescent endothelial cells into more invasive, tip cells via endothelial-mesenchymal transition. While this work focused on how matrix fibers induce a fibrosis propagating phenotype, further alterations of microenvironmental cues may maintain a partial EndMT tip cell state in lieu of a full EndMT transition into fibrosis propagating phenotypes. In combination (fibers + micropores), fibers may provide persistent contact guidance cues to direct tip cell formation and EC sprouting while micropores provide sufficient space in 3D to allow for sprout lumenization.

Matrix porosity encompasses a wide parameter space, yet to be carefully explored. The individual pore size and shape, and overall density or interconnectivity of pores all likely influence angiogenesis. Indeed, recent studies employing microporous annealed particles (MAP) hydrogels, where the pores lie in between microgels, thus yielding high interconnectivity, has demonstrated

enhanced angiogenesis and even hair neogenesis in dermal wound healing settings (Griffin et al., 2015, 2021). Overall, the continued advancement of tunable synthetic hydrogels with increasing physiologic accuracy will improve our understanding of how native tissue properties regulate cell function.

9.2.3 Dynamic characterization of cell and matrix states

To continue advancing our understanding of how cell and matrix states coevolve will require integration of multidisciplinary characterization techniques that probe cell-matrix interactions. In this thesis, lentiviral-based transduction of live-cell reporters and timelapse imaging was performed to characterize dynamic morphologic changes. However, cells also dynamically respond to matrix properties at the transcriptional level. The incorporation of methods such as Transcriptional Activity Cell aRray (TRACER) could provide dynamic assessment of transcription factor activity in response to changes in matrix state (Aguado et al., 2015). Additionally, advances in FRET-based molecular tension sensors have enabled the measurement of forces across cytoskeletal proteins and have provided key insights into mechanotransduction (Grashoff et al., 2010; Ham et al., 2019). However, both TRACER and molecular tension sensor approaches rely on relative fluorescent intensity to a baseline and, thus far, have been restricted to 2D culture studies. Employing these approaches in 3D settings will require improvements in imaging capabilities or z-dependent references due to fluorescent imaging attenuation in 3D.

In parallel to developing and integrating dynamic characterization tools of cell states, advances in characterizing matrix states are also a key future direction. In this thesis we tracked fluorescently-labelled matrix to identify morphologic changes (e.g. alignment, density), embedded bead deformations (e.g. fiber stretch), and collagen hybridizing peptides to assess relative matrix

degradation. While many mechanobiology-focused studies carefully characterize initial matrix states, several matrix properties are altered by cell-mediated processes. To characterize these dynamic changes, recent technologies should be integrated such as 1) metabolic labeling of secreted proteins to examine matrix deposition (Loebel, C, Mauck, RL, Burdick, 2019), 2) FRET-based protease microgels to assess protease activity (Leight et al., 2013; Shin et al., 2018), 3) magnetic bead microrheology to spatially characterize matrix stiffness at cell-relevant length scales (Juliar et al., 2018; Krajina et al., 2021), or 4) acoustically responsive scaffolds to spatiotemporally control matrix porosity (Aliabouzar et al., 2020; Huang et al., 2021). Overall, the continued development and deployment of such techniques will be essential in further elucidating critical aspects of cell–matrix mechanoreciprocity during cell migration.

Bibliography

Adams, T.S., Schupp, J.C., Poli, S., Ayaub, E.A., Neumark, N., Ahangari, F., Chu, S.G., Raby, B.A., DeIuliis, G., Januszyk, M., et al. (2020). Single-cell RNA-seq reveals ectopic and aberrant lung-resident cell populations in idiopathic pulmonary fibrosis. Sci. Adv. *6*, eaba1983.

Adamson, R.H., Huxley, V.H., and Curry, F.E. (1988). Single capillary permeability to proteins having similar size but different charge. Am. J. Physiol. Circ. Physiol. *254*, H304–H312.

Adamson, R.H., Lenz, J.F., and Curry, F.E. (1994). Quantitative Laser Scanning Confocal Microscopy on Single Capillaries: Permeability Measurement. Microcirculation *1*, 251–265.

Aguado, B.A., Wu, J.J., Azarin, S.M., Nanavati, D., Rao, S.S., Bushnell, G.G., Medicherla, C.B., and Shea, L.D. (2015). Secretome identification of immune cell factors mediating metastatic cell homing. Sci. Rep. *5*, 1–13.

Aguiar, R.S., Pohl, F., Morais, G.L., Nogueira, F.C.S., Carvalho, J.B., Guida, L., Arge, L.W.P., Melo, A., Moreira, M.E.L., Cunha, D.P., et al. (2020). Molecular alterations in the extracellular matrix in the brains of newborns with congenital Zika syndrome. Sci. Signal. *13*, 2597.

Aird, W.C. (2005). Spatial and temporal dynamics of the endothelium. J. Thromb. Haemost. *3*, 1392–1406.

Akaike, H., and A (1974). New Look At the Statistical Model Identification. IEEE Trans. Autom. Control AC-19 *19*, 716–723.

Akbari, E., Spychalski, G.B., and Song, J.W. (2017). Microfluidic approaches to the study of angiogenesis and the microcirculation. Microcirculation *24*, e12363.

Aleksandrova, A., Czirók, A., Szabó, A., Filla, M.B., Hossain, M.J., Whelan, P.F., Lansford, R., and Rongish, B.J. (2012). Convective tissue movements play a major role in avian endocardial morphogenesis. Dev. Biol. *363*, 348–361.

Aleksandrova, A., Czirok, A., Kosa, E., Galkin, O., Cheuvront, T.J., and Rongish, B.J. (2015). The endoderm and myocardium join forces to drive early heart tube assembly. Dev. Biol. *404*, 40–54.

Aliabouzar, M., Davidson, C.D., Wang, W.Y., Kripfgans, O.D., Franceschi, R.T., Putnam, A.J., Fowlkes, J.B., Baker, B.M., and Fabiilli, M.L. (2020). Spatiotemporal control of micromechanics and microstructure in acoustically-responsive scaffolds using acoustic droplet vaporization. Soft

Matter *16*, 6501–6513.

Alimperti, S., Mirabella, T., Bajaj, V., Polacheck, W., Pirone, D.M., Duffield, J., Eyckmans, J., Assoian, R.K., and Chen, C.S. (2017). Three-dimensional biomimetic vascular model reveals a RhoA, Rac1, and N -cadherin balance in mural cell–endothelial cell-regulated barrier function. Proc. Natl. Acad. Sci. *114*, 8758–8763.

Almog, N., Ma, L., Raychowdhury, R., Schwager, C., Erber, R., Short, S., Hlatky, L., Vajkoczy, P., Huber, P.E., Folkman, J., et al. (2009). Transcriptional switch of dormant tumors to fast-growing angiogenic phenotype. Cancer Res. *69*, 836–844.

Amano, M. (1997). Formation of Actin Stress Fibers and Focal Adhesions Enhanced by Rho-Kinase. Science (80-.). *275*, 1308–1311.

Amano, M., Ito, M., Kimura, K., Fukata, Y., Chihara, K., Nakano, T., Matsuura, Y., and Kaibuchi, K. (1996). Phosphorylation and activation of myosin by Rho-associated kinase (Rho-kinase). J. Biol. Chem. *271*, 20246–20249.

Arakawa, C., Gunnarsson, C., Howard, C., Bernabeu, M., Phong, K., Yang, E., DeForest, C.A., Smith, J.D., and Zheng, Y. (2020). Biophysical and biomolecular interactions of malaria-infected erythrocytes in engineered human capillaries. Sci. Adv. *6*, eaay7243.

Aratyn-Schaus, Y., Oakes, P.W., Stricker, J., Winter, S.P., and Gardel, M.L. (2010). Preparation of compliant matrices for quantifying cellular contraction. J. Vis. Exp. *46*, 1–6.

Arthur, W.T., and Burridge, K. (2001). RhoA inactivation by p190RhoGAP regulates cell spreading and migration by promoting membrane protrusion and polarity. Mol. Biol. Cell *12*, 2711–2720.

Ausprunk, D.H., and Folkman, J. (1977). Migration and proliferation of endothelial cells in preformed and newly formed blood vessels during tumor angiogenesis. Microvasc. Res. *14*, 53–65.

Baker, B.M., and Chen, C.S. (2012). Deconstructing the third dimension – how 3D culture microenvironments alter cellular cues. J. Cell Sci. *125*, 3015–3024.

Baker, B.M., Trappmann, B., Wang, W.Y., Sakar, M.S., Kim, I.L., Shenoy, V.B., Burdick, J.A., and Chen, C.S. (2015). Cell-mediated fibre recruitment drives extracellular matrix mechanosensing in engineered fibrillar microenvironments. Nat. Mater. *14*, 1262–1268.

Bangasser, B.L., Rosenfeld, S.S., and Odde, D.J. (2013). Determinants of maximal force transmission in a motor-clutch model of cell traction in a compliant microenvironment. Biophys. J. *105*, 581–592.

Bangasser, B.L., Shamsan, G.A., Chan, C.E., Opoku, K.N., Tüzel, E., Schlichtmann, B.W., Kasim, J.A., Fuller, B.J., McCullough, B.R., Rosenfeld, S.S., et al. (2017). Shifting the optimal stiffness for cell migration. Nat. Commun. *8*, 15313.

Bard, J.B.L., and Hay, E.D. (1975). THe behavior of fibroblasts from the developing avian cornea: Morphology and movement In Situ and In Vitro. J. Cell Biol. *67*, 400–418.

Beamish, J.A., Juliar, B.A., Cleveland, D.S., Busch, M.E., Nimmagadda, L., and Putnam, A.J. (2019). Deciphering the relative roles of matrix metalloproteinase- and plasmin-mediated matrix degradation during capillary morphogenesis using engineered hydrogels. J. Biomed. Mater. Res. Part B Appl. Biomater.

Berger, A.J., Linsmeier, K.M., Kreeger, P.K., and Masters, K.S. (2017). Decoupling the effects of stiffness and fiber density on cellular behaviors via an interpenetrating network of gelatin-methacrylate and collagen. Biomaterials *141*, 125–135.

Bernard, a, Renault, J.P., Michel, B., Bosshard, H.R., and Delamarche, E. (2000). Microcontact printing of proteins. Adv. Mater. *12*, 1067–1070.

Bershadsky, A.D., Balaban, N.Q., and Geiger, B. (2003). Adhesion-Dependent Cell Mechanosensitivity. Annu. Rev. Cell Dev. Biol. *19*, 677–695.

Best, D.J.; Roberts, D.E. (1975). The Upper Tail Probabilities of Spearman's Rho. *24*, 377–379.

Bissell, M.J., Hall, H.G., and Parry, G. (1982). How does the extracellular matrix direct gene expression? J. Theor. Biol. *99*, 31–68.

Bonvin, C., Overney, J., Shieh, A.C., Dixon, J.B., and Swartz, M.A. (2010). A multichamber fluidic device for 3D cultures under interstitial flow with live imaging: Development, characterization, and applications. Biotechnol. Bioeng. *105*, 982–991.

Bordeleau, F., Mason, B.N., Lollis, E.M., Mazzola, M., Zanotelli, M.R., Somasegar, S., Califano, J.P., Montague, C., LaValley, D.J., Huynh, J., et al. (2017). Matrix stiffening promotes a tumor vasculature phenotype. Proc. Natl. Acad. Sci. *114*, 492–497.

Boucher, J.M., Clark, R.P., Chong, D.C., Citrin, K.M., Wylie, L.A., and Bautch, V.L. (2017). Dynamic alterations in decoy VEGF receptor-1 stability regulate angiogenesis. Nat. Commun. *8*, 1–15.

Boudaoud, A., Burian, A., Borowska-Wykręt, D., Uyttewaal, M., Wrzalik, R., Kwiatkowska, D., and Hamant, O. (2014). FibrilTool, an ImageJ plug-in to quantify fibrillar structures in raw microscopy images. Nat. Protoc. *9*, 457–463.

Bowers, D.T., Song, W., Wang, L.H., and Ma, M. (2019). Engineering the vasculature for islet transplantation. Acta Biomater. *95*, 131–151.

Brock, A., Chang, E., Ho, C.C., LeDuc, P., Jiang, X., Whitesides, G.M., and Ingber, D.E. (2003). Geometric determinants of directional cell motility revealed using microcontact printing. Langmuir *19*, 1611–1617.

Burgstaller, G., Oehrle, B., Gerckens, M., White, E.S., Schiller, H.B., and Eickelberg, O. (2017). The instructive extracellular matrix of the lung: Basic composition and alterations in chronic

lung disease. Eur. Respir. J. *50*, 1601805.

Burridge, K., and Guilluy, C. (2016). Focal adhesions, stress fibers and mechanical tension. Exp. Cell Res. *343*, 14–20.

Caliari, S.R., and Burdick, J.A. (2016). A practical guide to hydrogels for cell culture. Nat. Methods *13*, 405–414.

Campeau, E., Ruhl, V.E., Rodier, F., Smith, C.L., Rahmberg, B.L., Fuss, J.O., Campisi, J., Yaswen, P., Cooper, P.K., and Kaufman, P.D. (2009). A versatile viral system for expression and depletion of proteins in mammalian cells. PLoS One *4*, e6529.

Cao, X., Ban, E., Baker, B.M., Lin, Y., Burdick, J.A., Chen, C.S., and Shenoy, V.B. (2017a). Multiscale model predicts increasing focal adhesion size with decreasing stiffness in fibrous matrices. Proc. Natl. Acad. Sci. 201620486.

Cao, Z., Lis, R., Ginsberg, M., Chavez, D., Shido, K., Rabbany, S.Y., Fong, G.H., Sakmar, T.P., Rafii, S., and Ding, B. Sen (2016). Targeting of the pulmonary capillary vascular niche promotes lung alveolar repair and ameliorates fibrosis. Nat. Med. *22*, 154–162.

Cao, Z., Ye, T., Sun, Y., Ji, G., Shido, K., Chen, Y., Luo, L., Na, F., Li, X., Huang, Z., et al. (2017b). Targeting the vascular and perivascular niches as a regenerative therapy for lung and liver fibrosis. Sci. Transl. Med. *9*.

Carmeliet, P. (2005). Angiogenesis in life, disease and medicine. Nature *438*, 932–936.

Carmeliet, P., and Jain, R.K. (2000). Angiogenesis in cancer and other diseases. Nature *407*, 249–257.

Cathcart, J., Pulkoski-Gross, A., and Cao, J. (2015). Targeting matrix metalloproteinases in cancer: Bringing new life to old ideas. Genes Dis. *2*, 26–34.

Chan, C.E., and Odde, D.J. (2008). Traction Dynamics of Filopodia on Compliant Substrates. Science (80-.). *322*, 1687–1691.

Chandler, C., Liu, T., Buckanovich, R., and Coffman, L.G. (2019). The double edge sword of fibrosis in cancer. Transl. Res. *209*, 55–67.

Charras, G., and Sahai, E. (2014). Physical influences of the extracellular environment on cell migration. Nat. Rev. Mol. Cell Biol. *15*, 813–824.

Chaudhuri, O., Gu, L., Klumpers, D., Darnell, M., Bencherif, S.A., Weaver, J.C., Huebsch, N., Lee, H., Lippens, E., Duda, G.N., et al. (2016). Hydrogels with tunable stress relaxation regulate stem cell fate and activity. Nat. Mater. *15*, 326–334.

Chaudhuri, O., Cooper-White, J., Janmey, P.A., Mooney, D.J., and Shenoy, V.B. (2020). Effects of extracellular matrix viscoelasticity on cellular behaviour. Nature *584*, 535–546.

Chen, W.-T. (1981). Mechanism of the trailing edge during fibroblast movement. J. Cell Biol. *90*, 187–200.

Chen, M.B., Whisler, J.A., Fröse, J., Yu, C., Shin, Y., and Kamm, R.D. (2017). On-chip human microvasculature assay for visualization and quantification of tumor cell extravasation dynamics. Nat. Protoc. *12*, 865–880.

Cheng, G., Liao, S., Wong, H.K., Lacorre, D.A., Di Tomaso, E., Au, P., Fukumura, D., Jain, R.K., and Munn, L.L. (2011). Engineered blood vessel networks connect to host vasculature via wrapping-and-tapping anastomosis. Blood *118*, 4740–4749.

Chiu, Y.C., Cheng, M.H., Engel, H., Kao, S.W., Larson, J.C., Gupta, S., and Brey, E.M. (2011). The role of pore size on vascularization and tissue remodeling in PEG hydrogels. Biomaterials *32*, 6045–6051.

Chun, T.H., Sabeh, F., Ota, I., Murphy, H., McDonagh, K.T., Holmbeck, K., Birkedal-Hansen, H., Allen, E.D., and Weiss, S.J. (2004). MT1-MMP-dependent neovessel formation within the confines of the three-dimensional extracellular matrix. J. Cell Biol. *167*, 757–767.

Chung, H.J., Kim, H.K., Yoon, J.J., and Park, T.G. (2006). Heparin immobilized porous PLGA microspheres for angiogenic growth factor delivery. Pharm. Res. *23*, 1835–1841.

Condeelis, J., and Segall, J.E. (2003). Intravital imaging of cell movement in tumours. Nat. Rev. Cancer *3*, 921–930.

Conklin, M.W., Eickhoff, J.C., Riching, K.M., Pehlke, C.A., Eliceiri, K.W., Provenzano, P.P., Friedl, A., and Keely, P.J. (2011). Aligned collagen is a prognostic signature for survival in human breast carcinoma. Am. J. Pathol. *178*, 1221–1232.

Cortesio, C.L., Boateng, L.R., Piazza, T.M., Bennin, D.A., and Huttenlocher, A. (2011). Calpain-mediated proteolysis of paxillin negatively regulates focal adhesion dynamics and cell migration. J. Biol. Chem. *286*, 9998–10006.

Crocker, J., and Grier, D. (1996). Methods of Digital Video Microscopy for Colloidal Studies. J. Colloid Interface Sci. *179*, 298–310.

Crosby, C.O., and Zoldan, J. (2019). Mimicking the physical cues of the ECM in angiogenic biomaterials. Regen. Biomater. *6*, 61–73.

Cross, V.L., Zheng, Y., Choi, N.W., Verbridge, S.S., Sutermaster, B.A., Bonassar, L.J., Fischbach, C., and Stroock, A.D. (2010). Dense type I collagen matrices that support cellular remodeling and microfabrication for studies of tumor angiogenesis and vasculogenesis in vitro. Biomaterials *31*, 8596–8607.

Davidson, C.D., Wang, W.Y., Zaimi, I., Jayco, D.K.P., and Baker, B.M. (2019). Cell force-mediated matrix reorganization underlies multicellular network assembly. Sci. Rep. *9*, 12.

Davidson, C.D., Jayco, D.K.P., Wang, W.Y., Shikanov, A., and Baker, B.M. (2020a). Fiber

Crimp Confers Matrix Mechanical Nonlinearity, Regulates Endothelial Cell Mechanosensing, and Promotes Microvascular Network Formation. J. Biomech. Eng. *142*.

Davidson, C.D., Jayco, D.K.P., Matera, D.L., DePalma, S.J., Hiraki, H.L., Wang, W.Y., and Baker, B.M. (2020b). Myofibroblast activation in synthetic fibrous matrices composed of dextran vinyl sulfone. Acta Biomater. *105*, 78–86.

Davidson, L.A., Dzamba, B.D., Keller, R., and Desimone, D.W. (2008). Live imaging of cell protrusive activity, and extracellular matrix assembly and remodeling during morphogenesis in the frog, Xenopus laevis. Dev. Dyn. *237*, 2684–2692.

DeClerck, K., and Elble, R.C. (2010). The role of hypoxia and acidosis in promoting metastasis and resistance to chemotherapy. Front. Biosci. *15*, 213–225.

Deen, W.M. (1998). Analysis of Transport Phenomena (Oxford University Press).

Dejana, E. (2004). Endothelial cell-cell junctions: Happy together. Nat. Rev. Mol. Cell Biol. *5*, 261–270.

Dejana, E., Hirschi, K.K., and Simons, M. (2017). The molecular basis of endothelial cell plasticity. Nat. Commun. *8*, 1–11.

Dembo, M., and Wang, Y. (1999). Stresses at the Cell-to-Substrate Interface during Locomotion of Fibroblasts. Biophys. J. *76*, 2307–2316.

Denais, C.M., Gilbert, R.M., Isermann, P., McGregor, A.L., Te Lindert, M., Weigelin, B., Davidson, P.M., Friedl, P., Wolf, K., and Lammerding, J. (2016). Nuclear envelope rupture and repair during cancer cell migration. Science (80-.). *352*, 353–358.

Depalma, S.J., Davidson, C.D., Stis, A.E., Helms, A.S., and Baker, B.M. (2021). Microenvironmental determinants of organized iPSC-cardiomyocyte tissues on synthetic fibrous matrices. Biomater. Sci. *9*, 93–107.

Desai, R.A., Khan, M.K., Gopal, S.B., and Chen, C.S. (2011). Subcellular spatial segregation of integrin subtypes by patterned multicomponent surfaces. Integr. Biol. *3*, 560–567.

Desai, S.S., Tung, J.C., Zhou, V.X., Grenert, J.P., Malato, Y., Rezvani, M., Español-Suñer, R., Willenbring, H., Weaver, V.M., and Chang, T.T. (2016). Physiological ranges of matrix rigidity modulate primary mouse hepatocyte function in part through hepatocyte nuclear factor 4 alpha. Hepatology *64*, 261–275.

Dickinson, R.B., Guido, S., and Tranquillo, R.T. (1994). Biased cell migration of fibroblasts exhibiting contact guidance in oriented collagen gels. Ann. Biomed. Eng. *22*, 342–356.

Diegelmann, R.F., and Evans, M.C. (2004). Wound healing: An overview of acute, fibrotic and delayed healing. Front. Biosci. *9*, 283–289.

van Dijk-Wotthuis, W.N.E., Franssen, O., Talsma, H., van Steenbergen, M.J., Kettenes-van den

Bosch, J.J., and Hennink, W.E. (1995). Synthesis, Characterization, and Polymerization of Glycidyl Methacrylate Derivatized Dextran. Macromolecules *28*, 6317–6322.

DiMilla, P.A., Barbee, K., and Lauffenburger, D.A. (1991). Mathematical model for the effects of adhesion and mechanics on cell migration speed. Biophys. J. *60*, 15–37.

Ding, B. Sen, Cao, Z., Lis, R., Nolan, D.J., Guo, P., Simons, M., Penfold, M.E., Shido, K., Rabbany, S.Y., and Rafii, S. (2014). Divergent angiocrine signals from vascular niche balance liver regeneration and fibrosis. Nature *505*, 97–102.

Divoux, A., and Clément, K. (2011). Architecture and the extracellular matrix: The still unappreciated components of the adipose tissue. Obes. Rev. *12*, e494–e503.

Dogterom, M., and Koenderink, G.H. (2019). Actin–microtubule crosstalk in cell biology. Nat. Rev. Mol. Cell Biol. *20*, 38–54.

Doyle, A.D. (2016). Generation of 3D collagen gels with controlled diverse architectures. Curr. Protoc. Cell Biol. *2016*, 10.20.1-10.20.16.

Doyle, A.D., Wang, F.W., Matsumoto, K., and Yamada, K.M. (2009). One-dimensional topography underlies three-dimensional fi brillar cell migration. J. Cell Biol. *184*, 481–490.

Doyle, A.D., Carvajal, N., Jin, A., Matsumoto, K., and Yamada, K.M. (2015). Local 3D matrix microenvironment regulates cell migration through spatiotemporal dynamics of contractility-dependent adhesions. Nat. Commun. *6*.

Doyle, A.D., Sykora, D.J., Pacheco, G.G., Kutys, M.L., and Yamada, K.M. (2021). 3D mesenchymal cell migration is driven by anterior cellular contraction that generates an extracellular matrix prestrain. Dev. Cell *56*, 826-841.e4.

Drifka, C.R., Tod, J., Loeffler, A.G., Liu, Y., Thomas, G.J., Eliceiri, K.W., and Kao, W.J. (2015). Periductal stromal collagen topology of pancreatic ductal adenocarcinoma differs from that of normal and chronic pancreatitis. Mod. Pathol. *28*, 1470–1480.

Du, Y., Herath, S.C.B., Wang, Q.G., Wang, D.A., Asada, H.H., and Chen, P.C.Y. (2016). Three-Dimensional Characterization of Mechanical Interactions between Endothelial Cells and Extracellular Matrix during Angiogenic Sprouting. Sci. Rep. *6*, 1–14.

Dull, T., Zufferey, R., Kelly, M., Mandel, R.J., Nguyen, M., Trono, D., and Naldini, L. (1998). A third-generation lentivirus vector with a conditional packaging system. J. Virol. *72*, 8463–8471.

Dumont, C.M., Carlson, M.A., Munsell, M.K., Ciciriello, A.J., Strnadova, K., Park, J., Cummings, B.J., Anderson, A.J., and Shea, L.D. (2019). Aligned hydrogel tubes guide regeneration following spinal cord injury. Acta Biomater. *86*, 312–322.

Duong, H., Wu, B., and Tawil, B. (2009). Modulation of 3D fibrin matrix stiffness by intrinsic fibrinogen-thrombin compositions and by extrinsic cellular activity. Tissue Eng. - Part A *15*, 1865–1876.

Durham, J.T., and Herman, I.M. (2011). Microvascular modifications in diabetic retinopathy. Curr. Diab. Rep. *11*, 253–264.

Ehling, J., Bartneck, M., Wei, X., Gremse, F., Fech, V., Möckel, D., Baeck, C., Hittatiya, K., Eulberg, D., Luedde, T., et al. (2014). CCL2-dependent infiltrating macrophages promote angiogenesis in progressive liver fibrosis. Gut *63*, 1960–1971.

Ehrbar, M., Sala, A., Lienemann, P., Ranga, A., Mosiewicz, K., Bittermann, A., Rizzi, S.C., Weber, F.E., and Lutolf, M.P. (2011). Elucidating the role of matrix stiffness in 3D cell migration and remodeling. Biophys. J. *100*, 284–293.

Elcin, A.E., and Elcin, Y.M. (2006). Localized angiogenesis induced by human vascular endothelial growth factor-activated PLGA sponge. Tissue Eng. *12*, 959–968.

Elosegui-Artola, A., Bazellières, E., Allen, M.D., Andreu, I., Oria, R., Sunyer, R., Gomm, J.J., Marshall, J.F., Jones, J.L., Trepat, X., et al. (2014). Rigidity sensing and adaptation through regulation of integrin types. Nat. Mater. *13*, 631–637.

Elosegui-Artola, A., Oria, R., Chen, Y., Kosmalska, A., Pérez-González, C., Castro, N., Zhu, C., Trepat, X., and Roca-Cusachs, P. (2016). Mechanical regulation of a molecular clutch defines force transmission and transduction in response to matrix rigidity. Nat. Cell Biol. *18*, 540–548.

Elosegui-Artola, A., Andreu, I., Beedle, A.E.M.E.E.M.E.E.M., Lezamiz, A., Uroz, M., Kosmalska, A.J., Oria, R., Kechagia, J.Z., Rico-Lastres, P., Le Roux, A.-L.L., et al. (2017). Force triggers YAP nuclear entry by mechanically regulating transport across nuclear pores. Cell *171*, 1397–1410.

Endlich, N., Otey, C.A., Kriz, W., and Endlich, K. (2007). Movement of stress fibers away from focal adhesions identifies focal adhesions as sites of stress fiber assembly in stationary cells. Cell Motil. Cytoskeleton *64*, 966–976.

Engler, A., Bacakova, L., Newman, C., Hategan, A., Griffin, M., and Discher, D. (2004). Substrate Compliance versus Ligand Density in Cell on Gel Responses. Biophys. J. *86*, 617–628.

Engler, A.J., Sen, S., Sweeney, H.L., and Discher, D.E. (2006). Matrix Elasticity Directs Stem Cell Lineage Specification. Cell *126*, 677–689.

Estabridis, H.M., Jana, A., Nain, A., and Odde, D.J. (2018). Cell Migration in 1D and 2D Nanofiber Microenvironments. Ann. Biomed. Eng. *46*, 392–403.

Etienne-Manneville, S., and Hall, A. (2001). Integrin-mediated activation of Cdc42 controls cell polarity in migrating astrocytes through PKCζ. Cell *106*, 489–498.

Etienne-Manneville, S., and Hall, A. (2002). Rho GTPases in cell biology. Nature *420*, 629–635.

Fernandez, I.E., and Eickelberg, O. (2012). New cellular and molecular mechanisms of lung injury and fi brosis in idiopathic pulmonary fi brosis. Lancet *380*, 680–688.

Ford, A.J., and Rajagopalan, P. (2018). Extracellular matrix remodeling in 3D : implications in tissue homeostasis and disease progression. *10*.

Fraisl, P., Mazzone, M., Schmidt, T., and Carmeliet, P. (2009). Regulation of Angiogenesis by Oxygen and Metabolism. Dev. Cell *16*, 167–179.

Fraley, S.I., Feng, Y., Krishnamurthy, R., Kim, D.-H., Celedon, A., Longmore, G.D., and Wirtz, D. (2010). A distinctive role for focal adhesion proteins in three-dimensional cell motility. Nat. Cell Biol. *12*, 598–604.

Francavilla, C., Maddaluno, L., and Cavallaro, U. (2009). The functional role of cell adhesion molecules in tumor angiogenesis. Semin. Cancer Biol. *19*, 298–309.

Friedl, P., and Alexander, S. (2011). Cancer invasion and the microenvironment: Plasticity and reciprocity. Cell *147*, 992–1009.

Friedl, P., and Gilmour, D. (2009). Collective cell migration in morphogenesis, regeneration and cancer. Nat. Publ. Gr. *10*.

Friedl, P., and Wolf, K. (2009). Proteolytic interstitial cell migration: A five-step process. Cancer Metastasis Rev. *28*, 129–135.

Friedl, P., and Wolf, K. (2010). Plasticity of cell migration: A multiscale tuning model. J. Cell Biol. *188*, 11–19.

Friedl, P., Sahai, E., Weiss, S., and Yamada, K.M. (2012). New dimensions in cell migration. Nat. Rev. Mol. Cell Biol. *13*, 743–747.

Geiger, B., Bershadsky, A., Pankov, R., and Yamada, K.M. (2001). Transmembrane extracellular matrix– cytoskeleton crosstalk. Nat. Rev. Mol. Cell Biol. *2*, 793–805.

Geiger, B., Spatz, J.P., and Bershadsky, A. (2009). Environmental sensing through focal adhesions. Nat. Rev. Mol. Cell Biol. *10*, 21–33.

Gerhardt, H., Golding, M., Fruttiger, M., Ruhrberg, C., Lundkvist, A., Abramsson, A., Jeltsch, M., Mitchell, C., Alitalo, K., Shima, D., et al. (2003). VEGF guides angiogenic sprouting utilizing endothelial tip cell filopodia. J. Cell Biol. *161*, 1163–1177.

Ghajar, C.M., Blevins, K.S., Hughes, C.C.W., George, S.C., and Putnam, A.J. (2006). Mesenchymal stem cells enhance angiogenesis in mechanically viable prevascularized tissues via early matrix metalloproteinase upregulation. Tissue Eng. *12*, 2875–2888.

Ghajar, C.M., Chen, X., Harris, J.W., Suresh, V., Hughes, C.C.W., Jeon, N.L., Putnam, A.J., and George, S.C. (2008). The effect of matrix density on the regulation of 3-D capillary morphogenesis. Biophys. J. *94*, 1930–1941.

Gillies, A.R., and Lieber, R.L. (2011). Structure and function of the skeletal muscle extracellular matrix. Muscle and Nerve *44*, 318–331.

Gillitzer, R., and Goebeler, M. (2001). Chemokines in cutaneous wound healing. J. Leukoc. Biol. *69*, 513–521.

Gjorevski, N., Piotrowski, A.S., Varner, V.D., and Nelson, C.M. (2015). Dynamic tensile forces drive collective cell migration through three-dimensional extracellular matrices. Sci. Rep. *5*, 11458.

Gobin, A.S., and West, J.L. (2002). Cell migration through defined, synthetic ECM analogs. FASEB J. *16*, 751–753.

Goligorsky, M.S. (2010). Microvascular rarefaction: The decline and fall of blood vessels. Organogenesis *6*, 1–10.

Gomes, E.R., Jani, S., and Gundersen, G.G. (2005). Nuclear movement regulated by Cdc42, MRCK, myosin, and actin flow establishes MTOC polarization in migrating cells. Cell *121*, 451–463.

Gong, H., Beauchamp, M., Perry, S., Woolley, A.T., and Nordin, G.P. (2015). Optical approach to resin formulation for 3D printed microfluidics. RSC Adv. *5*, 106621–106632.

Gong, X., Kulwatno, J., and Mills, K.L. (2020). Rapid fabrication of collagen bundles mimicking tumor-associated collagen architectures. Acta Biomater. *108*, 128–141.

Grainger, S.J., Carrion, B., Ceccarelli, J., and Putnam, A.J. (2013). Stromal cell identity influences the in vivo functionality of engineered capillary networks formed by co-delivery of endothelial cells and stromal cells. Tissue Eng. - Part A *19*, 1209–1222.

Grashoff, C., Hoffman, B.D., Brenner, M.D., Zhou, R., Parsons, M., Yang, M.T., McLean, M.A., Sligar, S.G., Chen, C.S., Ha, T., et al. (2010). Measuring mechanical tension across vinculin reveals regulation of focal adhesion dynamics. Nature *466*, 263–266.

Greenhalgh, D.G. (1998). The role of apoptosis in wound healing. Int. J. Biochem. Cell Biol. *30*, 1019–1030.

Griffin, D.R., Weaver, W.M., Scumpia, P.O., Di Carlo, D., and Segura, T. (2015). Accelerated wound healing by injectable microporous gel scaffolds assembled from annealed building blocks. Nat. Mater. *14*, 737–744.

Griffin, D.R., Archang, M.M., Kuan, C.H., Weaver, W.M., Weinstein, J.S., Feng, A.C., Ruccia, A., Sideris, E., Ragkousis, V., Koh, J., et al. (2021). Activating an adaptive immune response from a hydrogel scaffold imparts regenerative wound healing. Nat. Mater. *20*, 560–569.

Grigoryan, B., Paulsen, S.J., Corbett, D.C., Sazer, D.W., Fortin, C.L., Zaita, A.J., Greenfield, P.T., Calafat, N.J., Gounley, J.P., Ta, A.H., et al. (2019). Multivascular networks and functional intravascular topologies within biocompatible hydrogels. Science *364*, 458–464.

Guetta-Terrier, C., Monzo, P., Zhu, J., Long, H., Venkatraman, L., Zhou, Y., Wang, P.P., Chew, S.Y., Mogilner, A., Ladoux, B., et al. (2015). Protrusive waves guide 3D cell migration along

nanofibers. J. Cell Biol. *211*, 683–701.

Gundersen, G.G., and Worman, H.J. (2013). Nuclear positioning. Cell *152*, 1376–1389.

Gupton, S.L., and Waterman-Storer, C.M. (2006). Spatiotemporal Feedback between Actomyosin and Focal-Adhesion Systems Optimizes Rapid Cell Migration. Cell *125*, 1361–1374.

Guthold, M., Liu, W., Sparks, E.A., Jawerth, L.M., Peng, L., Falvo, M., Superfine, R., Hantgan, R.R., and Lord, S.T. (2007). A Comparison of the Mechanical and Structural Properties of Fibrin Fibers with Other Protein Fibers. Cell Biochem. Biophys. *49*, 165–181.

Habermann, A.C., Gutierrez, A.J., Bui, L.T., Yahn, S.L., Winters, N.I., Calvi, C.L., Peter, L., Chung, M.I., Taylor, C.J., Jetter, C., et al. (2020). Single-cell RNA sequencing reveals profibrotic roles of distinct epithelial and mesenchymal lineages in pulmonary fibrosis. Sci. Adv. *6*, eaba1972.

Hadden, W.J., Young, J.L., Holle, A.W., McFetridge, M.L., Kim, D.Y., Wijesinghe, P., Taylor-Weiner, H., Wen, J.H., Lee, A.R., Bieback, K., et al. (2017). Stem cell migration and mechanotransduction on linear stiffness gradient hydrogels. Proc. Natl. Acad. Sci. *114*, 5647–5652.

Hadjipanayi, E., Mudera, V., and Brown, R.A. (2009). Guiding cell migration in 3D: A collagen matrix with graded directional stiffness. Cell Motil. Cytoskeleton *66*, 121–128.

Hakkinen, K.M., Harunaga, J.S., Doyle, A.D., and Yamada, K.M. (2011). Direct comparisons of the morphology, migration, cell adhesions, and actin cytoskeleton of fibroblasts in four different three-dimensional extracellular matrices. Tissue Eng. Part A *17*, 713–724.

Hall, M.S., Alisafaei, F., Ban, E., Feng, X., Hui, C., Shenoy, V.B., and Wu, M. (2016). Fibrous nonlinear elasticity enables positive mechanical feedback between cells and extracellular matrices. Proc. Natl. Acad. Sci. *113*, 1–46.

Ham, T.R., Collins, K.L., and Hoffman, B.D. (2019). Molecular tension sensors: moving beyond force. Curr. Opin. Biomed. Eng. *12*, 83–94.

Hanna, S., and El-Sibai, M. (2013). Signaling networks of Rho GTPases in cell motility. Cell. Signal. *25*, 1955–1961.

Harris, A.K., Stopak, D., and Wild, P. (1981). Fibroblast traction as a mechanism for collagen morphogenesis. Nature *290*, 249–251.

Hashimoto, N., Phan, S.H., Imaizumi, K., Matsuo, M., Nakashima, H., Kawabe, T., Shimokata, K., and Hasegawa, Y. (2010). Endothelial-mesenchymal transition in bleomycin-induced pulmonary fibrosis. Am. J. Respir. Cell Mol. Biol. *43*, 161–172.

Hashizume, H., Baluk, P., Morikawa, S., McLean, J.W., Thurston, G., Roberge, S., Jain, R.K., and McDonald, D.M. (2000). Openings between defective endothelial cells explain tumor vessel

leakiness. Am. J. Pathol. *156*, 1363–1380.

Hayer, A., Shao, L., Chung, M., Joubert, L.M., Yang, H.W., Tsai, F.C., Bisaria, A., Betzig, E., and Meyer, T. (2016). Engulfed cadherin fingers are polarized junctional structures between collectively migrating endothelial cells. Nat. Cell Biol. *18*, 1311–1323.

Headen, D.M., Woodward, K.B., Coronel, M.M., Shrestha, P., Weaver, J.D., Zhao, H., Tan, M., Hunckler, M.D., Bowen, W.S., Johnson, C.T., et al. (2018). Local immunomodulation with Fas ligand-engineered biomaterials achieves allogeneic islet graft acceptance. Nat. Mater. *17*, 732–739.

Heck, T.A.M., Vaeyens, M.M., and Van Oosterwyck, H. (2015). Computational Models of Sprouting Angiogenesis and Cell Migration: Towards Multiscale Mechanochemical Models of Angiogenesis. Math. Model. Nat. Phenom. *10*, 108–141.

Heiss, M., Hellström, M., Kalén, M., May, T., Weber, H., Hecker, M., Augustin, H.G., and Korff, T. (2015). Endothelial cell spheroids as a versatile tool to study angiogenesis in vitro. FASEB J. *29*, 3076–3084.

Helvert, S. Van, Storm, C., and Friedl, P. (2018). Mechanoreciprocity in cell migration. Nat. Cell Biol. *20*, 8–20.

Van Hinsbergh, V.W.M., and Koolwijk, P. (2008). Endothelial sprouting and angiogenesis: Matrix metalloproteinases in the lead. Cardiovasc. Res. *78*, 203–212.

Hinz, B. (2007). Formation and function of the myofibroblast during tissue repair. J. Invest. Dermatol. *127*, 526–537.

Hinz, B. (2016). The role of myofibroblasts in wound healing. Curr. Res. Transl. Med. *64*, 171–177.

Hinz, B., and Gabbiani, G. (2003). Mechanisms of force generation and transmission by myofibroblasts. Curr. Opin. Biotechnol. *14*, 538–546.

Hinz, B., and Lagares, D. (2020). Evasion of apoptosis by myofibroblasts: a hallmark of fibrotic diseases. Nat. Rev. Rheumatol. *16*, 11–31.

Hinz, B., Phan, S.H., Thannickal, V.J., Galli, A., Bochaton-Piallat, M.L., and Gabbiani, G. (2007). The myofibroblast: One function, multiple origins. Am. J. Pathol. *170*, 1807–1816.

Hiraki, H.L., Matera, D.L., Wang, W.Y., Zarouk, A.A., Argento, A.E., Buschhaus, J.M., Humphries, B.A., Luker, G.D., Baker, B.M., and Professor, A. (2021). Fiber density and matrix stiffness modulate distinct cell migration modes in a 3D stroma mimetic composite hydrogel. BioRxiv 2021.02.27.433190.

Hotulainen, P., and Lappalainen, P. (2006). Stress fibers are generated by two distinct actin assembly mechanisms in motile cells. J. Cell Biol. *173*, 383–394.

Huang, L., Quesada, C., Aliabouzar, M., Fowlkes, J.B., Franceschi, R.T., Liu, Z., Putnam, A.J., and Fabiilli, M.L. (2021). Spatially-directed angiogenesis using ultrasound-controlled release of basic fibroblast growth factor from acoustically-responsive scaffolds. Acta Biomater.

Hughes, A.J., Miyazaki, H., Coyle, M.C., Zhang, J., Laurie, T., Chu, D., Vavru, Z., Schneider, R.A., Klein, O.D., and Gartner, J. (2017). Tissue Folding by Mechanical Compaction of the Mesenchyme. BioRxiv 1–14.

Hultgren, N.W., Fang, J.S., Ziegler, M.E., Ramirez, R.N., Phan, D.T.T., Hatch, M.M.S., Welch-Reardon, K.M., Paniagua, A.E., Kim, L.S., Shon, N.N., et al. (2020). Slug regulates the Dll4-Notch-VEGFR2 axis to control endothelial cell activation and angiogenesis. Nat. Commun. *11*, 1–16.

Huttenlocher, A., Palecek, S.P., Lu, Q., Zhang, W.L., Mellgren, R.L., Lauffenburger, D.A., Ginsberg, M.H., and Horwitz, A.F. (1997). Regulation of cell migration by the calcium-dependent protease calpain. J. Biol. Chem. *272*, 32719–31221.

Huxley, V., and Rumbaut, R. (2000). The Microvasculature As A Dynamic Regulator Of Volume And Solute Exchange. Clin. Exp. Pharmacol. Physiol. *27*, 847–854.

Huynh, J., Nishimura, N., Rana, K., Peloquin, J.M., Califano, J.P., Montague, C.R., King, M.R., Schaffer, C.B., and Reinhart-King, C.A. (2011). Age-related intimal stiffening enhances endothelial permeability and leukocyte transmigration. Sci. Transl. Med. *3*, 112ra122-112ra122.

Ilina, O., Campanello, L., Gritsenko, P.G., Vullings, M., Wang, C., Bult, P., Losert, W., and Friedl, P. (2018). Intravital microscopy of collective invasion plasticity in breast cancer. Dis. Model. Mech. dmm.034330.

Ilina, O., Gritsenko, P.G., Syga, S., Lippoldt, J., La Porta, C.A.M., Chepizhko, O., Grosser, S., Vullings, M., Bakker, G.J., Starruß, J., et al. (2020). Cell–cell adhesion and 3D matrix confinement determine jamming transitions in breast cancer invasion. Nat. Cell Biol. *22*, 1103–1115.

Isermann, P., and Lammerding, J. (2017). Consequences of a tight squeeze: Nuclear envelope rupture and repair. Nucleus *8*, 268–274.

Jain, R.K. (2005). Normalization of tumor vasculature: an emerging concept in antiangiogenic therapy. Science (80-.). *307*, 58–62.

Jakobsson, L., Franco, C.A., Bentley, K., Collins, R.T., Ponsioen, B., Aspalter, I.M., Rosewell, I., Busse, M., Thurston, G., Medvinsky, A., et al. (2010). Endothelial cells dynamically compete for the tip cell position during angiogenic sprouting. Nat. Cell Biol. *12*, 943–953.

Jimenez, S.A., and Piera-Velazquez, S. (2016). Endothelial to mesenchymal transition (EndoMT) in the pathogenesis of Systemic Sclerosis-associated pulmonary fibrosis and pulmonary arterial hypertension. Myth or reality? Matrix Biol. *51*, 26–36.

Johnson, J.M., Minson, C.T., and Kellogg, D.L. (2014). Cutaneous vasodilator and

vasoconstrictor mechanisms in temperature regulation. Compr. Physiol. *4*, 33–89.

Juliar, B.A., Keating, M.T., Kong, Y.P., Botvinick, E.L., and Putnam, A.J. (2018). Sprouting angiogenesis induces significant mechanical heterogeneities and ECM stiffening across length scales in fibrin hydrogels. Biomaterials *162*, 99–108.

Juliar, B.A., Beamish, J.A., Busch, M.E., Cleveland, D.S., Nimmagadda, L., and Putnam, A.J. (2020). Cell-mediated matrix stiffening accompanies capillary morphogenesis in ultra-soft amorphous hydrogels. Biomaterials *230*, 119634.

Kalluri, R., and Weinberg, R.A. (2009). The basics of epithelial-mesenchymal transition. J. Clin. Invest. *119*, 1420–1428.

Kanchanawong, P., Shtengel, G., Pasapera, A.M., Ramko, E.B., Davidson, M.W., Hess, H.F., and Waterman, C.M. (2010). Nanoscale architecture of integrin-based cell adhesions. Nature *468*, 580–584.

Kang, W., Ferruzzi, J., Spatarelu, C.-P., Han, Y.L., Sharma, Y., Koehler, S., Butler, J., Roblyer, D., Zaman, M., Guo, M., et al. (2020). Tumor invasion as non-equilibrium phase separation. BioRxiv 2020.04.28.066845.

Khalil, A.A., Ilina, O., Gritsenko, P.G., Bult, P., Span, P.N., and Friedl, P. (2017). Collective invasion in ductal and lobular breast cancer associates with distant metastasis. Clin. Exp. Metastasis *34*, 421–429.

Khetan, S., Guvendiren, M., Legant, W.R., Cohen, D.M., Chen, C.S., and Burdick, J.A. (2013). Degradation-mediated cellular traction.. supplement. Nat. Mater. *12*, 458–465.

Kidokoro, H., Yonei-Tamura, S., Tamura, K., Schoenwolf, G.C., and Saijoh, Y. (2018). The heart tube forms and elongates through dynamic cell rearrangement coordinated with foregut extension. Development *145*, dev.152488.

Kim, D.H., and Wirtz, D. (2013). Focal adhesion size uniquely predicts cell migration. FASEB J. *27*, 1351–1361.

Kim, S., Uroz, M., Bays, J.L., and Chen, C.S. (2021). Harnessing Mechanobiology for Tissue Engineering. Dev. Cell *56*, 180–191.

Kingston, R.E., Chen, C.A., and Okayama, H. (2004). Calcium Phosphate Transfection. Curr. Protoc. Cell Biol. *19*, 20.3.1-20.3.8.

Kinstlinger, I.S., and Miller, J.S. (2016). 3D-printed fluidic networks as vasculature for engineered tissue. Lab Chip *16*, 2025–2043.

Kiosses, W.B., McKee, N.H., and Kalnins, V.I. (1997). Evidence for the migration of rat aortic endothelial cells toward the heart. Arterioscler. Thromb. Vasc. Biol. *17*, 2891–2896.

Kirby, T.J., and Lammerding, J. (2018). Emerging views of the nucleus as a cellular

mechanosensor. Nat. Cell Biol. *20*, 373–381.

Kirkpatrick, N.D., Andreou, S., Hoying, J.B., and Utzinger, U. (2007). Live imaging of collagen remodeling during angiogenesis. Am. J. Physiol. - Hear. Circ. Physiol. *292*, H3198–H3206.

Klank, R.L., Decker Grunke, S.A., Bangasser, B.L., Forster, C.L., Price, M.A., Odde, T.J., SantaCruz, K.S., Rosenfeld, S.S., Canoll, P., Turley, E.A., et al. (2017). Biphasic Dependence of Glioma Survival and Cell Migration on CD44 Expression Level. Cell Rep. *18*, 23–31.

Kleinman, H.K., and Martin, G.R. (2005). Matrigel: Basement membrane matrix with biological activity. Semin. Cancer Biol. *15*, 378–386.

Klotzsch, E., Smith, M.L., Kubow, K.E., Muntwyler, S., Little, W.C., Beyeler, F., Gourdon, D., Nelson, B.J., and Vogel, V. (2009). Fibronectin forms the most extensible biological fibers displaying switchable force-exposed cryptic binding sites. Proc. Natl. Acad. Sci. *106*, 18267–18272.

Kniazeva, E., Weidling, J.W., Singh, R., Botvinick, E.L., Digman, M.A., Gratton, E., and Putnam, A.J. (2012). Quantification of local matrix deformations and mechanical properties during capillary morphogenesis in 3D. Integr. Biol. *4*, 431–439.

Koch, T.M., Munster, S., Bonakdar, N., Butler, J.P., and Fabry, B. (2012). 3D Traction Forces in Cancer Cell Invasion. PLoS One *7*.

Koh, T.J., and DiPietro, L.A. (2011). Inflammation and wound healing: the role of the macrophage. Expert Rev. Mol. Med. *13*.

Komatsu, N., Aoki, K., Yamada, M., Yukinaga, H., Fujita, Y., Kamioka, Y., and Matsuda, M. (2011). Development of an optimized backbone of FRET biosensors for kinases and GTPases. Mol. Biol. Cell *22*, 4647–4656.

Kosyakova, N., Kao, D.D., Figetakis, M., López-Giráldez, F., Spindler, S., Graham, M., James, K.J., Won Shin, J., Liu, X., Tietjen, G.T., et al. (2020). Differential functional roles of fibroblasts and pericytes in the formation of tissue-engineered microvascular networks in vitro. Npj Regen. Med. *5*, 1–12.

Krajina, B.A., LeSavage, B.L., Roth, J.G., Zhu, A.W., Cai, P.C., Spakowitz, A.J., and Heilshorn, S.C. (2021). Microrheology reveals simultaneous cell-mediated matrix stiffening and fluidization that underlie breast cancer invasion. Sci. Adv. *7*, eabe1969.

Kramer, N., Walzl, A., Unger, C., Rosner, M., Krupitza, G., Hengstschläger, M., and Dolznig, H. (2013). In vitro cell migration and invasion assays. Mutat. Res. Mutat. Res. *752*, 10–24.

Kraning-Rush, C.M., and Reinhart-King, C.A. (2012). Controlling matrix stiffness and topography for the study of tumor cell migration. Cell Adhes. Migr. *6*, 274–279.

Kraning-Rush, C.M., Carey, S.P., Lampi, M.C., and Reinhart-King, C.A. (2013). Microfabricated collagen tracks facilitate single cell metastatic invasion in 3D. Integr. Biol. *5*,

606.

Krause, M., Yang, W., Te Lindert, M., Isermann, P., Schepens, J., Maas, R.J., Eid, K., Venkataraman, C., Lammerding, J., Madzvamuse, A., et al. (2019). Cell migration through 3D confining pores: speed accelerations by deformation and recoil of the nucleus.

Kuntz, R.M., and Saltzman, W.M. (1997). Neutrophil motility in extracellular matrix gels: Mesh size and adhesion affect speed of migration. Biophys. J. *72*, 1472–1480.

Kupfer, a, Louvard, D., and Singer, S.J. (1982). Polarization of the Golgi apparatus and the microtubule-organizing center in cultured fibroblasts at the edge of an experimental wound. Proc. Natl. Acad. Sci. U. S. A. *79*, 2603–2607.

Kutys, M.L., and Yamada, K.M. (2014). An extracellular-matrix-specific GEF-GAP interaction regulates Rho GTPase crosstalk for 3D collagen migration. Nat. Cell Biol. *16*, 909–917.

Kuzuya, M., Satake, S., Ai, S., Asai, T., Kanda, S., Ramos, M.A., Miura, H., Ueda, M., and Iguchi, A. (1998). Inhibition of angiogenesis on glycated collagen lattices. Diabetologia *41*, 491–499.

Labernadie, A., Kato, T., Brugués, A., Serra-picamal, X., Derzsi, S., Arwert, E., Weston, A., González-tarragó, V., Elosegui-artola, A., Albertazzi, L., et al. (2017). A mechanically active heterotypic E-cadherin / N-cadherin adhesion enables fibroblasts to drive cancer cell invasion. Nat. Cell Biol. *19*.

Lämmermann, T., and Sixt, M. (2009). Mechanical modes of "amoeboid" cell migration. Curr. Opin. Cell Biol. *21*, 636–644.

Lauffenburger, D.A., and Horwitz, A.F. (1996). Cell migration: A physically integrated molecular process. Cell *84*, 359–369.

Lee, P.F., Bai, Y., Smith, R.L., Bayless, K.J., and Yeh, A.T. (2013). Angiogenic responses are enhanced in mechanically and microscopically characterized, microbial transglutaminase crosslinked collagen matrices with increased stiffness. Acta Biomater. *9*, 7178–7190.

Leight, J.L., Wozniak, M.A., Chen, S., Lynch, M.L., and Chen, C.S. (2012). Matrix rigidity regulates a switch between TGF-β1–induced apoptosis and epithelial–mesenchymal transition. Mol. Biol. Cell *23*, 781–791.

Leight, J.L., Alge, D.L., Maier, A.J., and Anseth, K.S. (2013). Direct measurement of matrix metalloproteinase activity in 3D cellular microenvironments using a fluorogenic peptide substrate. Biomaterials *34*, 7344–7352.

Leiss, M., Beckmann, K., Girós, A., Costell, M., and Fässler, R. (2008). The role of integrin binding sites in fibronectin matrix assembly in vivo. Curr. Opin. Cell Biol. *20*, 502–507.

Levental, K.R., Yu, H., Kass, L., Lakins, J.N., Egeblad, M., Erler, J.T., Fong, S.F.T., Csiszar, K., Giaccia, A., Weninger, W., et al. (2009). Matrix Crosslinking Forces Tumor Progression by

Enhancing Integrin Signaling. Cell *139*, 891–906.

Li, D., Wang, Y., and Xia, Y. (2003). Electrospinning of polymeric and ceramic nanofibers as uniaxially aligned arrays. Nano Lett. *3*, 1167–1171.

Li, L., Eyckmans, J., and Chen, C.S. (2017a). Designer biomaterials for mechanobiology. Nat. Mater. *16*, 1164–1168.

Li, S., Nih, L.R., Bachman, H., Fei, P., Li, Y., Nam, E., Dimatteo, R., Carmichael, S.T., Barker, T.H., and Segura, T. (2017b). Hydrogels with precisely controlled integrin activation dictate vascular patterning and permeability. Nat. Mater. *16*.

Li, Z., Chen, B., Dong, W., Kong, M., Fan, Z., Yu, L., Wu, D., Lu, J., and Xu, Y. (2019). MKL1 promotes endothelial-to-mesenchymal transition and liver fibrosis by activating TWIST1 transcription. Cell Death Dis. *10*, 1–13.

Liu, Y., Franco, A., Huang, L., Gersappe, D., Clark, R.A.F., and Rafailovich, M.H. (2009). Control of cell migration in two and three dimensions using substrate morphology. Exp. Cell Res. *315*, 2544–2557.

Liu, Y.J., Le Berre, M., Lautenschlaeger, F., Maiuri, P., Callan-Jones, A., Heuzé, M., Takaki, T., Voituriez, R., and Piel, M. (2015). Confinement and low adhesion induce fast amoeboid migration of slow mesenchymal cells. Cell *160*, 659–672.

Livne, A., and Geiger, B. (2016). The inner workings of stress fibers − from contractile machinery to focal adhesions and back. J. Cell Sci. *129*, 1293–1304.

Lo, C.M., Wang, H.B., Dembo, M., and Wang, Y.L. (2000). Cell movement is guided by the rigidity of the substrate. Biophys. J. *79*, 144–152.

Loebel, C, Mauck, RL, Burdick, J. (2019). Local nascent protein deposition and remodeling guide mesenchymal stromal cell mechanosensing and fate in three-dimensional hydrogels. Nat. Mater. *in press*, 1.

Loganathan, R., Rongish, B.J., Smith, C.M., Filla, M.B., Czirok, A., Bénazéraf, B., and Little, C.D. (2016). Extracellular matrix motion and early morphogenesis. Dev. *143*, 2056–2065.

Losordo, D.W., and Dimmeler, S. (2004). Therapeutic angiogenesis and vasculogenesis for ischemic disease. Part II: Cell-based therapies. Circulation *109*, 2692–2697.

Lutolf, M.P., Schmoekel, H.G., Metters, A.T., Weber, F.E., Fields, G.B., and Hubbell, J.A. (2003). Synthetic matrix metalloproteinase-sensitive hydrogels for the conduction of tissue regeneration : Engineering cell-invasion characteristics. Proc Natl Acad Sci U S A *100*, 5413–5418.

Luxton, G.W.G., and Gundersen, G.G. (2011). Orientation and function of the nuclear-centrosomal axis during cell migration. Curr. Opin. Cell Biol. *23*, 579–588.

Luxton, G.W.G., Gomes, E.R., Folker, E.S., Vintinner, E., and Gundersen, G.G. (2010). Linear arrays of nuclear envelope proteins harness retrograde actin flow for nuclear movement. Science *329*, 956–959.

Machacek, M., Hodgson, L., Welch, C., Elliott, H., Nalbant, P., Abell, A., Johnson, G.L., Hahn, K.M., and Danuser, G. (2009). Coordination of Rho GTPase activities during cell protrusion. Nature *461*, 99–103.

Magro, C.M., Waldman, W.J., Knight, D.A., Allen, J.N., Nadasdy, T., Frambach, G.E., Ross, P., and Marsh, C.B. (2006). Idiopathic Pulmonary Fibrosis Related to Endothelial Injury and Antiendothelial Cell Antibodies. Hum. Immunol. *67*, 284–297.

Maheshwari, G., Brown, G., Lauffenburger, D.A., Wells, A., and Griffith, L.G. (2000). Cell adhesion and motility depend on nanoscale RGD clustering. J. Cell Sci. *113*, 1677–1686.

Mao, A.S., Shin, J.W., Utech, S., Wang, H., Uzun, O., Li, W., Cooper, M., Hu, Y., Zhang, L., Weitz, D.A., et al. (2017). Deterministic encapsulation of single cells in thin tunable microgels for niche modelling and therapeutic delivery. Nat. Mater. *16*, 236–243.

Margolis, E.A., Cleveland, D.S., Kong, Y.P., Beamish, J.A., Wang, W.Y., Baker, B.M., and Putnam, A.J. (2021). Stromal cell identity modulates vascular morphogenesis in a microvasculature-on-a-chip platform. Lab Chip *21*, 1150–1163.

Martin, A., Komada, M.R., and Sane, D.C. (2003). Abnormal angiogenesis in diabetes mellitus. Med. Res. Rev. *23*, 117–145.

Martino, M.M., Briquez, P.S., Ranga, A., Lutolf, M.P., and Hubbell, J.A. (2013). Heparin-binding domain of fibrin(ogen) binds growth factors and promotes tissue repair when incorporated within a synthetic matrix. Proc. Natl. Acad. Sci. U. S. A. *110*, 4563–4568.

Martino, M.M., Brkic, S., Bovo, E., Burger, M., Schaefer, D.J., Wolff, T., Gürke, L., Briquez, P.S., Larsson, H.M., Gianni-Barrera, R., et al. (2015). Extracellular matrix and growth factor engineering for controlled angiogenesis in regenerative medicine. Front. Bioeng. Biotechnol. *3*, 45.

Mascharak, S., Benitez, P.L., Proctor, A.C., Madl, C.M., Hu, K.H., Dewi, R.E., Butte, M.J., and Heilshorn, S.C. (2016). YAP-dependent mechanotransduction is required for proliferation and migration on native-like substrate topography. Biomaterials *115*, 155–166.

Matera, D.L., Wang, W.Y., Smith, M.R., Shikanov, A., and Baker, B.M. (2019). Fiber Density Modulates Cell Spreading in 3D Interstitial Matrix Mimetics. ACS Biomater. Sci. Eng. *5*, 2965–2975.

Matera, D.L., DiLillo, K.M., Smith, M.R., Davidson, C.D., Parikh, R., Said, M., Wilke, C.A., Lombaert, I.M., Arnold, K.B., Moore, B.B., et al. (2020). Microengineered 3D pulmonary interstitial mimetics highlight a critical role for matrix degradation in myofibroblast differentiation. Sci. Adv. *6*, eabb5069.

McGregor, A.L., Hsia, C.R., and Lammerding, J. (2016). Squish and squeeze - the nucleus as a physical barrier during migration in confined environments. Curr. Opin. Cell Biol. *40*, 32–40.

Medici, D., Potenta, S., and Kalluri, R. (2011). Transforming growth factor-β2 promotes Snail-mediated endothelial - Mesenchymal transition through convergence of Smad-dependent and Smad-independent signalling. Biochem. J. *437*, 515–520.

Meehan, S., and Nain, A.S. (2015). Role of suspended fiber structural stiffness and curvature on single-cell migration, nucleus shape, and focal-adhesion-cluster length. Biophys. J. *107*, 2604–2611.

Mehta, D., and Malik, A.B. (2006). Signaling mechanisms regulating endothelial permeability. Physiol. Rev. *86*, 279–367.

Mescher, A.L. (2013). Junqueira's Basic Histology TEXT AND ATLAS.

Michaelis, U.R. (2014). Mechanisms of endothelial cell migration. Cell. Mol. Life Sci. *71*, 4131–4148.

Miller, J.S., Stevens, K.R., Yang, M.T., Baker, B.M., Nguyen, D.H.T., Cohen, D.M., Toro, E., Chen, A.A., Galie, P.A., Yu, X., et al. (2012). Rapid casting of patterned vascular networks for perfusable engineered three-dimensional tissues. Nat. Mater. *11*, 768–774.

Mirabella, T., Macarthur, J.W., Cheng, D., Ozaki, C.K., Woo, Y.J., Yang, M.T., and Chen, C.S. (2017). 3D-printed vascular networks direct therapeutic angiogenesis in ischaemia. Nat. Biomed. Eng. *1*, 0083.

Mitchison, T.J., Charras, G.T., and Mahadevan, L. (2008). Implications of a poroelastic cytoplasm for the dynamics of animal cell shape. Semin. Cell Dev. Biol. *19*, 215–223.

Moeendarbary, E., Valon, L., Fritzsche, M., Harris, A.R., Moulding, D.A., Thrasher, A.J., Stride, E., Mahadevan, L., and Charras, G.T. (2013). The cytoplasm of living cells behaves as a poroelastic material. Nat. Mater. *12*, 253–261.

Mohammed, S.F., Hussain, S., Mirzoyev, S.A., Edwards, W.D., Maleszewski, J.J., and Redfield, M.M. (2015). Coronary microvascular rarefaction and myocardial fibrosis in heart failure with preserved ejection fraction. Circulation *131*, 550–559.

Moissoglu, K., and Schwartz, M.A. (2006). Integrin signalling in directed cell migration. Biol. Cell *98*, 547–555.

Nagahashi, M., Ramachandran, S., Kim, E.Y., Allegood, J.C., Rashid, O.M., Yamada, A., Zhao, R., Milstien, S., Zhou, H., Spiegel, S., et al. (2012). Sphingosine-1-phosphate produced by sphingosine kinase 1 promotes breast cancer progression by stimulating angiogenesis and lymphangiogenesis. Cancer Res. *72*, 726–735.

Nakatsuji, N., and Johnson, K.E. (1984). Experimental manipulation of a contact guidance system in amphibian gastrulation by mechanical tension. Nature *307*, 453–455.

Natale, C.F., Ventre, M., and Netti, P.A. (2014). Tuning the material-cytoskeleton crosstalk via nanoconfinement of focal adhesions. Biomaterials *35*, 2743–2751.

Neto, F., Klaus-Bergmann, A., Ong, Y.T., Alt, S., Vion, A.C., Szymborska, A., Carvalho, J.R., Hollfinger, I., Bartels-Klein, E., Franco, C.A., et al. (2018). YAP and TAZ regulate adherens junction dynamics and endothelial cell distribution during vascular development. Elife *7*, 1–30.

Nguyen, D.-H.T., Stapleton, S.C., Yang, M.T., Cha, S.S., Choi, C.K., Galie, P. a, and Chen, C.S. (2013). Biomimetic model to reconstitute angiogenic sprouting morphogenesis in vitro. Proc. Natl. Acad. Sci. U. S. A. *110*, 6712–6717.

Nguyen, D.-H.T., Lee, E., Alimperti, S., Norgard, R.J., Wong, A., Lee, J.J.-K., Eyckmans, J., Stanger, B.Z., and Chen, C.S. (2019). A biomimetic pancreatic cancer on-chip reveals endothelial ablation via ALK7 signaling. Sci. Adv. *5*, eaav6789.

Van Nieuw Amerongen, G.P., Beckers, C.M.L., Achekar, I.D., Zeeman, S., Musters, R.J.P., and Van Hinsbergh, V.W.M. (2007). Involvement of Rho kinase in endothelial barrier maintenance. Arterioscler. Thromb. Vasc. Biol. *27*, 2332–2339.

Nimnual, A.S., Taylor, L.J., and Bar-Sagi, D. (2003). Redox-dependent downregulation of Rho by Rac. Nat. Cell Biol. *5*, 236–241.

Nobes, C.D., and Hall, A. (1995). Rho, Rac, and Cdc42 GTPases regulate the assembly of multimolecular focal complexes associated with actin stress fibers, lamellipodia, and filopodia. Cell *81*, 53–62.

Nourian Dehkordi, A., Mirahmadi Babaheydari, F., Chehelgerdi, M., and Raeisi Dehkordi, S. (2019). Skin tissue engineering: Wound healing based on stem-cell-based therapeutic strategies. Stem Cell Res. Ther. *10*, 1–20.

Novosel, E.C., Kleinhans, C., and Kluger, P.J. (2011). Vascularization is the key challenge in tissue engineering. Adv. Drug Deliv. Rev. *63*, 300–311.

Nowak-Sliwinska, P., Alitalo, K., Allen, E., Anisimov, A., Aplin, A.C., Auerbach, R., Augustin, H.G., Bates, D.O., van Beijnum, J.R., Bender, R.H.F., et al. (2018). Consensus guidelines for the use and interpretation of angiogenesis assays (Springer Netherlands).

Ohta, Y., Hartwig, J.H., and Stossel, T.P. (2006). FilGAP, a Rho- and ROCK-regulated GAP for Rac binds filamin A to control actin remodelling. Nat. Cell Biol. *8*, 803–814.

Oria, R., Wiegand, T., Escribano, J., Elosegui-Artola, A., Uriarte, J.J., Moreno-Pulido, C., Platzman, I., Delcanale, P., Albertazzi, L., Navajas, D., et al. (2017). Force loading explains spatial sensing of ligands by cells. Nature *552*, 219–224.

Osaki, T., Kakegawa, T., Kageyama, T., Enomoto, J., Nittami, T., and Fukuda, J. (2015). Acceleration of Vascular Sprouting from Fabricated Perfusable Vascular-Like Structures. PLoS One *10*, e0123735.

Padmanaban, V., Krol, I., Suhail, Y., Szczerba, B.M., Aceto, N., Bader, J.S., and Ewald, A.J. (2019). E-cadherin is required for metastasis in multiple models of breast cancer. Nature *573*, 439–444.

Paik, J.H., Chae Ss, S., Lee, M.J., Thangada, S., and Hla, T. (2001). Sphingosine 1-phosphate-induced endothelial cell migration requires the expression of EDG-1 and EDG-3 receptors and Rho-dependent activation of alpha vbeta3- and beta1-containing integrins. J. Biol. Chem. *276*, 11830–11837.

Pakshir, P., and Hinz, B. (2018). The big five in fibrosis: Macrophages, myofibroblasts, matrix, mechanics, and miscommunication. Matrix Biol. *68–69*, 81–93.

Palazzo, A.F., Joseph, H.L., Chen, Y.J., Dujardin, D.L., Alberts, A.S., Pfister, K.K., Vallee, R.B., and Gundersen, G.G. (2001). Cdc42, dynein, and dynactin regulate MTOC reorientation independent of Rho-regulated microtubule stabilization. Curr. Biol. *11*, 1536–1541.

Pang, X., Wu, J.P., Allison, G.T., Xu, J., Rubenson, J., Zheng, M.H., Lloyd, D.G., Gardiner, B., Wang, A., and Kirk, T.B. (2017). Three dimensional microstructural network of elastin, collagen, and cells in Achilles tendons. J. Orthop. Res. *35*, 1203–1214.

Pankov, R., Endo, Y., Even-Ram, S., Araki, M., Clark, K., Cukierman, E., Matsumoto, K., and Yamada, K.M. (2005). A Rac switch regulates random versus directionally persistent cell migration. J. Cell Biol. *170*, 793–802.

Park, D., Wershof, E., Boeing, S., Labernadie, A., Jenkins, R.P., George, S., Trepat, X., Bates, P.A., and Sahai, E. (2019). Extracellular matrix anisotropy is determined by TFAP2C-dependent regulation of cell collisions. Nat. Mater.

Parker, K.K., Brock, Amy Lepre Brangwynne, Robert J. Wang, N., Ostuni, Em., Geisse, Nicholas A.; Adams, J.C., Whitesides, G.M., and Ingber, D.E.. (2002). Directional control of lamellipodia extension by constraining cell shape and orienting cell tractional forces. FASEB J. *16*, 1195–1204.

Paszek, M.J., Zahir, N., Johnson, K.R., Lakins, J.N., Rozenberg, G.I., Gefen, A., Reinhart-King, C.A., Margulies, S.S., Dembo, M., Boettiger, D., et al. (2005). Tensional homeostasis and the malignant phenotype. Cancer Cell *8*, 241–254.

Patel, A.P., Tirosh, I., Trombetta, J.J., Shalek, A.K., Gillespie, S.M., Wakimoto, H., Cahill, D.P., Nahed, B. V, Curry, W.T., Martuza, R.L., et al. (2014). Single-cell RNA-seq highlights intratumoral heterogeneity in\nprimary glioblastoma. Science (80-.). *344*, 1396–1401.

Pathak, a., and Kumar, S. (2012). Independent regulation of tumor cell migration by matrix stiffness and confinement. Proc. Natl. Acad. Sci. *109*, 10334–10339.

Pathak, A., and Kumar, S. (2011). Biophysical regulation of tumor cell invasion: moving beyond matrix stiffness. Integr Biol *3*, 267–278.

Paul, C.D., Hung, W.-C., Wirtz, D., and Konstantopoulos, K. (2016a). Engineered Models of

Confined Cell Migration. Annu. Rev. Biomed. Eng. *18*, 159–180.

Paul, C.D., Mistriotis, P., and Konstantopoulos, K. (2016b). Cancer cell motility : lessons from migration in confined spaces. Nat. Publ. Gr. *17*, 131–140.

Pearson, K. (1895). Note on Regression and Inheritance in the Case of Two Parents. Proc. R. Soc. London *58*, 240–242.

Pelham, R.J., and Wang, Y.-L. (1997). Cell locomotion and focal adhesions are regulated by substrate flexibility. Proc. Natl. Acad. Sci. *94*, 13661–13665.

Pellegata, A.F., Tedeschi, A.M., and De Coppi, P. (2018). Whole organ tissue vascularization: Engineering the tree to develop the fruits. Front. Bioeng. Biotechnol. *6*, 56.

Perentes, J.Y., McKee, T.D., Ley, C.D., Mathiew, H., Dawson, M., Padera, T.P., Munn, L.L., Jain, R.K., and Boucher, Y. (2009). In vivo imaging of extracellular matrix remodeling by tumor-associated fibroblasts. Nat. Methods *6*, 143–145.

Petrie, R.J., and Yamada, K.M. (2012). At the leading edge of three-dimensional cell migration. J. Cell Sci. *125*, 5917–5926.

Petrie, R.J., Doyle, A.D., and Yamada, K.M. (2009). Random versus directionally persistent cell migration. Nat. Rev. Mol. Cell Biol. *10*, 538–549.

Petrie, R.J., Gavara, N., Chadwick, R.S., and Yamada, K.M. (2012). Nonpolarized signaling reveals two distinct modes of 3D cell migration. J. Cell Biol. *197*, 439–455.

Peyton, S.R., and Putnam, A.J. (2005). Extracellular Matrix Rigidity Governs Smooth Muscle Cell Motility in a Biphasic Fashion. *209*, 198–209.

Piera-Velazquez, S., Li, Z., and Jimenez, S.A. (2011). Role of endothelial-mesenchymal transition (EndoMT) in the pathogenesis of fibrotic disorders. Am. J. Pathol. *179*, 1074–1080.

Plotnikov, S. V., Pasapera, A.M., Sabass, B., and Waterman, C.M. (2012). Force fluctuations within focal adhesions mediate ECM-rigidity sensing to guide directed cell migration. Cell *151*, 1513–1527.

Polacheck, W.J., Zervantonakis, I.K., and Kamm, R.D. (2013). Tumor cell migration in complex microenvironments. Cell. Mol. Life Sci. *70*, 1335–1356.

Polacheck, W.J., Kutys, M.L., Yang, J., Eyckmans, J., Wu, Y., Vasavada, H., Hirschi, K.K., and Chen, C.S. (2017). A non-canonical Notch complex regulates adherens junctions and vascular barrier function. Nature *552*, 258–262.

Polacheck, W.J., Kutys, M.L., Tefft, J.B., and Chen, C.S. (2019). Microfabricated blood vessels for modeling the vascular transport barrier. Nat. Protoc. *14*, 1425–1454.

Pontes-Quero, S., Fernández-Chacón, M., Luo, W., Lunella, F.F., Casquero-Garcia, V., Garcia-

Gonzalez, I., Hermoso, A., Rocha, S.F., Bansal, M., and Benedito, R. (2019). High mitogenic stimulation arrests angiogenesis. Nat. Commun. *10*, 2016.

Potenta, S., Zeisberg, E., and Kalluri, R. (2008). The role of endothelial-to-mesenchymal transition in cancer progression. Br. J. Cancer *99*, 1375–1379.

Potente, M., Gerhardt, H., and Carmeliet, P. (2011). Basic and Therapeutic Aspects of Angiogenesis. Cell *146*, 873–887.

Pouthas, F., Girard, P., Lecaudey, V., Ly, T.B.N., Gilmour, D., Boulin, C., Pepperkok, R., and Reynaud, E.G. (2008). In migrating cells, the Golgi complex and the position of the centrosome depend on geometrical constraints of the substratum. J. Cell Sci. *121*, 2406–2414.

Provenzano, P.P., Eliceiri, K.W., Campbell, J.M., Inman, D.R., White, J.G., and Keely, P.J. (2006). Collagen reorganization at the tumor-stromal interface facilitates local invasion. BMC Med *4*, 38.

Provenzano, P.P., Inman, D.R., Eliceiri, K.W., Trier, S.M., and Keely, P.J. (2008). Contact guidance mediated three-dimensional cell migration is regulated by Rho/ROCK-dependent matrix reorganization. Biophys J *95*, 5374–5384.

Qu, F., Li, Q., Wang, X., Cao, X., Zgonis, M.H., Esterhai, J.L., Shenoy, V.B., Han, L., and Mauck, R.L. (2018). Maturation State and Matrix Microstructure Regulate Interstitial Cell Migration in Dense Connective Tissues. Sci. Rep. *8*, 3295.

Quinn, T.M., Dierickx, P., and Grodzinsky, A.J. (2001). Glycosaminoglycan network geometry may contribute to anisotropic hydraulic permeability in cartilage under compression. J. Biomech. *34*, 1483–1490.

Raab, M., Discher, D.E., Matthew Raab and Dennis E. Discher, Raab, M., and Discher, D.E. (2016). Matrix rigidity regulates the microtubule network polarization in migration. Cytoskeleton (Hoboken). 1–27.

Ramirez-San Juan, G.R., Oakes, P.W., and Gardel, M.L. (2017). Contact guidance requires spatial control of leading-edge protrusion. Mol. Biol. Cell *28*, 1043–1053.

Ray, A., Lee, O., Win, Z., Edwards, R.M., Alford, P.W., Kim, D.-H., and Provenzano, P.P. (2017a). Anisotropic forces from spatially constrained focal adhesions mediate contact guidance directed cell migration. Nat. Commun. *8*, 14923.

Ray, A., Slama, Z.M., Morford, R.K., Madden, S.A., and Provenzano, P.P. (2017b). Enhanced Directional Migration of Cancer Stem Cells in 3D Aligned Collagen Matrices. Biophys. J. *112*, 1023–1036.

Regen, C.M., and Horwitz, A.F. (1992). Dynamics of B1 integrin-mediated adhesive contacts in motile fibroblasts. J. Cell Biol. *119*, 1347–1359.

Rhee, S., Jiang, H., Ho, C.H., and Grinnell, F. (2007). Microtubule function in fibroblast

spreading is modulated according to the tension state of cell-matrix interactions. Proc. Natl. Acad. Sci. U. S. A. *104*, 5425–5430.

Riching, K.M., Cox, B.L., Salick, M.R., Pehlke, C., Riching, A.S., Ponik, S.M., Bass, B.R., Crone, W.C., Jiang, Y., Weaver, A.M., et al. (2015). 3D collagen alignment limits protrusions to enhance breast cancer cell persistence. Biophys. J. *107*, 2546–2558.

Ridley, A.J. (2001). Rho GTPases and cell migration. J Cell Sci *114*, 2713–2722.

Ridley, A.J. (2003). Cell Migration: Integrating Signals from Front to Back. Science (80-.). *302*, 1704–1709.

Ridley, A.J. (2015). Rho GTPase signalling in cell migration. Curr. Opin. Cell Biol. *36*, 103–112.

Ridley, A.J., and Hall, A. (1992). The small GTP-binding protein rho regulates the assembly of focal adhesions and actin stress fibers in response to growth factors. Cell *70*, 389–399.

Rochon, E.R., Menon, P.G., and Roman, B.L. (2016). Alk1 controls arterial endothelial cell migration in lumenized vessels. Development *143*, 2593–2602.

Rodriguez, L.L., and Schneider, I.C. (2013). Directed cell migration in multi-cue environments. Integr. Biol. *5*, 1306–1323.

Rosel, D., Fernandes, M., Sanz-Moreno, V., and Brábek, J. (2019). Migrastatics: Redirecting R&D in Solid Cancer Towards Metastasis? Trends in Cancer *5*, 755–756.

Rottner, K., Hall, A., and Small, J. V. (1999). Interplay between Rac and Rho in the control of substrate contact dynamics. Curr. Biol. *9*, 640–648.

Rouwkema, J., Koopman, B.F.J.M., Blitterswijk, C.A.V., Dhert, W.J.A., and Malda, J. (2009). Supply of nutrients to cells in engineered tissues. Biotechnol. Genet. Eng. Rev. *26*, 163–178.

Sabeh, F., Shimizu-Hirota, R., and Weiss, S.J. (2009). Protease-dependent versus-independent cancer cell invasion programs: Three-dimensional amoeboid movement revisited. J. Cell Biol. *185*, 11–19.

Sander, E.E., Ten Klooster, J.P., Van Delft, S., Van Der Kammen, R.A., and Collard, J.G. (1999). Rac downregulates Rho activity: Reciprocal balance between both GTPases determines cellular morphology and migratory behavior. J. Cell Biol. *147*, 1009–1021.

Schaks, M., Giannone, G., and Rottner, K. (2019). Actin dynamics in cell migration. Essays Biochem. *63*, 483–495.

Schmidt, S., and Friedl, P. (2010). Interstitial cell migration: Integrin-dependent and alternative adhesion mechanisms. Cell Tissue Res. *339*, 83–92.

Schultz, G.S., Davidson, J.M., Kirsner, R.S., Bornstein, P., and Herman, I.M. (2011). Dynamic

reciprocity in the wound microenvironment. Wound Repair Regen. *19*, 134–148.

Schütze, K., Maniotis, A., and Schliwa, M. (1991). The position of the microtubule-organizing center in directionally migrating fibroblasts depends on the nature of the substratum. Proc. Natl. Acad. Sci. U. S. A. *88*, 8367–8371.

Scott, J.E. (1988). Proteoglycan-fibrillar collagen interactions. Biochem. J. *252*, 313–323.

Sequeira, S.J., Soscia, D., Oztan, B., Mosier, A., Jean-Gilles, R., Gadre, A., Cady, N., Yener, B., Castracane, J., and Larsen, M. (2012). The regulation of focal adhesion complex formation and salivary gland epithelial cell organization by nanofibrous PLGA scaffolds. Biomaterials *33*, 3175–3186.

Shakiba, D., Alisafaei, F., Savadipour, A., Rowe, R.A., Liu, Z., Pryse, K.M., Shenoy, V.B., Elson, E.L., and Genin, G.M. (2020). The Balance between Actomyosin Contractility and Microtubule Polymerization Regulates Hierarchical Protrusions That Govern Efficient Fibroblast-Collagen Interactions. ACS Nano *14*, 7868–7879.

Shamloo, A., and Heilshorn, S.C. (2010). Matrix density mediates polarization and lumen formation of endothelial sprouts in VEGF gradients. Lab Chip *10*, 3061–3068.

Sharma, V.P., Beaty, B.T., Patsialou, A., Liu, H., Clarke, M., Cox, D., Condeelis, J.S., and Eddy, R.J. (2012). Reconstitution of in vivo macrophage-tumor cell pairing and streaming motility on one-dimensional micro-patterned substrates. Intravital (Print) *1*, 77–85.

Shin, D.S., Tokuda, E.Y., Leight, J.L., Miksch, C.E., Brown, T.E., and Anseth, K.S. (2018). Synthesis of Microgel Sensors for Spatial and Temporal Monitoring of Protease Activity. ACS Biomater. Sci. Eng. *4*, 378–387.

Siemann, D.W. (2011). The unique characteristics of tumor vasculature and preclinical evidence for its selective disruption by Tumor-Vascular Disrupting Agents. Cancer Treat. Rev. *37*, 63–74.

Skylar-Scott, M.A., Uzel, S.G.M., Nam, L.L., Ahrens, J.H., Truby, R.L., Damaraju, S., and Lewis, J.A. (2019). Biomanufacturing of organ-specific tissues with high cellular density and embedded vascular channels. Sci. Adv. *5*, eaaw2459.

Sokic, S., and Papavasiliou, G. (2012). Controlled Proteolytic Cleavage Site Presentation in Biomimetic PEGDA Hydrogels Enhances Neovascularization *In Vitro*. Tissue Eng. Part A *18*, 2477–2486.

Stewart, S.A., Dykxhoorn, D.M., Palliser, D., Mizuno, H., Yu, E.Y., An, D.S., Sabatini, D.M., Chen, I.S.Y., Hahn, W.C., Sharp, P. a, et al. (2003). Lentivirus-delivered stable gene silencing by RNAi in primary cells Lentivirus-delivered stable gene silencing by RNAi in primary cells. Rna *9*, 493–501.

Stroka, K.M., Jiang, H., Chen, S.H., Tong, Z., Wirtz, D., Sun, S.X., and Konstantopoulos, K. (2014). Water permeation drives tumor cell migration in confined microenvironments. Cell *157*, 611–623.

Swartz, M.A., Kaipainen, A., Netti, P.A., Brekken, C., Boucher, Y., J. Grodzinsky, A., and Jain, R.K. (1999). Mechanics of interstitial-lymphatic fluid transport: Theoretical foundation and experimental validation. J. Biomech. *32*, 1297–1307.

Swift, J., Ivanovska, I.L., Buxboim, A., Harada, T., Dingal, P.C.D.P., Pinter, J., Pajerowski, J.D., Spinler, K.R., Shin, J.W., Tewari, M., et al. (2013). Nuclear lamin-A scales with tissue stiffness and enhances matrix-directed differentiation. Science (80-.). *341*.

Takabe, K., Kim, R.H., Allegood, J.C., Mitra, P., Ramachandran, S., Nagahashi, M., Harikumar, K.B., Hait, N.C., Milstien, S., and Spiegel, S. (2010). Estradiol induces export of sphingosine 1-phosphate from breast cancer cells via ABCC1 and ABCG2. J. Biol. Chem. *285*, 10477–10486.

Tamura, M., Gu, J., Matsumoto, K., Aota, S., Parsons, R., and Yamada, K.M. (1998). Inhibition of Cell Migration, Spreading, and Focal Adhesions by Tumor Suppressor PTEN. Science (80-.). *280*, 1614–1617.

Tan, E.P.S., and Lim, C.T. (2016). Mechanical characterization of nanofibers – A review. Am. J. Org. Chem. *6*, 54–80.

Tan, X., Khaing Oo, M.K., Gong, Y., Li, Y., Zhu, H., and Fan, X. (2017). Glass capillary based microfluidic ELISA for rapid diagnostics. Analyst *142*, 2378–2385.

Thomson, K.S., Korte, F.S., Giachelli, C.M., Ratner, B.D., Regnier, M., and Scatena, M. (2013). Prevascularized microtemplated fibrin scaffolds for cardiac tissue engineering applications. Tissue Eng. - Part A *19*, 967–977.

Tibbitt, M.W., and Anseth, K.S. (2009). Hydrogels as extracellular matrix mimics for 3D cell culture. Biotechnol. Bioeng. *103*, 655–663.

Tien, J., Ghani, U., Dance, Y.W., Seibel, A.J., Karakan, M.Ç., Ekinci, K.L., and Nelson, C.M. (2020). Matrix Pore Size Governs Escape of Human Breast Cancer Cells from a Microtumor to an Empty Cavity. IScience *23*, 101673.

Di Tomaso, E., Capen, D., Haskell, A., Hart, J., Logie, J.J., Jain, R.K., McDonald, D.M., Jones, R., and Munn, L.L. (2005). Mosaic tumor vessels: Cellular basis and ultrastructure of focal regions lacking endothelial cell markers. Cancer Res. *65*, 5740–5749.

Tonnesen, M.G., Feng, X., and Clark, R.A.F.F. (2000). Angiogenesis in wound healing. J. Investig. Dermatology Symp. Proc. *5*, 40–46.

Traore, M.A., and George, S.C. (2017). Tissue Engineering the Vascular Tree. Tissue Eng. - Part B Rev. *23*, 505–514.

Trappmann, B., Baker, B.M., Polacheck, W.J., Choi, C.K., Burdick, J.A., and Chen, C.S. (2017). Matrix degradability controls multicellularity of 3D cell migration. Nat. Commun. *8*, 371.

Tseng, Q., Duchemin-Pelletier, E., Deshiere, A., Balland, M., Guillou, H., Filhol, O., and Thery, M. (2012). Spatial organization of the extracellular matrix regulates cell-cell junction

positioning. Proc. Natl. Acad. Sci. *109*, 1506–1511.

Turturro, M. V., Christenson, M.C., Larson, J.C., Young, D.A., Brey, E.M., and Papavasiliou, G. (2013). MMP-Sensitive PEG Diacrylate Hydrogels with Spatial Variations in Matrix Properties Stimulate Directional Vascular Sprout Formation. PLoS One *8*, e58897.

Vaeyens, M.M., Jorge-Peñas, A., Barrasa-Fano, J., Steuwe, C., Heck, T., Carmeliet, P., Roeffaers, M., and Van Oosterwyck, H. (2020). Matrix deformations around angiogenic sprouts correlate to sprout dynamics and suggest pulling activity. Angiogenesis 1–10.

Valenzi, E., Bulik, M., Tabib, T., Morse, C., Sembrat, J., Trejo Bittar, H., Rojas, M., and Lafyatis, R. (2019). Single-cell analysis reveals fibroblast heterogeneity and myofibroblasts in systemic sclerosis-associated interstitial lung disease. Ann. Rheum. Dis. *78*, 1379–1387.

Vernon, R.B., and Sage, E.H. (1999). A novel, quantitative model for study of endothelial cell migration and sprout formation within three-dimensional collagen matrices. Microvasc. Res. *57*, 118–133.

Vigen, M., Ceccarelli, J., and Putnam, A.J. (2014). Protease-sensitive PEG hydrogels regulate vascularization in vitro and in vivo. Macromol. Biosci. *14*, 1368–1379.

Vining, K.H., and Mooney, D.J. (2017). Mechanical forces direct stem cell behaviour in development and regeneration. Nat. Rev. Mol. Cell Biol. *18*, 728–742.

Vogel, V., and Sheetz, M. (2006). Local force and geometry sensing regulate cell functions. Nat. Rev. Mol. Cell Biol. *7*, 265–275.

Wang, H., Abhilash, A.S., Chen, C.S., Wells, R.G., and Shenoy, V.B. (2015). Long-range force transmission in fibrous matrices enabled by tension-driven alignment of fibers. Biophys. J. *107*.

Wang, N., Tytell, J.D., and Ingber, D.E. (2009). Mechanotransduction at a distance: mechanically coupling the extracellular matrix with the nucleus. Nat. Rev. Mol. Cell Biol. *10*, 75–82.

Wang, W., Kent III, R.N., Huang, S.A., Jarman, E.H., Shikanov, E.H., Davidson, C.D., Hiraki, H.L., Lin, D., Wall, M.A., Shin, J.-W., et al. (2021a). Direct Comparison of Angiogenesis in Natural and Synthetic Biomaterials Reveals Matrix Porosity Regulates Endothelial Cell Invasion Speed and Sprout Diameter. SSRN Electron. J.

Wang, W.Y., Pearson, A.T., Kutys, M.L., Choi, C.K., Wozniak, M.A., Baker, B.M., and Chen, C.S. (2018). Extracellular matrix alignment dictates the organization of focal adhesions and directs uniaxial cell migration. APL Bioeng. *2*, 046107.

Wang, W.Y., Davidson, C.D., Lin, D., and Baker, B.M. (2019). Actomyosin contractility-dependent matrix stretch and recoil induces rapid cell migration. Nat. Commun. *10*, 1186.

Wang, W.Y., Lin, D., Jarman, E.H., Polacheck, W.J., and Baker, B.M. (2020). Functional angiogenesis requires microenvironmental cues balancing endothelial cell migration and

proliferation. Lab Chip *20*, 1153–1166.

Wang, W.Y., Jarman, E.H., Lin, D., and Baker, B.M. (2021b). Dynamic Endothelial Stalk Cell–Matrix Interactions Regulate Angiogenic Sprout Diameter. Front. Bioeng. Biotechnol. *9*, 620128.

Waterman-Storer, C.M., Gregory, J., Parsons, S.F., and Salmon, E.D. (1995). Membrane/microtubule tip attachment complexes (TACs) allow the assembly dynamics of plus ends to push and pull membranes into tubulovesicular networks in interphase Xenopus egg extracts. J. Cell Biol. *130*, 1161–1169.

Weaver, J.D., Headen, D.M., Hunckler, M.D., Coronel, M.M., Stabler, C.L., and García, A.J. (2018). Design of a vascularized synthetic poly(ethylene glycol) macroencapsulation device for islet transplantation. Biomaterials *172*, 54–65.

Webb, D.J., Parsons, J.T., and Horwitz, A.F. (2002). Adhesion assembly, disassembly and turnover in migrating cells -- over and over and over again. Nat. Cell Biol. *4*, E97-100.

Wei, Y., Ji, Y., Xiao, L.L., Lin, Q. kui, Xu, J. ping, Ren, K. feng, and Ji, J. (2013). Surface engineering of cardiovascular stent with endothelial cell selectivity for in vivo re-endothelialisation. Biomaterials *34*, 2588–2599.

Wei, Z., Schnellmann, R., Pruitt, H.C., and Gerecht, S. (2020). Hydrogel Network Dynamics Regulate Vascular Morphogenesis. Cell Stem Cell *27*, 798-812.e6.

Weigelin, B., Bakker, G.-J., and Friedl, P. (2012). Intravital third harmonic generation microscopy of collective melanoma cell invasion. IntraVital *1*, 32–43.

Weiss, A., and Attisano, L. (2013). The TGFbeta superfamily signaling pathway. Wiley Interdiscip. Rev. Dev. Biol. *2*, 47–63.

Welch-Reardon, K.M., Ehsan, S.M., Wang, K., Wu, N., Newman, A.C., Romero-Lopez, M., Fong, A.H., George, S.C., Edwards, R.A., and Hughes, C.C.W. (2014). Angiogenic sprouting is regulated by endothelial cell expression of Slug. J. Cell Sci. *127*, 2017–2028.

Welch-Reardon, K.M., Wu, N., and Hughes, C.C.W. (2015). A role for partial endothelial-mesenchymal transitions in angiogenesis? Arterioscler. Thromb. Vasc. Biol. *35*, 303–308.

West, J.L., and Hubbell, J.A. (1999). Polymeric Biomaterials with Degradation Sites for Proteases Involved in Cell Migration. Macromolecules *32*, 241–244.

Wimmer, R.A., Leopoldi, A., Aichinger, M., Wick, N., Hantusch, B., Novatchkova, M., Taubenschmid, J., Hämmerle, M., Esk, C., Bagley, J.A., et al. (2019). Human blood vessel organoids as a model of diabetic vasculopathy. Nature *565*, 505–510.

Wipff, P.J., Rifkin, D.B., Meister, J.J., and Hinz, B. (2007). Myofibroblast contraction activates latent TGF-B1 from the extracellular matrix. J. Cell Biol. *179*, 1311–1323.

Wisdom, K.M., Adebowale, K., Chang, J., Lee, J.Y., Nam, S., Desai, R., Rossen, N.S., Rafat,

M., West, R.B., Hodgson, L., et al. (2018). Matrix mechanical plasticity regulates cancer cell migration through confining microenvironments. Nat. Commun. *9*, 1–13.

Wolf, K., and Friedl, P. (2011). Extracellular matrix determinants of proteolytic and non-proteolytic cell migration. Trends Cell Biol. *21*, 736–744.

Wolf, K., Wu, Y.I., Liu, Y., Geiger, J., Tam, E., Overall, C., Stack, M.S., and Friedl, P. (2007). Multi-step pericellular proteolysis controls the transition from individual to collective cancer cell invasion. Nat. Cell Biol. *9*, 893–904.

Wolf, K., Alexander, S., Schacht, V., Coussens, L.M., von Andrian, U.H., van Rheenen, J., Deryugina, E., and Friedl, P. (2009). Collagen-based cell migration models in vitro and in vivo. Semin. Cell Dev. Biol. *20*, 931–941.

Wood, L.B., Ge, R., Kamm, R.D., and Asada, H.H. (2012). Nascent vessel elongation rate is inversely related to diameter in in vitro angiogenesis. Integr. Biol. (Camb). *4*, 1081–1089.

Wozniak, M.A., Modzelewska, K., Kwong, L., and Keely, P.J. (2004). Focal adhesion regulation of cell behavior. Biochim. Biophys. Acta - Mol. Cell Res. *1692*, 103–119.

Wu, J., Wu, X., and Lin, F. (2013). Recent developments in microfluidics-based chemotaxis studies. Lab Chip *13*, 2484–2499.

Xie, J., Bao, M., Bruekers, S.M.C., and Huck, W.T.S. (2017). Collagen Gels with Different Fibrillar Microarchitectures Elicit Different Cellular Responses. ACS Appl. Mater. Interfaces *9*, acsami.7b03883.

Xu, J., Rodriguez, D., Petitclerc, E., Kim, J.J., Hangai, M., Moon Yuen, S., Davis, G.E., Brooks, P.C., Yuen, S.M., Davis, G.E., et al. (2001). Proteolytic exposure of a cryptic site within collagen type IV is required for angiogenesis and tumor growth in vivo. J. Cell Biol. *154*, 1069–1079.

Yamada, K.M., and Sixt, M. (2019). Mechanisms of 3D cell migration. Nat. Rev. Mol. Cell Biol. *20*, 738–752.

Yazdani, S., Bansal, R., and Prakash, J. (2017). Drug targeting to myofibroblasts: Implications for fibrosis and cancer. Adv. Drug Deliv. Rev. *121*, 101–116.

Yoon, C., Choi, C., Stapleton, S., Mirabella, T., Howes, C., Dong, L., King, J., Yang, J., Oberai, A., Eyckmans, J., et al. (2019). Myosin IIA–mediated forces regulate multicellular integrity during vascular sprouting. Mol. Biol. Cell *30*, 1974–1984.

Yu, Y., and Chau, Y. (2012). One-step “click” method for generating vinyl sulfone groups on hydroxyl-containing water-soluble polymers. Biomacromolecules *13*, 937–942.

Zaman, M.H., Trapani, L.M., Sieminski, A.L., Siemeski, A., Mackellar, D., Gong, H., Kamm, R.D., Wells, A., Lauffenburger, D., Matsudaira, P., et al. (2006). Migration of tumor cells in 3D matrices is governed by matrix stiffness along with cell-matrix adhesion and proteolysis. Proc. Natl. Acad. Sci. U. S. A. *103*, 10889–10894.

Zeisberg, E.M., Tarnavski, O., Zeisberg, M., Dorfman, A.L., McMullen, J.R., Gustafsson, E., Chandraker, A., Yuan, X., Pu, W.T., Roberts, A.B., et al. (2007). Endothelial-to-mesenchymal transition contributes to cardiac fibrosis. Nat. Med. *13*, 952–961.

Zhu, J., and Clark, R.A.F. (2014). Fibronectin at Select Sites Binds Multiple Growth Factors and Enhances their Activity : Expansion of the Collaborative ECM-GF Paradigm. J. Invest. Dermatol. *134*, 895–901.